On the Interaction between a Tunnel Boring Machine and the Surrounding Soil

PROEFSCHRIFT

ter verkrijging van de graad van doctor
aan de Technische Universiteit Delft,
op gezag van de Rector Magnificus prof. ir. K.C.A.M. Luyben,
voorzitter van het College voor Promoties,
in het openbaar te verdedigen op donderdag 8 januari 2015 om 10.00 uur
door Daniele FESTA

Laurea in Ingegneria Civile
University of Bologna

geboren te Faenza - Italië

Dit proefschrift is goedgekeurd door de promotor:
Prof. ir. J.W. Bosch

Copromotor:
Dr.ir. W. Broere

Samenstelling promotiecommissie:

Rector Magnificus,	Technische Universiteit Delft, voorzitter
Prof. ir. J.W. Bosch,	Technische Universiteit Delft, promotor
Dr. ir. W. Broere,	Technische Universiteit Delft, copromotor
Prof. dr. ir. J.G. Rots,	Technische Universiteit Delft
Dr. ir. K.J. Bakker,	Technische Universiteit Delft
Prof. dr. A. Gens,	Universitat Politècnica de Catalunya
Prof. dr. ir. A. Bezuijen,	Universiteit Gent
Prof. dr. -Ing. M. Thewes,	Ruhr-Universität Bochum
Prof. dr. ir. T. Heimovaara,	Technische Universiteit Delft, reservelid

Printed by:
Sieca Repro
Turbineweg 20
2627 BP Delft
The Netherlands
Telephone: +31 15 256 19 19
E-mail: sieca@sieca.nl

ISBN 978-90-823282-0-2

Printed in The Netherlands

Abstract

This thesis investigates the mechanical equilibrium of a Tunnel Boring Machine (TBM) driving in soft soil. The interaction between the TBM-shield and the soil is also investigated. The analysis is based on monitoring data gathered during the construction of the Hubertus tunnel in The Hague, Netherlands. The monitoring activities during tunnel construction are discussed in detail. Special care is given to explain how the recorded data can be processed in order to verify a number of physical processes induced by the TBM-shield advance. TBM-data (machine data) and soil monitoring data (from inclinometers and extensometers) are examined.

A kinematic model of TBM-shield behaviour is constructed from theoretical and geometrical considerations. The consequences of driving a TBM-shield in a curve are highlighted and validated against the TBM monitoring data. It is demonstrated how the kinematic model can provide the displacement history of the soil induced by the TBM-shield. Such displacements, referred to as shield-soil interface displacements, are processed further with a twofold purpose. On the one hand they are converted into stresses acting on the shield periphery in order to study the mechanical equilibrium of the TBM-shield. On the other hand the interface displacements are propagated through the soil such as to derive a customized pattern of induced soil displacement.

Stresses, forces and moments acting on the TBM are covered in detail. The focus is first on the forces intentionally applied to drive the TBM. Referred to as *active forces*, those are continuously measured, under the direct control of the TBM operator, and can be obtained from the machine monitoring data without difficulty. The active forces are counterbalanced by the *passive forces* which represent the soil reaction and can be obtained processing the shield-soil interface displacements with an appropriate soil reaction model.

The soil reaction model is derived from the analysis of the response of a horizontal cavity undergoing axial expansion, contraction, or a sequence of them. The resulting soil reaction curves are an upgrade of the simple linear subgrade reaction modulus and capture the soil non-linearity and the different responses in case of virgin loading or unloading-reloading. The curves are obtained through the interpolation and extrapolation of the results of Finite Elements analyses. Analytical formulations extend the results to any stress/strain combination within the limits of validity of the model. The proposed curves show limitations but allow the construction of a simplified numerical model which proves a good alternative to conducting more accurate but complex Finite Elements calculations at every advance step.

The reasoning and calculations underlying the decision not to take the shield-tail deformability into account are discussed.

Active and passive forces are combined and the equilibrium of the TBM-shield is considered. It is discussed which model features produce favourable conditions to the achievement of static equilibrium and which others may still hinder it. A quantitative assessment of the influence of the tail-void grouting is undertaken and uncertainties regarding the soil stiffness are discussed. The observed imbalances involving the static equilibrium are questioned.

The calculated interface displacements and those monitored into the soil are correlated. Where correlation is weak alternative explanations are proposed, including the penetration of pressurized grout mortar into the interspace between the TBM-shield and the excavated geometry. It is observed that a considerable amount of the total tunnelling induced soil displacements occurs during the phase of temporary support. It is also demonstrated that the pattern of the induced displacements is more articulated than assumed in the volume-loss scheme. That is the obvious consequence of the use of the mechanised shield tunnelling technique, the specific construction sequence of which sets it apart from the conditions for which the volume loss scheme was originally proposed.

Samenvatting

Dit proefschrift beschouwt het evenwicht van een Tunnel Boormachine (TBM) die zich voortbeweegt in slappe grond en de interactie met de omringende grond. De analyse is gebaseerd op data die is verzameld gedurende de bouw van de Hubertus Tunnel in Den Haag. Het monitoren tijdens de bouw is in detail beschouwd met aandacht hoe de opgenomen data kan worden gebruikt om een aantal fysieke processen te verifiëren, welke geïnduceerd zijn door het TBM-schild dat voortbeweegt door de grond. Zowel TBM-data (machine data) als grondmonitoringsdata (van inclinometers en extensometers) worden besproken.

Op basis van theoretische en geometrische afwegingen is een kinematisch model van het gedrag van een TBM-schild afgeleid. Dit model laat de effecten van sturen van het schild langs bochten zien en is gevalideerd met de gemonitorde TBM-data. Het kinematische model laat de accurate rekgeschiedenis zien die het schild veroorzaakt in de omliggende grond. De rekken, aangeduid als verplaatsingen op het raakvlak tussen schil en grond, zijn verder beschouwd met een tweedelig doel. Aan de ene kant worden de verplaatsingen verwerkt in een bijpassend grondreactiemodel, en omgezet in de overeenkomstige grondspanningen. Aan de andere kant wordt de (voortplanting van) verplaatsingen door de grond berekend om de deformatie rond het schild te bepalen.

Vervolgens is het systeem van spanningen, krachten en momenten die worden uitgeoefend op de TBM beschouwd. De focus is eerst op de actieve krachten gelegd; de krachten die zijn toegepast om de TBM aan te drijven en die daarom continu berekend worden en onder directe controle van de TBM-operator vallen. Gedemonstreerd wordt hoe de actieve krachten uit de machine monitoringsdata gehaald kunnen worden. De actieve krachten vormen een kant van de krachten op de TBM. Aan de andere kant zijn er passieve krachten. Dit zijn grondreacties verkregen door het combineren van de schild-grond interface verplaatsingen met een geschikt grondreactiemodel.

Het grondreactiemodel beschrijft de specifiek geometrische configuratie van een holte die een axiale symmetrische verplaatsing ondergaat (uitzetting of krimp). De resulterende grondreactiecurves zijn een uitbreiding van de simpele lineaire veerstijfheid reactiemodulus en beschrijven de niet-lineariteit van de bodem en de gevolgen in het geval van virgin loading of een unloading-reloading situatie. De grondreactiecurves zijn verkregen door het interpoleren en extrapoleren van een aantal eindige elementen analyses. Analytische formuleringen hebben de resultaten uitgebreid naar spanning-rek relaties binnen de modelgrenzen. De voorgestelde curves laten de limitaties van het model zien, maar maken een versimpeld numeriek model mogelijk in plaats van het uitvoeren van meer nauwkeurige, maar complexere eindige elementen berekenin-

gen bij elke stap. De invloed van schild-staartvervormingen is beschouwd en deze vervormingen zijn verder verwaarloosd.

Vervolgens worden de actieve krachten gecombineerd met de spanningen die verkregen zijn uit de kinematische interfaceverplaatsingen en het grondreactie model resulterend in een evenwichtsbeschouwing van het TBM-schild. Hierna wordt besproken welke aspecten van het model positief danwel negatief invloed hebben op het bereiken van het evenwicht. Vervolgens wordt de invloed van grouten in de staartspleet beschouwd als ook de invloed va de grondstijfheid en er wordt kritisch gekeken naar de geobserveerde tekortkomingen in de evenwichtsbeschouwing.

De berekende en gemeten interfaceverplaatsingen in de grond zijn gecorreleerd. Waar correlaties zwak zijn is een alternatieve modellering voorgesteld, met daarin de infiltratie van grout onder hoge druk in de staart van de TBM tussen het schild en het opgravingsprofiel. Gedurende een aanzienlijke deel van de boring treden grondverplaatsingen op tijdens de fase van tijdelijke ondersteuning. Deze verplaatsingen wijken af van het patroon zoals in de volumeverlies beschouwing aangenomen. Dat blijkt een duidelijk gevolg te zijn van het gebruik van een mechanisch tunnelboorschild, waarbij de specifieke volgorde van constructie afwijkt van de omstandigheden waar het model van volumeverlies was opgesteld.

Contents

In memory of Fabrizio and Mauro

Chapter 1

Introduction

Tunnel Boring Machines (TBMs) are used to construct tunnels in increasingly challenging environments (Maidl et al. [25]). There are at present hardly any technically and economically viable alternatives to TBMs when a tunnel has to be excavated underneath a built-up area founded on soft soil, especially underneath existing buildings. However, although TBM-tunnelling widely proves to be effective and socially accepted (Lancea and Anderson [24]), the public over the years has been setting increasingly stricter standards on tunnel designers, TBM manufacturers, and contractors in order to obtain optimal tunnelling performance with minimal influence on the surrounding structures and to reduce the costs for mitigating measures. Predictive risk analyses play a central role between tunnelling professionals and the public since both political and technical decisions are based upon them.

Risk analyses are performed during the design stage to predict how the tunnel construction will affect its surroundings. The prediction of the tunnelling-induced soil displacements at ground level and below is a crucial aspect of such analyses. However, most predictions remain based upon experience gained from previous projects in similar soil conditions, therefore often lacking adequate case-specificity (Mair and Taylor [29]). The expected level of risk is often defined through a range of so called *volume loss* rates recorded at other projects in similar circumstances. The volume loss is then processed via empirical (Peck [37]), analytical (Verruijt [48]), or numerical analyses (Komiya et al. [22], Sugimoto and Sramoon [42], Sugimoto et al. [43], Nagel [32]) to derive the expected absolute and differential displacements of the surrounding soil and buildings (Kaalberg and Hentschel [19], Mair et al. [28], Netzel [34]). Finally, it is judged whether the project is technically feasible and socially acceptable based on criteria of acceptable damage (Mair [30]) and on economic considerations.

In Mair and Taylor [29] the practical value of the empirical method was recognized, at least when previous case histories of tunnelling in similar ground conditions using similar construction techniques are available. In the same work a major limitation of the empirical method was found to be in selecting an appropriate value of volume loss. The value of closed form solutions was also recognized as useful prediction method although limited to elastic-perfectly plastic continua under axisymmetric conditions. In [29] it was also underscored that finite element analyses are commonly used in engineering practice but that sophisticated soil models are required to achieve realistic predictions of the shape and width of the transverse settlement trough. Non-linearity, K_0, and anisotropy were pointed out to have meaningful implications on the model outcome. The value of physical modelling was finally acknowledged with special reference to centrifuge testing.

In the framework of the volume loss-based approaches, settlement predictions are hardly correlated with aspects such as the TBM features and its real kinematic behaviour when driving through the soil. The complexity of tunnel-boring is often merged into a single but comprehensive parameter basically describing a convergence of the excavated geometry. The result is a model that captures little of the actual tunnel boring process and which can only be reliably used to estimate the resulting settlements for a range of input volume losses. In fact, such models cannot be used to figure out which processes occur during construction. Neither can they be used to study the separate influence of each construction process on ground settlement and soil deformation. The disregard concerning the consequences of the TBM's features and its operation is surprising considering that longitudinal settlement profiles often show that a significant part of the overall induced settlements is related to the shield transit. This is shown, among others, by the shield-soil interaction models by Sugimoto and Sramoon [42], Kasper and Meschke [21], Nagel et al. [33], and Standing and Selemetas [40].

In Sugimoto and Sramoon [42] a model for the shield-soil kinematic interaction was introduced as well as an embryonic soil-reaction model targeting the specific problem of shield-soil interaction. The Authors concluded that the soil displacements occurring at the excavated surface play an important role in the immediate soil movements during shield tunnelling. They also added that in order to investigate soil movements for all stages of shield tunnel constructions it is necessary to take into account all field conditions such as pressure at the face and behind the shield tail, imperfection of backfill grouting, and consolidation or creep of the grout.

The work by Sugimoto and Sramoon [42] was in turn based on a previous study by Sugimoto and Luong [41] in which an attempt was made to derive a number of soil parameters from a numerical model of mechanical equilibrium of the TBM. In that study Sugimoto and Luong derived the coefficient of earth pressure at rest, the coefficients of soil reaction in vertical and horizontal direction, the mobilized friction rate on the shield-skin in circumferential direction, and the coefficient of skin friction in dynamic conditions from a numerical model encompassing a number of loads acting on the shield, among which were the forces on the shield skin.

Bezuijen and Talmon ([3] [44]), supported by measurement results, hypothesised the penetration of the process fluids (face support slurry and tail grout) around the shield periphery. They observed that overcutting at the tunnel face can lead to bentonite flow over the TBM-shield from the face towards the tail. Similarly, pressurized tail-grout usually injected at higher pressure than the total soil stress can displace the soil surrounding the TBM and flow towards the front. In this respect grout on the TBM-shield was observed several times at the end of tunnelling operations. The flow of process fluids is likely to affect the stress distribution around the TBM-shield. The Authors also formulated a number of challenging propositions concerning for example the exact position of the TBM during the tunnelling process, the interaction between the TBM and the lining, and the predicted pressures around the TBM, and they recognized that as long as such aspects remain unsolved more sophisticated numerical calculations will present the same uncertainties.

Nagel [32], in turn based on Kasper [20], proposed an algorithm for the implementation in a Finite Elements code of the tunnel construction sequence, including aspects of the phase of temporary support by the TBM-shield. A parametric study was performed in which the influence of the process parameters on the surface settlements, the soil deformations, and the loading of the lining tube was demonstrated. Among others, results from their theoretical model demonstrated that the flow of process fluids around the TBM has a large influence onto the surface settlements, but also on the shape of the settlement trough and the required jacking forces. Their simulation results also demonstrated that a simplified modelling of the contact between TBM and soil may lead to significantly different settlement results.

Ninič and Meschke [35] recognized the difficult applicability of fully 3D finite element models to real time practical cases. The Authors considered that lighter computational models need to be developed in order to achieve efficient simulation-supported real-time steering. In this framework the authors propose to train an Artificial Neural Network by means of a full scale simulation model for a certain tunnel section during the design stage. As result expensive and time-requiring 3D numerical simulations can be replaced in the construction stage by pre-trained Neural Networks for the purpose e.g. of real-time predictions of surface settlements, parameter identification, and process optimization.

While on the one hand volume loss-based methods are useful to assess the overall effect of tunnelling, on the other hand they are arguable when employed for studying the physical causes of the induced soil displacements. The volume loss approach remains popular among engineers probably due to an incomplete understanding of the physics governing the interaction between the TBM-shield and the surrounding soil. The same lack of understanding is perhaps the underlying cause of the resilience of the trial-and-error TBM driving procedure which still requires the utmost care by the driving crews. For scientists, this is unsatisfying.

1.1 Outline of the thesis

This thesis focuses on the interaction between the TBM-shield and the surrounding soil. The shield-soil interaction problem is isolated from the construction sequence which also involves the soil excavation and support at the shield front (Broere [5]), the tunnel lining response to the applied soil stresses (Hashimoto et al. [18]), and the tail-grout consolidation and hardening within the tail gap. The analysis is thus confined to the phase of temporary support of the surrounding soil. The boundaries of the temporary support phase are the transit of the front and rear ends of the TBM-shield across a hypothetical transversal cross section. An improved understanding of the processes occurring at the shield-soil interface during the phase of temporary support will contribute to improve the overall reliability of the tunnel boring process.

The shield-soil interaction is studied by means of a numerical model for the static equilibrium of the TBM. It is considered that the advancing shield goes through consecutive configurations of static equilibrium which implies that all applied forces and moments are constantly in mechanical balance. The driving forces are applied to move and steer the shield and are balanced by external reactions exerted by the surrounding soil and, when present, by the groundwater and other process fluids. Only the case of drained response of a granular material is illustrated in this study. That is consistent with sandy soil as mostly encountered at the location of the case study presented in Chapter 2.

The groundwater-induced uplift force obeys Archimedes' principle. The reaction of the surrounding soil depends upon the characteristics of the soil and its stress-deformation state. Whereas the initial state of the soil is determined by its deposition history and possible previous human activities, the tunnelling induced stress-strain changes are determined by the sequence of tunnel construction operations. A considerable amount of those changes is expected to be due to the specific driving pattern of the TBM-shield within the geometry excavated at its front.

The exact shape of the excavated geometry and the accurate position and orientation of the shield are determined at every advance stage by means of a so-called shield kinematic model. Comparing the location of the excavated geometry and that of the shield surface allows quantifying the amount of soil compression and relaxation at the interface between the shield and the soil. The so-obtained shield-soil interface displacements are the input for a soil reaction model which in turn provides the distribution of the soil stresses at the shield periphery. The stresses are finally combined with the driving actions and the shield equilibrium is evaluated.

This work is based on the monitoring data collected during the construction of the Hubertus Tunnel, a double-tube road tunnel located in The Hague, Netherlands. The tunnel, completed in 2007, was selected for the combined availability of the TBM and soil-displacement monitoring data and for the overall good quality of both. The tunnel was excavated by means of a slurry-shield type machine. TBM monitoring data provided information on multiple physical processes among which are the following: spatial position and orientation of the TBM-shield; pressures in the hydraulic cylinders by means of which internal and external forces are applied; tensions and currents in the electro-mechanic installations; hydraulic pressure of the face support fluid and of the grout mortar. Chapter 2 provides a comprehensive review.

The focal point of this research is on the TBM, as most of the monitoring data available are machine-related. However, once decent equilibrium is achieved, the perspective is reversed and the effect of the shield on the surrounding soil investigated. This allows validating the kinematic model against independently measured horizontal and vertical soil displacements.

The monitoring data serves two purposes. First the recorded parameters and their accuracy determine what kind of numerical model can be derived. Second, different data sets are used for cross-validating the proposed model. A number of monitoring data serves as input to the model whereas other data is compared against the output to verify the new model.

Chapter 2

The Hubertus tunnel and its monitoring data

2.1 Case study: the Hubertus tunnel

The Hubertus tunnel, constructed between 2006 and 2007 in The Hague, Netherlands, consists of two parallel tubes, North and South, each containing two car lanes. Situated in a residential area, the tunnel passes close to the foundations of some residential houses and underpasses low buildings on a barracks. At the west-end it underpasses a manmade sand dune, the Hubertusduin.

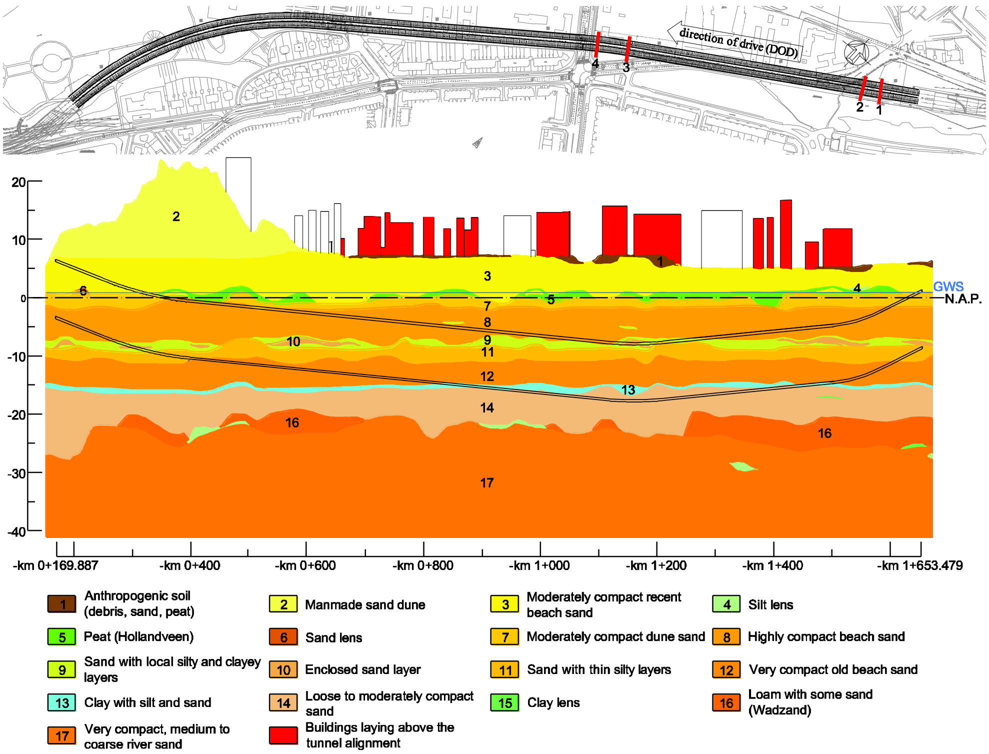

Figure 2.1: Plan view and stratigraphy of the south tube. Qualitative description of the geologic units and indication of the instrumented monitoring sections

The Hubertus tunnel was excavated using one single slurry-shield TBM for both tubes. The machine was provided by Herrenknecht AG. The North and South tubes are 1,496.81 m and 1,483.59 m long, respectively. The TBM had a non-articulated 10,680 mm long shield, with a front diameter of 10,510 mm, and a rear one of 10,490 mm (i.e. with a radial tapering of 10 mm). A permanent radial overcut of 10 mm was used. The cutting wheel, supported by a longitudinally displaceable spherical bearing, was handled via three sets of hydraulic cylinders. A cross section of the TBM with indication of the main mechanical components is shown in Figure 2.2.

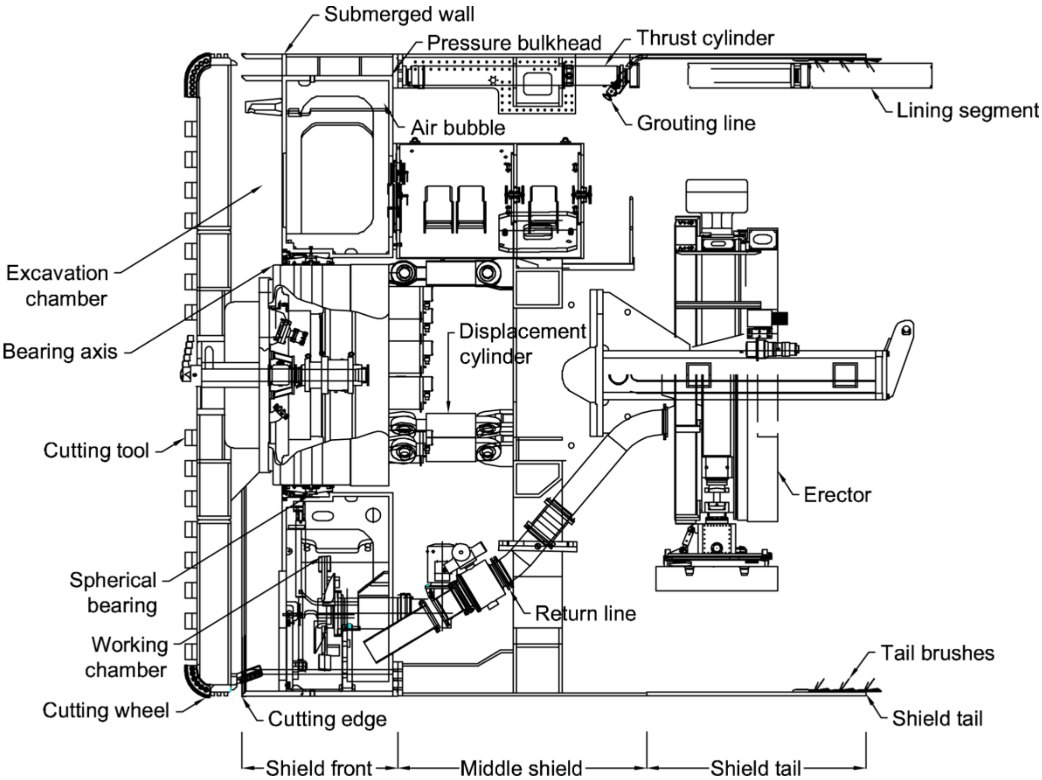

Figure 2.2: Cross section of the TBM used at Hubertus tunnel

The permanent lining is formed by 2 m long prefab reinforced-concrete elements, with an external diameter of 10,200 mm. Each ring is formed by 7 elements and a key stone. The theoretical tail-void gap is 145 mm. The tail-void was grouted via the upper four of the six injection openings available at the shield tail.

The sharpest horizontal curve, with a curvature radius of 542.3 m, is located in the south alignment and was bored in leftward direction. At its deepest point the tunnel axis is located 27.73 m below surface, at about -12.82 m N.A.P. (Dutch Reference System approximately equivalent to Mean Sea Level). The groundwater table is assumed at +1.0 m N.A.P.. A reference stratigraphic profile of the Hubertus tunnel is provided in Figure 2.1. In the plan view, four cross-sections indicate the locations where extensometers and inclinometers were installed.

The tunnel was bored mainly through sand with varying degree of density. Some geotechnical parameters are summarized in Table 2.1. The upper and lower limits are provided for each parameter, according to the statistical analysis indicated in NEN 6740 and recalled in the Geotechnical Base Report [46] and Geotechnical Interpretation Report [47]. According to the method the real values have 90% likelihood to fit within the indicated interval.

Table 2.1: Geotechnical units

Layer #	Layer name	q_c [Mpa]	γ_{dry} [kN/m^3]	γ_{sat} [kN/m^3]	c' [kPa]	φ' [°]
1	Anthropogenic soil	0.1 2.0	16.8 19.2	17.8 20.2	0	25 31.4
2	Manmade sand dune	4.1 13.6	14.0 16.8	18.7 20.2	0	26.9 39.6
3	Moderately compact recent beach sand	3.5 13.7	14.7 16.2	19.0 19.9	0	32.6 36.2
4	Silt lens	1.0 8.2	13.0 14.4	18.0 18.9	0	25.0 31.4
5	Peat (Hollandveen)	1.1 3.2	1.7 6.9	9.5 13.3	10 15	15.0 18.8
6	Sand lens	2.9 7.4	12.8 14.6	17.3 19.6	0	30.0 37.7
7	Moderately compact dune sand	6.9 15.6	13.9 15.8	17.8 20.1	0	31.0 38.9
8	Highly compact beach sand	17.3 38.7	14.9 15.7	19.2 19.6	0	35.6 43.4
9	Sand with local silty and clayey layers	2.4 15.3	12.6 15.8	17.7 19.7	0	25.3 38.2
10	Enclosed sand layers	4.9 21.9	13.9 15.8	17.7 20.3	0	30.0 37.7
11	Sand with thin silty layers	9.4 19.5	14.9 16.1	19.2 19.9	0	27.7 35.8
12	Very compact old beach sand	21.0 40.1	15.1 16.1	19.3 19.9	0	32.6 41.6
13	Clay with silt and sand	3.1 7.8	14.1 16.1	18.1 20.5	0	28.0 35.2
14	Loose to moderately compact sand	11.1 22.9	14.4 15.7	18.9 19.7	0	28.3 36.7
15	Clay lens	1.6 5.1	4.5 5.1	11.4 12.9	10 15	25.0 31.4
16	Loam with some sand	6.1 13.5	11.1 14.0	16.8 18.6	0	27.5 34.5
17	Very compact, medium to coarse river sand	28.2 52.2	15.1 16.1	19.3 19.9	0	38.0 47.7

Figure 2.3: West entrance (courtesy of Siemens AG – Reference Number: soicmol201408-11)

Figure 2.4: East entrance (courtesy of Siemens AG – Reference Number: soicmol201408-10)

2.2 TBM monitoring data

The machine data is stored in separate computer files, each pertaining to the drive for one single ring. The south and north tubes consist of 742 and 749 rings, respectively. The instant of ring change, and implicitly of file change, was selected manually by the TBM driver by inputting the process status parameter. The process status indicates which part of the tunnel construction sequence is taking place (e.g. advance, ring erection, intermediate stop, end of boring, etc.). 262 different data (channels) was logged every 5 to 6 seconds, as is shown in the parameter list in Appendix A.

The logged data covers, among others, the shield position and orientation, the operation of the cutting wheel and of the advance cylinders, the process fluids (face support fluid and tail grout mortar), the excavated material, and the tail sealant (grease). Only a selection of the overall machine data is of practical use for this research. Also, not all data is recorded continuously. For instance the shield positioning data is not collected during ring building although the position changes.

The machine data concerning the entire south tube consists of 1,690,075 rows of data which, with 262 channels for each log, leads to 442,799,650 values. For the north alignment the number of rows is slightly larger, totalling 1,748,054, which leads to 457,990,148 values. Filtering is necessary for removing overlaps and reducing the computation time. Different filters are applied for the kinematic and for the static analysis.

Düllmann et al. [10] indicate that the TBM monitoring data should always be checked against their actual physical meaning. The Authors highlight that without such control the risk is real of giving false data interpretation. Accordingly, also in this work an effort is made to validate the monitoring data against the physical processes that those represent.

2.2.1 *Kinematic analysis*

A distance-based data filter is applied for the kinematic analysis. The logged progressive distance is observed to often remain constant at two or more consecutive readings. That happens during ring building, when the positioning system is switched off, but also during minor stops. Additionally, in case of low advance rates inaccuracies in the positioning system may even indicate small rearward movements.

As this research mainly aims to study the process of shield advance unique increasing shield-advance values are selected. That reduces by about 77% the size of the original data-set, at least with reference to the south tube. This simplification is adopted whenever time-related processes are deemed not relevant for the analysis.

The TBM driving strategy is based on two reference points, located inside the TBM-shield, which are due to follow the design alignment. The deviations of the two reference points from the alignment are logged during advance (see also Chapter 3). When multiple recordings with the same advance are encountered, the one with the largest logged deviations is selected and the others discarded.

The information on tunnel advance derived from the shield positioning system is combined with the logged extension of the advance cylinders. The cylinders' extension is the most reliable indicator of shield advance, but is limited by the reset which takes place at the start of each ring. With a superior precision (± 1 mm), the cylinders' extensions perfectly integrate and refine the spatial positioning data. For each ring, the advance increment as from the shield positioning system is "normalized" by dividing it by the advance increment over the same ring as measured by the advance cylinders. The initial and final shield advances are derived from the shield positioning system, while the intermediate advances are obtained via the cylinders' extensions "normalized" by means of the above ratio.

When time-dependent physical processes are studied the full data-set is used. That is the case for instance for the separation of the excavated soil from the support fluid, as presented in Chapter 3. As the circulation of excavation fluid goes on during standstill, distance-based filtering would hide valuable information.

Unrealistic scatters affecting the deviations of the TBM reference points are removed by means of two data filters: the first filter removing the deviations exceeding 100 mm, which were observed not having physical sense in this project; the second checking the increment of the monitored deviations. If the difference between two consecutively recorded deviations is larger than 6 mm, then the latest of the two is skipped and the first following log is checked.

The positioning system was recalibrated every few tens of metres of advance during construction. The distance between two recalibration events is based, among others, on the line of sight between the optical targets and on the curvature of the tunnel alignment. Accuracy often decreases over the stretch between two recalibration events and the cumulated error is only recognized at the end of it. The logged monitoring data may therefore indicate sudden shifts of the TBM-position which did not occur. Lack of log books for recalibration activity means this cannot be settled conclusively, but useful considerations are introduced below and in Chapter 8.

2.2.2 Static analysis

A filter is applied before processing the logged pressures and forces data. Based on the process status, only the data logged during actual advance is retained.

The tail-void grouting pressures are regularized by a running average over the preceding and following five values, providing a more regular pattern (see Figure 2.5). At the TBM-face, two of the four pressure gauges for the support fluid pressure went out of order after about 700 m of drive in the south tube. The corresponding values are dismissed along the entire south alignment.

Other logged parameters do not show peculiarities requiring extensive filters. However, local irregularities may always occur and a qualitative overview of the general trends points out the need for manual removal of measuring faults.

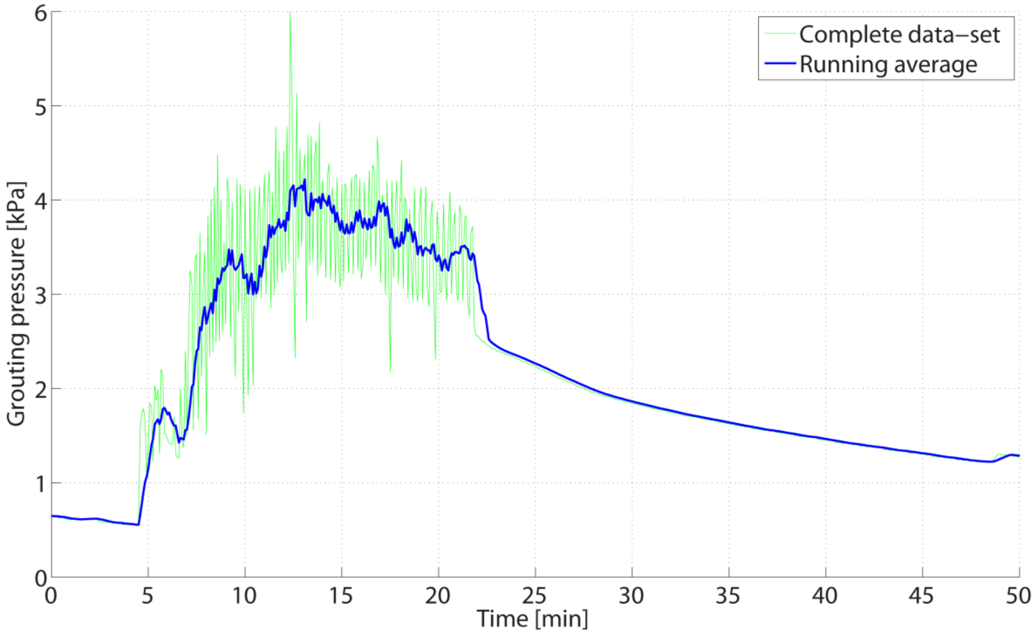

Figure 2.5: Regularization of the monitored grouting pressures at a sample advance

2.3 The TBM positioning system

The positioning system consists of measuring devices and reference points located both inside the shield and along the tunnel lining. A laser-signal receiving box (ALTU in Figure 2.6) is located in the upper part of the shield around mid-shield. The ALTU, equipped with two target plates and two inclinometers, provides position and orientation of the machine. The two reference points meant to follow the planned tunnel alignment lie along the longitudinal axis of the shield, the front one in the plane of the shield face, and the rear one in the same plane where the ALTU is also located (RPF and RPR, respectively). Figures 2.7 and 2.8 show the total station, usually located few metres up to tens of metres behind the TBM-shield, and a reference point placed along the permanent tunnel, respectively.

Every 5 seconds the monitoring system provides the TBM operator with the actual position of the reference points versus the optimal one. Horizontal and vertical deviations from the planned alignment are arbitrarily given positive values for rightward and upward deviations, respectively. The system also provides other (i.e. tendencies, pitch, roll, yaw).

Operators aim to follow the design alignment with both target points. However, that is not always possible as it sometimes requires high driving forces paired with the risk of damaging the concrete lining. In those cases it may be preferable to keep a slightly skewed orientation of the machine when this involves smaller driving forces. The skewing required for a smooth drive may differ in direction and amount along the alignment. Understanding and modelling these driving configurations is an implicit aim of this research.

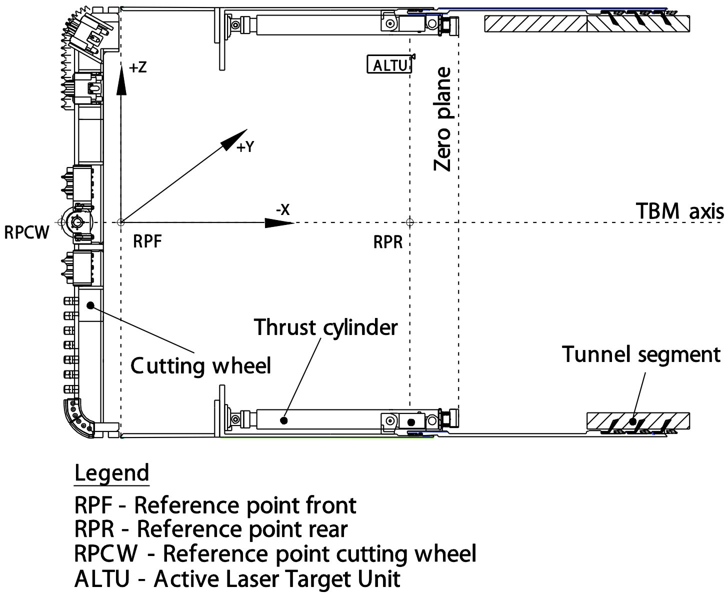

Figure 2.6: Shield positioning system (courtesy of VMT GmbH)

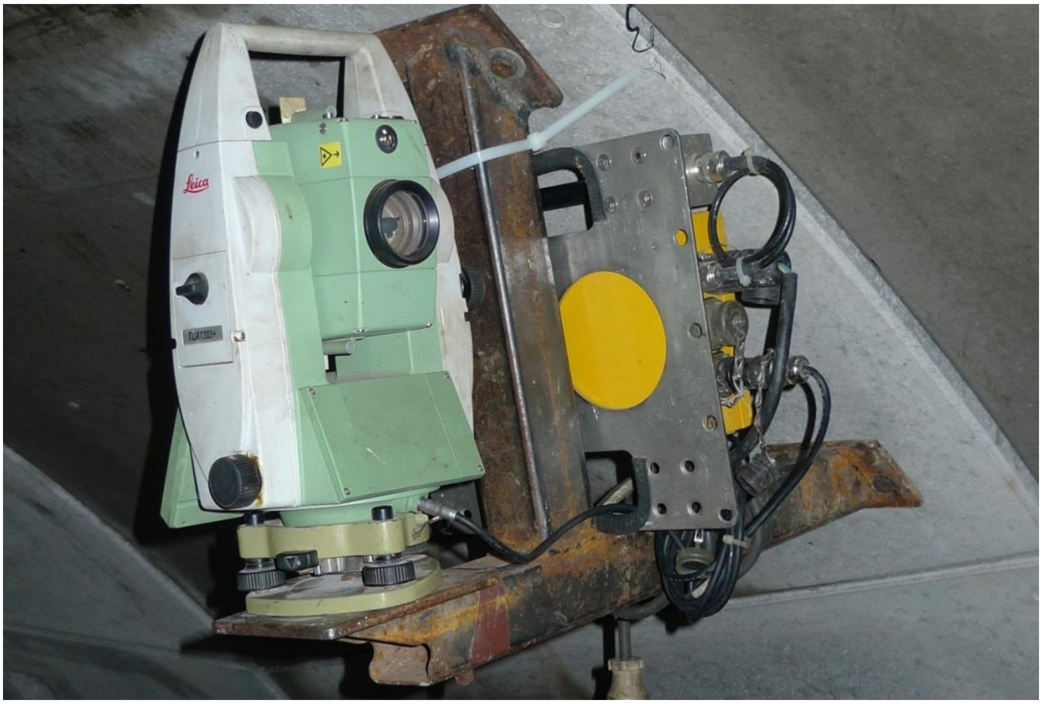

Figure 2.7: Total station (usually from few metres up to few tens of metres behind the shield)

Figure 2.8: A reference point along the tunnel (behind the total station)

2.4 Monitored soil displacements

Surface and subsurface soil displacements were captured by means of automatic measuring systems. Inclinometers and extensometers were installed in separate dedicated boreholes. On top of each borehole a reference point provided absolute vertical and horizontal displacements.

For the south alignment the extensometer and inclinometer readings are stored in 1585 and 1992 separate computer files, respectively. The files are named after their log time. The displacements of the reference points on top of the boreholes are stored in additional 3485 files, also named after their log time. Extensometer and inclinometer sensors are identified by a unique code which is used to match the information distributed among the different files.

Extensometer data reports the evolution in time of the distance between consecutive points in each extensometer borehole. The average distance between two consecutive measuring points was about 2 m. Extensometer monitoring data was initially provided in the form of distances, whereas in reality electrical frequencies are measured (vibrating wire sensors) and then converted into distances by means of correlation formulas. Raw monitoring data was only subsequently provided and reprocessed, however confirming the validity of the initial input.

Inclinometer monitoring data indicates the angle to the vertical of the line connecting two consecutive points in the inclinometer borehole. The raw data reports electrical signals which can be converted into angles by means of correlation formulas. The angles can be further transformed to indicate the relative horizontal displacement between two consecutive points. Also in this case processed data was initially provided and raw data was obtained only at a later moment. The reprocessing of the raw data indicates the presence of anomalies among the data-set initially provided, the origin of which cannot be clearly stated. A set of manual measurements performed during construction validates the displacement profile as obtained from the reprocessing of the raw data.

2.5 Shield-tail deformability

TBM-shields are usually stiffer at the front and more deformable at the rear side. The Hubertus TBM was no exception in this sense. Although the shield-skin was actually thicker at the rear than at the front (60 mm versus 50 mm), the higher rigidity of the front part was due to the presence of internal reinforcing elements like the bulkhead wall and other structural elements. A completely stiff front section and a deformable rear section are assumed in the analysis for simplicity. The passage from stiff to deformable shield is fixed at 4.272 m from the shield front, in accordance with the TBM design drawings.

The deformability of the shield tail was investigated earlier by, among others, Van der Vliet [50] and Verruijt [49].

Verruijt considered the problem of the elastic deformation of a circular cylinder due to a relatively small initial load and a relatively large isotropic pressure. The Author modelled the cylinder as a circular ring supported by linear springs, with the springs representing the interaction with the surrounding soil. The cylinder was supposed to represent the steel tail skin of a tunnelling machine, although with the stiffening effect of the shield at one end of the cylinder disregarded. The basic data of his study were selected to represent the tail skin of the Westerschelde tunnelling machine. Verruijt found that the elastic displacements of the ring should remain in the order 15 mm, and that the stresses in the cylinder remain well below the yield limit of the steel.

Van der Vliet combined analytical and numerical analyses to find that the interaction between TBM and surrounding soil depends on shield shape (tapering), process parameters such as slurry pressure, overcut and grout injection pressure, and soil properties (stress level and stiffness). The Author also observed that under certain circumstances the TBM may lose contact with the soil, giving space for slurry or grout to penetrate and load the shield from the outside. As long as the TBM remains in contact with soil, the elastic foundation prevents large deformations by providing enough bedding. Without soil support however the shield becomes sensitive to large deformations, anisotropic loading and buckling.

The TBM-shield deformability is investigated here by means of a 3D FEM analysis conducted with the commercial software COMSOL Multiphysics 4.3. The TBM-shield is modelled like a frustum (truncated cone) with 5.255 m and 5.245 m front and rear radius, respectively. The 10,680 m long frustum is subdivided in 10 by 36 rectangular sectors, as in Figure 2.9. The subdivision allows to assign distinct properties to each sector. A fictional skin thickness of 250 mm is assigned to the first four rings starting from the front in order to represent the stiff shield behaviour in that sector. The actual thickness of 60 mm is assigned to the remainder of the shield length. Material continuity between front and rear part is assured. Displacements of the shield front are impeded but rotations are free. A 2.05 GPa Young's modulus and a 0.28 Poisson's ratio are assumed for the steel of which the TBM-shield is made.

The shield-tail deformability is of special interest in relation to the stiffness of the surrounding soil. From the kinematic analysis of Chapter 4 the calculated shield-soil interface displacements are derived assuming a rigid shield. The interface displacements which induce soil compression are reduced if the shield deforms as consequence of the newly applied stress. The actual compressive interface displacements depend on the shield-tail and soil deformability.

The problem is simplified by ideally connecting springs to the sectors in which the frustum is discretized. The springs are pre-deformed as initial condition. When released, the initial deformation redistributes between the springs, which represent the soil, and the shield, proportionally to their reciprocal stiffness. The effect of different spring stiffness is studied.

In the first load configuration different pre-deformation levels are assigned to three regions, each made up of eight elementary sectors (Figure 2.10). Pre-deformations of 10, 20, and 30 mm are assigned in increasing order from the front towards the tail. In Figures 2.12 to 2.16 the shield deformation at five different levels of spring stiffness is simulated (1 to 50 MPa/m).

The spring stiffness indicated here must not be confused with the elastic modulus of the soil. The spring stiffness is in fact equivalent to the subgrade reaction modulus. In Section 5.2.4 it is demonstrated that 12.5 MPa/m already represents a high value of subgrade modulus corresponding to a soil stiffness of ${E_{50}}^{ref} = 40$ MPa at the usual tunnel depths. The investigated range of spring stiffness therefore covers the real values for the undrained behaviour of a granular material.

In Figure 2.14, which refers to a spring modulus of 10 MPa/m, the shield deformation appears not disregardable, with a peak of 13.5 mm. However, with a closer look at the loading-unloading patterns in Section 5.2 we conclude that the upper limit of 12.5 MPa/m for the subgrade reaction modulus only applies to horizontal displacements with 200 kPa radial initial effective stress. These conditions combined are never encountered in the case study. When the radial position deviates from the horizontal one or for lower initial stress the subgrade modulus drops sharply. With lower subgrade modulus, shield deformations of few millimetres are expected, more in line with those indicated in Figures 2.12 and 2.13.

The applied pre-deformation pattern considered in this example is more severe than encountered in reality. Soil compression is in real cases less localised, thus distributed over larger sectors of the shield. More distributed loads cause more modest shield deformations due to the arching effect with which the shield resists to the applied stresses. This is demonstrated applying the pre-deformations of Figure 2.10 in combination with those of Figure 2.17. The shield deforms in this case as in Figure 2.18, which compared to Figure 2.14 makes us conclude that with less concentrated loads the shield deformation is even more modest. Some results are summarized in Table 2.2. According to this line of reasoning the shield-tail deformability is disregarded in the remainder of the analysis, being in many cases limited to few millimetres.

Table 2.2: Maximum shield deformations

Spring modulus [MPa/m]	Load type	Max. shield deformation [mm]
1	Concentrated (Figure 2.10)	2.5
5	Concentrated (Figure 2.10)	9.1
10	Concentrated (Figure 2.10)	13.5
10	Distributed (Figure 2.17)	6.4
20	Concentrated (Figure 2.10)	18.0
50	Concentrated (Figure 2.10)	22.7

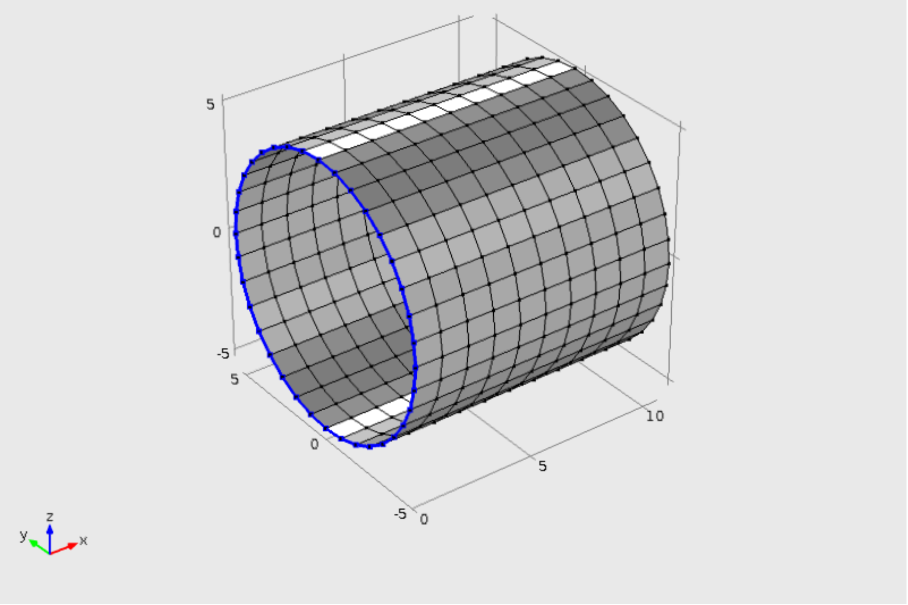

Figure 2.9: Fixed constraints

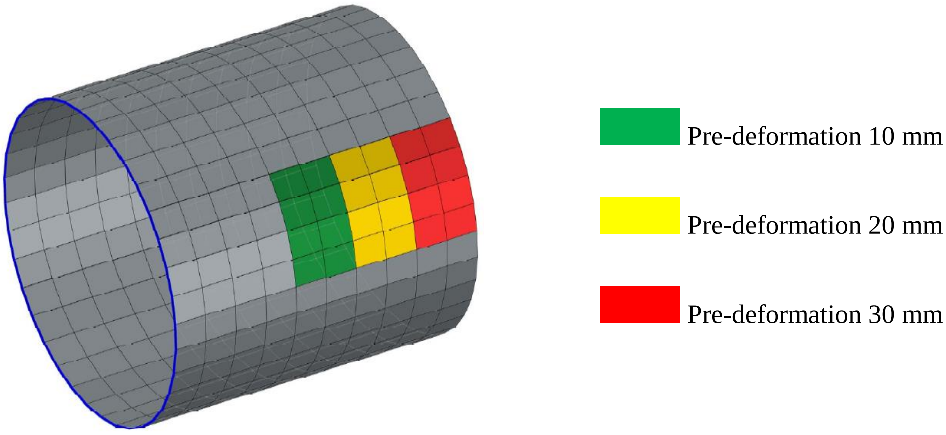

Figure 2.10: Sample loading. Concentrated pre-deformations

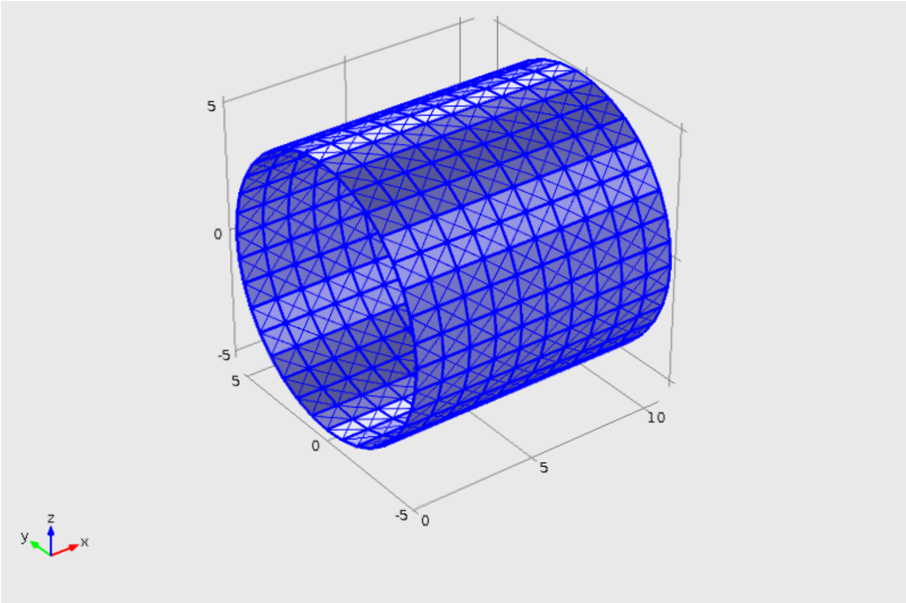

Figure 2.11: FEM mesh

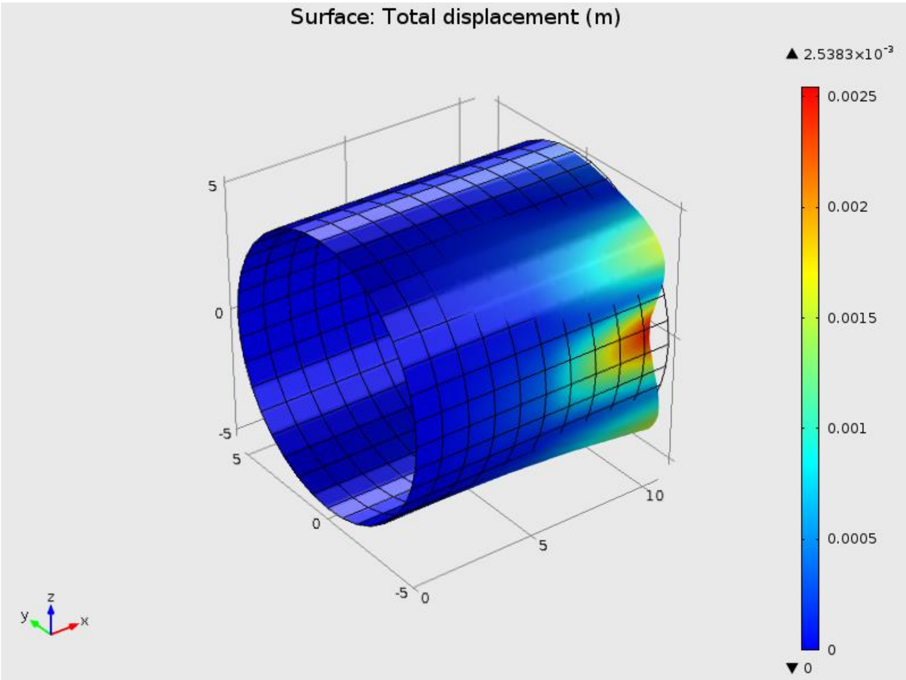

Figure 2.12: k = 1 MPa/m. Applied displacements: see Figure 2.10

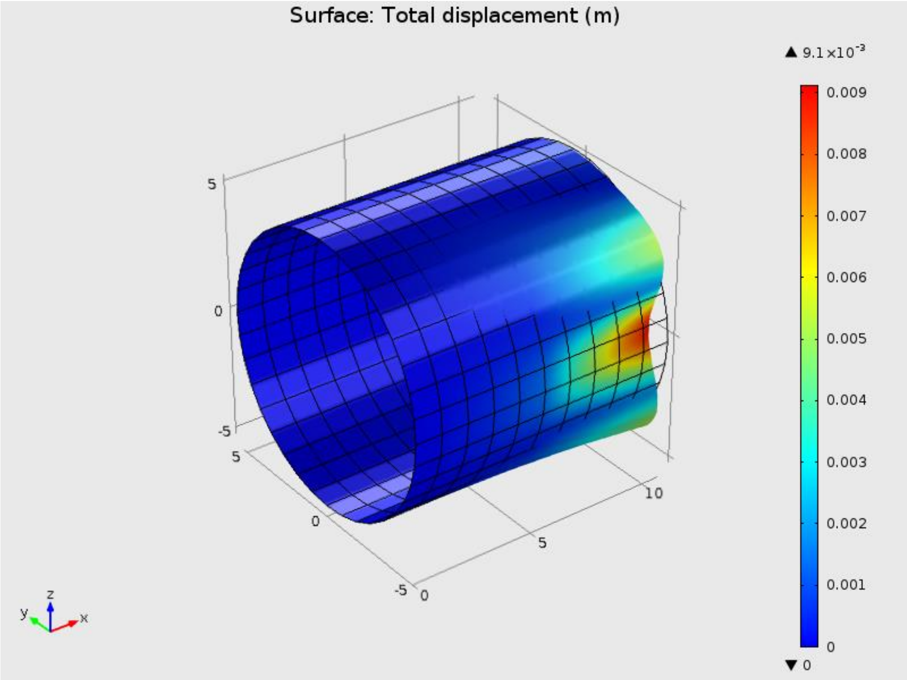

Figure 2.13: k = 5 MPa/m. Applied displacements: see Figure 2.10

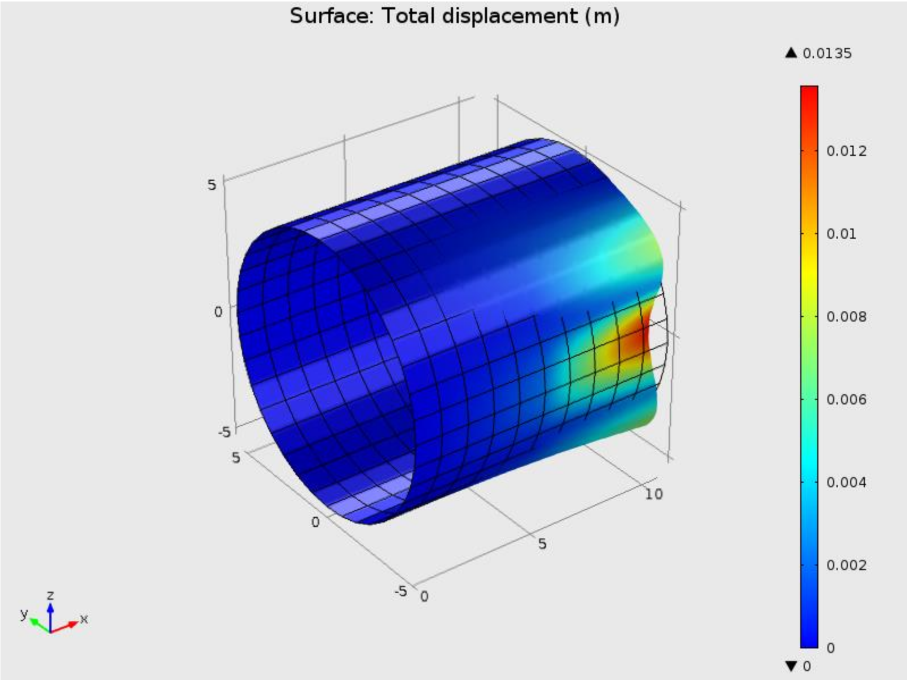

Figure 2.14: k = 10 MPa/m. Applied displacements: see Figure 2.10

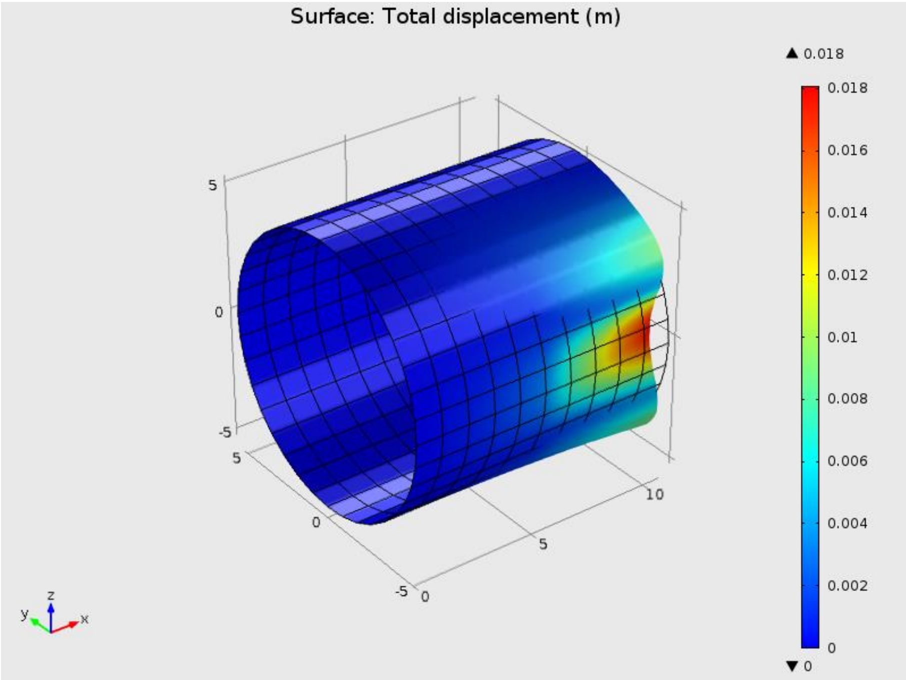

Figure 2.15: k = 20 MPa/m. Applied displacements: see Figure 2.10

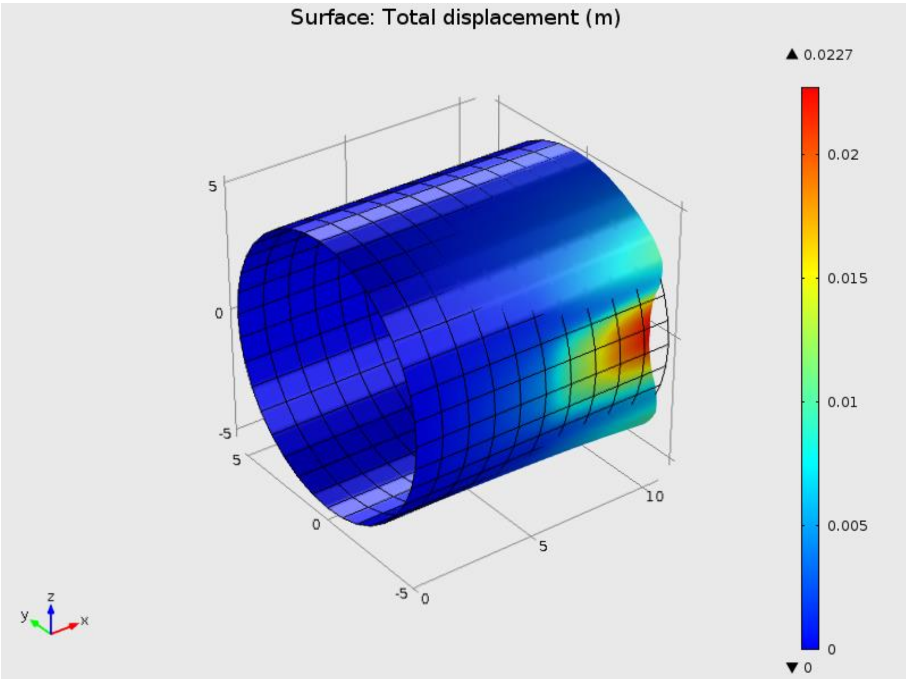

Figure 2.16: k = 50 MPa/m. Applied displacements: see Figure 2.10

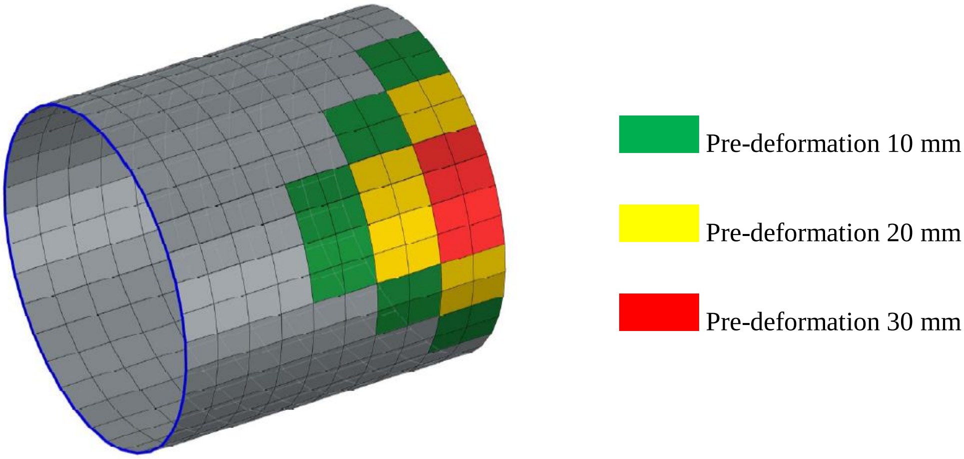

Figure 2.17: Sample loading. Distributed pre-deformations

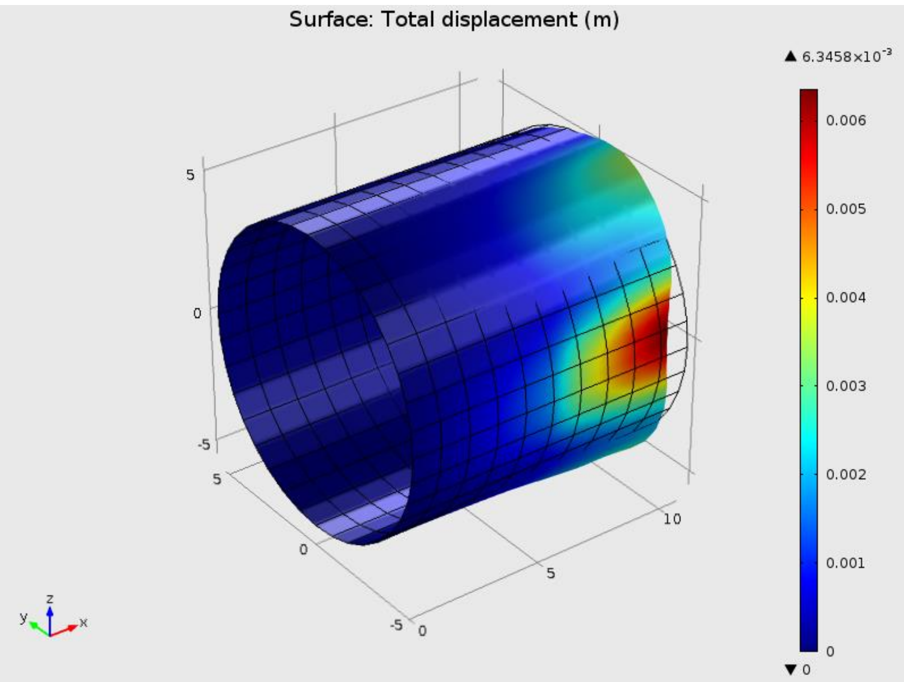

Figure 2.18: k=10 MPa/m. Distributed load. Applied displacements: see Figure 2.10

Chapter 3

On the forces applied to drive a TBM in soft soil

Controlling the TBM driving parameters is a well-established practice for construction purposes, and for that aim data often undergoes time-based averaging. This research mined the complete series of recorded data instead, and investigated how these can contribute to an improved understanding of the interaction between the TBM and the surrounding soil. In this Chapter data concerned with the applied pressures and forces and the information implicitly stored in them are investigated.

The spatial and temporal distribution are preliminarily investigated in order to improve the understanding of the TBM-soil interaction process. Results point at the soil reaction on the TBM needed to equilibrate the system of forces and moments applied to drive it. This Chapter is based on Festa et al. [14].

3.1 Overview of forces

Forces and pressures acting on a TBM-shield can be subdivided in active and passive as already recognized in Maidl et al. [25] and in DAUB [8],. The active forces represent the actions under the direct control of the TBM driver (e.g. support pressure, advancing force, etc.) expressly applied to drive the shield. The passive forces include the reaction of the surrounding soil and fluids, and the interaction with the already installed concrete lining, i.e. all those actions which are not directly under control of the TBM driver but represent the response of the system instead.

The proposed distinction reflects another difference between the active and the passive group. While active forces and pressures can be derived from the TBM data set with limited processing, the passive ones can at the moment only be modelled. A list of all active and passive forces is given below, with further explanations in Figures 3.1 and 3.2. A more detailed description and their connection to the TBM data is provided later on.

Active components:

- $p_{cw-soil}$: contact stress between the cutting wheel and the soil;
- p_{sl}: hydrostatic pressure exerted by the face support fluid;
- $\overrightarrow{F_{cw}}$: cutting-wheel self-weight. It also includes the weights of the wheel support structure and of the main drive. The buoyancy effect is also accounted for when needed;
- $\overrightarrow{F_{sl}}$: weight of the support fluid filling the excavation chamber and (part of) the working one. Its value depends on the specific weight of the fluid and on the actual fluid level in the working chamber;
- $\overrightarrow{F_{sw1}}$, $\overrightarrow{F_{sw2}}$, and $\overrightarrow{F_{sw3}}$:
  weights of the TBM-shield's front, central, and rear sector, respectively;
- $\overrightarrow{F_{sw4}}$: self-weight of the concrete segment handled by the erector before installation;
- $\overrightarrow{F_{btr}}$: pull-force due to the back-train;
- $\overrightarrow{F_{thr}}$: longitudinal component of the advance force generated by the thrust cylinder;
- $\overrightarrow{M_{cw}}$: torque of the cutting-wheel.

Passive components:

- $\overrightarrow{F_{bu}}$: buoying force on the TBM-shield;
- $\overrightarrow{T_{thr}}$: shearing (transversal) component of the advance force generated by the thrust cylinders. This action can arise for at least two distinct reasons (or a combination of them). The first reason is a transversal displacement between the TBM and the last installed ring. A displacement may be caused for example by a differential buoying force per unit length between the TBM-shield (or at least its rear part) and the tunnel lining (Bogaards and Bakker [4] and Talmon and Bezuijen [45]). The second reason is a non-perfect alignment of the thrust cylinders with the shield longitudinal axis. Consequently, the thrust force is no more perpendicular to the plane where the cylinders are connected to the shield, and a transversal component may arise;
- $\overrightarrow{F_{tb}}$ and $\overrightarrow{T_{tb}}$: normal and shear contact forces between the tail-brushes and the last-installed ring. The tail brushes are designed to adhere to the final lining such as to prevent the inflow of the tail-void grout back into the TBM. The adhesion is provided by their mechanical deformation and by the injection of pressurized grease between adjacent rows of brushes. At Hubertus, three rings of brushes were present, and therefore two rings of pressurized grease. If the final lining becomes eccentric with the shield, an uneven radial distribution of the brushes' deformations occurs and that may originate a transversal component of force. An uneven radial distribution of the friction between the tail brushes and the concrete lining would provoke the rise of a turning moment;

- p_{shl}: normal contact effective stress between the shield skin and the surrounding soil;
- τ_{shl}: tangential contact stress between the TBM-shield and the soil.

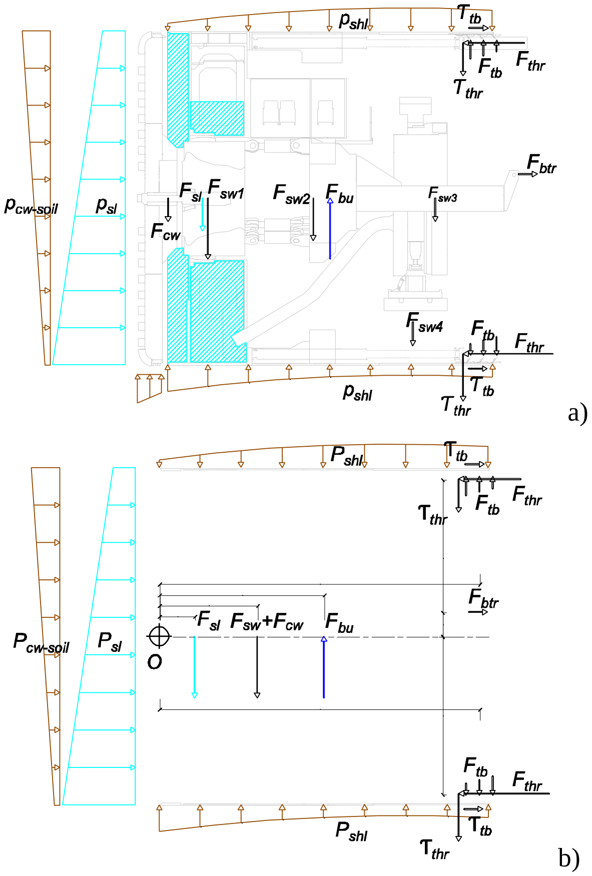

Figure 3.1: Forces on the Hubertus tunnel TBM: schematic view (a) and calculation scheme (b)

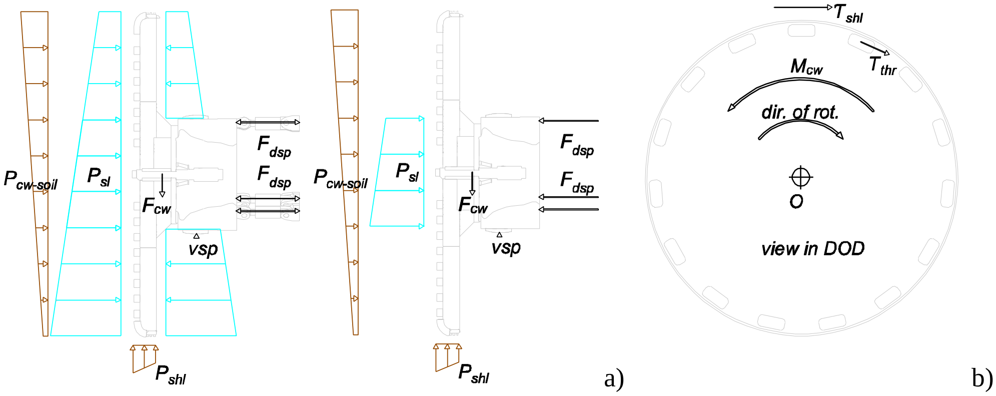

Figure 3.2: Forces on the cutting wheel: decomposition of forces and internal actions (a) and transversal cross section (b)

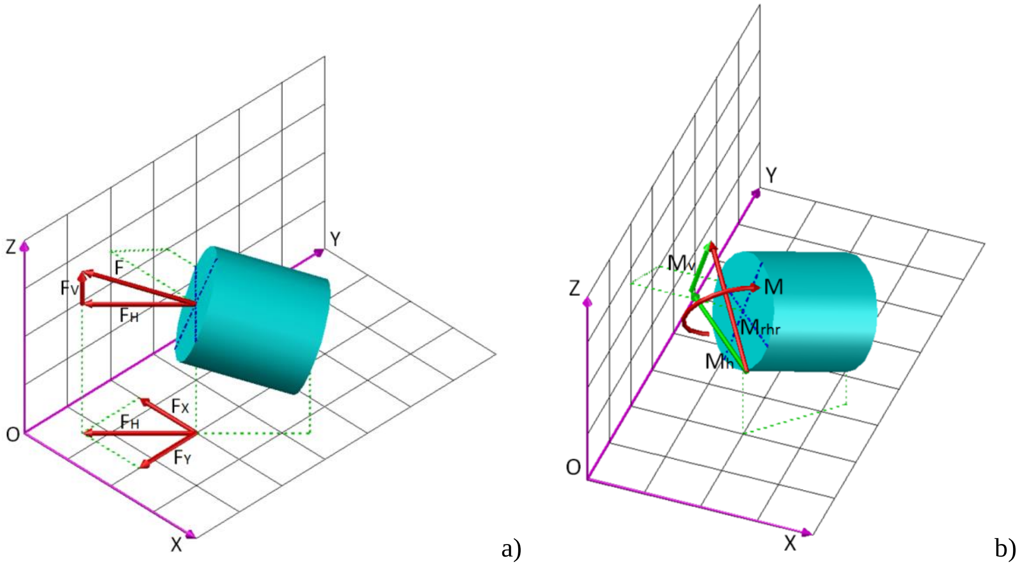

Figure 3.3: Sign convention for forces (a) and moments (b)

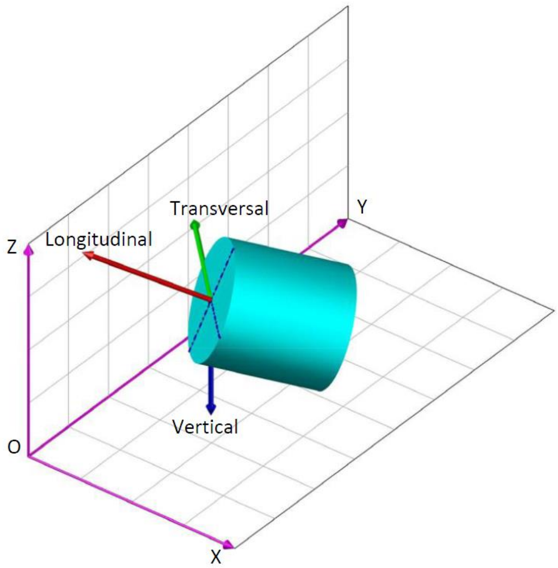

Figure 3.4: Directions of calculated equilibrium (Section 6.1). Red: longitudinal; green: transversal; blue: vertical

Point O in 3.1b indicates the reference point around which the balance of moments is calculated. The arms of the forces with respect to O are also indicated. The sign convention is shown in Figure 3.3.

The forces are decomposed in vertical and horizontal components ($\overrightarrow{F_v}$ and $\overrightarrow{F_h}$), and $\overrightarrow{F_h}$ adopts the sign of $\overrightarrow{F_x}$. In this scheme the active forces (including the passive $\overrightarrow{F_{bu}}$) can only be vertical or parallel to the shield-axis. Over the sector of investigated tunnel alignment the longitudinal slope was smaller than 1%. Consequently the difference between an axial force and its horizontal projection is limited to 0.05% and the two are used indistinctly.

The moments are also decomposed in vertical and horizontal components ($\overrightarrow{M_v}$ and $\overrightarrow{M_h}$). $\overrightarrow{M_{rhr}}$ represents the moment $\vec{M}$ according to the right-hand-rule. $\overrightarrow{M_h}$ is (by definition) horizontal and perpendicular to the shield-axis, which follows the simplifying assumption that the active forces were applied co-axially to the TBM-shield and perpendicular to the front and rear faces of the shield.

3.2 From the monitoring data to the active forces

In the current section it is shown how the active driving forces are derived from the monitoring data. For each force the analytical formulation is provided along with an example of the path of the said action over the tunnelling sector from ring 78 to ring 84 in the south alignment.

In this Section the monitoring TBM data are assumed as deterministic values. Also mechanical imperfections or friction forces in the mechanical components are not accounted for. Düllman et al. [11] demonstrate in fact that those need not be correct assumptions. The Authors in particular argue that the loss of sensors calibration during tunnelling and the intrinsic resistance of the mechanical components have to be correctly evaluated such as to avoid misinterpretation of TBM-soil interaction mechanisms. Such critical analysis of the raw data should be performed with the aim of further improving the analysis presented hereafter.

3.2.1 Hydrostatic action of the support fluid

Four pressure gauges installed on the front side of the submerged wall measured the fluid pressure in the excavation chamber. Only two of the four sensors provided reliable measurements as the other two went out of order for unknown reasons. The two meaningful gauges were both located at the left-hand side of the submerged wall, 0.94 m and 4.54 m above the mid-height of the excavation chamber.

The pressures at the face top (p_{top}), mid-height (p_{mid}), and bottom (p_{bot}) positions are obtained through linear interpolation of the measured values (3.5a). The hydrostatic force due to the pressurized slurry is obtained as:

$$\overrightarrow{F_{sl}} = -p_{mid} \cdot R_{front}{}^2 \cdot \pi \cdot \overrightarrow{ax} \tag{3.1}$$

with R_{front} shield front radius and $\overrightarrow{ax}$ unit vector of the shield longitudinal axis (Figure 3.6a).

The moment due to the triangular distribution of the hydrostatic pressures (trapezoidal, actually, but only the triangular part contributed) $\overrightarrow{M_{sl}}$ is obtained applying the resultant force

$$\overrightarrow{F_{slm}} = \frac{(p_{bot}-p_{top})}{2} \cdot R_{front}{}^2 \cdot \pi \cdot \overrightarrow{ax} \tag{3.2}$$

at 5/8 of the face height (measured from the top) such that

$$\overrightarrow{M_{sl}} = \overrightarrow{F_{slm}} \times (\vec{b} \cdot \frac{R_{front}}{4}) \tag{3.3}$$

in which $\vec{b}$ is the unit vector oriented from the bottom to the middle point of the shield face (Figure 3.6b).

The measured pressures provide an indirect estimate of the specific weight of the face support fluid (γ_{sl}) in the excavation chamber according to the expression

$$\gamma_{sl} = \frac{(p_{bot} - p_{top})}{\Delta h} \tag{3.4}$$

in which Δh represents the vertical distance between the two gauges (3.6 m) (see Figures 3.7a and b). Figure 3.7a shows the increasing ‘contamination’ of the bentonite-slurry as the excavation for one ring proceeds. 3.7b illustrates the removal of the excavated soil from the slurry with subsequent decrease of the specific weight during standstill for ring construction.

The air pressure in the working chamber was measured. A pressure difference ranging between 10 and 15 kPa is observed between the fluid pressure (p_{sl_ec}) in the excavation chamber and the air pressure (p_{A_wc}) in the working chamber (see Figures 3.5b, and 3.8a and b). Both pressures are referred to the free surface in the excavation chamber. The pressure delta between the two chambers can be explained either by a poor calibration of the sensors or by a difference in the fluid specific weight between excavation and working chamber.

The difference in terms of slurry specific weight needed to justify the measured pressure difference between the excavation and the working chamber is obtained diving the pressure difference by the vertical distance between the fluid level in the working chamber and the gate connecting excavation and working chambers (h_{sl_wc}):

$$\Delta\gamma_{sl} = \frac{p_{A\_wc} - p_{sl\_ec}}{h_{sl\_wc}} \tag{3.5}$$

The resulting variation in the slurry specific weight is shown in Figures 3.9a and b. That is in good agreement with the range of the fluid specific weights in the excavation chamber calculated in the different phases of the ring construction (Figure 3.7). The observed pressure difference could also be partly caused by a pressure drop due to flow of non-perfect fluid from the working chamber to the excavation chamber, but that effect is not calculated here.

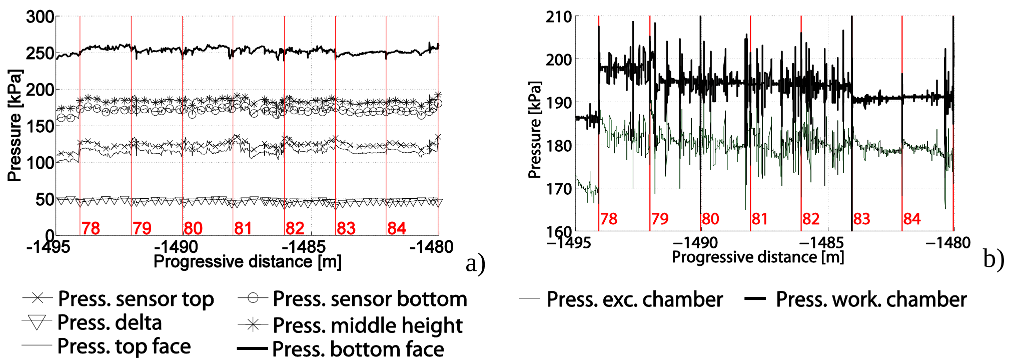

Figure 3.5: Slurry pressure (measured and derived values) at different heights (a); slurry pressure (in the excavation chamber) and air pressure (in the working chamber) at the level of the fluid free surface in the working chamber (b). Ring numbers in red

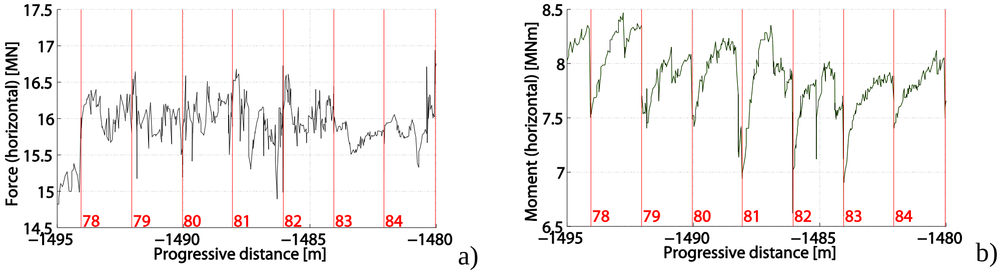

Figure 3.6: Horizontal component of the (hydrostatic) pressure distribution of the excavation fluid on the submerged wall (a) and horizontal component of the moment due to the same pressures (b). Ring numbers in red

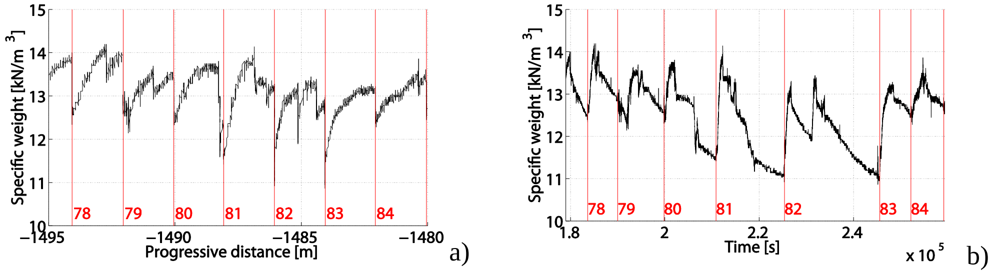

Figure 3.7: Slurry specific weight in the excavation chamber plotted vs. distance (a) and time (b). Ring numbers in red

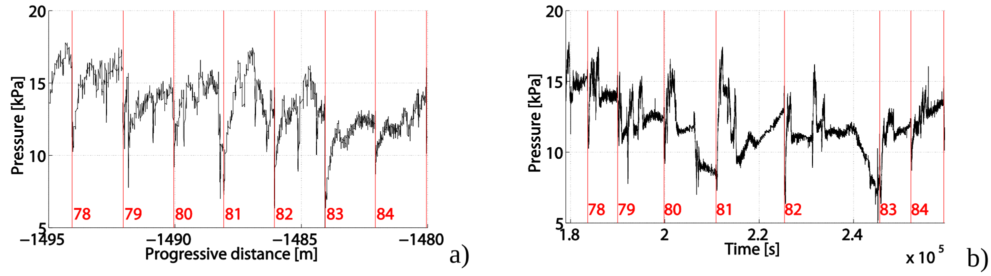

Figure 3.8: Pressure difference between working and excavation chambers, at the level of the free surface in the working chamber, plotted vs. distance (a) and time (b). Ring numbers in red

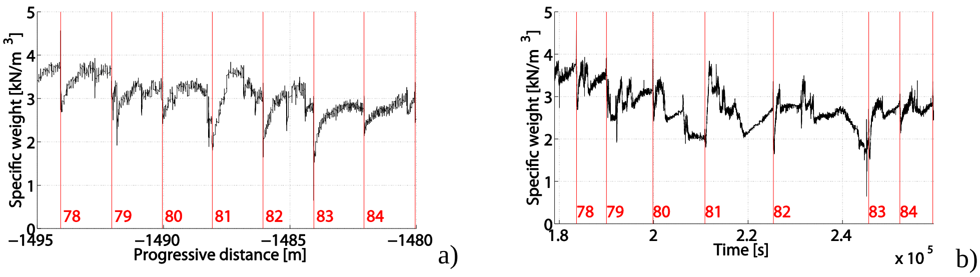

Figure 3.9: Specific weight delta between excavation and working chamber, plotted vs. distance (a) and time (b). Ring numbers in red

3.2.2 Self-weight of the support fluid

For the calculation of the self-weight of the support fluid the excavation chamber is assumed completely filled, and the working chamber filled up to the monitored fluid level. The volume occupied by the wheel supporting structure in the excavation chamber is not yet subtracted, although that should be the case for completeness. However, its effect is expected to be limited due to the modest volume of that part of the steel construction. The time- and chamber-dependant specific weight of the support fluid is also taken into account. With V_{exc} the volume of fluid in the excavation chamber and V_{work} the volume of fluid in the working chamber, and γ_{exc} and γ_{work} their specific weights, respectively, the force is defined as:

$$\overrightarrow{F_{slw}} = (V_{exc} \cdot \gamma_{exc} + V_{work} \cdot \gamma_{work}) \cdot (-\overrightarrow{e_z}) \tag{3.6}$$

in which $\overrightarrow{e_z}$ represents an upward oriented unit vector (see Figures 3.10a and b).

The moment resulting from $\overrightarrow{F_{slw}}$ around a horizontal axis crossing the point O (as in Figure 3.3b) and perpendicular to the tunnel alignment is calculated as:

$$\overrightarrow{M_{slw}} = (V_{exc} \cdot \gamma_{exc} \cdot (-\overrightarrow{e_z})) \times \overrightarrow{a_{exc}} + \left(V_{work} \cdot \gamma_{work} \cdot (-\overrightarrow{e_z})\right) \times \overrightarrow{a_{work}} \tag{3.7}$$

in which $\overrightarrow{a_{exc}}$ and $\overrightarrow{a_{work}}$ represent the vectors connecting the centres of gravity of the fluid volumes in the excavation and working chambers with O, respectively. The results are plotted in Figure 3.11.

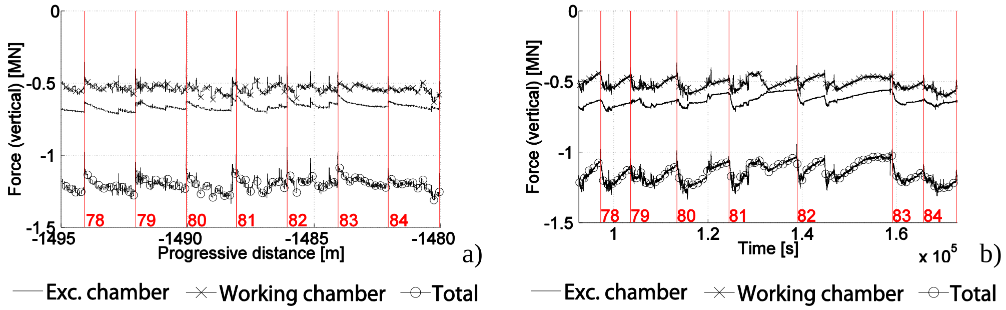

Figure 3.10: Weight of the excavation fluid in the excavation and working chambers, plotted vs. distance (a) and time (b). Ring numbers in red

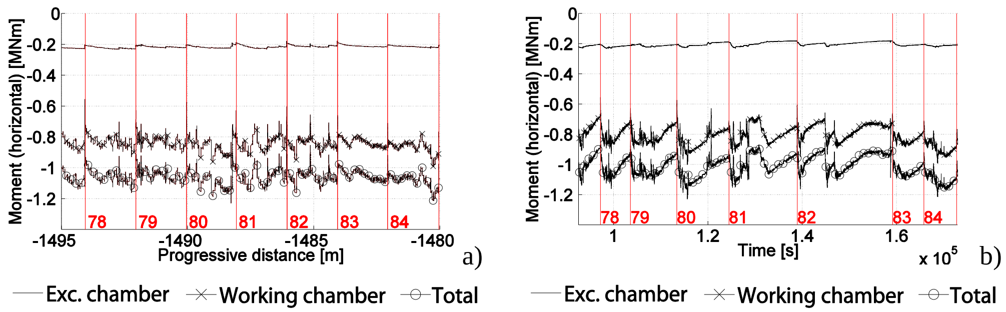

Figure 3.11: Moment of the excavation fluid weight in the excavation and working chambers vs. distance (a) and time (b). Ring numbers in red

3.2.3 Contact stress between the cutting wheel and the excavation front

The contact action between the cutting wheel and the excavation front ($p_{cw-soil}$) was not directly retrievable from the logged data, but is derived according to the decomposition of forces of Figure 3.2a. The cutting wheel is subject to vertical and horizontal forces. The only vertical force is the wheel's self-weight, and that is counteracted by the spherical bearing represented by vsp in Figure 3.2a. However, because the wheel's centre of gravity is not vertically aligned with its supporting point a frontward turning moment arises. The immersed self-weights of the cutting wheel and of its supporting structure are assumed as both were immersed in the bentonite slurry.

Horizontally, $p_{cw-soil}$ and p_{sl} are balanced by $\overrightarrow{F_{dsp}}$, which is the resultant of the forces generated by the wheel displacement cylinders. Few assumptions underlie the formulations of $p_{cw-soil}$ and p_{sl}, as hereafter summarized. Identical hydrostatic profiles are hypothesized in the excavation chamber in front and behind the cutting wheel to describe the horizontal pressure of the support fluid (slurry). An impermeable filter-cake is assumed in the soil in front of the cutting wheel preventing the ingress of groundwater into the excavation chamber. The front side of the cutting wheel, except for the cutting tools, is thought in contact with fluid bentonite slurry, thus not in direct contact with the soil skeleton. The cutting tools on the front side of the cutting wheel, by penetrating into the soil to be excavated, come in contact with the granular skeleton and with the groundwater. In the current model no distinction is made between the effective stresses and the pore pressure acting on the cutting tools, but the total action is considered.

In the hypothesis of identical hydrostatic profiles in front and behind the cutting wheel only part of p_{sl} is actually absorbed by the cylinders, the remaining being self-balanced by the support fluid behind the wheel (see comparison Figure 3.2a left and right). The only unknown is $p_{cw-soil}$, which can be derived. The turning moment is balanced through the spatial distribution of the $\overrightarrow{F_{dsp}}$ components.

Friction forces in the mechanical parts of the TBM are disregarded. Düllmann et al. [11] demonstrate that the monitored TBM raw data should undergo critical judgment before further processing. They show for example that when mechanical imperfections in the displacement cylinders and in the spherical bearing of the cutting wheel are not correctly accounted for the contact stress between cutting wheel and soil skeleton can be misinterpreted. Such critical analysis on the raw data, although not performed as part of this research, should be done in order to improve the estimate of the contact stress between the cutting wheel and the soil.

The three pairs of wheel displacement cylinders (A, B, and C) are positioned along an imaginary circle concentric with the shield axis and with a radius of 1675 mm. The cylinders are located at top (group A), 128° clockwise (group B) and 128° counter clockwise (group C). The groups were used to shift back and forward the cutting wheel (when evenly displaced), or to orientate the wheel's axis independently from the shield's axis (through the differential displacement of the groups).

Since the hydraulic pressures in the groups were also measured, applied forces and moments can be derived. The force applied by each cylinder is obtained as:

$$\overrightarrow{F_{dsp}} = \left(p_{piston} \cdot A_{piston} - p_{rod} \cdot A_{rod}\right) \cdot \overrightarrow{ax} \tag{3.8}$$

while the turning moment with respect to the usual point O is obtained from the product:

$$\overrightarrow{M_{dspi}} = \overrightarrow{F_{dspi}} \times \overrightarrow{r_{cwi}} \tag{3.9}$$

in which $\overrightarrow{r_{cwi}}$ is the vector connecting each group's end (wheel-side) with O. The overall moment applied by the displacement cylinders becomes:

$$\overrightarrow{M_{dsp}} = \sum_{i=1}^{3} \overrightarrow{M_{dspi}} \tag{3.10}$$

The displacement cylinders balance the wheel-soil contact action, the hydrostatic pressure exerted by the face-support fluid on the wheel bearing axis, and the turning moment due to the distribution of weights of the rotating system (cutting wheel, supporting structure, and main drive), with respect to the support point vsp of Figure 3.2a. Mechanical imperfections and frictions are not accounted for in this approximation. The wheel-soil contact action remains the only unknown, and that can be derived once the other actions are defined.

The resultant force and turning moment induced by the hydrostatic pressures distribution on the cutting-wheel bearing axis are obtained with the same procedure as for the hydrostatic pressure on the shield front wall. Results are shown in Figures 3.12a and b, and 3.13a.

The partial and total forces and moments applied through the wheel displacement groups are plotted in Figures 3.13b, and 3.14a and b. The groups A, B, and C are named *Top*, *Bottom-left*, and *Bottom-right*, respectively. In Figure 3.15a the turning moment derived from the weights distribution is shown. The results for contact forces and moments are presented in Figures 3.15b, and 3.16a and b.

About 80% of the axial force exerted by the wheel displacement cylinders equilibrates the hydrostatic action of the support fluid acting on the wheel axis. Only 20% of the force, corresponding to about 0.5 MN as from Figure 3.15b, is directly transferred to the soil, at least according to the calculation scheme. Furthermore, Figure 3.16a shows that the horizontal contact moment fluctuated between -0.5 and -1 MNm. The negative sign points at a higher contact stress at the upper half of the cutting wheel than at the lower one. Similarly, the plot of the vertical contact moment in Figure 3.16b suggests higher contact stresses at the left-hand half of the cutting wheel than at the right-hand one (in Direction Of Drive). The vertical moment varied between -0.2 and +0.4 MNm.

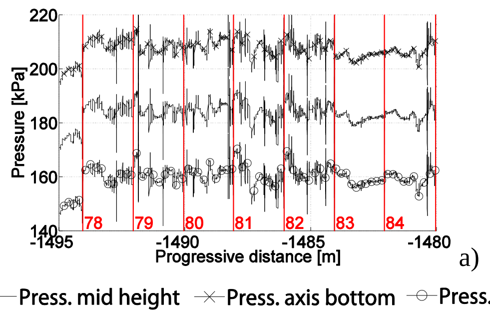

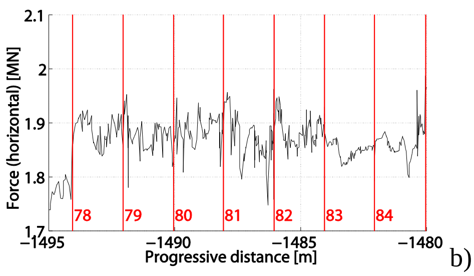

Figure 3.12: Slurry pressure (measured and derived values) at different heights (a); horizontal component of the hydrostatic pressures of the slurry on the wheel axis (b). Ring numbers in red

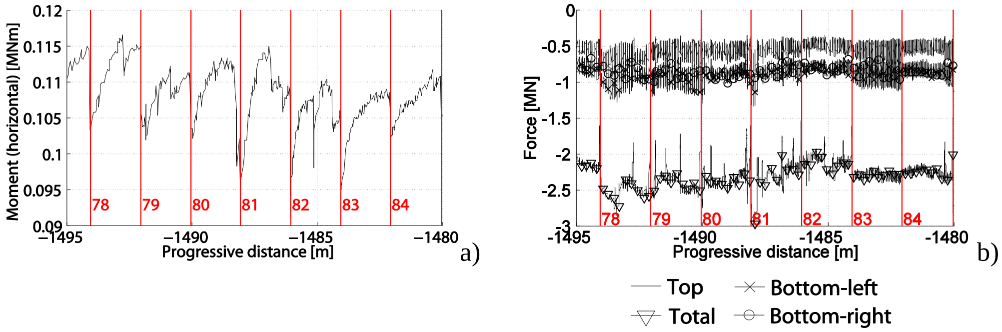

Figure 3.13: Horizontal component of the moment given by the (hydrostatic) distribution of pressures of the excavation fluid on the wheel axis (a); forces of the wheel-displacement cylinders (b). Ring numbers in red

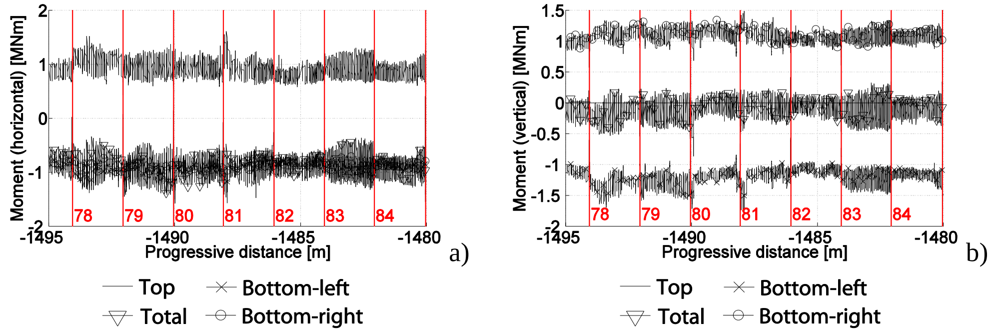

Figure 3.14: Moment of forces of the wheel-displacement cylinders, horizontal (a) and vertical (b). Ring numbers in red

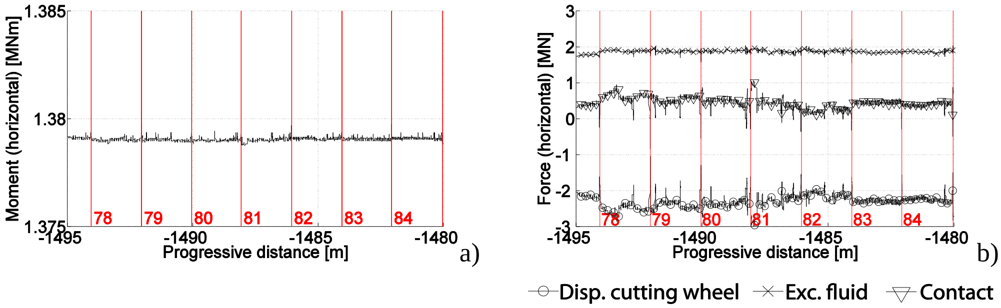

Figure 3.15: Horizontal moment of the wheel self-weight (a) and horizontal partial and total contact forces (b). Ring numbers in red

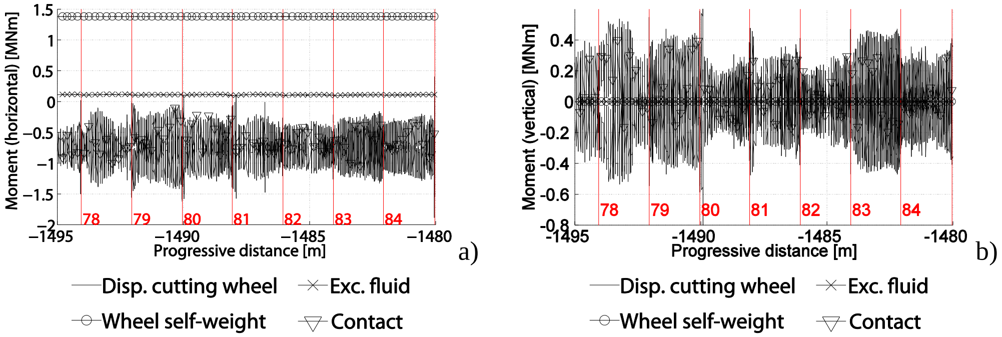

Figure 3.16: Partial and total contact moments, horizontal (a), and vertical (b). Ring numbers in red

3.2.4 *Shield buoyancy force*

The uplift force due to the shield-buoyancy F_{bu} is calculated as:

$$\overrightarrow{F_{bu}} = \left(\frac{R_{front}+R_{rear}}{2}\right)^2 \cdot \pi \cdot L \cdot \gamma_f \cdot \overrightarrow{e_z} \tag{3.11}$$

in which γ_f stands for the specific weight of the fluid, R_{rear} for the radius of the shield-tail, and L for the shield length. The turning moment due to the buoyancy effect is obtained from

$$\overrightarrow{M_{bu}} = \overrightarrow{F_{bu}} \times \left(\overrightarrow{ax} \cdot \frac{L}{2}\right) \tag{3.12}$$

and the results are presented in Figure 3.17.

γ_f is assumed equal to 10 kN/m^3 in first approximation, but that needs not be a valid assumption. Should for example fluids other than water flow around the shield (e.g. bentonite-slurry or tail grout), the specific weight would be different. However, were such non-newtonian fluids actually present, the buoyancy-force as above estimated would not make much sense, and a more detailed description of the pressure distribution around the shield would be more appropriate. Debrauwer [9], analysing the mechanical equilibrium of the tunnel lining surrounded by fluid grout, showed that the buoyancy effect is larger than would be obtained accounting for the hydraulic gradient due to groundwater. This concept is not developed further here. Even if the buoyancy force was constant, the resulting moment was not, due to small changes in the shield's orientation. As shown in Figure 3.17b, the moment fluctuations can be disregarded accounting for a minimal fraction only of the nominal value.

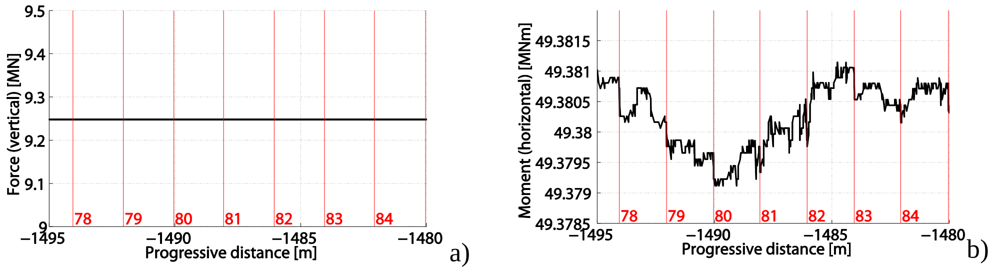

Figure 3.17: Shield buoyancy actions: force (a), and horizontal moment (b). Ring numbers in red

3.2.5 Shield self-weight

The weights of the TBM and their spatial distribution are determined according to the TBM design report and drawings and the resultant force and moment are derived. The shield is subdivided in three sectors: front, centre, and rear. For each sector a distinct weight is provided: $\overrightarrow{F_{front}}$, $\overrightarrow{F_{mid}}$, and $\overrightarrow{F_{tail}}$, respectively. The weight of the erector is provided separately ($\overrightarrow{F_{erec}}$), as well as for the cutting wheel ($\overrightarrow{F_{cww}}$), its supporting structure ($\overrightarrow{F_{cwss}}$), and the main drive ($\overrightarrow{F_{cwdr}}$). Differently from Section 3.2.3, the weights of the cutting wheel and of its supporting structure are adopted here with their nominal values, and not as immersed weights. An evenly distributed additional weight $\overrightarrow{F_{dw}}$ is also considered to represent the weight of the equipment not separately accounted for. The overall weight of the TBM is 9 MN, calculated as:

$$\overrightarrow{F_{sw}} = \overrightarrow{F_{front}} + \overrightarrow{F_{mid}} + \overrightarrow{F_{tail}} + \overrightarrow{F_{erec}} + \overrightarrow{F_{cww}} + \overrightarrow{F_{cwss}} + \overrightarrow{F_{cwdr}} + \overrightarrow{F_{dw}} \tag{3.13}$$

The overall turning moment is given by the algebraic sum of the cross products of the individual weight and the vector connecting the point of application of each component with O, as in Equation (3.14).The sign of the arms' lengths is positive for the forces behind O and negative for those in front of it. The results presented in Figures 3.18a and b show that although the self-weight force was constant, the resulting moment is not due to small changes in the shield's orientation. However the moment's fluctuations is small and can be disregarded.

$$\overrightarrow{M_{sw}} = \left(\frac{L_{front}}{2} \cdot \overrightarrow{F_{front}} + \left(L_{front} + \frac{L_{mid}}{2}\right) \cdot \overrightarrow{F_{mid}} + \left(L_{front} + L_{mid} + \frac{L_{tail}}{2}\right) \cdot \overrightarrow{F_{tail}} + L_{erec} \cdot \overrightarrow{F_{erec}} + L_{cww} \cdot \overrightarrow{F_{cww}} + L_{cwss} \cdot \overrightarrow{F_{cwss}} + L_{cwdr} \cdot \overrightarrow{F_{cwdr}} + \frac{L}{2} \cdot \overrightarrow{F_{dw}}\right) \times \overrightarrow{ax} \tag{3.14}$$

The TBM self-weight and the uplift force (buoyancy) are well balanced, as from the comparison of Figures 3.17a and 3.18a. However, the moments of the same two forces sensibly differ due to their different application points. The delta in terms of moment amounts to about 21 MNm, and the positive sign indicates the TBM's tendency to tilt frontward, which is a common behaviour for TBMs with forward unbalanced self-weights.

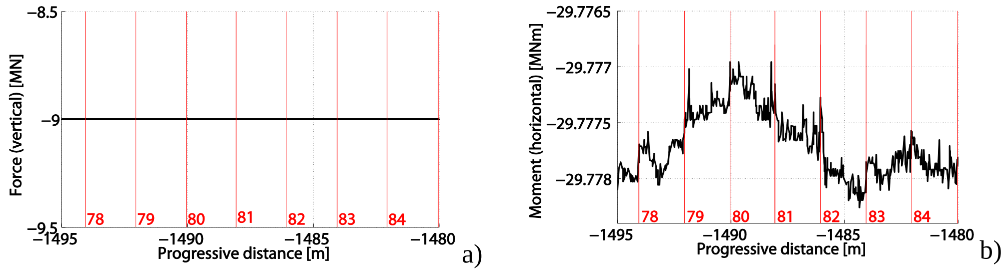

Figure 3.18: Shield self-weight: force (a), and horizontal moment (b). Ring numbers in red

3.2.6 The thrust or driving force

The thrust force was applied through 30 hydraulic cylinders organized in 5 groups (A-E), each made of three pairs of cylinders. The groups were: A (top); B (72° cw); C (144° cw); D and E symmetrical of C and B with respect to the vertical axis. The hydraulic pressure was constant in the cylinders of the same group. Figure 3.19 shows the total thrust force vs. distance and time.

In Figure 3.19a complete and filtered data are plotted. This shows, on the one side, the consistency between the two data sets during driving, and on the other a discrepancy during standstills. During standstills the filtered data fails to catch the lowest values. At ring changes the solid black line (full data) reaches values lower than those shown by the line with circles (filtered data). The distance-based filter proves not suitable to represent standstills, during which a time-based approach should be used. Figure 3.19b shows the thrust force vs. time and the stepped release of the groups of thrust cylinders for ring construction can be seen.

The turning moments applied by the thrust-cylinders are represented in Figures 3.20 (vertical component) and 3.21 (horizontal component). A cut-out with increased detail is provided in Figures 3.22 and 3.23a. The effects of the ring installation segment by segment are visible and it can be observed that the groups were retracted one by one. Also interesting from Figure 3.23a that at the end of the ring construction the horizontal applied turning moment was close to 0 MN, compared to the value of the same horizontal moment which during drive was around -40 MN. This is expected to influence the shield behaviour. The pull force on the TBM's back-trail is plotted Figure 3.23b. Given the low monitored values the pull force is disregarded.

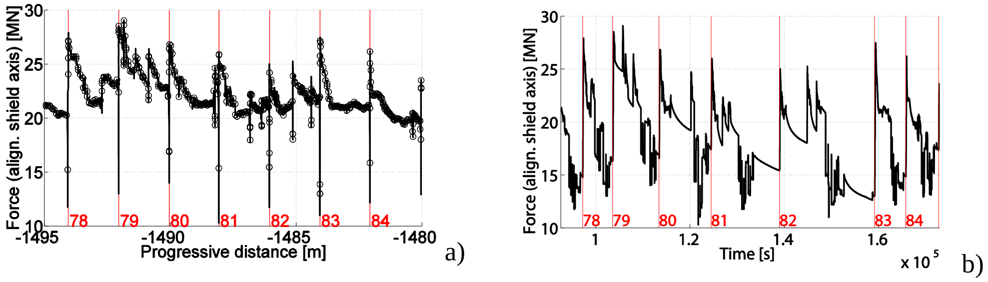

Figure 3.19: Total thrust force plotted vs. distance (a) and time (b). Ring numbers in red

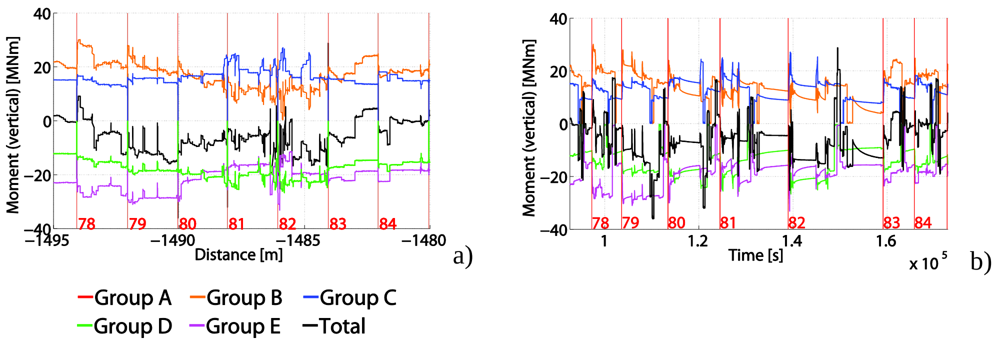

Figure 3.20: Vertical moments of the thrust groups vs. distance (a) and time (b). Ring numbers in red

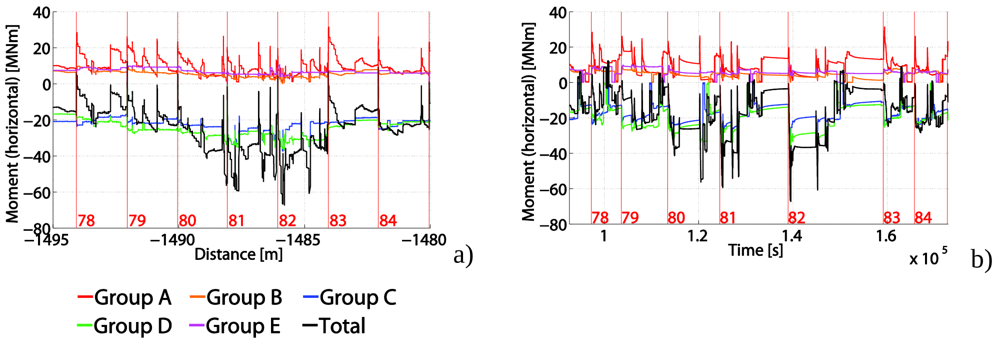

Figure 3.21: Horizontal moment due to the thrust groups and total value vs.distance (a) and time (b). Ring numbers in red

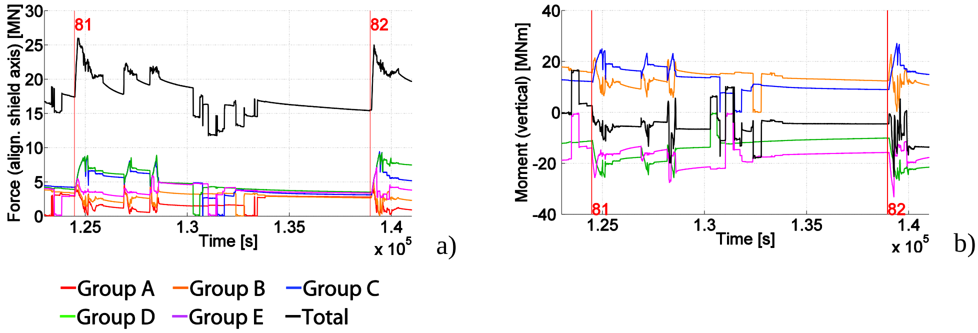

Figure 3.22: Detail of the construction of ring 81 for thrust force (a) and vertical moment (b) vs. time. Ring numbers in red

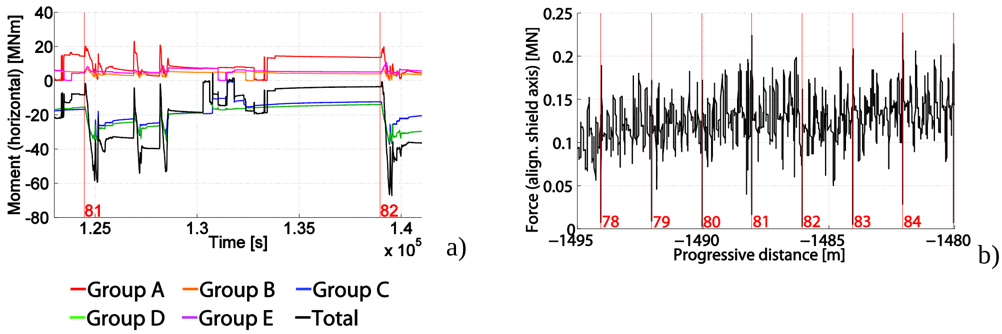

Figure 3.23: Detail of the construction of ring 81 for horizontal moment vs. time (a). Pull force on the back-train (b). Ring numbers in red

3.3 Resultant active forces and moments

The thrust force and the hydrostatic action of the face support fluid were largely predominant in the horizontal longitudinal direction. The longitudinal resultant ranged between -10 and -5 MN during driving, with a decreasing tendency (in absolute value) over the driving for each ring. Negative sign indicates a forward orientation of the resultant. During standstills for ring erection the longitudinal resultant often dropped to 0 MN and lower meaning that the shield is being pushed backward.

The predominant forces in vertical direction were the TBM-weight, the buoyancy due to the groundwater, and, at a lower order, the self-weight of the face support fluid in the excavation and working chambers. The other actions can be disregarded. The vertical resultant fluctuated around 0 MN, as shown in Figure 3.25, suggesting that the vertical balance of the TBM is fully captured in these forces. Still, the buoyancy effect was derived assuming a specific weight $\gamma_f = 10$ kN/m^3, and assuming a different specific weight would affect the vertical equilibrium proportionally. For example, a fluid specific weight of 12 kN/m^3 would provide a resultant upward force of 1.8 MN.

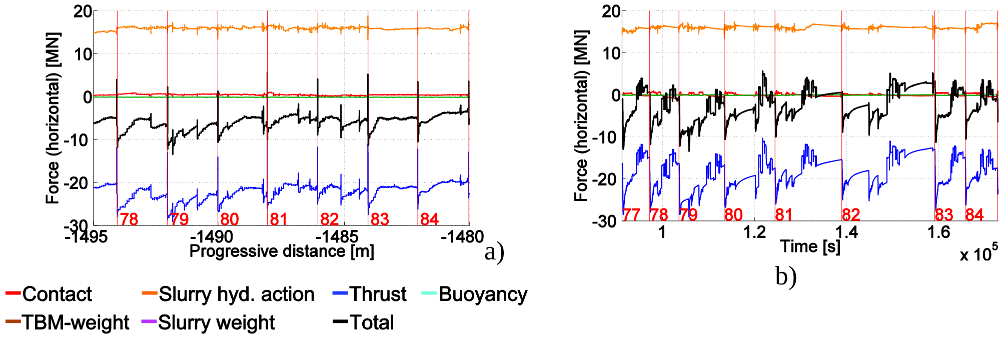

Figure 3.24: Balance horizontal longitudinal forces vs. distance (a) and time(b). Ring numbers in red

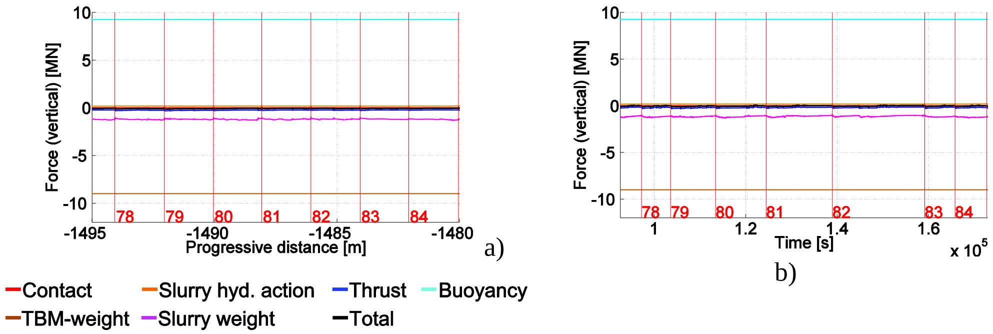

Figure 3.25: Balance of the vertical forces versus distance (a)) and time(b)). Ring numbers in red

The contributions to the turning moments were generally constant in space and time, except for those derived from the spatial distribution of the thrust forces. Consequently, the path of the resultant turning moments closely followed that of the thrust moments (or steering moments) (Figures 3.26 and 3.27).

Along the stretch of tunnel investigated (from -1495 to -1480 m), the resultant horizontal moment ranged from -40 to +40 MNm (Figure 3.26a). The applied horizontal moment appears to vary significantly also when looking at the drive for one single ring. For example, over ring 81 (Figure 3.26a) the resultant horizontal moment ranged from -35 to +30 MNm. Similar observation can be formulated with reference to the vertical moments, as in Figure 3.27b.

The peaks of the applied moments were often reached during ring construction. That was a direct consequence of the staged retraction of the thrust cylinders for the installation of the corresponding ring segment (one group at a time). The staged retraction of the thrust cylinders provokes drops in the thrust force but originates peaks in the thrust moment. However, as those peaks were reached during standstills, limited consequences are expected in terms of shield kinematic behaviour (i.e. side drift). The continued application of a given driving moment during actual advance affected the TBM-shield steering behaviour instead.

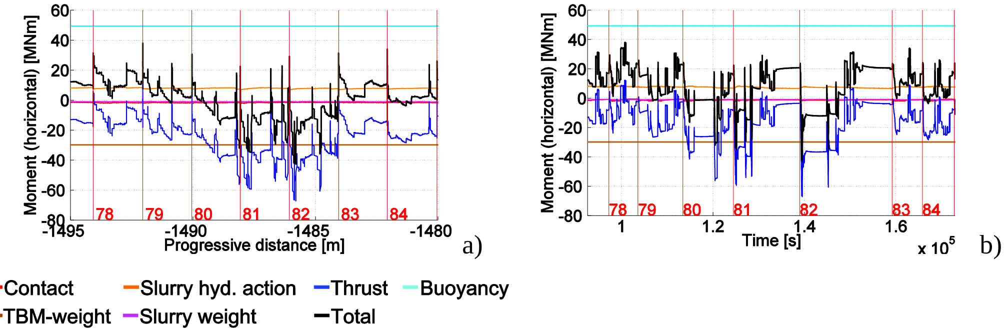

Figure 3.26: Balance horizontal moment versus distance (a) and time(b). Ring numbers in red

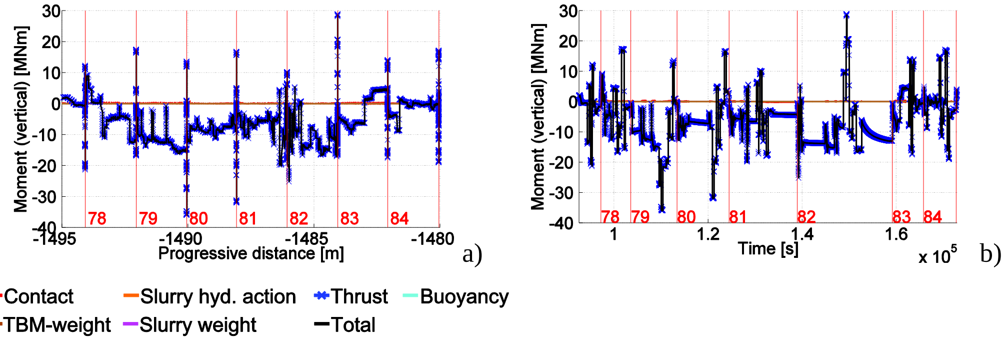

Figure 3.27: Balance vertical moment versus distance (a) and time(b). Ring numbers in red

3.4 Partial conclusions on the active forces on a TBM

The analysis of the TBM driving actions (pressures, forces, and moments), or *active forces*, provides an overview of the actions applied. Since the active system remains unbalanced, an equilibrating system must exist. The *passive system* is formed in our reasoning by the soil and process-fluids actions around the shield-skin (p_{shl} and τ_{shl} in 3.1), the radial and longitudinal actions due to the contact between tail-brushes and concrete lining ($\overrightarrow{F_{tb}}$ and $\overrightarrow{T_{tb}}$), and the transversal component of the thrust forces ($\overrightarrow{T_{thr}}$).

As the passive system was not monitored, the passive forces could not be derived through direct data analysis, but have to be modelled instead. The modelling will be based on the results of the kinematic analysis of Chapter 4, in turn processed through the soil model proposed in Chapter 5. The combination of active and passive forces will be presented and discussed in Chapter 6.

Chapter 4

The shield kinematic model

The shield kinematic model captures several aspects of the kinematic behaviour of a TBM. The model, based on theoretical and geometrical considerations, is verified against TBM monitoring data obtained during the construction of the Hubertus Tunnel. Results show the amplitude and spatial distribution of the soil displacement around the shield periphery as they occurred in practice. The current section is based on a paper currently under review (Festa et al. (2014) [16]) and on Festa et al. (2012) [12] and Festa et al. (2011) [13].

4.1 Theoretic kinematic model

The features of the shield positioning system described in Chapter 2 suggest that the motion of a TBM can be described by the consecutive positions occupied by only two of its points (shield roll is not covered here). Similarly, the motion of a non-deformable rectangle (i.e. a simplified cross section of a TBM-shield in which tapering and overcutting are disregarded) driven along a circular path with constant curvature is fully caught by a centre of rotation, a curvature, and by the angle between the curvature radius and the rectangle's longitudinal axis. Different combinations of these elements lead to different motion paths.

In Figures 4.1 and 4.2 the centre of rotation is connected to the bottom-left and to the bottom-right corner of the rectangle, respectively. The size of the rectangle, the curvature of the trajectory, and the angle between the rectangle and the curvature radius are the same. The trajectories of the paths followed by the four corners illustrate the interaction between the TBM and the soil. The first set-up (Figure 4.1) shows that the trajectory of the top-left corner falls inside that of the top-right one. The second set-up (Figure 4.2) shows a reversed situation. This indicates that even if in both cases a purely rotational movement takes place, in the first case the top side must displace the surrounding soil during advance, while in the second one the soil surrounding the same top side is excavated and can relax after the TBM face has passed. Similar but reversed considerations can be made with reference to the rectangle's bottom-side.

These two limit configurations are unlikely to represent reality. Two additional configurations are introduced, with the centre of rotation connected to the mid-point and to the first quarter (front-half) of the bottom side (Figures 4.3 and 4.4, respectively).

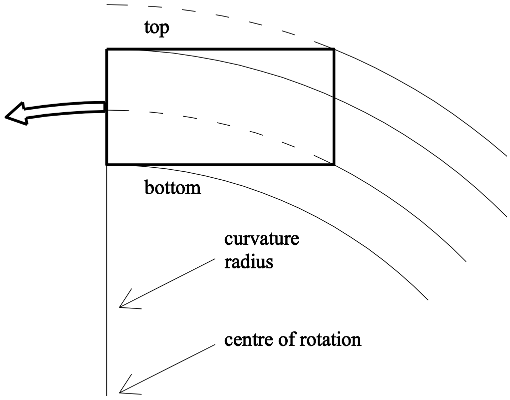

Figure 4.1: Centre of rotation connected to the bottom-left edge

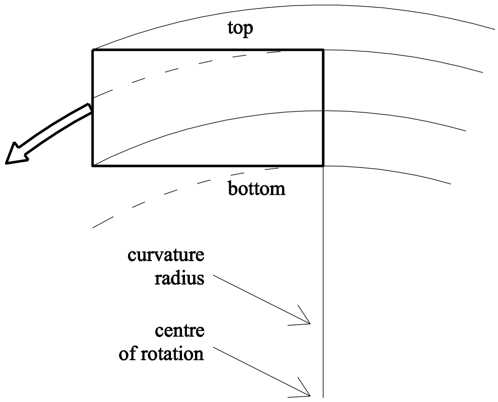

Figure 4.2: Centre of rotation connected to the bottom-right edge

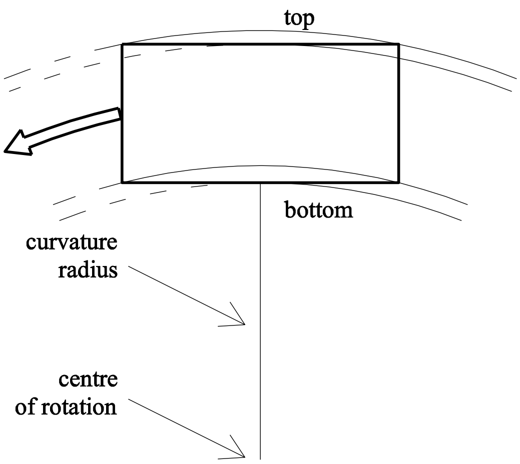

Figure 4.3: Centre of rotation connected to the bottom-centre

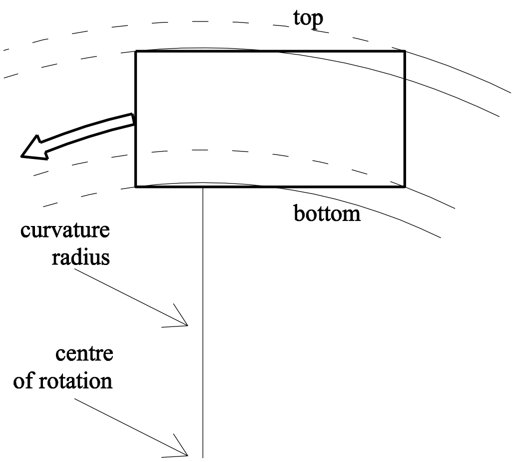

Figure 4.4: Centre of rotation connected to the mid-point of the first half of the bottom side

The configuration of Figure 4.3 leads to a mixed behaviour in which, at the top side, first a phase of relaxation (from the top-left edge to the mid-point), and then a re-compression of the pre-relaxed surrounding soil (from the mid-point to the top-right edge) occurs. At the bottom side the opposite occurs, with a phase of compression followed by a phase of relaxation. This specific arrangement leads to the paired overlap of the trajectories drawn by the four corners. The configuration of Figure 4.4 is intermediate between the last one presented and that of Figure 4.1. At the top side a phase of relaxation is followed by the recompression of the pre-relaxed surrounding soil. After that, the outward drifting of the rear half of the rectangle displaces the surrounding soil beyond the range disturbed by the passage of the first half. Opposite behaviour is observed at the bottom side.

Among the four described configurations the last one (Figure 4.4) most closely models the real steering system and the observed TBM behaviour. The analysis highlights that the steering method influences the interaction with the surrounding soil. Compression-relaxation cycles of the surrounding soil occur particularly along curves. When that happens the soil is said to undergo unloading-reloading stages.

4.2 Logged data and kinematic model

A similar study of the TBM's kinematic behaviour with respect to the surrounding soil is conducted based on the observed positioning data. With that aim the horizontal and vertical deviations from the planned alignment of the front and rear reference points are processed in order to obtain the shield's position and orientation at each tunnel advance. The average monitored advance step between two consecutive readings is in the order of few mm.

At each advance the actual position of the shield is compared with the excavated geometry, i.e. the cavity created through the soil by the cutter head. The excavated geometry is in turn obtained as the record of the positions incrementally occupied by the cutter head as the TBM advances. The comparison allows to quantify the displacements induced by the advancing shield. The shield body is assumed non-deformable. Given the soil conditions and the shield features, this condition appears acceptable for the front part of the shield, but is indeed less perfect for its tail, as demonstrated in Section 2.5.

The numerical model implemented in MATLAB quantifies the amount and distribution of the displacements induced by the advancing shield on the surrounding soil. Figure 4.5 presents a colour-scale view of the induced displacements at an example location. In the example full green and full red correspond to a relaxation and a compression of 80 mm, respectively. An animated sequence of such plots would show the full 3D shield-soil interaction in space and time. Here specific locations around the shield periphery are investigated instead (top, bottom, left, and right). More examples of shield-soil kinematic interaction are presented in Figures 4.6 to 4.11.

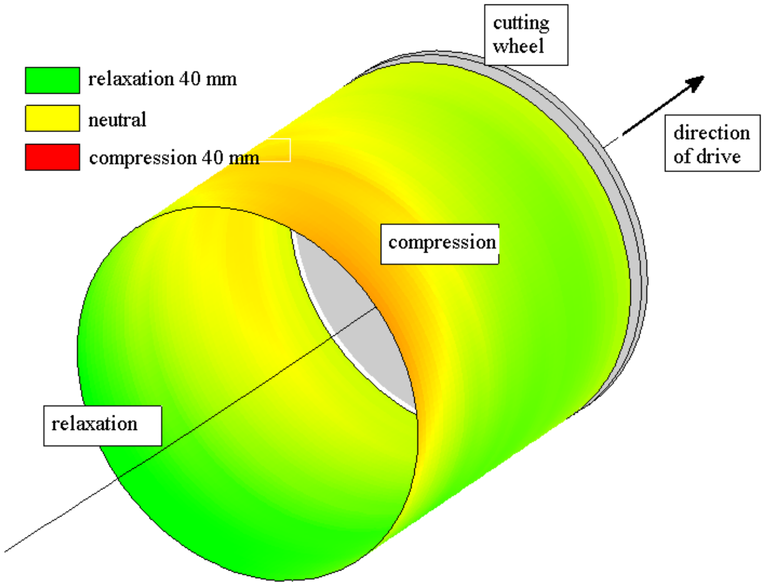

Figure 4.5: 3D frustum with colour-scale view of relaxation and compression sectors

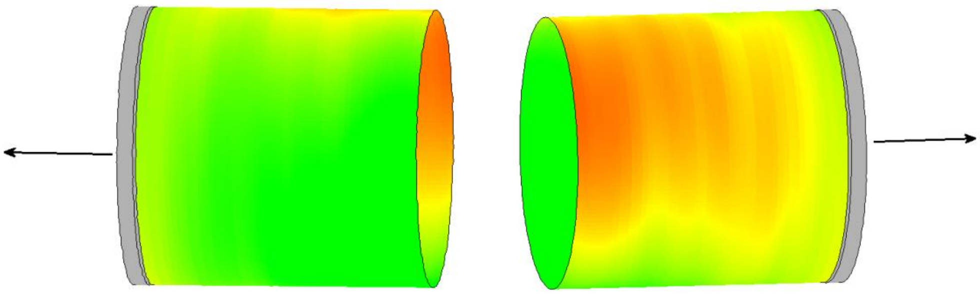

Figure 4.6: Kinematic interface interaction at advance -1276.123 m

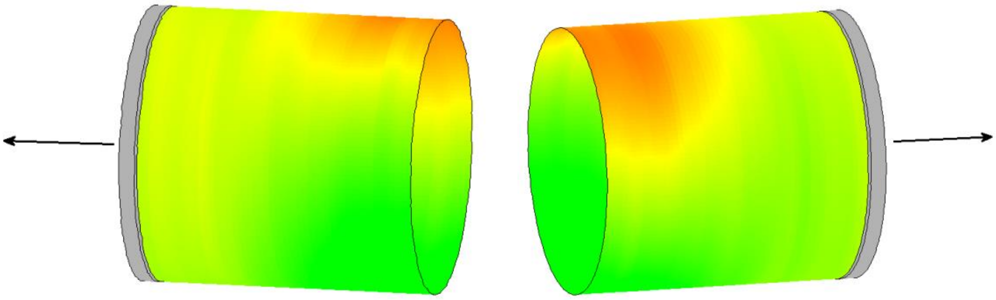

Figure 4.7: Kinematic interface interaction at advance -970.950 m

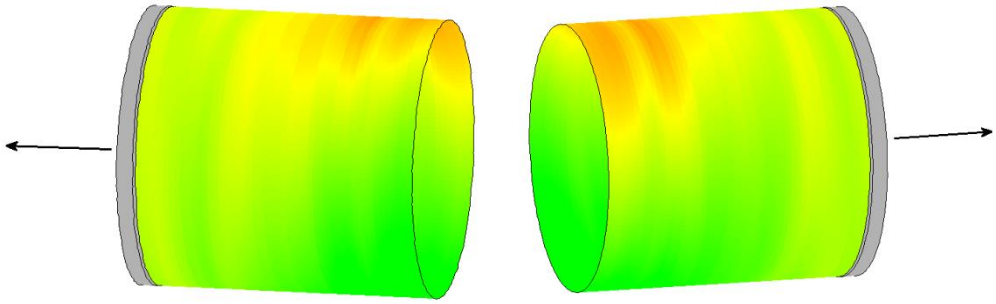

Figure 4.8: Kinematic interface interaction at advance -891.326 m

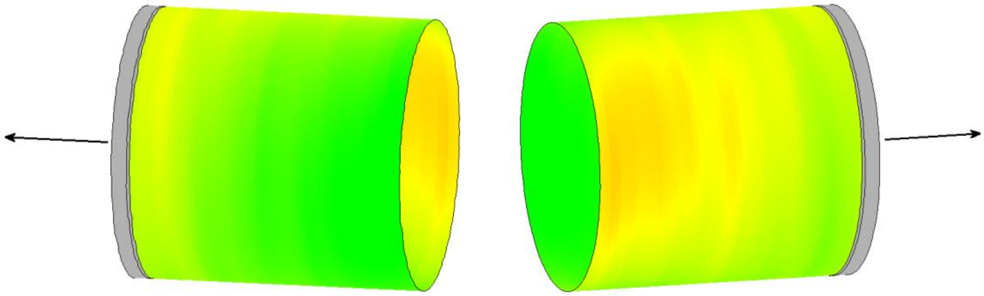

Figure 4.9: Kinematic interface interaction at advance -806.328 m

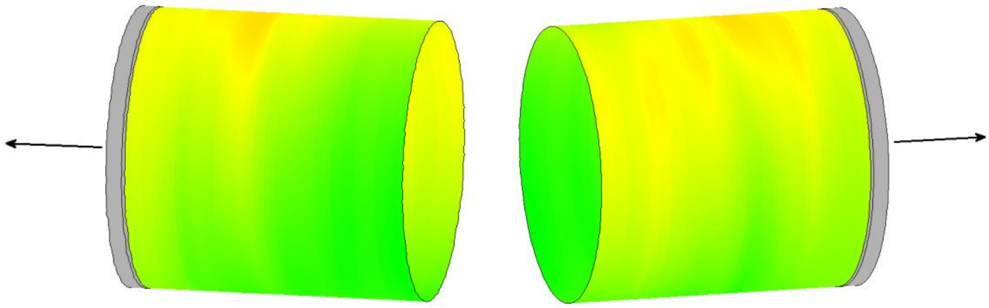

Figure 4.10: Kinematic interface interaction at advance -803.185 m

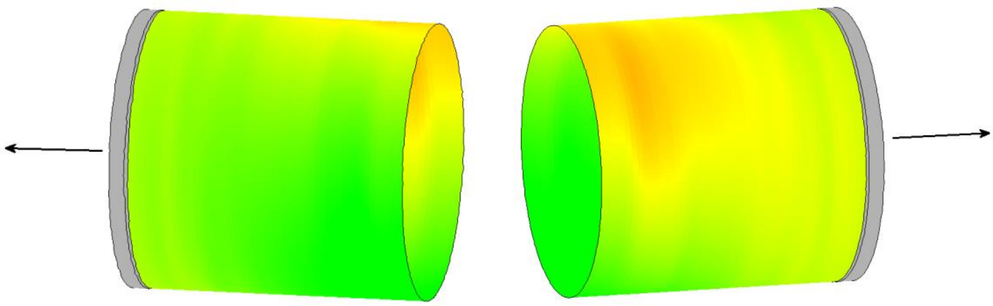

Figure 4.11: Kinematic interface interaction at advance -680.306 m

4.2.1 Shield position and orientation

The logged shield positioning data does not explicitly report the spatial coordinates of the reference points. The coordinates of the front and rear RPs are obtained by combining the observed deviations with the spatial coordinates of their corresponding points on the design alignment. The design alignment consists of a sequence of points evenly spaced at 1 m, and each point is assigned a unique tunnel advance measured along the discretized alignment. On the other hand the deviations are also provided in pair with their corresponding advance. The tunnel advance is therefore used to match the coordinates of the points on the design alignment with the corresponding observed deviations. A numerical example clarifies this aspect.

At advance km -1+340,108 the following set of deviations is recorded:

Table 4.1: Example deviations RPs

(measures in m)	Horizontal	Vertical
RPF (Reference Point Front)	-0.006 (f_h)	-0.006 (f_v)
RPR (Reference Point Rear)	+0.003 (r_h)	+0.008 (r_v)

The coordinates of the corresponding point on the design alignment, if not available, can be obtained through interpolation. For instance, the spatial coordinates at km -1+340,108 are obtained by interpolating those at advances km -1+340,000 and km -1+341,000.

Table 4.2: Example calculation interpolated point

Advance	X	Y	Z
km -1+340,000	81891.8903	458035.6331	-11.2887
km -1+341,000	81892.7367	458036.1656	-11.2788
km -1+340,108 (interpolated)	81891.9818	458035.6907	-11.2876
coordinates (in m) refer to the Dutch Reference System Rijksdriehoekcoördinaten (RD)			

The horizontal deviations are assumed to be right-angled (normal) to the horizontal projection of the tunnel alignment. The vertical deviations are assumed aligned with the force of gravity. The latter approximation is acceptable if the alignment's slope is small, as it usually is the case. Being

$\overrightarrow{F_t^i}$ (theoretical XYZ coordinates of RPF at advance i),

$\overrightarrow{R_t^i}$ (theoretical XYZ coordinates of RPR at advance i),

and

$\underline{\underline{I}}$ (3x3 identity matrix),

the unit vector tangent to the trajectory is expressed as:

$$\overrightarrow{T^i} = \left(\overrightarrow{F_t^i} - \overrightarrow{R_t^i}\right) \cdot \underline{\underline{I}} \cdot \left(1/\left\|\overrightarrow{F_t^i} - \overrightarrow{R_t^i}\right\|\right), \quad (4.1)$$

while the unit vector normal to the same trajectory is:

$$\overrightarrow{N_i} = \overrightarrow{T_i} \cdot \begin{bmatrix} 0 & -1 & 0 \\ 1 & 0 & 0 \\ 0 & 0 & 0 \end{bmatrix} \cdot 1/\left\|\overrightarrow{T_i} \cdot [1 \quad 1 \quad 0]\right\|, \tag{4.2}$$

The real spatial coordinates of RPF and RPR at advance i are:

$$\text{RPF: } \overrightarrow{F_i} = \overrightarrow{F_{i,t}} + \overrightarrow{N_i} \cdot f_h + [0 \quad 0 \quad 1] \cdot f_v \tag{4.3}$$

$$\text{RPR: } \overrightarrow{R_i} = \overrightarrow{R_{i,t}} + \overrightarrow{N_i} \cdot r_h + [0 \quad 0 \quad 1] \cdot r_v \tag{4.4}$$

The TBM-shield is represented by a frustum of cone (truncated cone) discretized according to a regular grid of 50 by 180 sectors in axial and circumferential direction, respectively. The front and rear diameters coincide with those of the TBM, that is 10,510 mm and 10,490 mm, respectively; the length is 10,235 mm. The frustum, initially located at the origin of the axis, is repositioned according to consecutive RPs' coordinates.

The frustum's coordinates are translated and rotated for getting it into position. The translation is achieved by adding a constant vector of displacement $\overrightarrow{D_i}$. The rotation is implemented via a rotation matrix $\underline{\underline{M_{ri}}}$. The columns of $\underline{\underline{M_{ri}}}$ contain an orthonormal triad defining the shield orientation at advance i. In symbols:

$$\underline{\underline{M_{ri}}} = \begin{bmatrix} T_{1x}^i & T_{2x}^i & T_{3x}^i \\ T_{1y}^i & T_{2y}^i & T_{3y}^i \\ T_{1z}^i & T_{2z}^i & T_{3z}^i \end{bmatrix}, \tag{4.5}$$

in which $\overrightarrow{T_1^i}, \overrightarrow{T_2^i}$, and $\overrightarrow{T_3^i}$ represent the unit vectors aligned with the longitudinal axis ($\overrightarrow{T_3^i}$), perpendicular to the longitudinal axis and horizontal ($\overrightarrow{T_1^i}$), and perpendicular to the previous two ($\overrightarrow{T_2^i}$). $\overrightarrow{T_1^i}, \overrightarrow{T_2^i}$, and $\overrightarrow{T_3^i}$, which are referred to the shield orientation, in principle do not coincide with $\vec{N}, \vec{B}$, and $\vec{T}$ (normal, binormal, and tangent), which are referred to the tunnel alignment, instead. Rotation and translation of the coordinates are applied as:

$$\overrightarrow{X_r} = \vec{X} \cdot \underline{\underline{M_{ri}}} + \overrightarrow{D_i}. \tag{4.6}$$

The deviations from the planned alignments are summarized in Figures 4.12 and 4.13. The tunnel advance is represented on the x-axis with negative sign as both tunnel tubes were driven in opposite direction to that originally planned. The sign change allows to preserve increasing tunnel advances during drive.

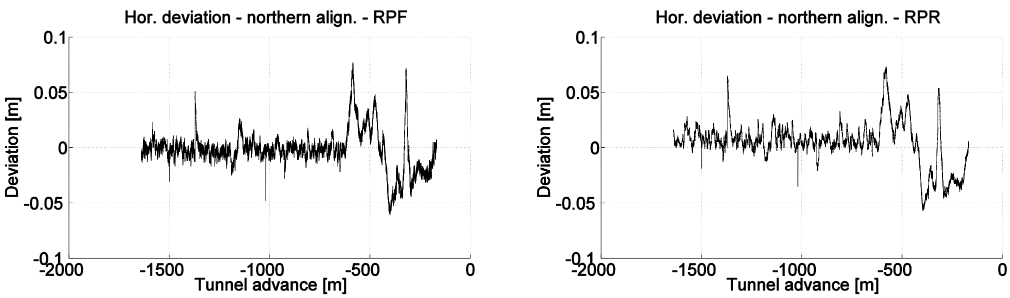

Figure 4.12: Horizontal deviations from the planned tunnel alignments. In DOD, positive values represent rightward deviations

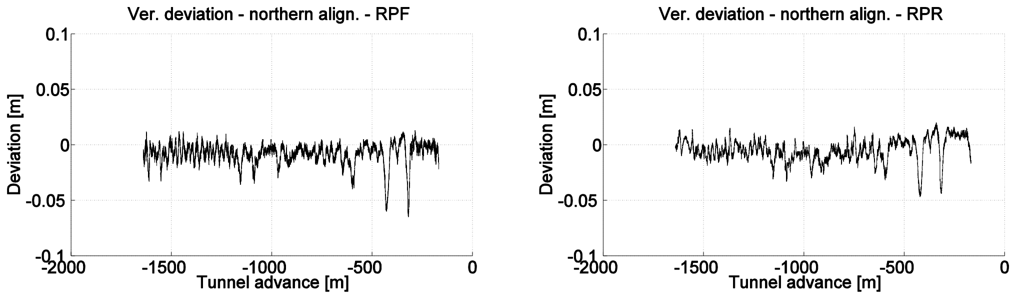

Figure 4.13: Vertical deviations from the planned tunnel alignments. In DOD, positive values represent upward deviations

4.2.1 Shield tendencies and corrections to the monitored values

Two relevant data sets are the horizontal and vertical tendencies of the TBM. Tendencies are obtained as the difference per unit length of the deviations of the reference points from the theoretical alignment. Tendencies provide indication of the relative positioning of the shield compared to its theoretical one at the same advance stage. The higher the tendencies the more pronounced the yawing/pitching behaviour of the shield is. For instance, the horizontal tendency T_h is defined as:

$$T_h = (f_h - r_h)/d_{RP}, \tag{4.7}$$

where f_h is the horizontal deviation of RPF, r_h the horizontal deviation of RPR, and d_{RP} is the distance between RPF and RPR, equal to 5.806 m in this project.

Tendencies may vary a lot even between closely spaced tubes excavated with the same TBM. This suggests that tendencies are at the same time a picture of the actual driving behaviour of the shield, but they are also the combined result of constructive, measuring, and geological uncertainties and other factors not easy to spot and isolate. Moreover, it is well known in tunnel practice but hardly mentioned in the pertinent literature that each TBM tends to show an individual intrinsic tendency which, if not taken into due account, can hide the actual TBM-soil interaction. For example, a poor calibration of the ALTU may as a result indicate an apparent side-ways tendency not actually present. However, no corrections of such kind are applied here as large tendencies necessitating that were not identified.

Other corrections are applied instead. At several locations the logged horizontal deviation jumps several centimetres without any apparent physical explanation. For instance, at advance -322.450 m of the south alignment both RPF and RPR shift in rightward direction of 40 mm when the TBM stands still. A possible reason is the realignment of the positioning system along the tunnel, although it is hard to know whether the measuring flaw occurred before or after the realignment took place. No mention of a recalibration is made in the daily logs. In conclusion, the corrections in Table 4.3 are applied to the horizontal deviations of both RPF and RPR. Figure 3.12 takes those already into account.

Table 4.3: Corrections to the horizontal deviations

south alignment		north alignment	
sector	**adjustment**	**sector**	**adjustment**
km -0+322,450 ÷ -0+290,490	-0.040 m	km -0+322,450 ÷ -0+290,490	-0.041 m
km -0+290,490 ÷ -0+288,470	-0.090 m	-	-

4.2.2 Cutting wheel articulation

The cutting wheel articulation system allows to produce an overcutting effect where needed. The cutting wheel is mounted on a supporting structure in turn connected to the main body of the TBM-shield via a spherical bearing, whose centre is located along the longitudinal axis of the shield. The wheel supporting structure is connected to the main shield via three pairs of so called *displacement cylinders*. The cylinders are connected on the one side to the rear of the spherical bearing, and on the opposite side to the TBM's main body.

The complex cutting wheel-spherical bearing can be shifted along the shield axis, i.e. the cutter head can be translated back and forth with respect to the shield body with an even retraction or elongation of the cylinders, respectively. Also the orientation of the wheel can be adjusted, and that takes place via the differential extension of three pairs of cylinders. In Direction Of Drive (DOD), the displacement cylinders are located at a radial distance of 1675 mm from the shield axis and positioned at noon (group A), +128° (group B), and -128° (group C) (positive direction clockwise).

Being l_a, l_b, and l_c the extension of the pairs of cylinders, the relative position and orientation of the cutter head with respect to the shield-body is determined as

$$\begin{cases} l_a = \left\|\vec{A} - \overrightarrow{A_0}\right\| \\ l_b = \left\|\vec{B} - \overrightarrow{B_0}\right\|, \\ l_c = \left\|\vec{C} - \overrightarrow{C_0}\right\| \end{cases} \tag{4.8}$$

in which $\vec{A}$, $\vec{B}$, and $\vec{C}$ point to the cylinders' ends at the wheel side, and $\overrightarrow{A_0}$, $\overrightarrow{B_0}$, and $\overrightarrow{C_0}$ to the cylinders' ends at the TBM side. Equations (3.8) are rewritten in a reference system with its origin in the middle of the spherical bearing and with the introduction of three parameters: l, which is the distance between the centre of the spherical bearing and the centre of the circle described by the end points of $\vec{A}$, $\vec{B}$, and $\vec{C}$; α, which is the rotation of the wheel around the vertical axis; β, which is the rotation of the wheel around the horizontal axis.

In the new reference system the unit vectors $\vec{V} = [v_1\ v_2\ v_3] = [0\ 0\ 1]$ and $\vec{H} = [h_1\ h_2\ h_3] = [1\ 0\ 0]$ are defined. Looking rearward, or against DOD, V and H point upward and rightward, respectively. The same vectors are then rotated according to α and β, together with the cutting wheel, and then transformed into $\overrightarrow{V_r}$ and $\overrightarrow{H_r}$. For a rotation α around the vertical axis, writing $K = 1 - cos\alpha$ for shortness, the rotation matrix writes

$$\underline{\underline{R_v}} = \begin{bmatrix} {v_1}^2 \cdot K + cos\alpha & v_1 \cdot v_2 \cdot K - v_3 \cdot sin\alpha & v_1 \cdot v_3 \cdot K + v_2 \cdot sin\alpha \\ v_1 \cdot v_2 \cdot K + v_3 \cdot sin\alpha & {v_2}^2 \cdot K + cos\alpha & v_2 \cdot v_3 \cdot K - v_1 \cdot sin\alpha \\ v_1 \cdot v_3 \cdot K - v_2 \cdot sin\alpha & v_2 \cdot v_3 \cdot K + v_1 \cdot sin\alpha & {v_3}^2 \cdot K + cos\alpha \end{bmatrix}, \tag{4.9}$$

and it follows $\overrightarrow{H_r} = [h_{r1}\ h_{r2}\ h_{r3}] = \underline{\underline{R_v}} \cdot \vec{H}$.

For a rotation β around the horizontal axis, writing $K = 1 - cos\beta$ for shortness, the rotation matrix is

$$\underline{\underline{R_h}} = \begin{bmatrix} {h_1}^2 \cdot K + cos\beta & h_1 \cdot h_2 \cdot K - h_3 \cdot sin\beta & h_1 \cdot h_3 \cdot K + h_2 \cdot sin\beta \\ h_1 \cdot h_2 \cdot K + h_3 \cdot sin\beta & {h_2}^2 \cdot K + cos\beta & h_2 \cdot h_3 \cdot K - h_1 \cdot sin\beta \\ h_1 \cdot h_3 \cdot K - h_2 \cdot sin\beta & h_2 \cdot h_3 \cdot K + h_1 \cdot sin\beta & {h_3}^2 \cdot K + cos\beta \end{bmatrix}, \tag{4.10}$$

and it follows $\overrightarrow{V_r} = [v_{r1}\ v_{r2}\ v_{r3}] = \underline{\underline{R_h}} \cdot \vec{V}$. The rotations α and β are combined in the rotation matrix

$$\underline{\underline{M_r}} = \begin{bmatrix} h_{r1}(1) & l_{r1}(1) & v_{r1}(1) \\ h_{r2}(2) & l_{r2}(2) & v_{r2}(2) \\ h_{r3}(3) & l_{r3}(3) & v_{r3}(3) \end{bmatrix}, \tag{4.11}$$

in which $\overrightarrow{L_r} = [l_{r1}\ l_{r2}\ l_{r3}] = \overrightarrow{V_r} \times \overrightarrow{H_r}$.

The coordinates of the fixed end points of the displacement cylinders with reference to the centre point X_o are

$$\begin{aligned} \overrightarrow{\mathrm{A_t}} &= [0; 0; 1675] \\ \overrightarrow{B_t} &= \left[-1675 \cdot \cos\left(\frac{38}{180} \cdot \pi\right); 0; -1675 \cdot \sin\left(\frac{38}{180} \cdot \pi\right)\right] \\ \overrightarrow{C_t} &= \left[1675 \cdot \cos\left(\frac{38}{180} \cdot \pi\right); 0; -1675 \cdot \sin\left(\frac{38}{180} \cdot \pi\right)\right]. \end{aligned} \tag{4.12}$$

$\overrightarrow{A_{tr}}$, $\overrightarrow{B_{tr}}$, and $\overrightarrow{C_{tr}}$ are the transformed of $\overrightarrow{A_t}$, $\overrightarrow{B_t}$, and $\overrightarrow{C_t}$ according to $\underline{\underline{M_r}}$, and $\overrightarrow{X_c}$ the middle point of the mobile ends of the displacements cylinders

$$\overrightarrow{X_c} = [-l \cdot sin\alpha \cdot cos\beta; l \cdot cos\alpha \cdot cos\beta; l \cdot sin\beta]. \tag{4.13}$$

The spatial coordinates of the cylinders' ends can be rewritten as

$$\begin{aligned} &\vec{A} = \overrightarrow{X_c} + \overrightarrow{A_{tr}}; \vec{B} = \overrightarrow{X_c} + \overrightarrow{B_{tr}}; \vec{C} = \overrightarrow{X_c} + \overrightarrow{C_{tr}} \\ &\overrightarrow{A_0} = \overrightarrow{X_0} + \overrightarrow{A_t}; \overrightarrow{B_0} = \overrightarrow{X_0} + \overrightarrow{B_t}; \overrightarrow{C_0} = \overrightarrow{X_0} + \overrightarrow{C_t} \end{aligned} \tag{4.14}$$

and the system of linear equations solved in the three unknowns l, α, and β.

4.2.3 Determination of the excavated cavities

The front and rear reference points are used to determine the position and the orientation of the tapered shield. The geometry of the excavated cavities are obtained by keeping track of the consecutive positions occupied by the cutting wheel and the cutting edge – front cross section of the shield – as the shield advances along the monitored alignment. In this way the cutting wheel and the cutting edge create two separate cavities, as the TBM advances through the soil. The two cavities are then combined into a single one, implicitly including the effect of the cutting wheel articulation.

The so-obtained discretized cavities are overly detailed and not evenly spaced. The high degree of detail is the result of the relatively short sampling time (few seconds) with low – normal for TBM excavation – but varying advance speeds (speeds between 0 and 70 mm/min were often observed). Frequent changes affecting the advance speed determine the irregular spacing of the grid.

More adequate grid resolution and regularity are obtained by interpolating the initial values on a rectangular mesh with elements' size around 150 ÷ 300 mm in longitudinal direction (Direction Of Drive) and 200 mm in circumferential direction. The grid's regularization turns out to be important for the stability of the algorithm for the calculation of the relative distance between the shield skin and the boundaries of the excavated geometry.

The regularization is performed by first calculating the longitudinal moving average of the $[x\ y\ z]$ coordinates on selected corners of the irregular grid. One grid's corner every ten corners counted in longitudinal direction is isolated, and the longitudinal average is calculated on the spatial coordinates of the grouped 15 preceding and 15 following points with respect to the one under consideration. The newly obtained grid is at this point formed by consecutive rings more widely spaced than before. The actual spacing is then expressly checked.

The distance between each pair of consecutive rings is checked not to be lower than 150 mm. If that is the case, then one ring is skipped. After that the distance between the consecutive rings is checked not to be larger than 300 mm. If that is the case, then a linear interpolation is performed and each original interval exceeding 300 mm is subdivided in a number of sectors equal to the result of the integer division of the original interval by 150 mm. In this way the longitudinal spacing between adjacent rings may only range between 150 and 300 mm.

4.2.4 Calculation of the interaction displacements

The interaction displacements between the TBM-shield and the excavated geometry will be referred to as shield-soil interface displacements. The displacements are quantified by means of the relative distance between the shield-skin and the boundaries of the excavated geometry. In Section 4.1 it was shown that the theoretical drive of a TBM results in sectors where the surrounding soil is compressed and others where it is relaxed. Such behaviour is expected to occur during the drive of actual TBMs as well.

As demonstration, the position of the shield-skin is compared to the excavated geometry at each advance stage. At each step of the TBM advance the relative distance is calculated between the discretized grids of the shield and of the excavated geometry. Additionally, specifying their relative position (external or internal to each other) allows distinguishing between compression and relaxation states.

For each node of the shield's grid the five closest points on the grid of the excavated geometry are identified. Then a Principal Component Analysis (PCA) is performed on the coordinates of those five points in order to identify the perpendicular to the best fit interpolating plane. The distance between TBM and excavated geometry is assumed equal to that between two parallel planes, also parallel to the interpolation plane, and intersecting the node of the shield's grid and the first of the set of five nodes on the excavated geometry.

4.2.5 Unloading-reloading configurations

The outlined approach for the determination of the shield-soil interface displacements lacks flexibility in view of the development of a tailored shield-soil interaction model. Defining the interface displacements as the distance between the shield skin and the "virgin" excavated geometry does make sense only if the surrounding soil behaves elastically. In case of elastic soil behaviour the load path does not matter and the strain history is irrelevant. The relative position of the shield-skin and of the virgin surface (i.e. the excavated geometry) does then suffice to convert the displacement/strain field into the stress one via an elastic soil constitutive model. But elastic soil constitutive models generally provide a poor description of the ground behaviour and response (Muir Wood [31]). This suggests the need for a conceptual framework suitable for the implementation of more realistic elastic-plastic constitutive models (Mari and Taylor [27]).

In the theoretical driving configuration of Figure 4.4 at the inner side of the curve the first half of the shield side partly displaces the surrounding soil beyond the line excavated by the cutting wheel. This creates a temporarily compressed area which is then released as the shield advances further. A realistic quantification of the soil relaxation at the shield tail should be thus based upon the distance between the shield-skin and the most outward configuration reached at any excavation stage, either caused by actual excavation or by shield-induced displacement. In this more refined approach the soil profile excavated by the cutting wheel is updated accounting for the outward displacements, if any, applied to it by the advancing shield.

Such unloading-reloading behaviour was already shown to occur based on the theoretical driving of curves following the geometrical arrangement of the reference points along the shield axis (Section 4.1). Unloading-reloading of the surrounding soil may also occur as consequence of the so-named snake-like motion of the shield (Sugimoto and Sramoon [42]). TBM-shields often fluctuate several centimetres around the planned alignment and that may lead to unloading-reloading configurations even in straight sectors or amplify it along curves.

4.3 Results of the kinematic analysis and discussion

The interface displacements continuously change along and around the shield. Comparing the interface displacements' distribution between 3D plots of the kind of Figure 4.5 taken at consecutive advances is interesting but not an effective way of summarizing the results. The interface behaviour is investigated at key locations around the TBM-shield instead. The shield tail is one such locations. For instance, in Figures 4.14 and 4.15 the interface displacements are shown at the left, top, right, and bottom positions along the shield tail circumference. Both south and north alignments are represented. Each graph presents the path of the interface displacements at one of the key positions of the shield tail. Selected alignment features are summarized in Table 4.4.

In the horizontal curves in sectors 2 and 5 compression occurs at the right-hand side and extension at the left-hand one. The compression rate is generally higher in sector 5 than in sector 2, and this is consistent with the smaller curvature radius in sector 5. In the same sectors the TBM shows higher compression and extension rates in the north alignment than in the south one. Although the reasons for that are not fully clarified, the exertion of higher steering forces in the north alignment compared to the south one may well be the cause. Should that actually be the case than the horizontal tendency of the TBM becomes naturally more pronounced and reflects onto the interface displacements, too.

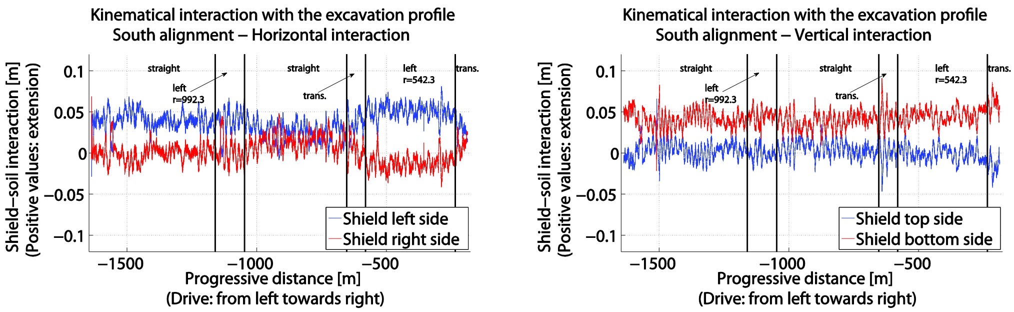

Figure 4.14: Kinematic interactions between the shield tail and the excavated geometry – south alignment. On the x-axis is the longitudinal distance (advance of the Reference Point Front minus the length of the shield); on the y-axis are the displacements, negative for compressed surrounding soil

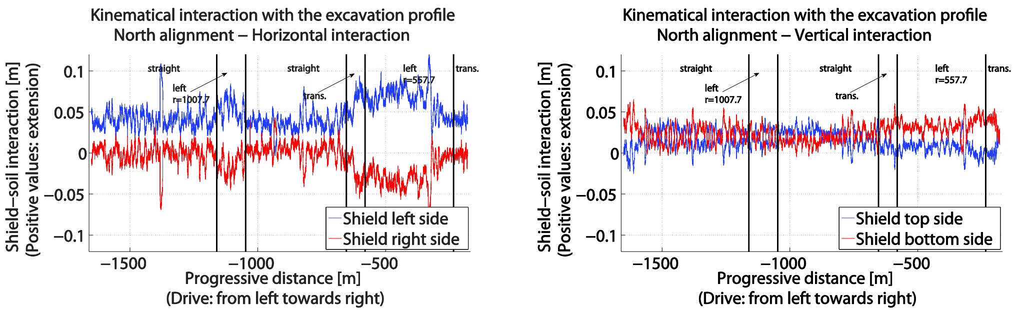

Figure 4.15: Kinematic interactions between the shield tail and the excavated geometry – north alignment. On the x-axis is the longitudinal distance (advance of the Reference Point Front minus the length of the shield); on the y-axis are the displacements, negative for compressed surrounding soil

Table 4.4: Features of the tunnel alignments

#	sector [m]	direction	horizontal radius south alignment [m]	horizontal radius north alignment [m]
1	-1660.088 ÷ -1160.200	-	straight	straight
2	-1160.200 ÷ -1074.090	left	992.300	1007.700
3	-1074.090 ÷ -653.220	-	straight	straight
4	-653.220 ÷ -580.490	left	transition	transition
5	-580.490 ÷ -233.820	left	542.300	557.700
6	-233.820 ÷ -169.891	left	transition	transition

In sector 1 the right-hand side of the shield tail follows the excavated geometry in both alignments as the interface displacements on that side show by fluctuating around 0. Similar behaviour is observed in sector 3 of the north drive. In contrast, in sector 3 of the south tube the shield appears well balanced in the middle of the steering gap. That is highlighted by the fact that the interface displacements fluctuate around 0.02 m at both sides. The steering gap of 0.02 m proves consistent with the gap obtained combining the shield tapering (0.01 m radial) and the standard overcutting (also 0.01 m radial).

Vertically, over the south alignment the TBM appears to advance with a negative tendency. That is demonstrated by the constant contact of the top point with the excavation track, highlighted by interaction values fluctuating around 0. At the bottom side the opposite happens with the presence of a “gap” ranging between 40 and 50 mm. In contrast, such vertical tendency is hardly observed over the north alignment in which the shield appears to fit well in the middle of the steering gap.

The results so far presented concern only the interaction of the shield tail with the surrounding soil and not the distribution of the interface displacements along the shield length. Figure 4.16 presents instead in the same graphs the interaction displacements over the shield length at a specific advance (-539.900 m) together with the tail interactions over few metres of tunnelling before that.

The horizontal interaction profiles over the shield length assumed in the geometrical analysis of Section 4.1 are confirmed. At the left-hand side, that is at the inner side of the leftward curve, after a short length over which the shield side adheres to the wall of the excavated geometry a “gap” originates and progressively increases up to 60 mm in the tail region. At the right-hand side, that is at the outer side, a sector with soil relaxation is followed by a recompression increasing towards the shield tail. The unloading-reloading behaviour is therefore reencountered here. Vertically, positive interaction values along the entire shield length confirm the fitting of the shield within the excavated geometry.

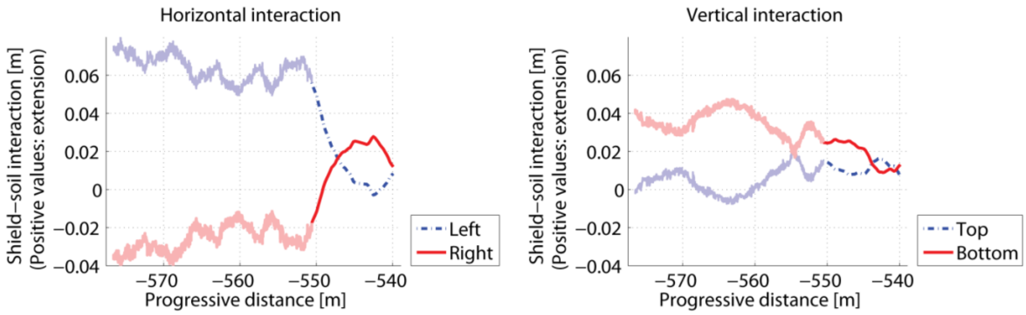

Figure 4.16: Kinematic interactions along the shield side – north alignment – Advance -539.000 m. The displacements along the shield length are plotted in blue and red (bright colours). The displacements at the shield tail are plotted in dimmed colours

4.3.1 On the possible effects of simplifications

One assumption in this study is the non-deformability of the shield tail. A deformable tail would lead to lower compression stresses. A more advanced analysis of shield-soil interaction should take this aspect into account even if in Section 2.5 it is shown that the effect of the shield tail deformation belongs to a lower order of magnitude in the case study under consideration.

Another assumption is that the logged deviations of the reference points (RPF and RPR) are correct and therefore processed further without substantial adjustments. Even though this project provides no specific indication concerning the need for such adjustments, preliminary studies on similar projects indicated at times the presence of odd kinematic configurations blindly assumed as representative of the real shield behaviour. This yields that the kinematic configurations should always be checked against the corresponding static likelihood.

That may be explained considering the kinematic configuration of Figure 4.1 which indicates that soil compression occurs at one side only whereas at the opposite one the soil is relaxed. In such condition the transversal equilibrium is impossible. The kinematic configuration should be considered with scepsis and corrections should be sought for. The case could also be that the pressurized tail grout penetrating around the shield skin where the surrounding soil is relaxed compensates the action of the compressed soil. This concept is developed in Chapter 6.

The third assumption consists of deriving the TBM's features mainly from the design drawings and in second place from discussions with the people involved in the design of the TBM and the construction of the tunnel. Construction flaws and size differences cannot be ruled out completely and could slightly alter the findings [ref: private communications].

It is finally worthwhile to observe that the results of the kinematic analysis presented in this Chapter substantially differ from the information usually provided by the shield positioning systems employed in tunnelling. Traditional systems indicate the actual position and orientation of the TBM with respect to its optimal one in which the Reference Points Front and Rear (RPF and RPR) are due to follow the design alignment of the tunnel. The proposed approach does not distinguish between optimal and real driving configurations. Instead, the proposed approach investigates the real driving behaviour, from that derives the excavated geometry, and then compares the current TBM position and orientation with the excavated geometry in order to provide a picture of the interaction with the surrounding soil.

4.4 Partial conclusions on the shield kinematic model

The analysis of the kinematic behaviour of a TBM driving in soft soil yields a reliable tool for determining the physical interaction between the TBM-shield and the surrounding soil. This seems relevant in order to improve the reliability of those numerical models that aim to predict the tunnelling-induced soil displacements by modelling the staged construction of bored tunnels. Those models often show significant improvement if a more realistic description of the shield-soil interaction process is included, that is when the phase of temporary support of the surrounding soil is better understood.

This study shows that the shield-soil interaction can be numerically modelled by processing the shield positioning data. The model compares the excavated track, created through the soil by the combined effect of the cutting wheel and of the cutting edge, with the spatial position of the shield-skin at each advance step along the tunnel alignment. The results match the theoretical expected shield-soil kinematic interactions based upon geometrical considerations on the shield shape and on the features of the shield positioning system. On the other hand, a possible weakness of the model is that it is largely based on the TBM positioning data and their accuracy. The monitoring data, as any other data-set derived from real processes, involve tolerances due to calibration and to the intrinsic precision of the monitoring equipment.

The model can be further validated by means of a static model of shield equilibrium whose construction steps are listed here. Firstly, the interface displacements derived in the kinematic analysis are transformed into a corresponding stress distribution acting on the shield periphery. Such transformation can be accomplished with the introduction of an appropriate soil-structure interaction model (Chapter 5). Secondly, the presence of face support and grout fluids around the shield periphery is considered (Bezuijen and Talmon [3]). Both fluids have the potential to infiltrate around the shield whenever the fluid pressure is locally higher than the contact stress between the shield and the wall of the excavated geometry. If penetration occurs, the stress state is not only determined by the soil stiffness anymore (Chapter 6). Thirdly, the measured and modelled forces and pressures acting on the shield are combined in the search for the static equilibrium. This validation strategy is pursued in Chapter 6.

Another validation approach consists in matching the displacements calculated at the shield-soil interface with those observed in the soil in the vicinity of the tunnel under construction. These are usually observed with subsurface displacement monitoring equipment such as inclinometers and extensometers. This analysis is presented in Chapter 7. Both validation strategies can be used to establish the validity of the kinematic model and to show possible directions of improvement.

Chapter 5

Deformation patterns and soil response

5.1 Most used soil reaction models in tunnelling problems

Most soil types exhibit a strongly non-linear stress-strain response which is dependent on their previous deformation history. Simplified soil-reaction models such as the Mohr-Coulomb linear elastic-perfectly plastic model can therefore lead to a poor estimate of the stresses at the shield-soil interface. In Chapter 4 the history of the soil deformation around the shield skin was obtained through the kinematic analysis of the TBM-shield. We now introduce a relatively simple but consistent soil-reaction model for the conversion of those displacements into stresses.

Both analytical and numerical soil models offer advantages when simplifications are introduced. For instance, in tunnelling problems the analytical approach has a closed form solution when the deformation field is assumed axially symmetric and the soil constitutive model linear elastic. Unfortunately, both simplifications are quite unrealistic. On the other hand numerical methods, although more flexible, are negatively affected by the computation effort required when such methods are used to solve problems with a level of detail such as that of this study.

Alternative solutions have been proposed in literature. Some are based on simplified soil reaction curves with upper and lower stress cut-offs based on the concepts of active and passive stress states (Sramoon and Sugimoto [39]). One interesting aspect of such curves is their dependency on the radial position around the tunnel or, as in our case, around the shield. For instance, the coefficient of passive lateral stress is assumed larger in horizontal than in vertical direction. The opposite holds for the coefficient of active lateral stress.

Although the models based on such simplified soil reaction curves take advantage of computation simplicity, they do not consider aspects as the dependency of the soil stiffness on the actual stress level and disregard the unloading-reloading response of the soil. Neither do they account for the fact that the soil mass above the tunnel is more limited than underneath. In this respect it will be shown that the soil responds differently at the shield top and bottom sides even in case of equal initial effective stress and applied displacements.

5.1.1 Novel soil reaction curves for the tunnelling problem

To overcome these shortcomings, novel soil reaction curves are proposed for modelling the planar problem of a circular cavity undergoing axially symmetric contractive and expansive displacements, or a sequence of them. The cavity is assumed not deformable, with ovalization prevented. The vertical displacements of the cavity are also prevented. Only the drained behaviour of a granular material (sand) is studied. Cohesive soils or partially drained soil response can represent a natural extension of this study.

Both model simplifications, that is the axial-symmetry of the displacements and the planar nature of the problem are debatable. In Chapter 4 it was indeed found that the displacements at the shield-soil interface are not axially-symmetric, neither are they constant along the shield length at fixed radial positions. For instance, one side of the shield could experience soil compression at the tail, neutral behaviour at the front, and soil extension in between. Both simplifications were considered acceptable for the current model, as detailed in Section 5.2.2.

The new soil reaction curves are defined interpolating the soil response curves obtained from FE analyses. The analyses were performed with the commercial code PLAXIS 2D on a wide range of conditions in terms of initial stress states and deformation patterns. A circular cavity with radius equal to that of the TBM-shield was defined (5.255 m). The cavity was located at -15, -20, and -25 m for simulating different tunnel depths and their matching initial stress states. The cavity was lined with a very stiff but weightless ring that prevented ovalization. The geometric centre of the cavity was fixed so that the groundwater-induced buoyancy effect could be excluded.

Loading-unloading and unloading-reloading patterns were alternatively implemented during which the stress-displacement relations at representative locations around the tunnel were observed. The loading-unloading case consisted in an areal expansion of 1.5% followed by an areal contraction of equal extent, corresponding to a radial change of about 40 mm. Vice-versa for the unloading-reloading case. The expansion rates were increased to 2% for the study of the soil response at different levels of deformation (see Sections 5.2.5 and 5.2.6). A 2% areal change corresponds to a radial increase/decrease of about 50 mm. In the loading configuration the surrounding soil is first compressed and then extended. The coincidence between the expansion and contraction rates makes so that the boundary of the cavity goes back to the initial position at the end of the cycle. The unloading-reloading case consists of a concentric convergence followed by an expansion of the same extent. Again the initial position of the boundary of the cavity is restored at the end of the loading cycle.

The rationale behind converting FE results into an analytical fit was allowing the construction of a simplified numerical model replacing more accurate but certainly more complex FE calculations to be repeated at every advance step. The explicit analytical expressions of soil response can instead be directly applied to the calculated deformation history of each of the 50x180 regions in which the shield periphery had been discretized, providing an approximated but quick response.

The PLAXIS model had a width of 100 m and a height of 50 m (see Figure 5.1). The groundwater table was located at ground level. The Hardening Soil constitutive model was adopted and drained conditions were applied. Sandy conditions were assumed as most of the tunnel was drilled through sand layers. The main soil parameters are summarized in Table 5.1 and are derived from the Geotechnical Reports of the Hubertus Tunnel ([46] [47]) (see also Chapter 2). Given a lack of data on the unloading-reloading behaviour, ${E_{ur}}^{ref}$ has been set at $3{E_{50}}^{ref}$, in accordance with the PLAXIS 2D (2012) Material Models Manual. A discussion on the value of k_0 is provided in Section 5.2.2.

The use of a numerical model for continuum mechanics, such as PLAXIS, implies that material continuity is assumed at all deformation stages between the tunnel and the surrounding soil. That needs not be the case in practical circumstances. Depending on the soil stiffness, on the drainage conditions and on the size and pattern of the applied displacements the mechanism of soil arching can prevail and a gap may originate between the excavated geometry and the tunnel, which in the context of this research represents the TBM-shield. PLAXIS cannot account for such mechanism. However, as described in Chapter 6, a hybrid approach is proposed in which the total stress calculated in the continuum mechanics model is compared to the grout pressure injected at the shield tail. Where the fluid pressure prevails than the presence of fluid grout is assumed. The same approach was already proposed by Bezuijen [1].

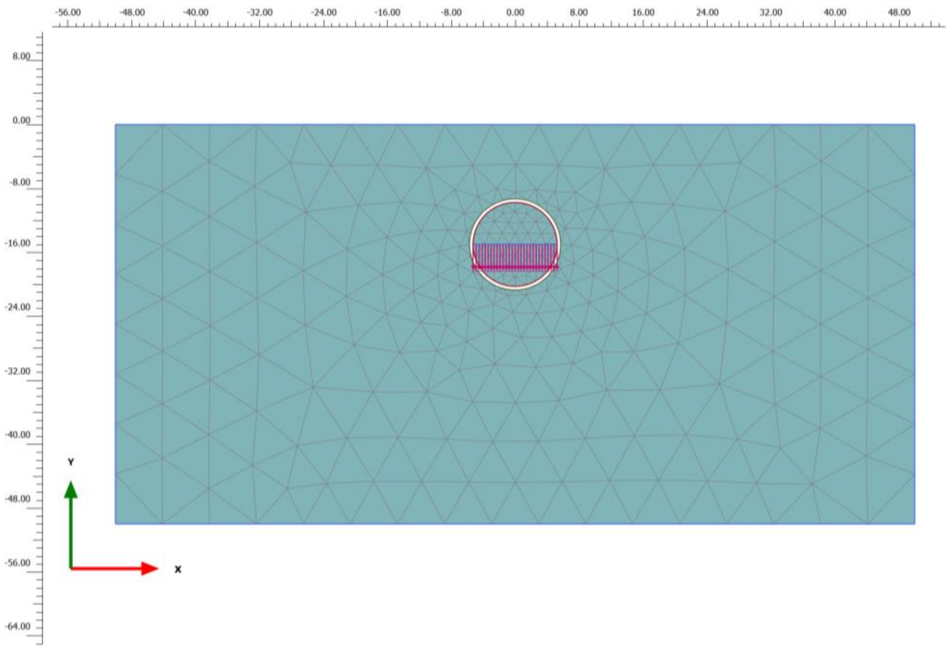

Figure 5.1: Connectivities of the FE model. Tunnel depth: 15 m

Table 5.1: Soil parameters FEM simulations

Parameter	Unit	Value
Material model	-	Hardening Soil Model
γ_{unsat}	[kN/m^3]	17
γ_{sat}	[kN/m^3]	20
E_{50}^{ref}	[kN/m^2]	40·10^3
E_{oed}^{ref}	[kN/m^2]	40·10^3
E_{ur}^{ref}	[kN/m^2]	120·10^3
$\varphi'(phi)$	[°]	32
$\psi(psi)$	[°]	2
c'_{ref}	[kN/m^2]	0
$k_0(1 - sin(\varphi'))$	-	0.4701

5.2 Analytical expressions of the novel soil reaction curves

The soil behaviour at representative locations around the shield is captured in a number of simplified analytical expressions in order to match the modelled path of the normal effective stresses versus the corresponding radial displacement at the shield-soil interface. Given the axial symmetry of the problem only half tunnel will be investigated.

5.2.1 Loading-unloading curves

Figures 5.2 to 5.4 show the graphs of the loading-unloading soil response curves at the three tunnel depths. At each depth of the tunnel-axis the initial stress changed according to the radial position. A different radial position implies a different soil cover and orientation even at a fixed depth of the tunnel axis. For example, the depth difference between the top and the bottom is 10.51 m, which with an effective volumetric weight of 10 kN/m^3 leads to a vertical effective stress difference of 105 kPa. Comparing the top and the right-hand side positions the vertical effective stress changes by 52.5 kPa and the orientation of the perpendicular to the tunnel turns from vertical to horizontal.

The first remarkable aspect is the very different soil stiffness when comparing for instance the top and bottom curves, and even more those to the right-hand one. The change in normal interface effective stress along the loading arm is larger at the bottom side than at the top one. This hints to a larger resistance to being displaced of the mass of soil underneath the tunnel than of the more limited amount above it.

The different soil behaviour between top and bottom sides is particularly visible at -15 m (5.2) and attenuates progressively with increasing depth (Figures 5.3 and 5.4). This is consistent with the fact that at large depths the ratio between the size of the cavity and of the tunnel depth diminishes, and the stiffness at top and bottom sides converges towards a unique vertical stiffness value. The difference between horizontal and vertical stiffness instead does not attenuate with increasing depth. In this respect it is observed that the difference in normal stress between the bottom and the right-hand sides decreases by almost the same amount at the end of the loading arm at all three depths.

The pressure drop in unloading is generally larger than the maximum stress at the end of loading. For example, the maximum stress level reaches at the end of loading -360 kPa, -440 kPa, and -520 kPa for the tunnel at -15, -20, and -25 m depth, respectively. However, the stress ends up around 0 kPa after unloading in all three conditions. The same reasoning can be extended to the other radial directions. During unloading the stiffness is usually higher at the lower half of the tunnel than at the upper one and the effect is more pronounced the shallower the tunnel is.

Figures 5.5 and 5.6 show the horizontal soil effective stresses and Figures 5.7 and 5.8 the vertical ones. Particularly in Figures 5.5 and 5.7 the selected radial locations appear to well catch the spatial distribution of the interface normal stresses. Figure 5.5 shows that the maximum horizontal stresses were modelled at the level of the spring line, which is one of the selected locations. Similarly Figure 5.7 shows that a local maximum of the vertical interface stress occurred around the upper quarter position (135° from bottom), also among the 5 selected locations.

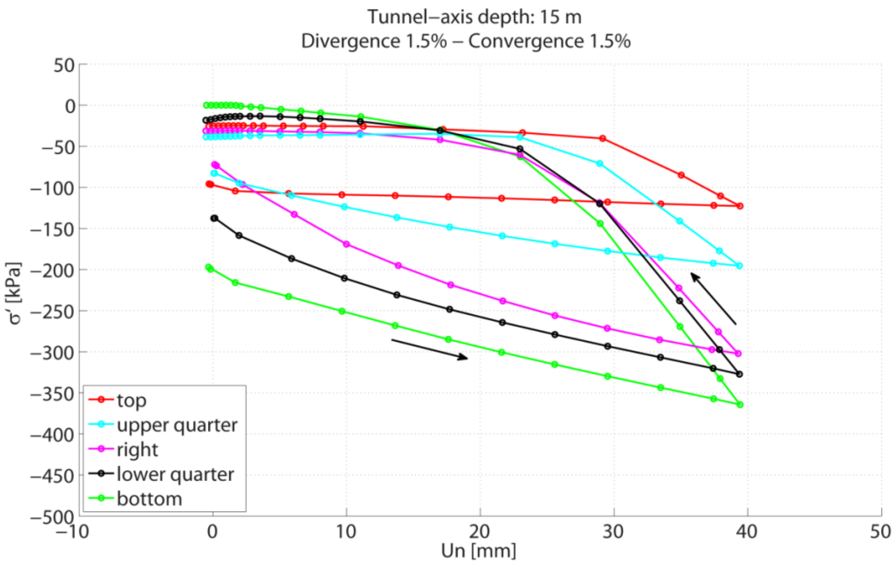

Figure 5.2: Expansion-contraction loading pattern. Tunnel depth: -15 m. The positions top, upper quarter, right, lower quarter, and bottom correspond to 180°, 135°, 90°, 45°, and 0° measured from bottom and in counter-clockwise direction, respectively

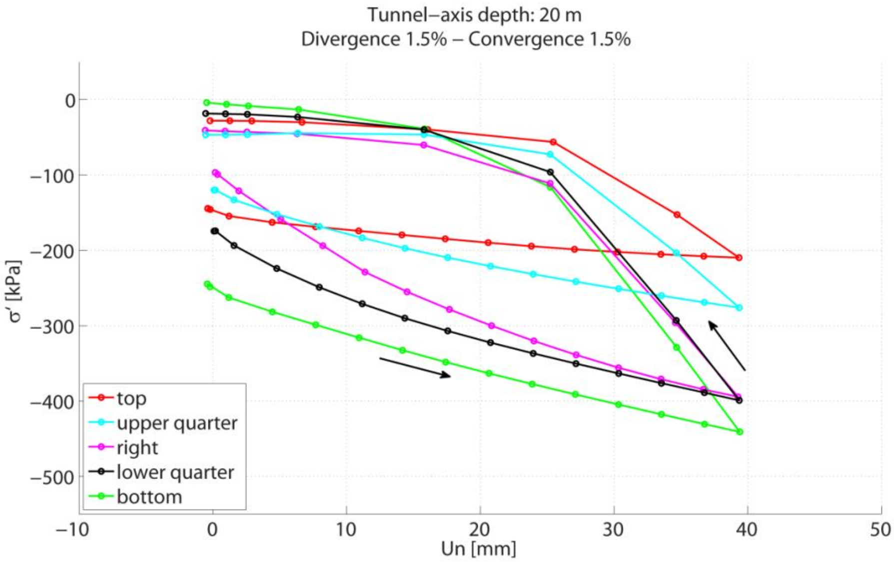

Figure 5.3: Expansion-contraction loading pattern. Tunnel depth: -20 m. The positions top, upper quarter, right, lower quarter, and bottom correspond to 180°, 135°, 90°, 45°, and 0° measured from bottom and in counter-clockwise direction, respectively

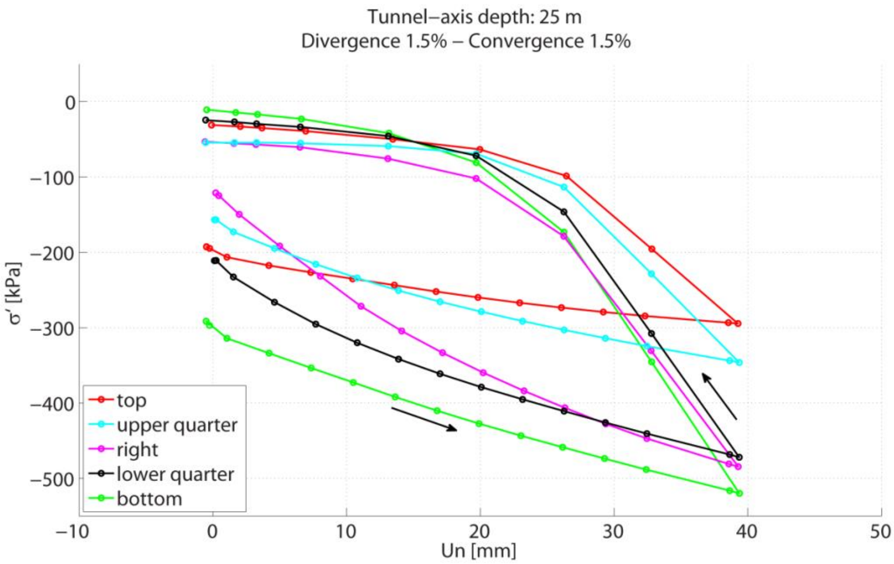

Figure 5.4: Expansion-contraction loading pattern. Tunnel depth: -25 m. The positions top, upper quarter, right, lower quarter, and bottom correspond to 180°, 135°, 90°, 45°, and 0° measured from bottom and in counter-clockwise direction, respectively

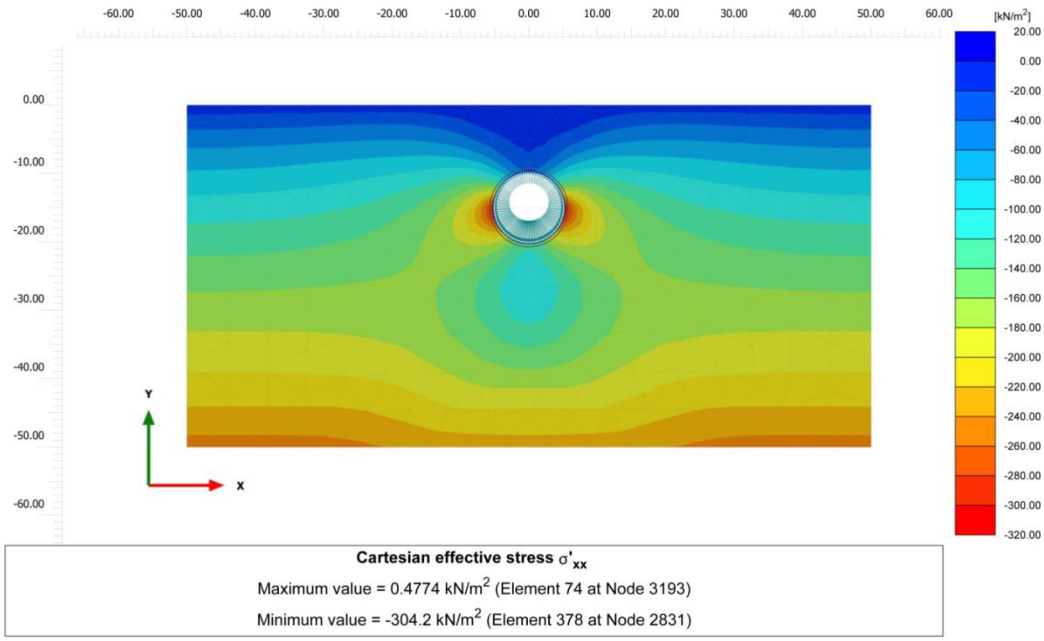

Figure 5.5: Expansion-contraction loading pattern. Horizontal effective stresses at the end of the expansion phase (PLAXIS 2012)

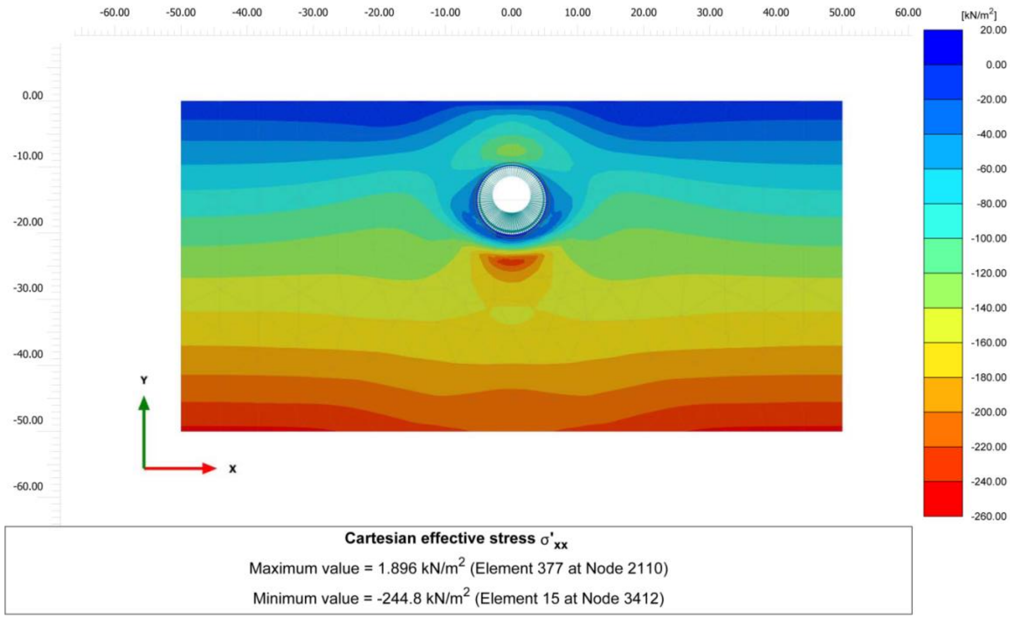

Figure 5.6: Expansion-contraction loading pattern. Horizontal effective stresses at the end of the contraction phase (PLAXIS 2012)

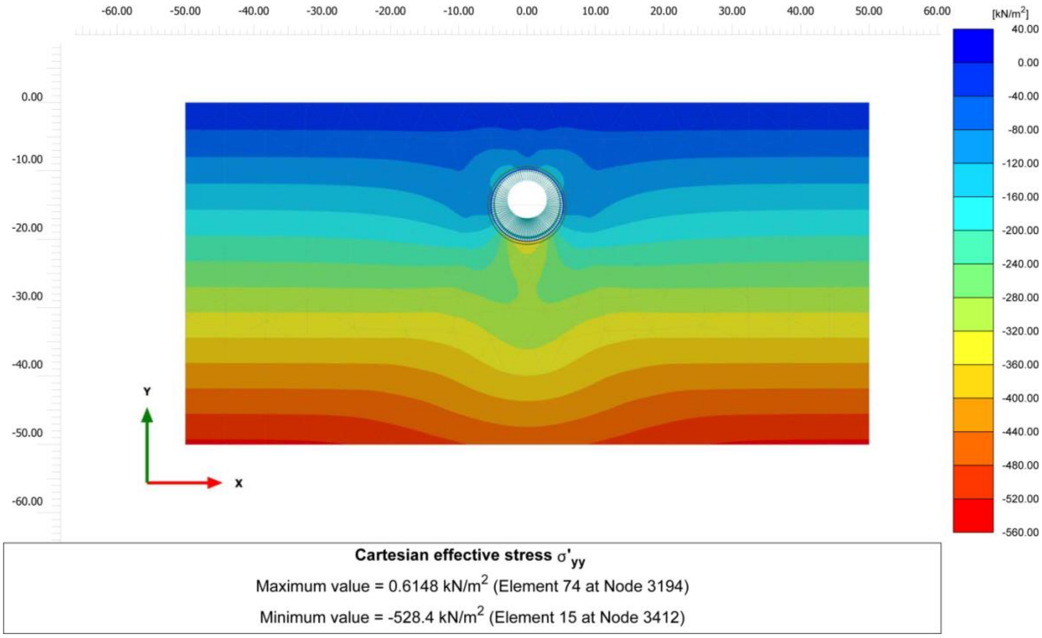

Figure 5.7: Expansion-contraction loading pattern. Vertical effective stresses at the end of the expansion phase (PLAXIS 2012)

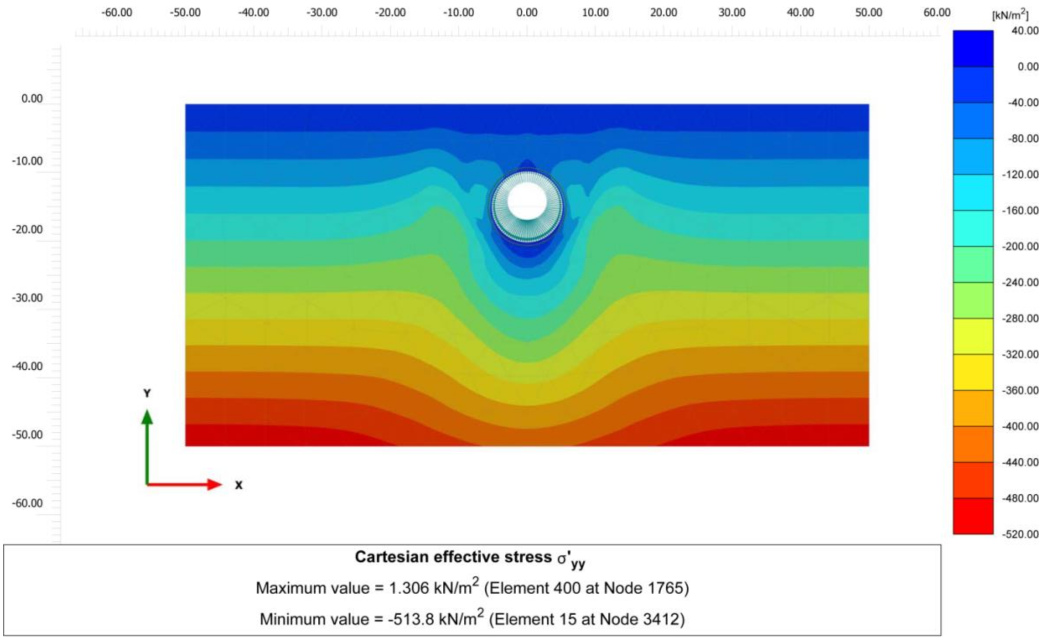

Figure 5.8: Expansion-contraction loading pattern. Vertical effective stresses at the end of the contraction phase (PLAXIS 2012)

5.2.2 Discussion on some model approximations

In Chapter 4 the interface displacement associated with each of the 50x180 sectors in which the shield has been discretized change gradually between adjacent sectors in radial and longitudinal direction. This suggests that axial-symmetric displacements and planar behaviour of the tunnel cavity are acceptable simplifications. The results of two PLAXIS models are studied to verify this hypothesis.

The first model is the same as used to plot Figure 5.9 and is used to retrieve the soil reaction curves following a sequence of axial-symmetric expansion and contraction of the tunnel cavity. In the second model the tunnel cavity is displaced horizontally and vertically, and the associated soil response is recorded. The soil response at the depth of the spring line of the tunnel is obtained by first displacing the tunnel cavity 40 mm horizontally from its original position and then bringing it back. The soil response at the top and at the bottom of the tunnel cavity is obtained by displacing the tunnel cavity vertically and then returning to the original position. The results of the axial-symmetric model and of the 2D model are summarized in Figure 5.9.

The results indicate a generally good agreement during loading, particularly at the tunnel bottom. The largest difference at the end of the loading phase is at the right side. The increase in horizontal effective stress associated with a horizontal displacement of 40 mm is about -470 kPa in the axial-symmetric model and -400 kPa in the 2D one, i.e. a difference around 20%.

In the unloading phase the match between the two models is acceptable at the right and bottom but less so at the top. In the axial-symmetric model at the tunnel top an arching effect seems to be into play. During contraction the effective stress there strongly decreases to -30 kPa. In the 2D model on the other end the effective stress changes little, and that seems to indicate that the wedge of soil beneath the tunnel cavity follows the vertical movements of the cavity itself without a pronounced soil arching effect.

The choice between axially-symmetric and 2D model appears a sensitive point of the analysis, in light of this comparison. However, the axial-symmetric option is preferred in this study as the simplicity of the numerical model for TBM equilibrium remains a governing point for this research. Another comparison between axial-symmetric and anti-symmetric condition is performed in Sections 6.4.3.1 and 6.4.3.2.

In Table 5.1 the coefficient of lateral stress K_0 was assigned a fixed value of 0.4701, obtained as $K_0 = 1 - sin\varphi'$. That needs not be a correct assumption and different values for K_0 are possible. The effect on the soil reaction curves of different K_0 values is checked hereafter.

Figures 5.10 shows the soil reaction curves at the five reference locations for a 15 m deep expanding-contracting tunnel cavity. The graphs show the curves for three different values of K_0: 0.4, 0.4701, and 0.6, respectively. The said interval covers a range which seems reasonable for normally consolidated sands.

For $K_0 = 0.6$ the increase in effective stress at the tunnel top along the loading arm is about -25 kPa, and that reduces to about 0 kPa for $K_0 = 0.4$. At the level of the spring line the increase in effective stress is -200 kPa and -230 kPa for $K_0 = 0.6$ and $K_0 = 0.4$, respectively. At the tunnel bottom the increase in effective stress is -200 kPa and -160 kPa for $K_0 = 0.6$ and $K_0 = 0.4$, respectively.

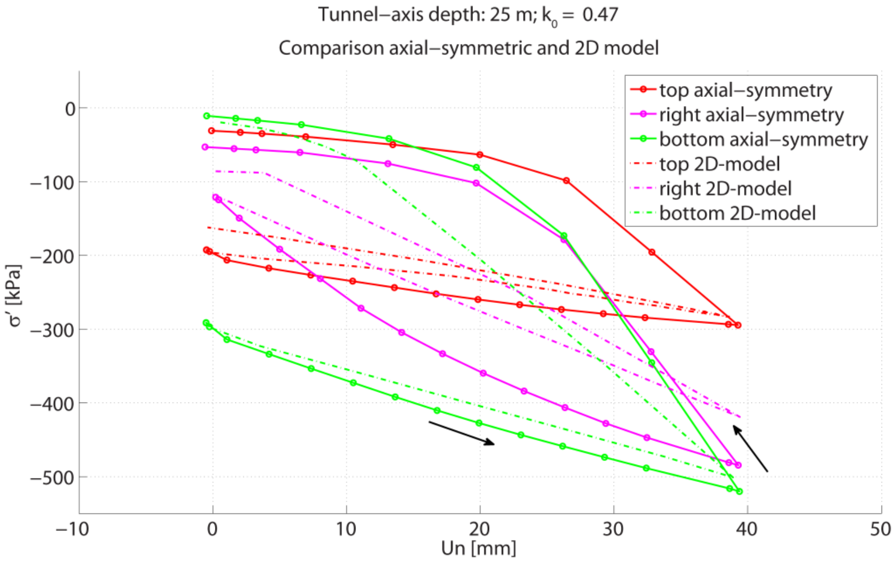

Figure 5.9: Comparison expansion-contraction loading pattern and anti-symmetrical displacements (horizontal and vertical). Tunnel depth: -25 m. The positions top, right, and bottom correspond to 180°, 90°, and 0° measured from bottom and in counter-clockwise direction, respectively

The unloading arms also differ. Looking at the bottom side of the tunnel, Figure 5.11 ($K_0 = 0.6$) shows that a convergence of 20 mm from the point of maximum expansion leads to a stress drop of -350 kPa. The same convergence in Figure 5.13 leads to a stress drop of -300 kPa.

The error in the calculated effective stress as a result of different values of K_0 appears limited to about 20 % even in unfavourable circumstances, both during loading and unloading. Assuming $K_0 = 0.47$ the possible error in the approximation reduces to about 10%. In the framework of this research that seems an acceptable simplification.

The graphs in Figure 5.11 reflect the effect of the elastic modulus E_{50} on the soil reaction curves. The results for $E_{50} = 20\ MPa$ and $E_{50} = 40\ Mpa$ are compared. At the tunnel bottom the increase in effective stress at the end of the loading phase totals -100 kPa and -165 kPa for moduli of 20 MPa and 40 MPa, respectively. At the depth of the tunnel spring line the effective stress increase is -160 kPa and -230 kPa for the same moduli of 20 MPa and 40 MPa, respectively. At the tunnel top the stress increase is in both cases similar and limited to about -20 kPa.

With differences in terms of effective stress increase in the order of 50 % the elastic constant E_{50} seems to have a larger effect on the soil reaction curves than K_0 or the axial-symmetric simplification of the applied displacements. This comparison is in fact far from perfect as the investigated variation ranges of E_{50} and of K_0 are not strictly comparable. On the other hand the assumed ranges cover a realistic variation of the said parameters for the problem investigated in this research. An estimate of the effect of the value of E_{50} on the equilibrium of the TBM-shield is presented in Section 6.4.3.

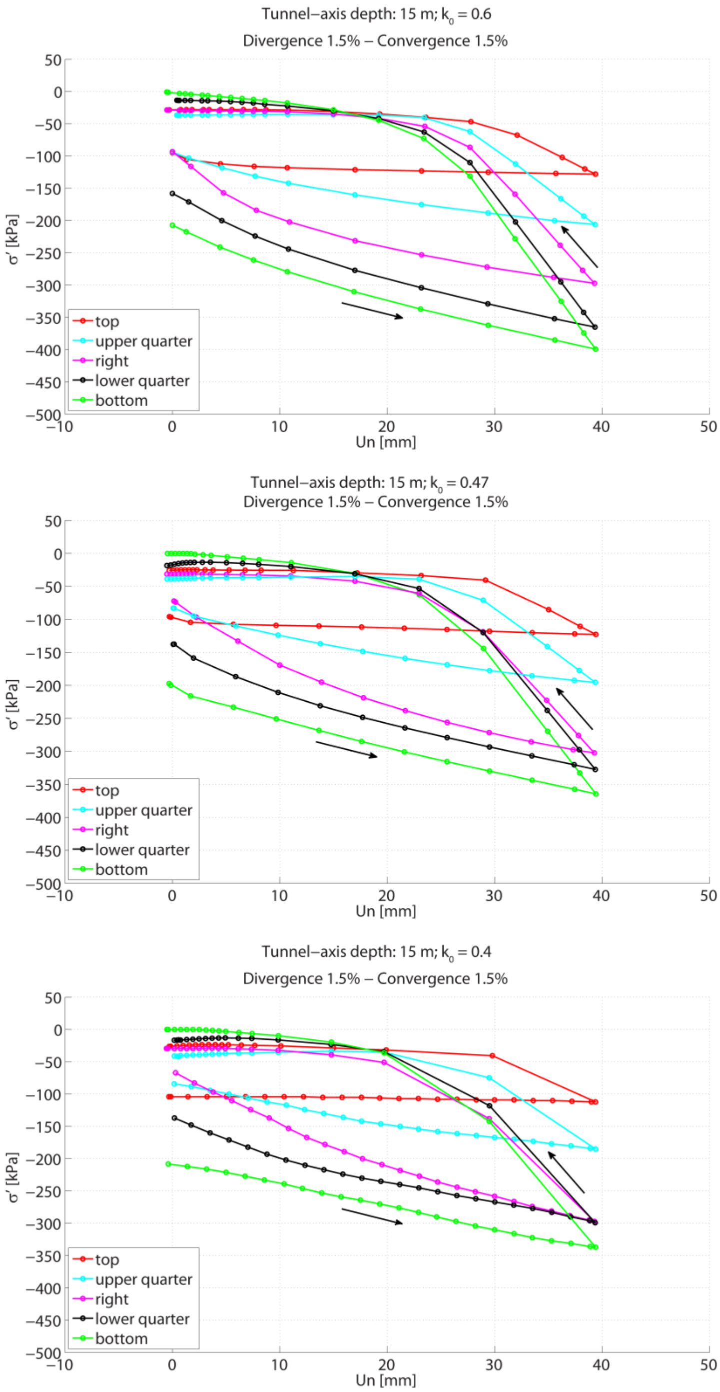

Figure 5.10: Expansion-contraction loading pattern. Tunnel depth: -15 m. $K_0 = 0.6/0.47/0.4$. The positions top, upper quarter, right, lower quarter, and bottom correspond to 180°, 135°, 90°, 45°, and 0° measured from bottom and in counter-clockwise direction, respectively

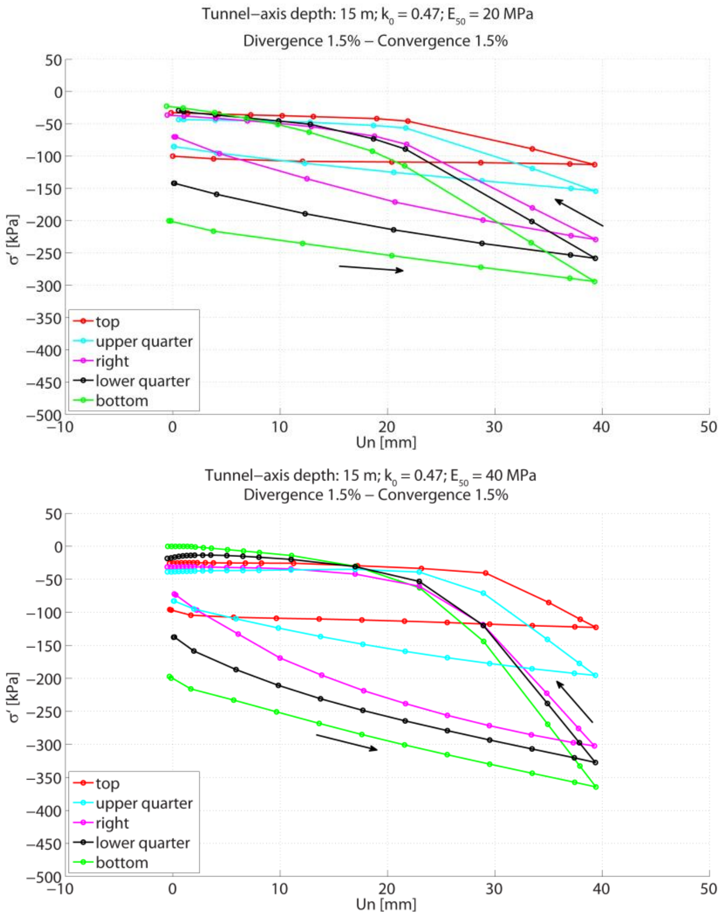

Figure 5.11: Expansion-contraction loading pattern. Tunnel depth: -15 m. The positions top, upper quarter, right, lower quarter, and bottom correspond to 180°, 135°, 90°, 45°, and 0° measured from bottom and in counter-clockwise direction, respectively

5.2.3 Unloading-reloading curves

The unloading-reloading curves of soil response curves are plotted in Figures 5.12 to 5.14. At each tunnel depth the initial normal stress level changes according to the radial position as different radial positions imply different soil cover and different orientation to the tunnel cavity.

The surrounding soil during unloading shows a stiffer response in the lower half of the tunnel than in the upper one. That emerges when comparing the bottom position with the top one. At all depths the model indicates that there is barely any effective stress left at the bottom side after a contraction of only 20 mm. The zones of zero contact stress move upward towards the right-hand side position first and then towards the top side as unloading continues. Zero contact effective stress opens up the possibility for cavities to be present, in fact bringing the theory of continuum mechanics to its limit.

The stresses at the top side along the contraction arm decrease more the deeper the tunnel is. That is explained by arching of the surrounding soil above the contracting cavity. During the contraction phase, in case of a shallow tunnel, the arching mechanism can build up with difficulty and the weight of the overlying soil continues to act on the tunnel lining, notwithstanding the contraction (Figure 5.12). For deeper tunnels, the arching effect occurs more easily, transferring part of the overlying weight towards the sides of the tunnel and decreasing the stresses on the tunnel lining.

The stiffness in the re-loading arms is similar among the different radial positions, at least during the first stages of re-loading. After further re-loading the stiffness differentiates between the different radial directions similarly to what already observed in Section 5.2.1. At the bottom side the stress recovery is larger than at the top. Even larger recovery is observed at the right-hand side.

Figures 5.15 and 5.16 provide an overview of the horizontal soil effective stress and Figures 5.17 and 5.18 the vertical ones. It is observed that the five selected radial locations well represent the spatial distribution of the interface normal stresses around the shield. The maximum and minimum stresses usually occur in correspondence of one of the selected locations. The only exception is in Figure 23 in which the maximum vertical effective stress was modelled at an intermediate location between the bottom and the lower quarter ones, approximately 22° from bottom. However, due to the modest contribution of such singularity, the selected locations represent an acceptable approximation within the scope of the present work.

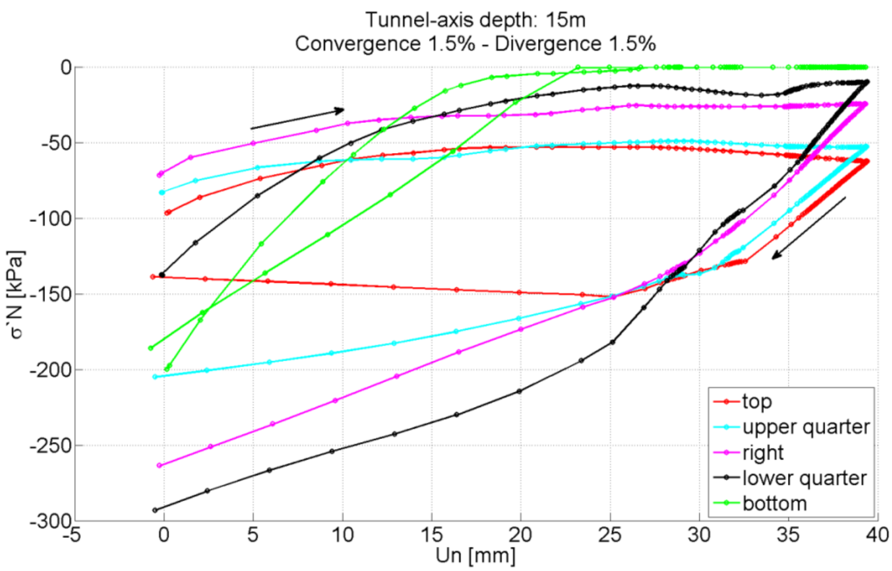

Figure 5.12: Contraction-expansion loading pattern. Tunnel depth: -15 m. The positions top, upper quarter, right, lower quarter, and bottom correspond to 180°, 135°, 90°, 45°, and 0° measured from bottom and in counter-clockwise direction, respectively. Arrows indicate the loading path

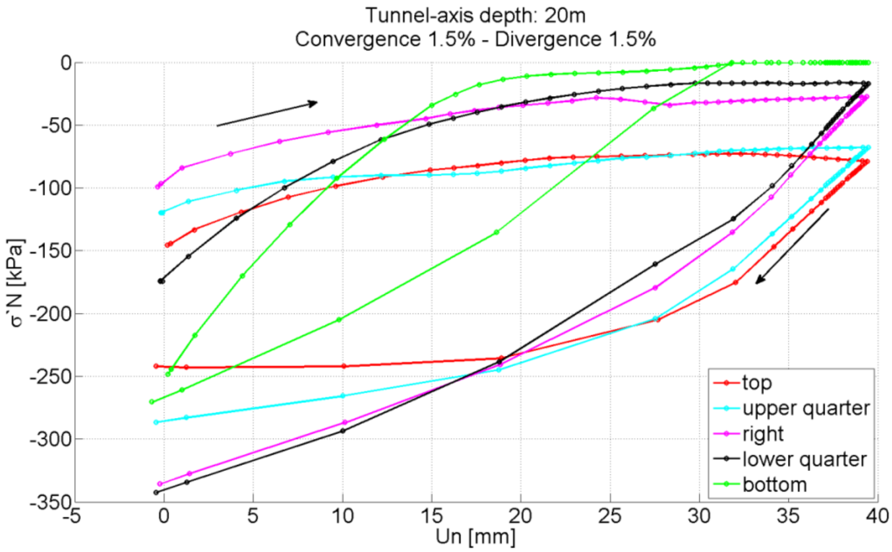

Figure 5.13: Contraction-expansion loading pattern. Tunnel depth: -20 m. The positions top, upper quarter, right, lower quarter, and bottom correspond to 180°, 135°, 90°, 45°, and 0° measured from bottom and in counter-clockwise direction, respectively. Arrows indicate the loading path

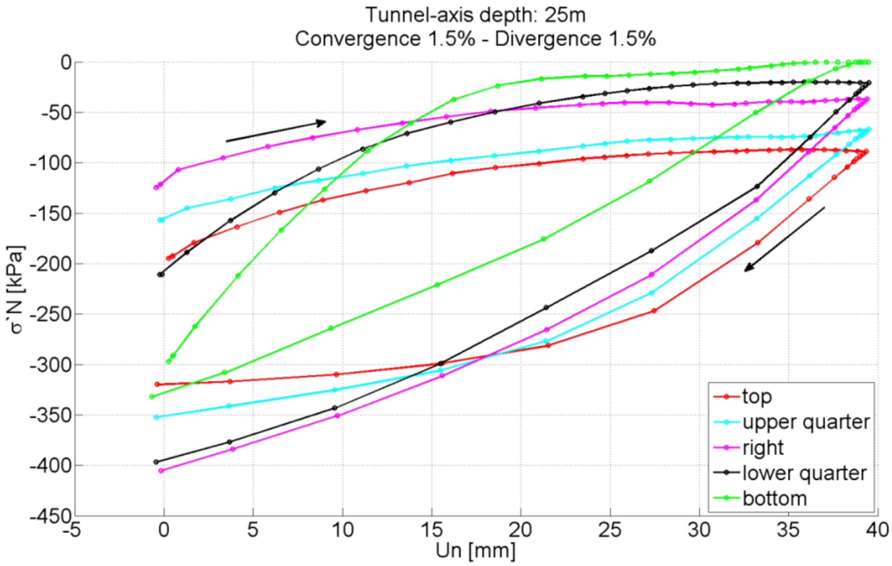

Figure 5.14: Contraction-expansion loading pattern. Tunnel depth: -25 m. The positions top, upper quarter, right, lower quarter, and bottom correspond to 180°, 135°, 90°, 45°, and 0° measured from bottom and in counter-clockwise direction, respectively. Arrows indicate the loading path

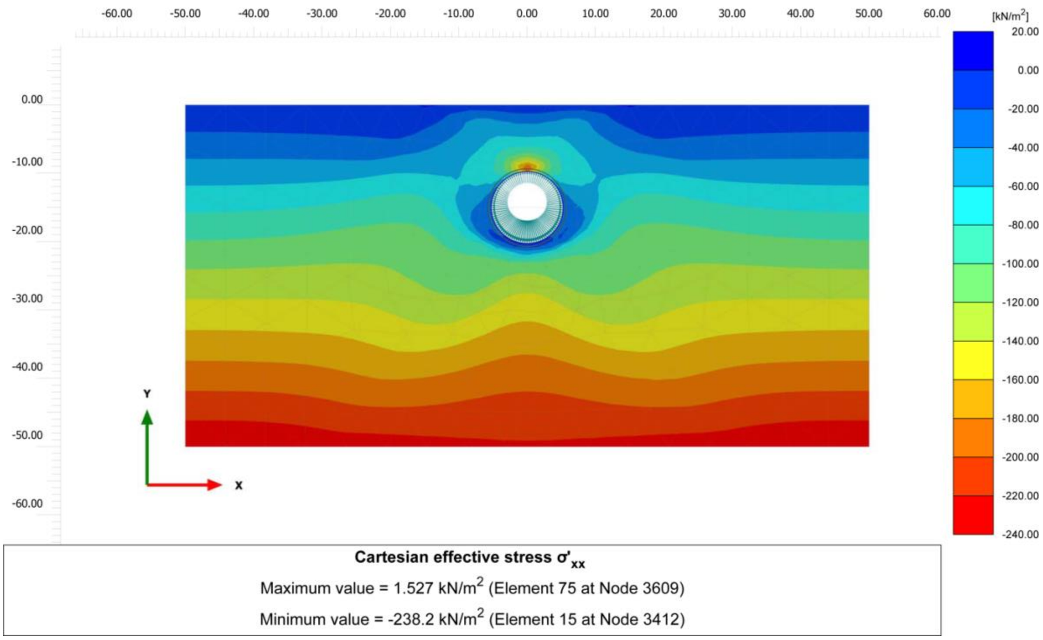

Figure 5.15: Contraction-expansion loading pattern. Horizontal effective stresses at the end of the contraction phase (PLAXIS 2012)

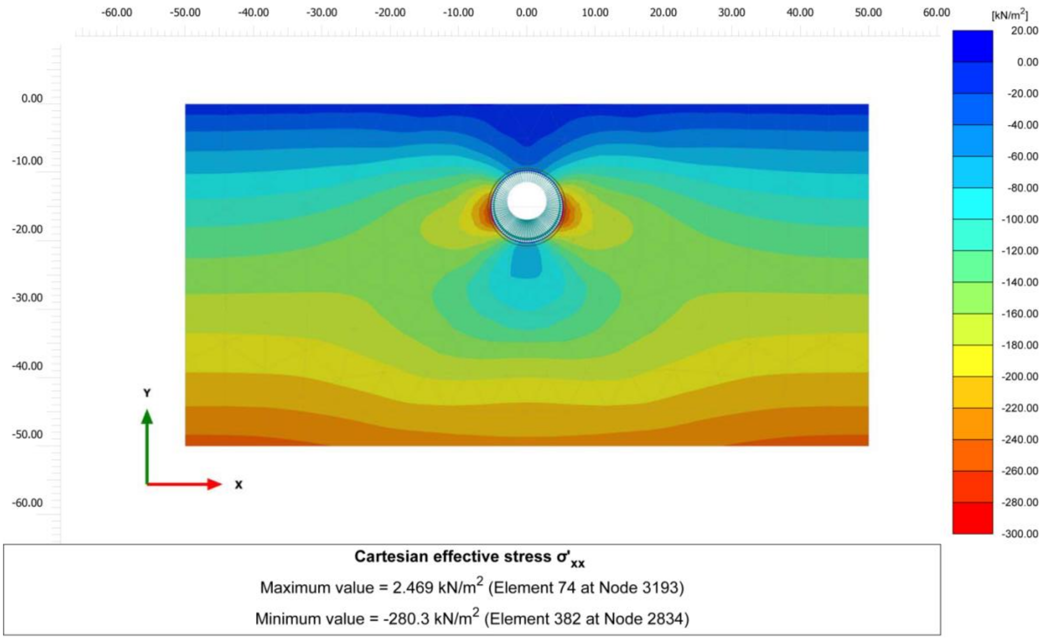

Figure 5.16: Contraction-expansion loading pattern. Horizontal effective stresses at the end of the expansion phase (PLAXIS 2012)

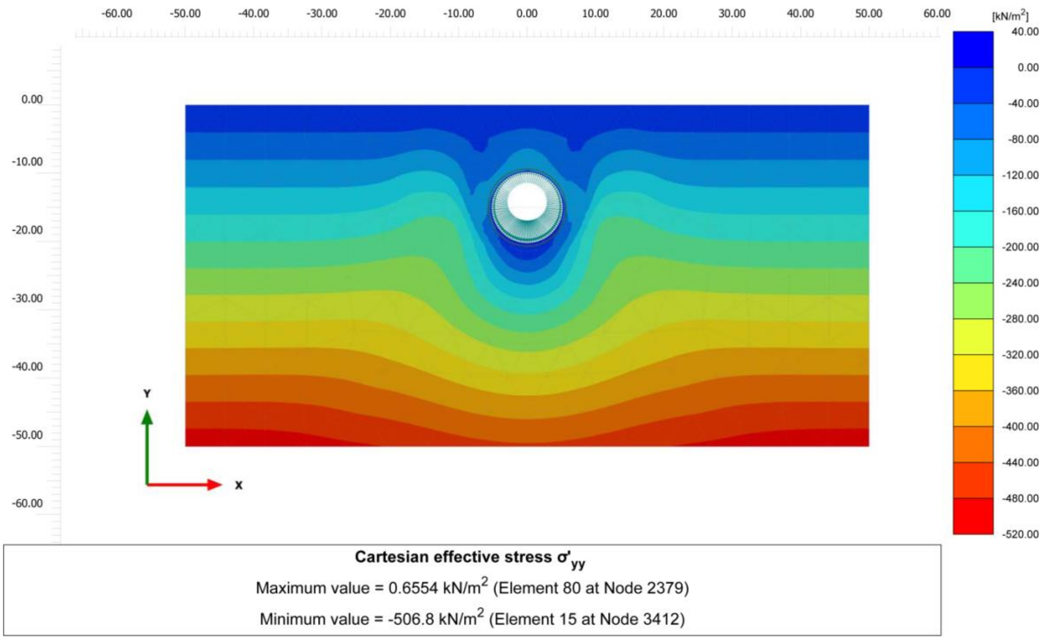

Figure 5.17: Contraction-expansion loading pattern. Vertical effective stresses at the end of the contraction phase (PLAXIS 2012)

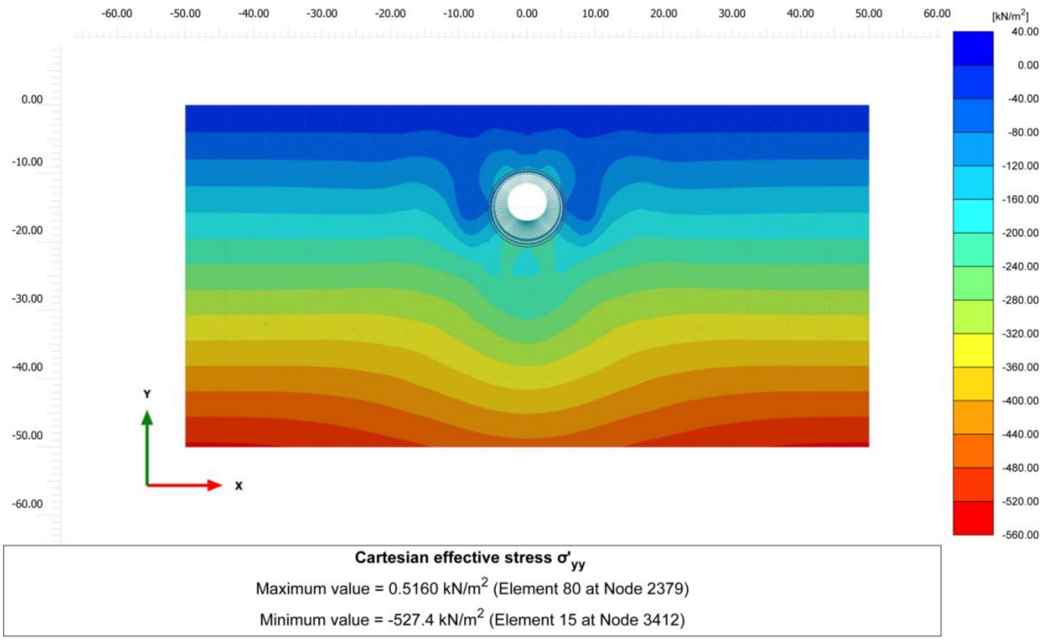

Figure 5.18: Contraction-expansion loading pattern. Vertical effective stresses at the end of the expansion phase (PLAXIS 2012)

5.2.4 Effect of radial direction

The loading-unloading curves presented in Section 5.2.1 start from different initial stress levels, depending on tunnel depth and radial orientation. This Section gives a qualitative overview of the loading-unloading behaviour starting from an effective normal stress of -200 kPa. Figure 5.19 shows a loading-unloading cycle up to a deformation of 40 mm. The results are obtained by applying the Hardening Soil constitutive model and a triaxial stiffness ${E_{50}}^{ref} = 40$ MPa.

The equal initial stress at different orientations is obtained by positioning the tunnel at different depths. The normal stress level depends on the overburden but also on the orientation, according to the coefficient of lateral earth pressure at rest K_0. Different soil responses are observed. The direction showing the stiffest behaviour is the right-hand one (90°). Linearly connecting the initial and the end points of the loading arm allows to define a subgrade reaction modulus. The ratio between the stress increment and the displacement increment provides

$$\frac{\Delta\sigma'}{\Delta Un} \cong \frac{500}{40} = 12.5 \text{ MPa/m} \tag{5.1}$$

The direction with the smallest stiffness during loading is the top one (red line). The stiffness during loading quickly increases towards the right-hand side and then decreases further downward. At equal initial stress the observed stiffness at the bottom is higher than at the top. The observed stiffnesses during unloading are consistent with those during loading, that is larger unloading stiffnesses corresponded to larger loading ones. The unloading curves also show a sort of bilinear response, with the first sector showing a much more pronounced stiffness than the second one. A fixed ratio between the average stiffness during loading and during the first unloading sector could not be established.

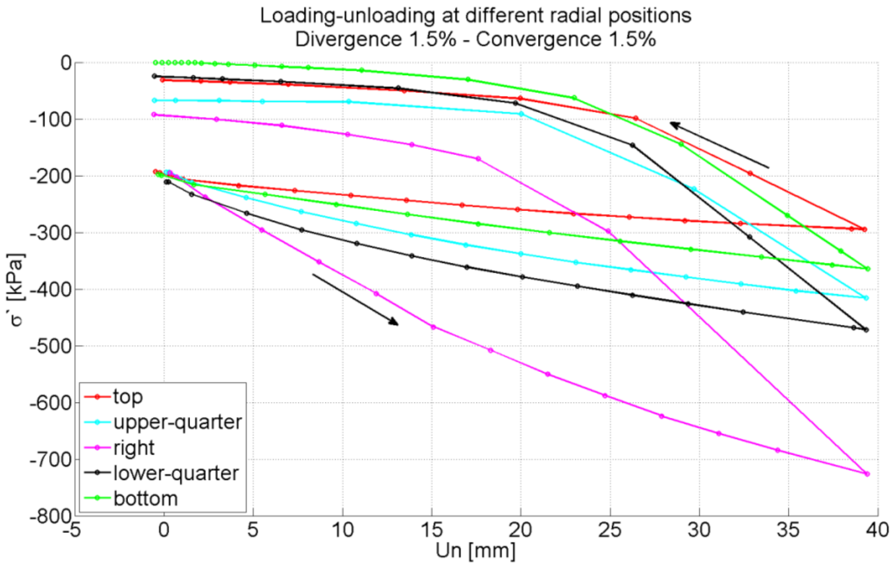

Figure 5.19: Loading-unloading for multiple directions with common initial normal effective stress. The positions top, upper quarter, right, lower quarter, and bottom correspond to 180°, 135°, 90°, 45°, and 0° measured from bottom and counter-clockwise, respectively. Arrows indicate the loading path

Figure 5.20 shows the different unloading-reloading responses starting from an initial stress level of -200 kPa. The soil behaviour at the bottom side shows that after a relaxation of 20 mm the residual stress is close to 0. The tendency of the effective stresses to drop sharply decreases moving towards the top side. In all cases, at 40 mm extension unloading seems to have reached an asymptotic value, but it should be noted that the validity of the FE analysis diminishes for very large displacements as phenomena like shear band formation, liquefaction or soil flow are not taken into account.

As already observed for the loading curves in Figure 5.19 the stiffest behaviour appears at the right-hand side. The unloading stiffness then decreases towards the bottom and the top positions. Particularly remarkable is the reloading curve at the bottom side. During unloading close to 0 kPa effective stress was reached at about 20 mm deformation. Remarkably, during reloading stress recovery started around the deformation stage at which the 0 stress condition was first reached and recompression from 40 to 20 mm occurred without stress increase. This condition will be explicitly modelled in Section 5.2.5.

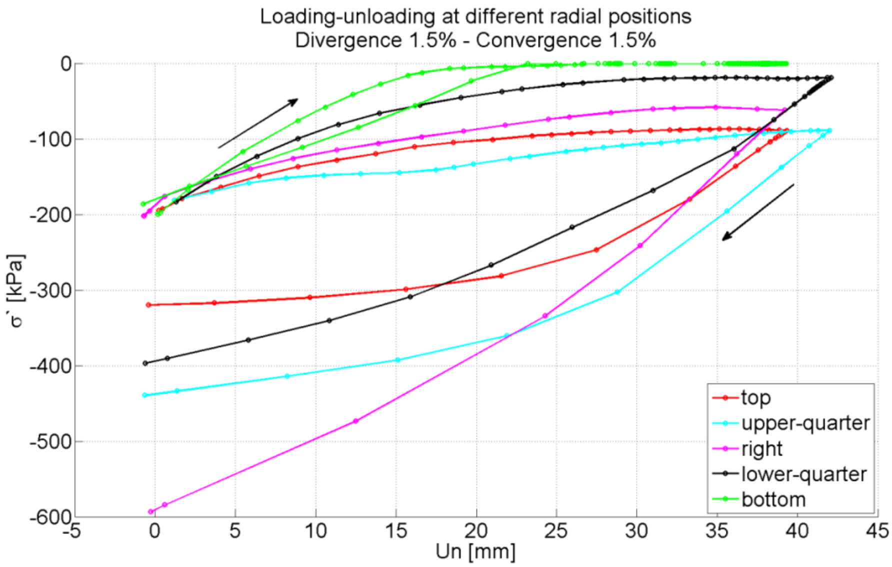

Figure 5.20: Unloading-reloading for multiple directions with common initial normal effective stress. The positions top, upper quarter, right, lower quarter, and bottom correspond to 180°, 135°, 90°, 45°, and 0° measured from bottom and counter-clockwise, respectively. Arrows indicate the loading path

5.2.5 Analytical formulation of loading-unloading curves

The FE-modelled loading-unloading soil response around the shield at different stress levels will be captured in a series of simplified analytical formulations. That will largely simplify subsequent calculations as the need to repeat FE calculations at every advance step is prevented. Loading and unloading are captured by different expressions. These expressions are established in order to provide a good interpolation of the observed values as obtained from the PLAXIS model.

An appropriate representation of the relationship between the imposed radial expansion and the normal stress is found to be

$$\sigma_L^{ref} = a_L \cdot (x + x_0)^{b_L} \tag{5.2}$$

in which x stands for the radial increase (in mm) and σ_L^{ref} for the normal stress (in kPa). The formula is calibrated on an initial normal effective stress $p_{ref} = -200$ kPa and $x_0 = 4$ mm. The subscript L indicates that loading is considered. a_L and b_L are calibration parameters that account for the dependency on the radial position around the shield ϑ, and are defined as:

$$\vartheta \leq \frac{\pi}{2} \qquad \begin{cases} a_L = a_3 + a_1 \cdot \sin^{a_2} \vartheta \\ b_L = b_3 + b_1 \cdot \sin^{b_2} \vartheta \\ c_L = Re(c_1 - c_2 \cdot \cos^{c_3} 2\vartheta) \end{cases} \tag{5.3}$$

and

$$\frac{\pi}{2} < \vartheta \leq \pi \qquad \begin{cases} a_L = a_6 + a_4 \cdot \sin^{a_5} \vartheta \\ b_L = b_6 + b_4 \cdot \sin^{b_5} \vartheta \\ c_L = Re(c_4 - c_5 \cdot \cos^{c_6} 2\vartheta) \end{cases} \tag{5.4}$$

The numerical values of the parameters are

$$\begin{gathered} \vec{A} = [a_{i=1..6}] = \\ [51.9581, 4.3892, -134.1923, 71.2577, 2.0695, -153.4918] \\ \vec{B} = [b_{i=1..6}] = [0.3264, 3.7365, 0.2560, 0.4134, 2.7172, 0.1690] \\ \vec{C} = [c_{i=1..6}] = [2 + 0i, -2 + 0i, 1 + 0.1371i, 2 + 0i, -3 + 0i, 1 + 0.2662i] \end{gathered} \tag{5.5}$$

Equation (5.2) is generalized for the generic initial stress level p_0 by means of its first spatial derivative. Differentials are indicated noting the independent variable as subscript. For a given $f(x)$ one has $f_x = \frac{\partial f}{\partial x}$. Consequently

$$\sigma_{L,x}^{ref} = a_L \cdot b_L \cdot (x + x_0)^{b_L - 1} \tag{5.6}$$

The initial value ($x = 0$) of the first derivative at the generic initial stress p_0 is defined as

$$\sigma_{L,x(x=0)} = \sigma_{L,x(x=0)}^{ref} \cdot \frac{p_0}{p_{ref}} \tag{5.7}$$

The loading curve with p_0 as initial stress state is obtained by successive increments according to

$$\sigma_L^i = \sigma_L^{i-1} + \sigma_{L,x}^{i-1} \cdot (x^i - x^{i-1}) \tag{5.8}$$

in which the generic first derivative is expressed as

$$\sigma_{L,x} = \sigma_{L,x(x=0)} \cdot \left(\frac{\sigma_L}{p_0}\right)^{-c_L} \tag{5.9}$$

The superscripts in Equation (5.8) indicate the sequential numbering over the explicit integration scheme. A numerical example is provided. Assuming an initial stress of $p_0 = -300$ kPa at the shield right-hand side ($\vartheta = \frac{\pi}{2}$), Equation (5.3) provides

$$a_L = -82.2345$$
$$b_L = 0.5824 \tag{5.10}$$
$$c_L = 0.7$$

Equations (5.6) and (5.7) then give

$$\sigma_{L,x(x=0)} = a_L \cdot b_L \cdot (x + x_0)^{b_L - 1} \cdot \frac{p_0}{p_{ref}} = -40.2667 \text{ kPa/mm} \tag{5.11}$$

The subsequent points on the loading curve can be obtained by means of Equation (5.8) assuming for instance load steps $\Delta x = 1$ mm. The second point is obtained as

$$\sigma_L^2 = \sigma_L^1 + \sigma_{L,x}^1 \cdot (x^2 - x^1) = -300 + (-40.2667) \cdot (1 - 0) = -340.2667 \text{ kPa} \tag{5.12}$$

The value of the first derivative at the current integration step can then be derived from Equation (5.9) and the explicit procedure extended until the desired displacement.

The relationship between the radial contraction following a previous expansion and the associated normal stresses is approximated by

$$\sigma_U^{ref} = a_U + b_U \cdot (x)^{c_U} \tag{5.13}$$

in which x now stands for the radial contraction (in mm) and σ_U^{ref} for the normal stress (in kPa). Expression (5.13) is only for the unloading soil response taking place after a pre-occurred expansion of 50 mm in turn started from an initial stress $p_{ref} = -200$ kPa. The independent variable x is defined in increasing direction. a_U, b_U, and c_U are calibration parameters that also account for the dependency on the radial position around the shield:

$$\vartheta \leq \frac{\pi}{2} \qquad \begin{cases} a_U = a_1 + a_2 \cdot \sin^{a_3} \vartheta \\ b_U = b_1 + b_2 \cdot \sin^{b_3} \vartheta \\ c_U = c_1 + c_2 \cdot \sin^{c_3} \vartheta \end{cases} \tag{5.14}$$

and

$$\frac{\pi}{2} < \vartheta \leq \pi \qquad \begin{cases} a_U = a_4 + a_5 \cdot \sin^{a_6} \vartheta \\ b_U = b_4 + b_5 \cdot \sin^{b_6} \vartheta \\ c_U = c_4 + c_5 \cdot \sin^{c_6} \vartheta \end{cases} \tag{5.15}$$

The numerical values of the parameters are

$$\begin{gathered} \vec{A} = [a_{i=1..6}] = \\ [-1.7824, -83.5225, 4.1351, -33.3449, -51.9601, 2.5910] \\ \vec{B} = [b_{i=1..6}] = \\ [-5.8769 \cdot 10^{-5}, -0.0024, 9.3086, -3.1514 \cdot 10^{-5}, 2.7172, 0.1690] \\ \vec{C} = [c_{i=1..6}] = [3.9791, -0.7957, 4.0444, 4.0357, -0.8523, 4.0829] \end{gathered} \tag{5.16}$$

Equation (5.13) at the initial point ($x = 0$) of the reference unloading curve yields

$$\sigma_U^{ref,1} = a_U + b_U \cdot (x)^{c_U} = a_U + b_U \cdot (0)^{c_U} = a_U \tag{5.17}$$

and at the end point ($x = 50$)

$$\sigma_U^{ref,n} = a_U + b_U \cdot (x)^{c_U} = a_U + b_U \cdot (50)^{c_U} \tag{5.18}$$

The first spatial derivative of Equation (5.13) is

$$\sigma_{U,x}^{ref} = b_U \cdot c_U \cdot (x)^{c_U - 1} \tag{5.19}$$

which at the end point of the curve yields

$$\sigma_{U,x}^{ref,n} = b_U \cdot c_U \cdot (x^n)^{c_U - 1} = b_U \cdot c_U \cdot (50)^{c_U - 1} \tag{5.20}$$

Equation (5.13) describes a family of unloading curves following a pre-loading of 50 mm in turn started from a fixed initial stress of $p_{ref} = -200$ kPa. The unloading curve has now to be adapted to the deformation x_L^n actually reached during the compression phase, as well as to the real stress level present before pre-loading.

The actual initial deformation level of the unloading curve (x^f) coincides with the actual deformation level at the end of the reference loading curve. Based on Equation (5.2) and indicating with x_L the independent variable during loading we can write

$$\sigma_U^{ref,f} = \sigma_L^{ref,n} = a_L \cdot (x_L^n + x_{L0})^{b_L} \tag{5.21}$$

The initial value of the first derivative of the unloading curve at the actual initial deformation level $x^1 = x_L^n$ is obtained from Equation (5.20) as

$$\sigma_{U,x}^{ref,f} = \sigma_{U,x}^{ref,n} \cdot \left(\frac{\sigma_U^{ref,f} - \sigma_U^{ref,1}}{\sigma_U^{ref,n}} \right)^m \tag{5.22}$$

with $m = 0.7$ a calibration parameter. The superscript f indicates in the following the unloading curve originating from the pre-deformation level x^f. The subsequent points of the unloading curve originating from x^f but still based on the initial stress before loading $p_{ref} = -200$ kPa are obtained, in decreasing order, as

$$\sigma_U^{ref,f,i} = \sigma_U^{ref,f,i-1} + \sigma_{U,x}^{ref,f,i-1} \cdot (x^i - x^{i-1}) \tag{5.23}$$

and successive values of the first spatial derivative are obtained as

$$\sigma_{U,x}^{ref,f,i} = \sigma_{U,x}^{ref,f,1} \cdot \left(\frac{\sigma_U^{ref,f,i} - \sigma_U^{ref,1}}{\sigma_U^{ref,f,1}} \right)^m \tag{5.24}$$

The unloading curve adapted to the actual pre-loading deformation level is then adapted to the actual stress level. The initial stress level of the unloading curve coincides with the stress level at the end of loading starting from the initial stress p_0 and processed further by successive increments according to Equation (5.8)

$$\sigma_U^1 = \sigma_L^n \tag{5.25}$$

The initial value of the first derivative of the unloading curve at pre-deformation level x^f and at the stress level p_0 is expressed as

$$\sigma_{U,x}^1 = \sigma_{U,x}^{ref,f,1} \cdot \left(\frac{\sigma_U^1}{\sigma_U^{ref,f}} \right)^m \tag{5.26}$$

The subsequent steps of the unloading curve and of its derivative are then defined by

$$\sigma_U^i = \sigma_U^{i-1} + \sigma_{U,x}^{i-1} \cdot (x^i - x^{i-1}) \tag{5.27}$$

$$\sigma_{U,x}^i = \sigma_{U,x}^{ref,f,i} \cdot \left(\frac{\sigma_U^i}{\sigma_U^{ref,f,i}} \right)^m \tag{5.28}$$

Unloading can produce close to zero residual effective stresses. When that is the case, the FE model indicated that during possible subsequent reloading the actual stress recovery only starts when the recompression passes the deformation stage at which the zero stress level was first reached. Consequently, during unloading a check is performed to record if a stress level lower than an arbitrary -5 kPa was reached and at which deformation level that occurred. Such information is then stored for the definition of a possible reloading curve.

The soil often undergoes a displacement history even more convoluted than so far described. Under specific circumstances the unloading more than compensates the previous pre-loading displacement, in fact shifting the deformations from the compression to the extension field, beyond the original rest position before the initial loading. If after such extensions recompression occurs a compression-extension-recompression sequence occurs in fact.

An analytical expression for this last case is specifically formulated. However, it is observed that the recompression is essentially similar to the unloading-reloading case introduced later in Section 5.2.6 to which the reader is readdressed for a complete description. For convenience, selected aspects are anticipated here.

In the context of the unloading-reloading case the reference reloading curve is

$$\sigma_R^{ref} = a_R \cdot (x + x_0)^{b_R} \tag{5.29}$$

with $x_0 = 1$ mm. The equation describes the soil response when reloaded after a pre-relaxation of 50 mm at the end of which the effective normal stress is -100 kPa. Justification for selecting the reference value -100 kPa is provided in Section 5.2.6 (after Equation (5.40)). The first derivative of Equation (5.29) is

$$\sigma_{R,x}^{ref} = a_R \cdot b_R \cdot (x + x_0)^{b_R - 1} \tag{5.30}$$

The start of the reloading curve at the actual stress level p_0 coincides with the end point of the unloading one, the latter obtained through successive increments according to Equation (5.27). In other words

$$\sigma_R^1 = \sigma_U^n \tag{5.31}$$

The reloading curve is defined by successive increments according to the expression

$$\sigma_R^i = \sigma_R^{i-1} + \sigma_{R,x}^{ref,i-1} \cdot \left(\frac{\sigma_R^{i-1}}{\sigma_R^{ref,i-1}} \right)^k \cdot (x^i - x^{i-1}) \tag{5.32}$$

in which fit parameter $k = 0.5$ holds. It was stated earlier that if during unloading the soil stress drops below an arbitrarily fixed level of -5 kPa, then the deformation level at which such drop occurs is assumed as the actual starting point for the reloading curve. That unloading behaviour might therefore determine the values of x^i.

The validity of the proposed analytical formulation is investigated through comparison of the stress-displacement curves from the FE model with those obtained through interpolation. Figures 5.21 to 5.25 present the comparison between the two families of curves at one radial position at a time. The possible reloading curves are not presented graphically. In each Figure several unloading curves are plotted, each starting from a different pre-loading rate (Equations (5.21) to (5.24)).

Based on the plots it can be stated that the interpolation of the numerical values is satisfactorily achieved. The proposed formulation proves able to take into account both the non-linear behaviour in loading as well as the considerably stiffer soil during unloading. The interpolating curves prove however less precise for the smallest deformation levels especially at the upper-quarter and right-hand-side positions (Figures 5.22 and 5.23).

The validity of the loading-unloading interpolation with variable initial stress is checked in Figures 5.26 to 5.30. The match between observed and interpolated values is satisfactorily achieved in all the directions investigated. Limited inaccuracies are encountered at the end of the unloading stage at the top and upper-quarter positions.

The range of initial stresses covered here represents the soil stresses encountered during drive for the current case study. Assuming the water table at ground level and a saturated soil specific weight of 20 kN/m^3, a soil stress at the top side of -100 to -200 kPa indicates a depth of the tunnel axis from -15 to -25 m. Similar depth ranges are also covered at the upper quarter, lower quarter, and bottom positions. The initial stresses investigated at the right-hand side (Figure 5.28) cover an even broader depth range, from 15 to 40 m. In conclusion, the proposed formulation works reasonably well over the stress and deformation range covered by the problem under investigation.

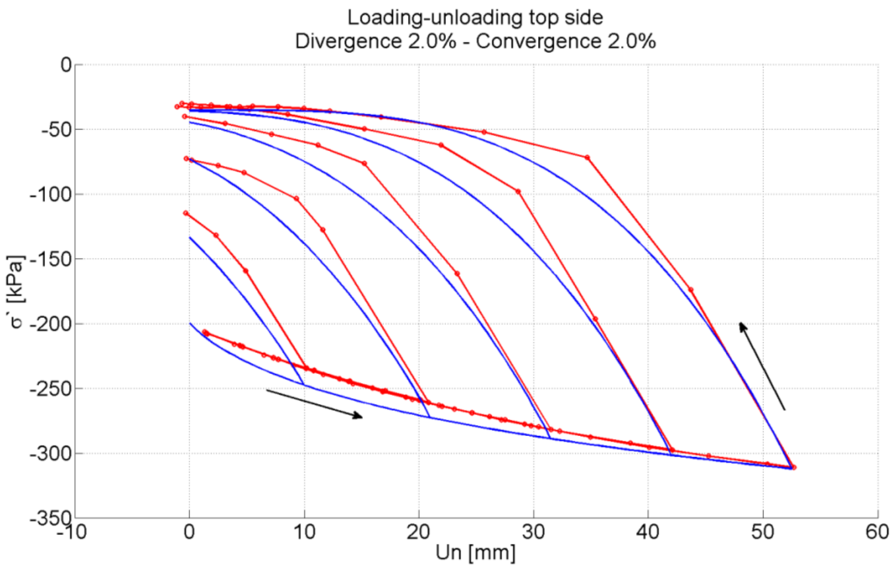

Figure 5.21: Loading-unloading patterns at the top side (180°) for multiple deformation stages. The red lines with markers represent the results of the FE model. The continuous blue lines represent the interpolated values as from the analytical expressions. Arrows indicate the loading path

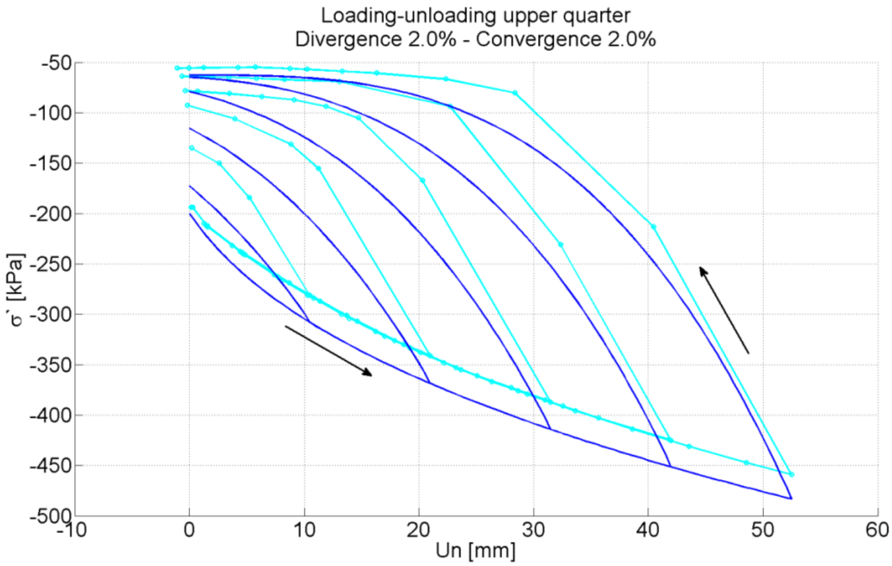

Figure 5.22: Loading-unloading patterns at the upper-quarter (135°) for multiple deformation stages. The cyan lines with markers represent the results of the FE model. The continuous blue lines represent the interpolated values as from the analytical expressions. Arrows indicate the loading path

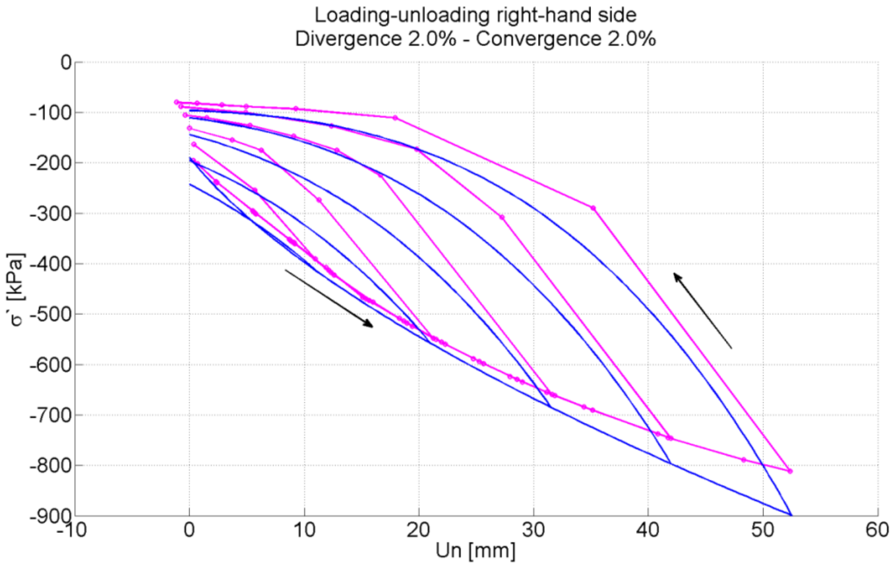

Figure 5.23: Loading-unloading patterns at the right-hand side (90°) for multiple deformation stages. The magenta lines with markers represent the results of the FE model. The continuous blue lines represent the interpolated values as from the analytical expressions. Arrows indicate the loading path

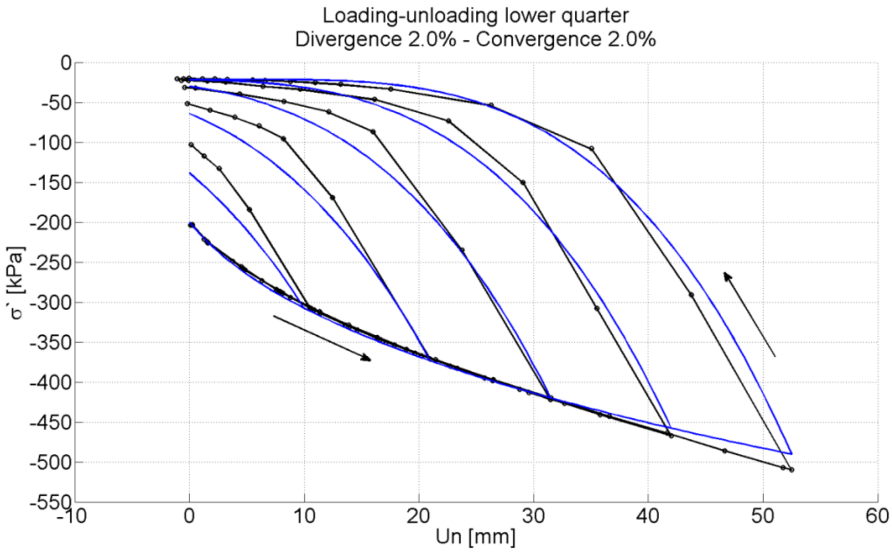

Figure 5.24: Loading-unloading patterns at the lower quarter (45°) for multiple deformation stages. The black lines with markers represent the results of the FE model. The continuous blue lines represent the interpolated values as from the analytical expressions. Arrows indicate the loading path

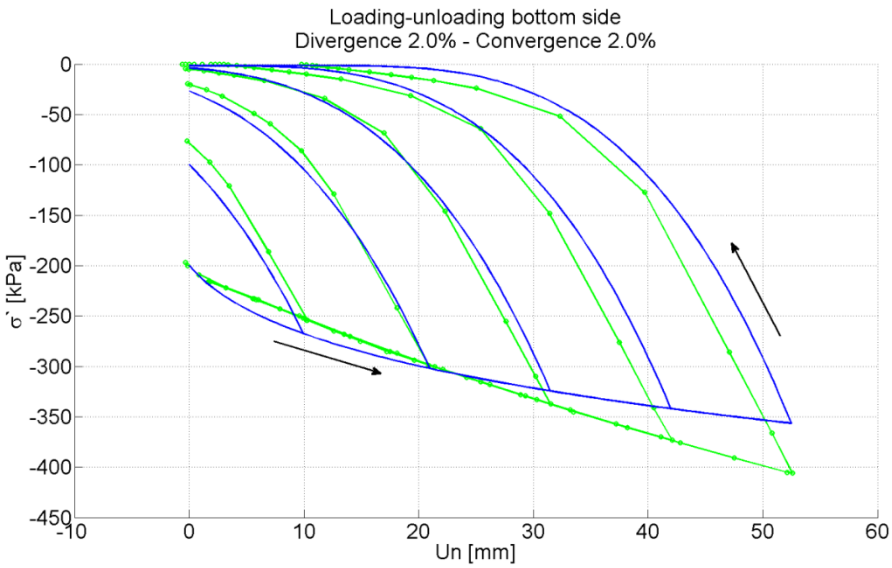

Figure 5.25: Loading-unloading patterns at the bottom side (0°) for multiple deformation stages. The green lines with markers represent the results of the FE model. The continuous blue lines represent the interpolated values as from the analytical expressions. Arrows indicate the loading path

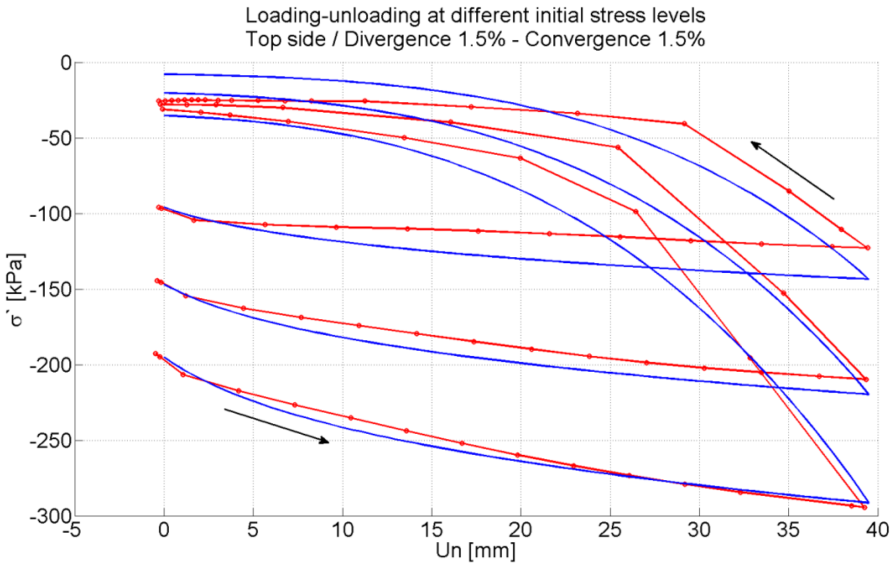

Figure 5.26: Loading-unloading patterns at the top side (180°) for multiple initial stress levels. The red lines with markers represent the results of the FE model. The continuous blue lines represent the interpolated values as from the analytical expressions. Arrows indicate the loading path

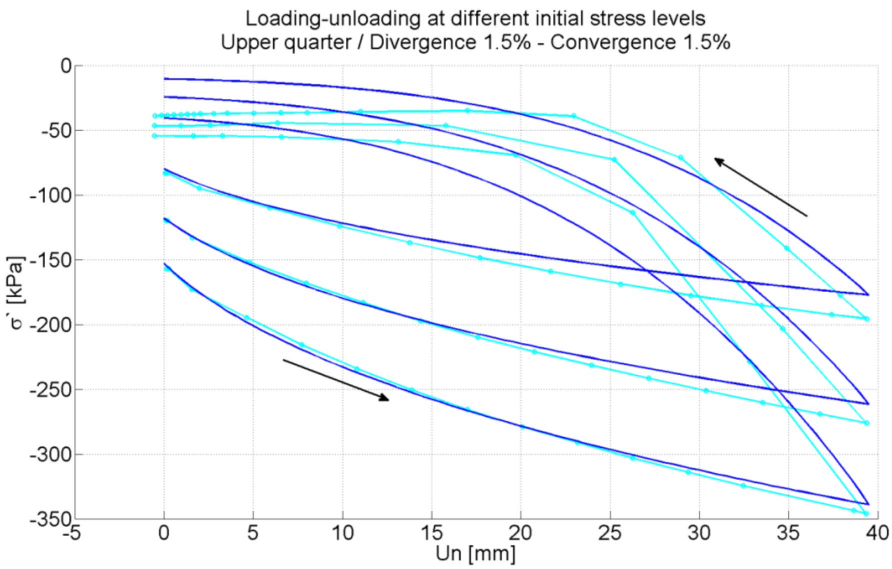

Figure 5.27: Loading-unloading patterns at the upper quarter (135°) for multiple initial stress levels. The cyan lines with markers represent the results of the FE model. The continuous blue lines represent the interpolated values as from the analytical expressions. Arrows indicate the loading path

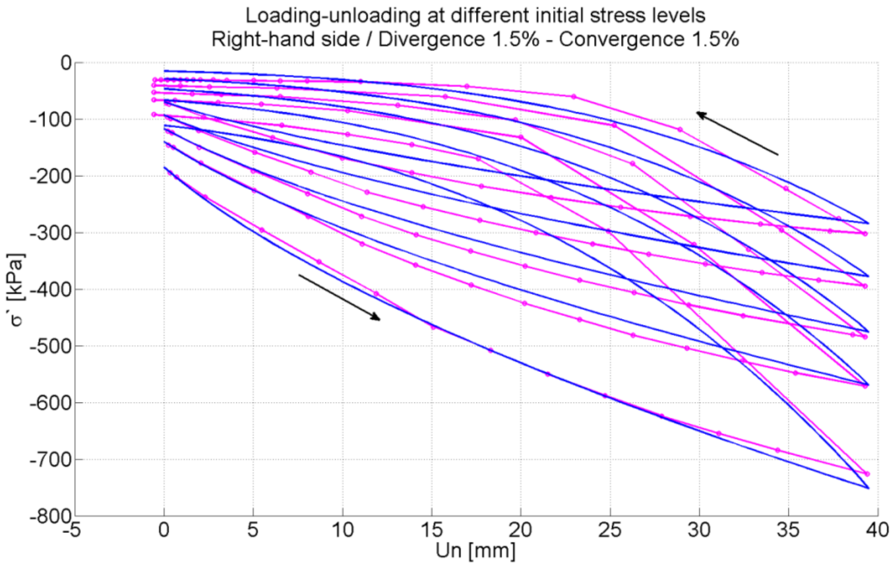

Figure 5.28: Loading-unloading patterns at the right-hand side (90°) for multiple initial stress levels. The magenta lines with markers represent the results of the FE model. The continuous blue lines represent the interpolated values as from the analytical expressions. Arrows indicate the loading path

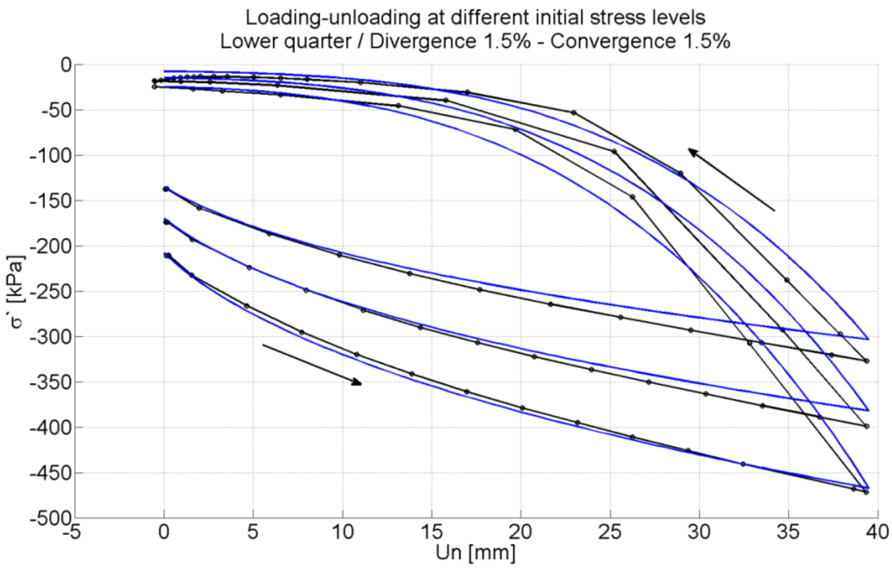

Figure 5.29: Loading-unloading patterns at the lower quarter (45°) for multiple initial stress levels. The black lines with markers represent the results of the FE model. The continuous blue lines represent the interpolated values as from the analytical expressions. Arrows indicate the loading path

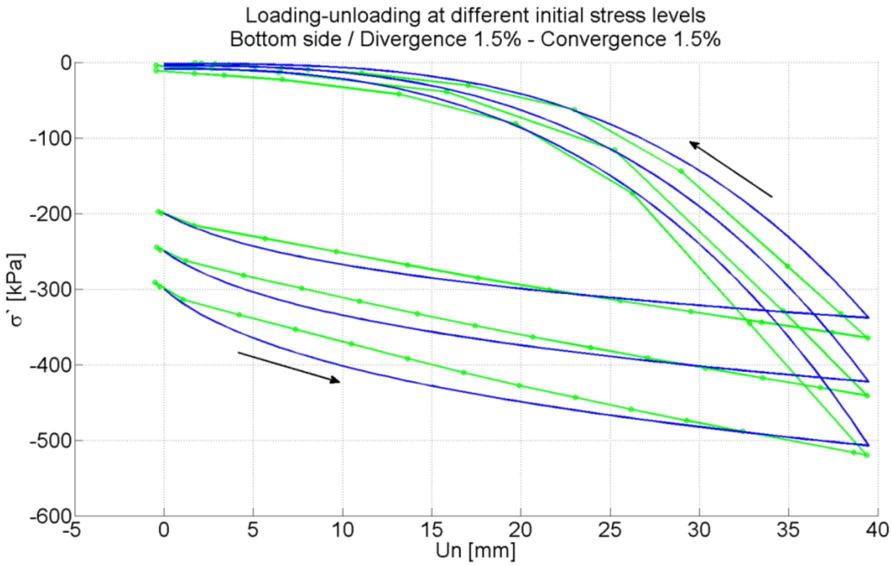

Figure 5.30: Loading-unloading patterns at the bottom side (0°) for multiple initial stress levels. The green lines with markers represent the results of the FE model. The continuous blue lines represent the interpolated values as from the analytical expressions. Arrows indicate the loading path

5.2.6 Analytical formulation of the unloading-reloading curves

The FE-modelled unloading-reloading soil response around the shield at different stress levels will be captured in a series of simplified analytical formulations. That will largely simplify subsequent calculations as the need to repeat FE calculations at every advance step is prevented. Unloading and reloading are captured by different expressions. These expressions are established in order to provide a good interpolation of the observed values as obtained from the PLAXIS model.

The unloading and the reloading behaviour will be captured in analytical expressions in a similar manner.

The reference unloading curve at the initial stress $p_{ref} = -200$ kPa is

$$\sigma_U^{ref} = p_{ref} + b_U \cdot \tanh\frac{x}{a_U} \tag{5.33}$$

and its first spatial derivative

$$\sigma_{U,x}^{ref} = \frac{b_U}{a_U} \cdot \left(1 - \tanh^2\frac{x}{a_U}\right) \tag{5.34}$$

in which x stands for the radial decrease (in mm) and σ_U for the normal stress (in kPa).

The parameter a_U depends on the radial position as follows

$$\begin{array}{ll} \vartheta \leq \frac{\pi}{2} & a_U = a_1 + a_2 \cdot \sin^2\vartheta \\ \frac{\pi}{2} < \vartheta \leq \frac{3}{4}\pi & a_U = a_3 + a_4 \cdot \sin^2\vartheta \\ \frac{3}{4}\pi < \vartheta \leq \pi & a_U = a_5 + a_6 \cdot \sin^2\vartheta \end{array} \tag{5.35}$$

whereas b_U is defined as

$$b_U = b_1 \cdot \cos\vartheta + b_2 \tag{5.36}$$

The numerical values of the fit parameters are

$$\begin{aligned} \vec{A} &= [a_{i=1..6}] = [10.4679, 9.0794, 19.5473, 9.4657, 13.5211, 15.4918] \\ \vec{B} &= [b_{i=1..2}] = [42.7534, 153.3838] \end{aligned} \tag{5.37}$$

For a generic initial stress p_0 the corresponding unloading curve is initialized according to:

$$\sigma_U^1 = p_0 \tag{5.38}$$

and the subsequent points of the curve are obtained from

$$\sigma_U^i = \sigma_U^{i-1} + \sigma_{U,x}^{ref,i-1} \cdot \left(\frac{\sigma_U^{i-1}}{\sigma_U^{ref,i-1}}\right)^m \cdot (x^i - x^{i-1}) \tag{5.39}$$

in which $m = 0.7$. At times the unloading is so large that the residual effective stresses become close to zero. When that is the case, the FE model indicates that during reloading the actual stress recovery starts only once the recompression has passed the deformation stage at which the zero stress level was achieved for the first time. Consequently, during unloading a check is performed to monitor and record if a stress level lower than the arbitrary one of -5 kPa is reached and at which deformation that occurs for the first time. Such information is then stored for the definition of the reloading curve.

The reference reloading relation is formulated as

$$\sigma_R^{ref} = a_R \cdot (x + x_0)^{b_r} \tag{5.40}$$

in which x stand for the radial increase (in mm) and σ_R for the normal stress (in kPa), and $x_0 = 1$ mm. The relationship describes the soil response when reloaded after a previous relaxation of 50 mm at the end of which the normal effective stress is -100 kPa. -100 kPa was selected as reference value for the residual stress after unloading as it resulted achievable at most radial locations with the tunnel at realistic depths (except for the bottom position). From Figures 5.31 to 5.36 it emerges that a residual normal stress after unloading of for instance -200 kPa would have not been achieved starting from real depths and associated stress levels. Therefore the choice of a different reference value for this part of the analysis.

The parameters a_R and b_R are

$$\begin{aligned} &\vartheta \le \frac{\pi}{4} && \begin{cases} a_R = a_3 + a_1 \cdot \cos^{a_2}(2\,\vartheta) \\ b_R = c_3 + c_1 \cdot \cos^{c_2}\left(2\,\vartheta - \frac{\pi}{2}\right) \end{cases} \\ &\frac{\pi}{4} < \vartheta \le \frac{\pi}{2} && \begin{cases} a_R = a_3 + a_1 \cdot \cos^{a_2}(2\,\vartheta) \\ b_R = d_3 + d_1 \cdot \cos^{d_2}\left(2\,\vartheta - \frac{\pi}{2}\right) \end{cases} \\ &\frac{\pi}{2} < \vartheta \le \pi && \begin{cases} a_R = b_3 + b_1 \cdot \cos^{b_2}(2\,\vartheta) \\ b_R = e_3 + e_1 \cdot \cos^{e_2}\left(2\,\vartheta - \frac{\pi}{2}\right) \end{cases} \end{aligned} \tag{5.41}$$

The numerical values of the fit parameters are

$$\begin{aligned}
&\vec{A} = [a_{i=1..3}] = \\
&[17.27897 - 2.4611 \cdot 10^{-14} i, 1 + i, -82.8708 + 1.8015 \cdot 10^{-14} i] \\
&\vec{B} = [b_{i=1..3}] = [1.5537, 5.9224, -104.2172] \\
&\vec{C} = [c_{i=1..3}] = \\
&[-0.0669 + 8.6228 \cdot 10^{-18} i, 2.000 + 6.7484 \cdot 10^{-16} i, 0.5964 - 2.9801 \cdot 10^{-20} i] \\
&\vec{D} = [d_{i=1..3}] = \\
&[-0.0193 + 6.6305 \cdot 10^{-18} i, 2.0000 + 1.6859 \cdot 10^{-15}, 0.5487 - 1.4995 \cdot 10^{-20} i] \\
&\vec{E} = [e_{i=1..3}] = [0.2318, 2.5325, 0.3169]
\end{aligned} \tag{5.42}$$

The first spatial derivative of Equation (5.40) is

$$\sigma_{R,x}^{ref} = a_R \cdot b_R \cdot (x + x_0)^{b_r - 1} \tag{5.43}$$

The starting point of the reloading curve at the actual stress level coincides with the end point of the unloading one, the latter obtained through successive increments according to Equation (5.39). In other words

$$\sigma_R^1 = \sigma_U^n \tag{5.44}$$

The subsequent points of the reloading curve are defined by successive increments according to

$$\sigma_R^i = \sigma_R^{i-1} + \sigma_{R,x}^{ref,i-1} \cdot \left(\frac{\sigma_R^{i-1}}{\sigma_R^{ref,i-1}}\right)^m \cdot (x^i - x^{i-1}) \tag{5.45}$$

in which the x values are defined in decreasing order and $m = 0.5$. If during unloading the stress drops below the arbitrarily fixed level of -5 kPa, the deformation level at which such drop occurs is assumed as starting point for the reloading curve (see also remarks in Section 5.2.5). The unloading behaviour may therefore determine the range of the x^i values and in particular its starting point.

Equation (5.45) represents reloading even when recompression is so pronounced as to induce a compression state in the soil even compared to the original excavation profile, therefore with a full recovery of the primary unloading deformation and beyond. However, if after such pronounced recompression relaxation would occur, the conditions and formulas of the loading-unloading case would apply.

Figures 5.31 to 5.36 show the comparison between modelled and interpolated results for the unloading-reloading case. All graphs except Figure 5.36 show unloading paths starting from an initial stress of -200 kPa. Several reloading curves are indicated for different levels of unloading. The quality of the interpolation, quite good for the larger deformations, deteriorates as the amount of pre-occurred unloading decreases.

Figure 5.35 shows the case of the effective stresses dropping close to zero. That occurred as a combination of the modest initial effective stress and of the bottom position known for showing a stiff unloading response. The interpolated reloading curves differ quite considerably from the modelled ones in this case. However, the interpolation at least manages to catch the singularity mentioned earlier that reloading does not actually start until the deformation level is equal to that at which the stress level became close to zero.

Figure 5.36 shows the loading-unloading curves at the bottom side for a much higher level of initial stress. This shows that the accuracy achieved by the interpolation technique is quite stable at any radial position around the shield. However, limitations emerge for small deformations and in those cases in which during unloading very low levels of stress are reached.

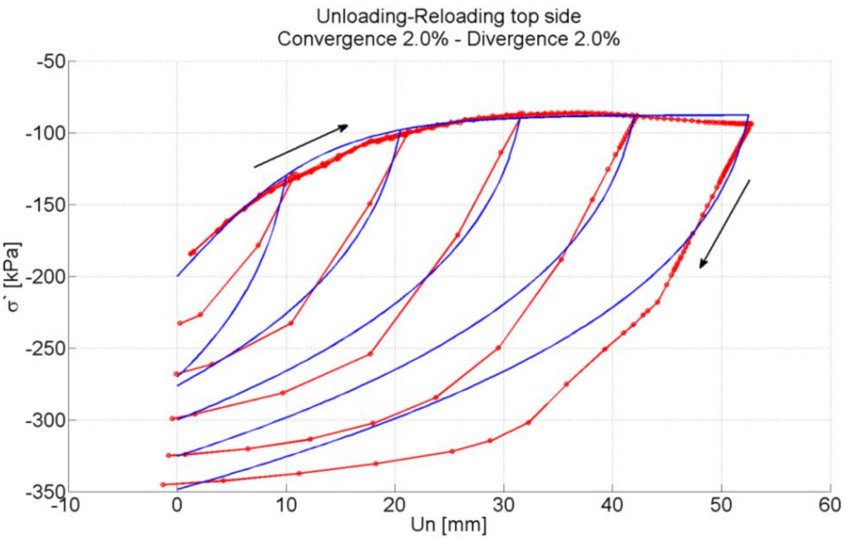

Figure 5.31: Unloading-reloading patterns at the top side (180°) for multiple deformation stages. The red lines with markers represent the results of the FE model. The continuous blue lines represent the interpolated values as from the analytical expressions. Arrows indicate the loading path

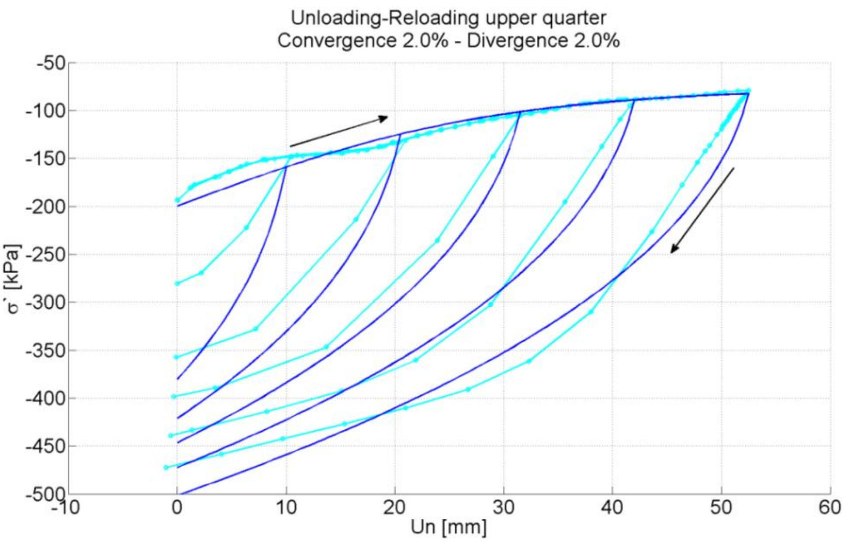

Figure 5.32: Unloading-reloading patterns at the upper quarter (135°) for multiple deformation stages. The cyan lines with markers represent the results of the FE model. The continuous blue lines represent the interpolated values as from the analytical expressions. Arrows indicate the loading path

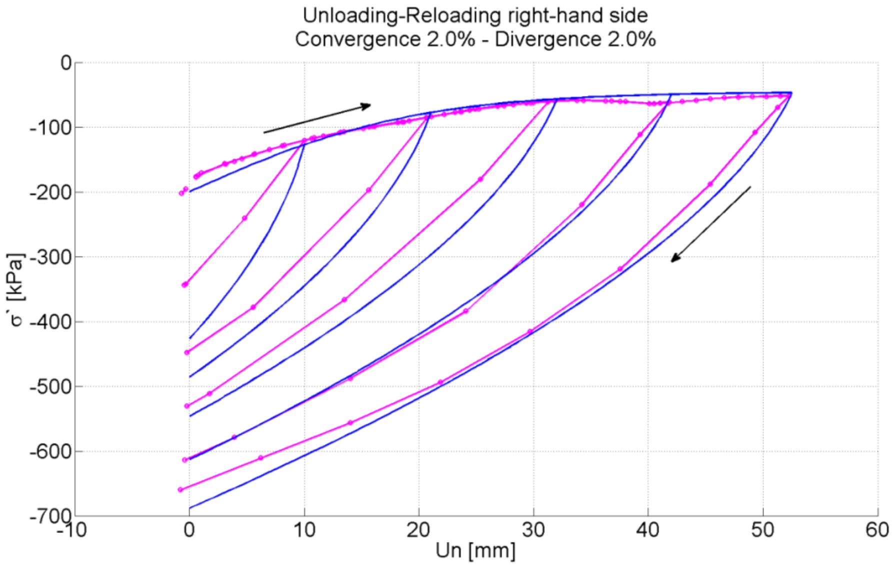

Figure 5.33: Unloading-reloading patterns at the right-hand side (90°) for multiple deformation stages. The magenta lines with markers represent the results of the FE model. The continuous blue lines represent the interpolated values as from the analytical expressions. Arrows indicate the loading path

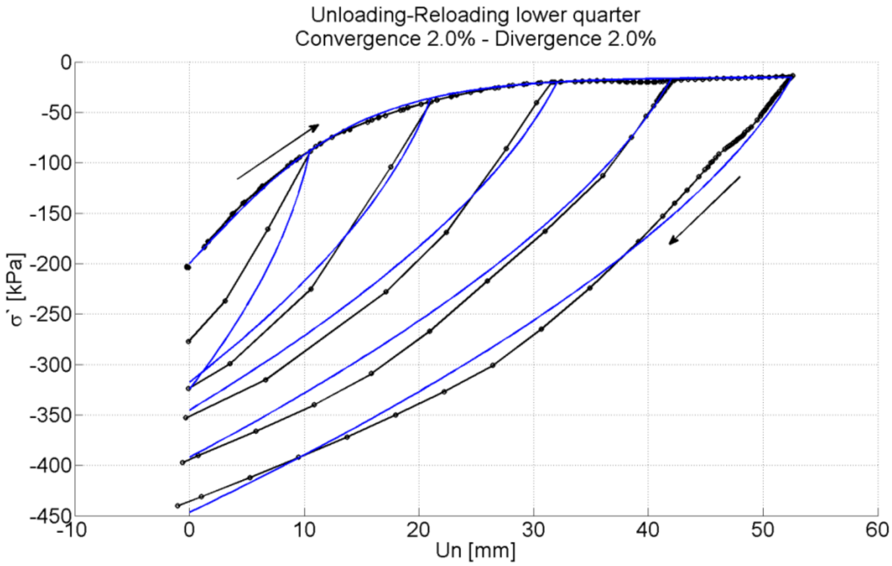

Figure 5.34: Unloading-reloading patterns at the lower quarter (45°) for multiple deformation stages. The black lines with markers represent the results of the FE model. The continuous blue lines represent the interpolated values as from the analytical expressions. Arrows indicate the loading path

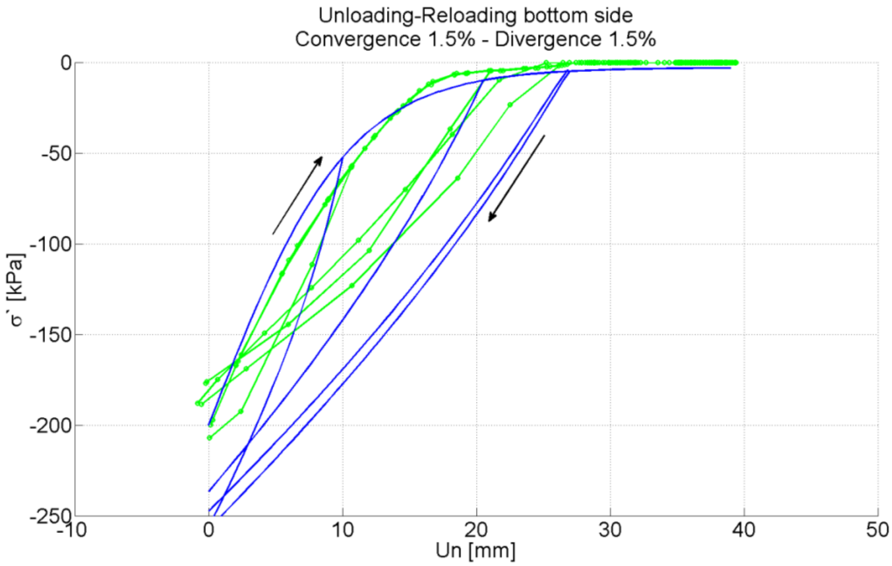

Figure 5.35: Unloading-reloading patterns at the bottom side (0°) for multiple deformation stages. Initial vertical effective stress -200 kPa. The green lines with markers represent the results of the FE model. The continuous blue lines represent the interpolated values as from the analytical expressions. Arrows indicate the loading path

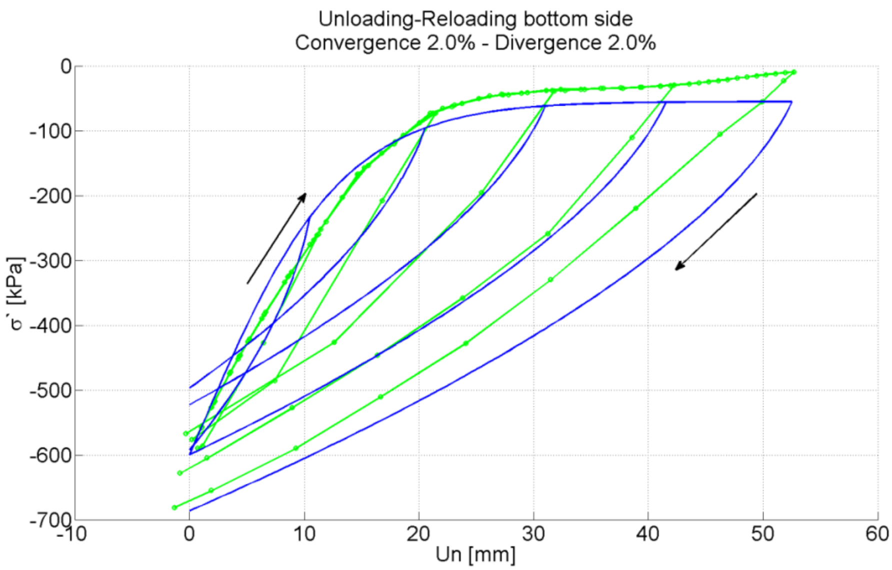

Figure 5.36: Unloading-reloading patterns at the bottom side (0°) for multiple deformation stages. Initial vertical effective stress -600 kPa. The green lines with markers represent the results of the FE model. The continuous blue lines represent the interpolated values as from the analytical expressions. Arrows indicate the loading path

The analytical formulation for the unloading-reloading soil response proves satisfactory for unloading but less for reloading. Figures 5.37 to 5.41 show a good match between the observed and the interpolated lines during unloading. A poor fit is however seen in the top and the upper-quarter sectors at large displacements and lower initial stresses (Figures 5.37 and 5.38).

The interpolated reloading curves instead match the general trend only and do not provide a good numerical assessment of the stress state after recompression. However, having caught at least the trend, and particularly the tendency of the stiffness to decrease as the recompression level increases, seems already a significant achievement. That seems to inform us of a mainly elastic, or even linear elastic response during the first stages of recompression. As recompression continues more plastic deformations appear, with a consequent sagging shape of the reloading arms.

The unloading-reloading at the bottom side proves problematic. Due to the stiffer soil response a close to zero stress is reached there even when starting from higher initial stresses (up to -300 kPa in 5.41). However, understanding at which extension the critically low stress level is reached remains an unsolved challenge which cannot be completely disregarded as those points do also represent the actual start of the recompression arms.

For the current application of the model the curves are sufficiently accurate and no further adaptations are made.

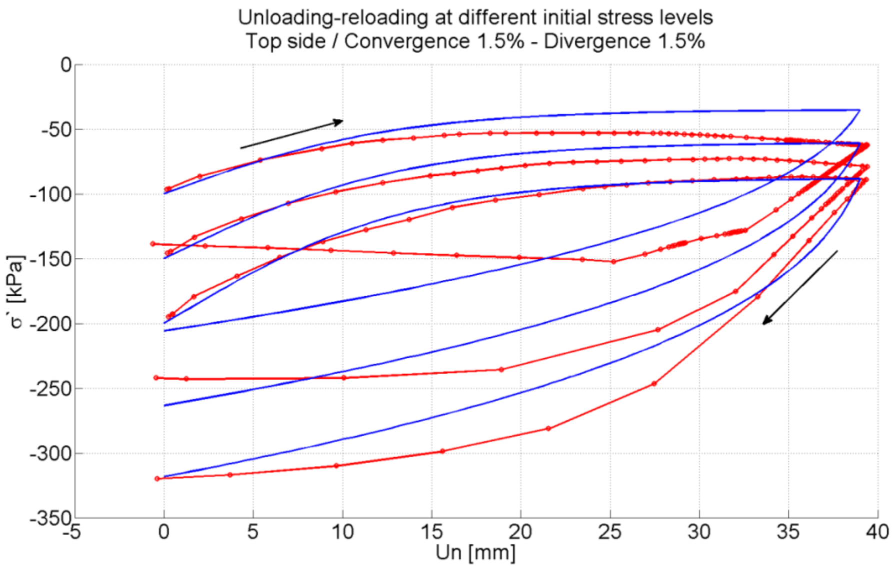

Figure 5.37: Unloading-reloading patterns at the top side (180°) for multiple initial stress levels. The red lines with markers represent the results of the FE model. The continuous blue lines represent the interpolated values as from the analytical expressions. Arrows indicate the loading path

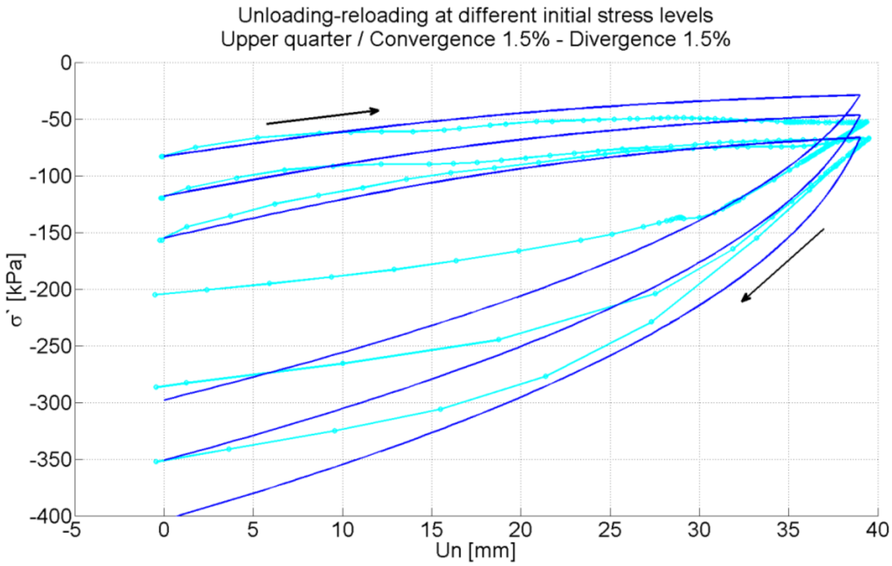

Figure 5.38: Unloading-reloading patterns at the upper quarter (135°) for multiple initial stress levels. The cyan lines with markers represent the results of the FE model. The continuous blue lines represent the interpolated values as from the analytical expressions. Arrows indicate the loading path

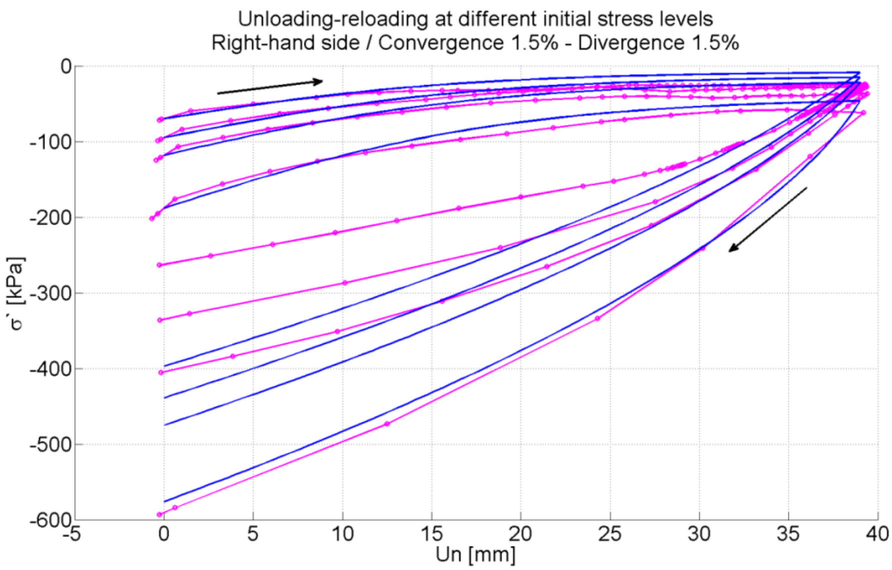

Figure 5.39: Unloading-reloading patterns at the right-hand side (90°) for multiple initial stress levels. The magenta lines with markers represent the results of the FE model. The continuous blue lines represent the interpolated values as from the analytical expressions. Arrows indicate the loading path

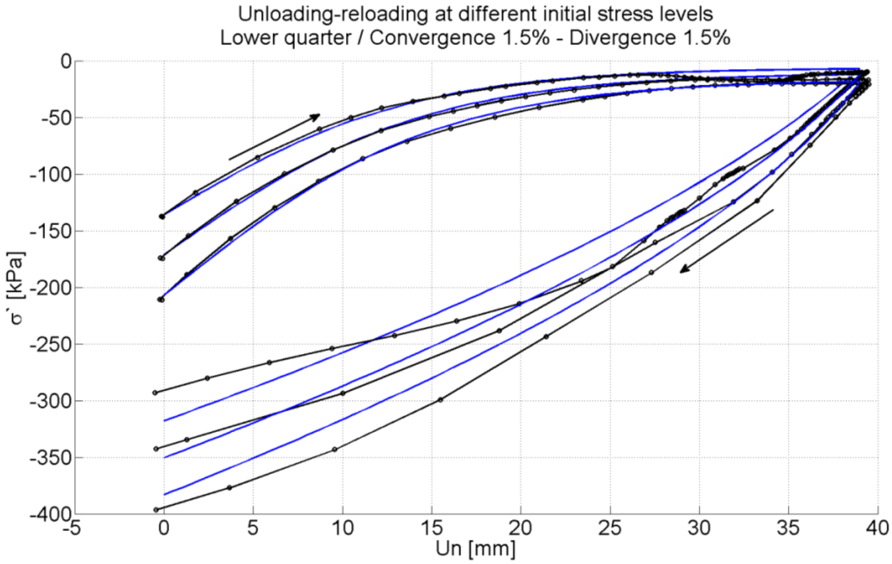

Figure 5.40: Unloading-reloading patterns at the lower quarter (45°) for multiple initial stress levels. The black lines with markers represent the results of the FE model. The continuous blue lines represent the interpolated values as from the analytical expressions. Arrows indicate the loading path

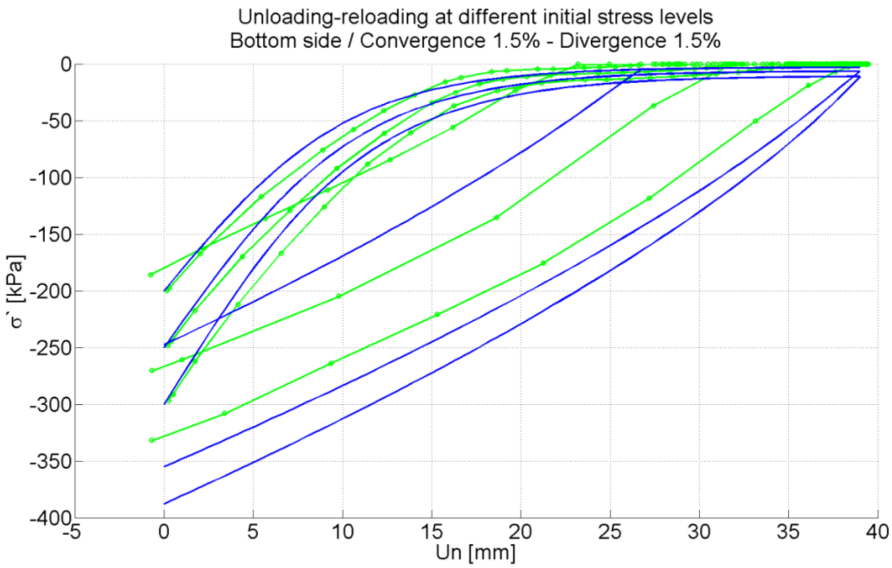

Figure 5.41 : Unloading-reloading patterns at the bottom side (0°) for multiple initial stress levels. The green lines with markers represent the results of the FE model. The continuous blue lines represent the interpolated values as from the analytical expressions. Arrows indicate the loading path

Chapter 6

Mechanical equilibrium of the TBM-shield

6.1 Introductory considerations and global results

Mechanical equilibrium of the TBM-shield requires that forces and moments acting on it are in balance. Unfortunately, the numerical analysis presented in this Chapter did not always result in equilibrium. Therefore, the consequences of a number of model assumptions will be reconsidered.

The condition of global equilibrium of forces dictates that equilibrium must be satisfied in any direction in space. For simplicity three principal directions are defined. The first direction is assumed coincident with the TBM axis (longitudinal component), the second one transversal to it in horizontal direction (transversal component), and the third one aligned with the Earth's gravity (vertical component). The three directions are shown in Figure 3.4.

The calculated equilibrium of the horizontal components of forces in longitudinal and transversal direction is plotted in Figures 6.1 and 6.2, respectively, whereas Figure 6.3 shows the calculated equilibrium of forces in vertical direction. Average values are indicated in red. The graphs were obtained according to the procedures described in Chapters 3, 4, and 5.

The resultant vertical and horizontal turning moments acting on the TBM are plotted in Figure 6.4 and 11, respectively. The average values are indicated in blue. The driving moments are plotted in black. Vertical and horizontal moments were defined in Chapter 3. The vertical moment is correlated to the yaw of the TBM, whereas the horizontal one is correlated to its pitch. The driving moment is derived by processing the driving forces which are applied through the thrust cylinders (see also Chapter 3).

The graphs in Figures 6.1 to 6.5 show that equilibrium has been only locally achieved. In fact, even if the model has accurately caught the physics of the shield-soil interaction over several sectors, in several others mechanical equilibrium has not been derived. The aim is now to check if the physical processes not yet accounted for could complement the current model. That will be done by carefully investigating a number of sectors in which mechanical equilibrium was not reached.

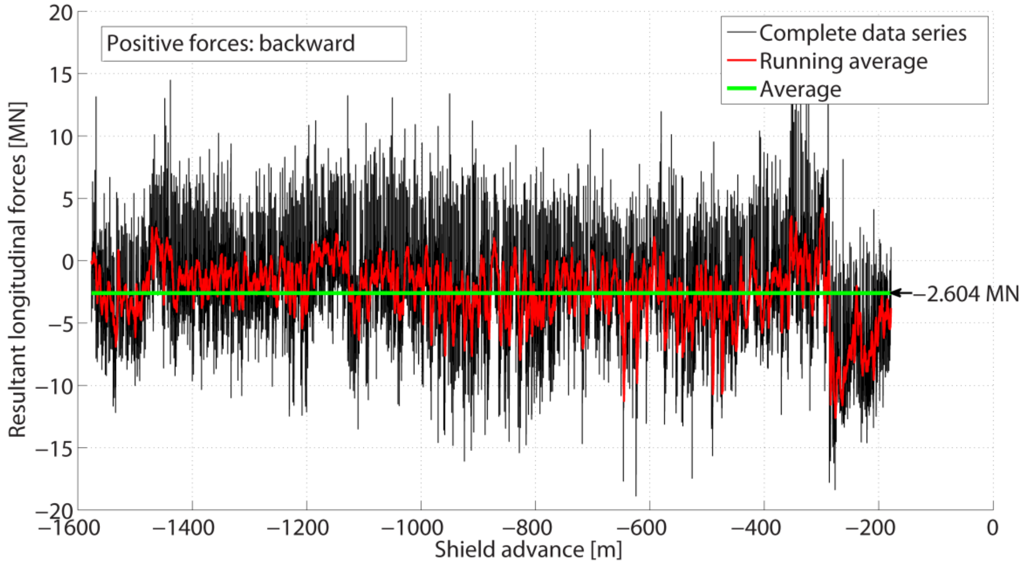

Figure 6.1: Resultant of forces in longitudinal direction (black). In green the average value

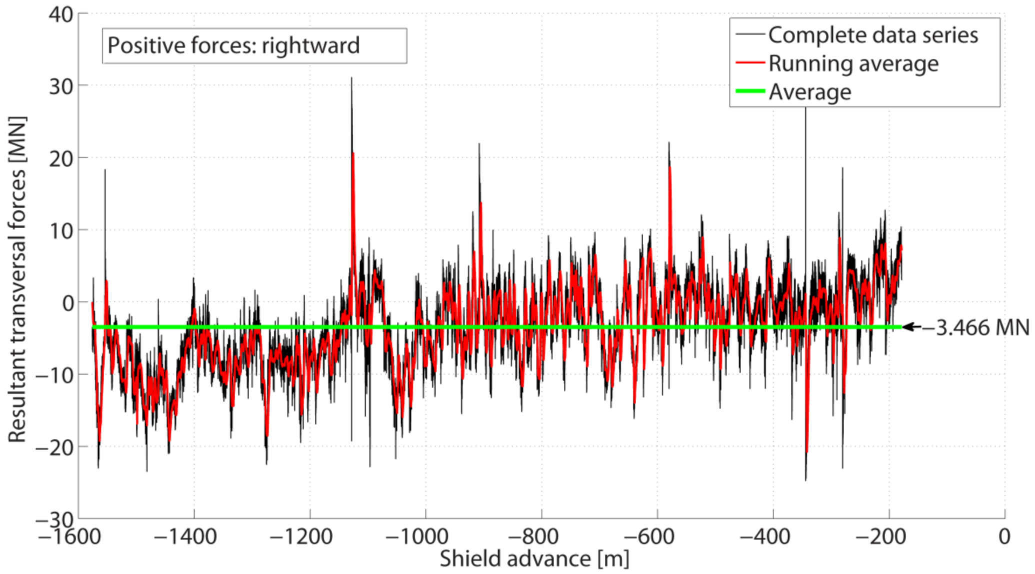

Figure 6.2: Resultant of forces in horizontal transversal direction (black). In green the average value

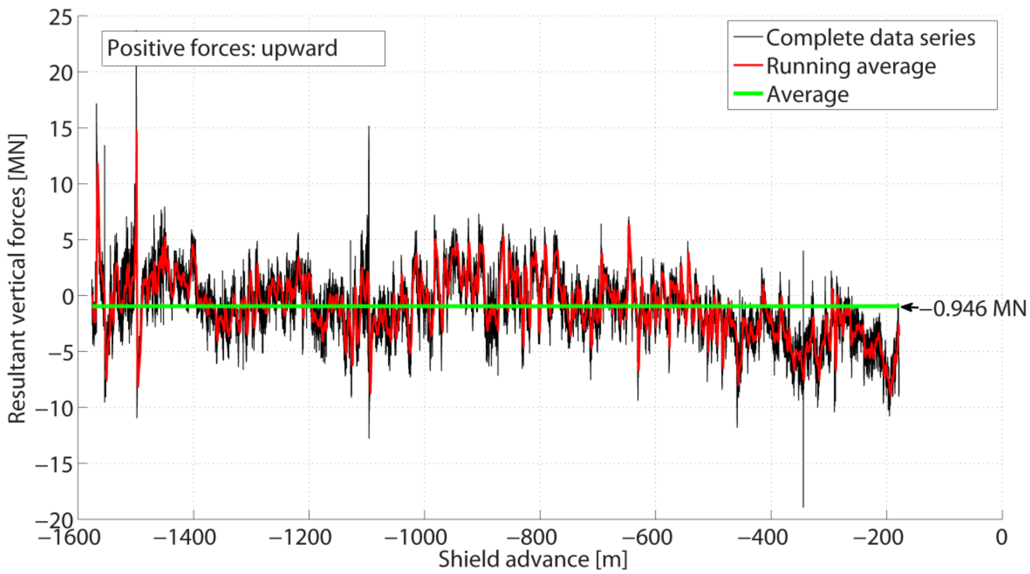

Figure 6.3: Resultant of forces in vertical direction (black). In green the average value

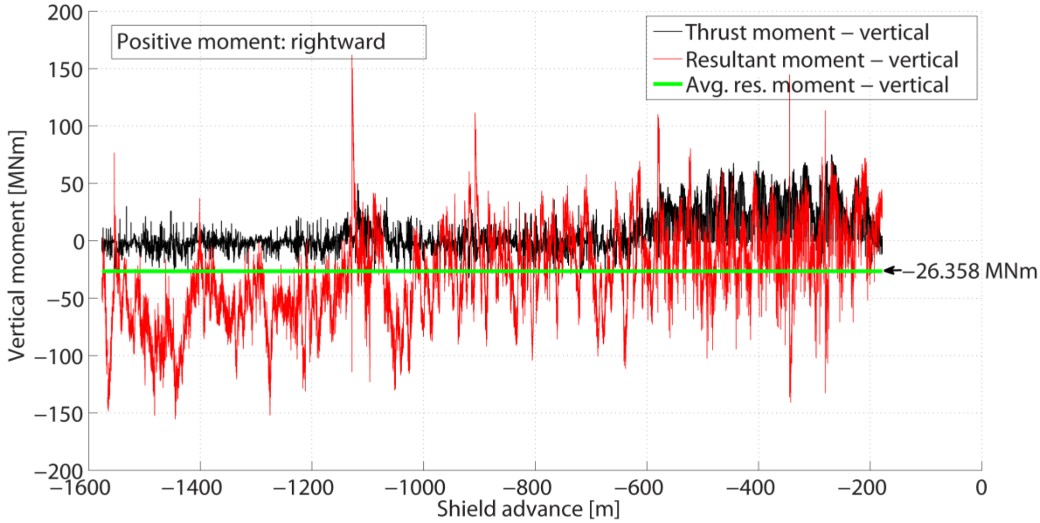

Figure 6.4: Resultant of vertical moments (red) and vertical thrust moments (black). In green the average value

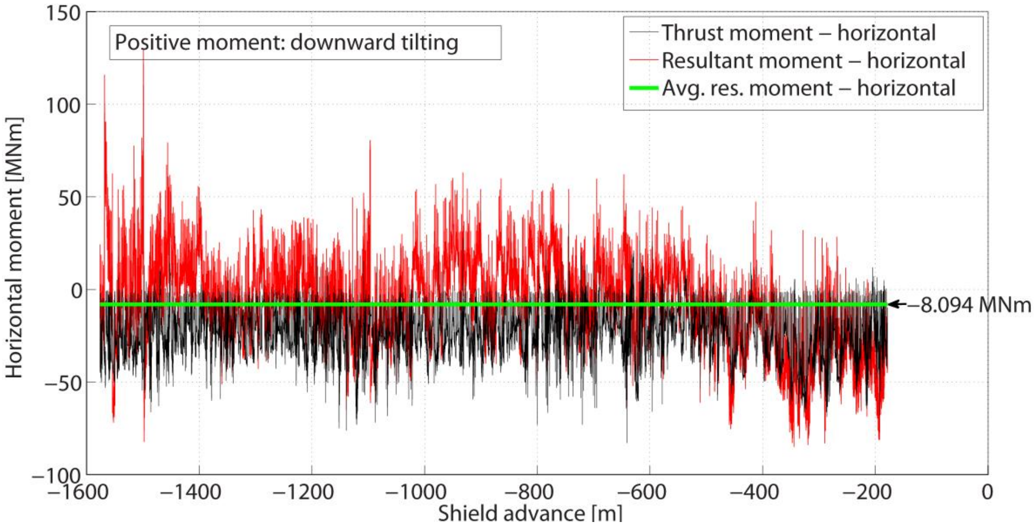

Figure 6.5: Resultant of horizontal moments (red) and horizontal thrust moments (black). In green the average value

6.2 On the correlation between resultant forces and moments

The moments of forces are calculated around the centre point of the shield's front cross section, the Reference Point Front (RPF). The horizontal transversal forces are correlated with the vertical moment and the vertical forces with the horizontal one. Other moments would also arise were the resultants of the tangential longitudinal stresses at the shield-soil interface not symmetrical between opposite sides of the shield. A vertical moment would arise if for example the resultant of the tangential longitudinal stresses at the right-hand side of the shield differed from that at the left-hand one. In that case the tangential stresses would lack symmetry with respect to a longitudinal vertical plane. The same would occur to the horizontal moment if symmetry lacked with respect to a horizontal plane.

The overall consistency of the proposed model is checked by plotting the resultants of forces and moments versus each other. In Figures 6.6 and 6.7 trend lines are given in red.

The correlation coefficients are based on Pearson's formulation

$$r = \frac{\sum_{i=1}^{n}(X_i - \bar{X})(Y_i - \bar{Y})}{\sqrt{\sum_{i=1}^{n}(X_i - \bar{X})^2}\sqrt{\sum_{i=1}^{n}(Y_i - \bar{Y})^2}} \tag{6.1}$$

in which X and Y represent the two populations and $\bar{X}$ and $\bar{Y}$ their median values. The high correlation coefficient in the case of vertical moments in Figure 6.6 (0.96) indicates a strong linear correlation between the two populations. The static model, based on the shield kinematic behaviour, captures the mechanism of horizontal interaction with the surrounding soil correctly.

The correlation coefficient is also relatively high in the case of horizontal moments in Figure 6.7 (0.89), and that confirms the overall validity of the static model on the aspect of vertical interaction with the surrounding soil.

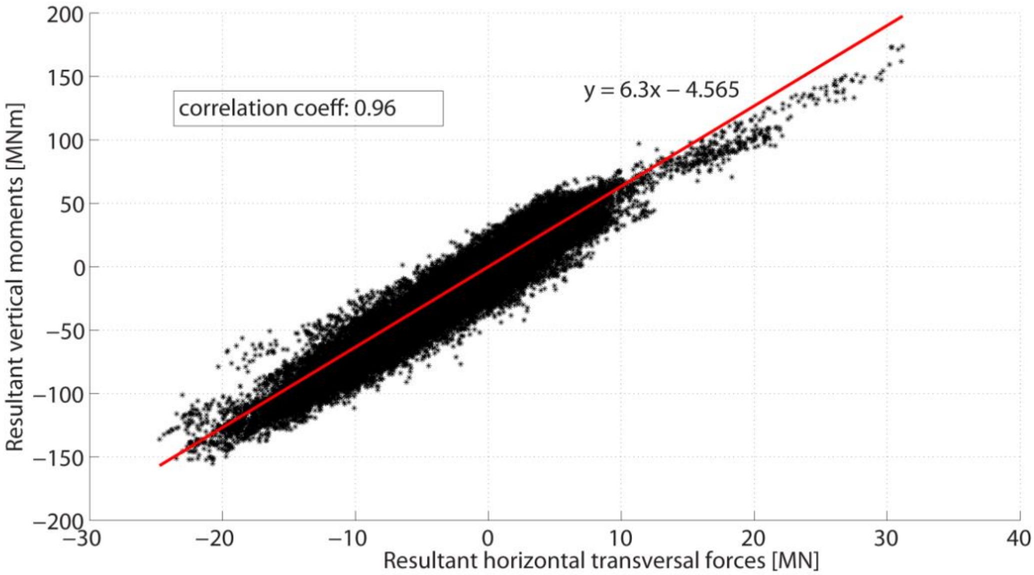

Figure 6.6: Resultants of the vertical moments versus resultants of the horizontal transversal forces

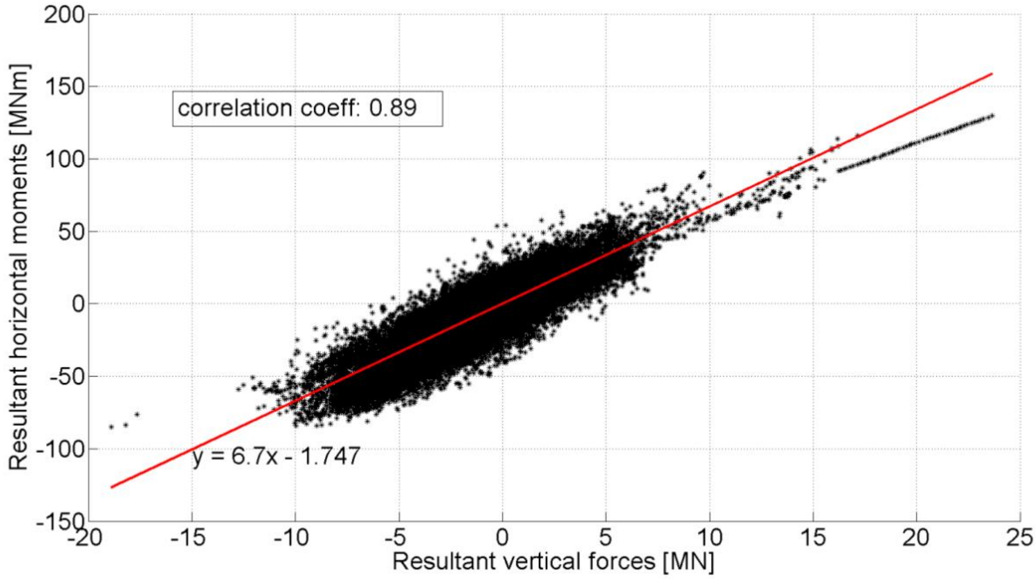

Figure 6.7: Resultants of the horizontal moments versus resultants of the vertical forces

The coefficients of the trend lines deserve consideration. The slope represents the arm, measured from the shield front, where the equivalent resultant force should be located in order to generate the corresponding turning moment. The intercept value, close to zero in both cases, suggests that in the modelled mechanical system the balance of forces would automatically provide for the balance of moments.

It is crucial to recall that the shield is steered by adjusting the magnitude and the spatial distribution of the advance forces applied through the thrust cylinders. The thrust cylinder are equipped at both ends with multidirectional hinges. That makes possible to slightly adjust the relative geometrical alignment between the longitudinal axis of the shield and that of the individual thrust cylinders. The hinges protect the cylinders from unwanted bending moments that could harm them. The end articulations also limit the transversal force which can be transferred between the TBM and the tunnel lining already in place. However, it cannot be excluded that some shear force can still pass, even if direct measurement measurements of it are not known to the author. This fact is also proven indirectly by Bogaards, Bakker [4] and Talmon and Bezuijen [45] who by studying the vertical equilibrium of the tunnel lining conclude that vertical balance in the liquid zone is not achievable unless a transversal force from the TBM is also accounted for. In the author’s opinion it remains true that to a large extent the transversal forces (either vertical or horizontal) arise as consequence of the shield interaction with the soil around it. Were the model perfect, the resultant of the transversal forces would be zero. As that is not the case, the possible reasons for the lack of transversal horizontal and vertical balance are investigated in Sections 6.4 and 6.5, respectively.

6.3 Longitudinal equilibrium

6.3.1 On the definitions of calculated and measured drag force

The *calculated* resistance to the shield advance, or *calculated* drag force, is obtained as the integral over the shield surface of the longitudinal tangential stresses between the shield-wall and the surrounding soil. The tangential stresses are in turn derived as the product of the normal soil effective stresses and the friction coefficient. A sound assessment of the normal stresses and of the friction coefficient are both important for a correct determination of the *calculated* drag. The normal effective stresses are in turn obtained by processing the calculated interface displacements through the soil reaction curves introduced in Chapter 5.

The *calculated* drag force is opposed to the *measured* resistance to shield advance, or *measured* drag force. The *measured* drag is a direct assessment of the average tangential stresses between the shield and the soil and derived by subtracting the hydrostatic action at the shield front from the thrust force. While minor contributions such as the drag of the back train and the contact forces between the cutting wheel and the excavation front are disregarded, the *measured* drag represents a good guess of the soil action on the shield and is often used in tunnelling practice.

6.3.2 Friction coefficients

Laboratory experiments on the skin friction between soil and various construction materials were conducted by Potyondy [38]. As result of that the skin friction between smooth steel and granular soil (sand) was determined from stress and strain controlled shear box tests both in dry sand and saturated sand. The angle of skin friction resulting from the experiments ranged between 24° 50’ and 23° 30’, with ratios between angle of skin friction and angle of internal friction in the range 0.43 ÷ 0.46. Potyondy’s experiments indicated ratios between normal and tangential stress within the interval 0.47 ÷ 0.57. Later experiments by Brumund and Leonards [6] confirmed Potyondy’s results for sands with angles of internal friction of 40° and 48°.

Further experimental results by Butterfield and Andrawes [7] concern the comparison between static and kinematic friction coefficients. They defined the static friction angle as the one relating normal and tangential forces at the onset of slow relative motion, and kinematic friction angle as the one relating perpendicular and tangential forces during subsequent slow relative motion. They found that the soil/steel friction angle decreased by 2° from static to kinematic condition. Even for lower angles of internal friction, in the range 30° ÷ 35°, ratios between normal and tangential stresses between 0.30 and 0.40 could still be expected in case of direct contact between granular soil and polished steel.

Here, an average friction coefficient of 0.05 (5% of the normal stress) is assumed at first, then applied to the shield surface and extended over the whole alignment. This low value is selected as we do not aim to catch the frictional mechanism between the sand grains and the steel surface. The average friction coefficient is chosen instead as a calibration factor and adjusted to provide a good level of longitudinal equilibrium over most tunnel length. In the present Chapter it is shown that an overall average longitudinal equilibrium is achieved with this low friction coefficient and that even in the most unfavourable configurations a friction coefficient of 0.25 would suffice to provide balance.

As the longitudinal tangential stresses are the product of the normal effective stresses and the friction coefficient, overestimation of the normal stresses cannot be a priori excluded, which in turn would require a reduction of the friction factor in order to achieve longitudinal equilibrium. However, this hypothesis is implicitly rejected through the analysis of the transversal and vertical equilibrium presented in Sections 6.4 and 6.5, respectively. It is shown there that the calculated normal effective stresses are required to justify equilibrium in those directions, and a large reduction of such stresses would not be admissible.

In light of the possibilities and limitations indicated above we will show how the shield-soil interface may have altered such as to impose a strong reduction of the average friction coefficient. We will show that the penetration of process fluids (face support slurry and tail void grout) into the shield-soil interface is possible and that it can lead to the required low average friction. The analysis will focus on confirmations to the hypothesized mechanisms through correlations between the TBM monitoring data. A number of specific locations will be presented in Section 6.3.7.

6.3.3 Calculated drag force

The resultant of the longitudinal forces and the thrust force in the south alignment are compared in Figure 6.8. However, the plot scale there hides the degree of correlation between them. The correlation can be better appreciated in Figure 6.9, which shows data over a shorter sector.

The resultant of the longitudinal forces $\overrightarrow{F_r}$ is defined as:

$$\overrightarrow{F_r} = \overrightarrow{F_{sl}} + \overrightarrow{F_{cw}} + \overrightarrow{F_{fr}} + \overrightarrow{F_{tg}} + \overrightarrow{F_{thr}} + \overrightarrow{F_{bt}} \tag{6.2}$$

in which $\overrightarrow{F_{sl}}$ is the hydrostatic action of the face support fluid, $\overrightarrow{F_{cw}}$ the longitudinal component of the contact force between the cutting wheel and the excavation front, $\overrightarrow{F_{fr}}$ the *calculated* drag force given by the skin friction between shield and soil, $\overrightarrow{F_{tg}}$ the contribution to the advance force given by the pressurized tail grout acting on the combined thickness of the shield tail and tail brushes, $\overrightarrow{F_{thr}}$ the advance force, and $\overrightarrow{F_{bt}}$ the drag force of the back-train. Subtracting the resultant longitudinal thrust force from the thrust force one obtains:

$$\overrightarrow{F_{thr}} - \overrightarrow{F_r} = -\left(\overrightarrow{F_{sl}} + \overrightarrow{F_{cw}} + \overrightarrow{F_{fr}} + \overrightarrow{F_{tg}} + \overrightarrow{F_{bt}}\right) \cong -\left(\overrightarrow{F_{sl}} + \overrightarrow{F_{fr}}\right) \tag{6.3}$$

The most relevant components are $\overrightarrow{F_{sl}}$ and $\overrightarrow{F_{fr}}$, as previously shown in Chapter 3. $\overrightarrow{F_{sl}}$ results from the measured support pressures at the shield front.

Figure 6.10 shows the path of the drag force $\overrightarrow{F_{fr}}$. Two distinct increases of the drag force occur at advances -1475 ÷ -1435 m and -355 ÷ -285 m. In both sectors the shield positioning system provided wrong readings concerning the deviations of the reference points and such errors could not be properly fixed. Consequently, high normal stresses were calculated as a consequence of the apparent sharp transversal movements of the shield. These normal stresses were finally converted into unrealistically high tangential longitudinal stresses and that gave the sudden increase of the (calculated) drag force. For that reason such sectors are not of interest and should be disregarded.

More realistic is the progressive increase of the drag force which starts at advance -600 m. At that location also the horizontal and then vertical curvatures of the alignment begin. The drag force increase matches well the kinematic shield behaviour discussed in Chapter 4. We demonstrated there how driving the shield along a curved alignment impacts the spatial distribution around the shield of the shield-soil interface displacements. We showed there how the steering moment which is applied through a non-symmetric distribution of the thrust forces must be counteracted by an equivalent reaction moment. In particular, we showed how such reaction must derive from a couple of forces in turn originating from the interaction displacements' distribution.

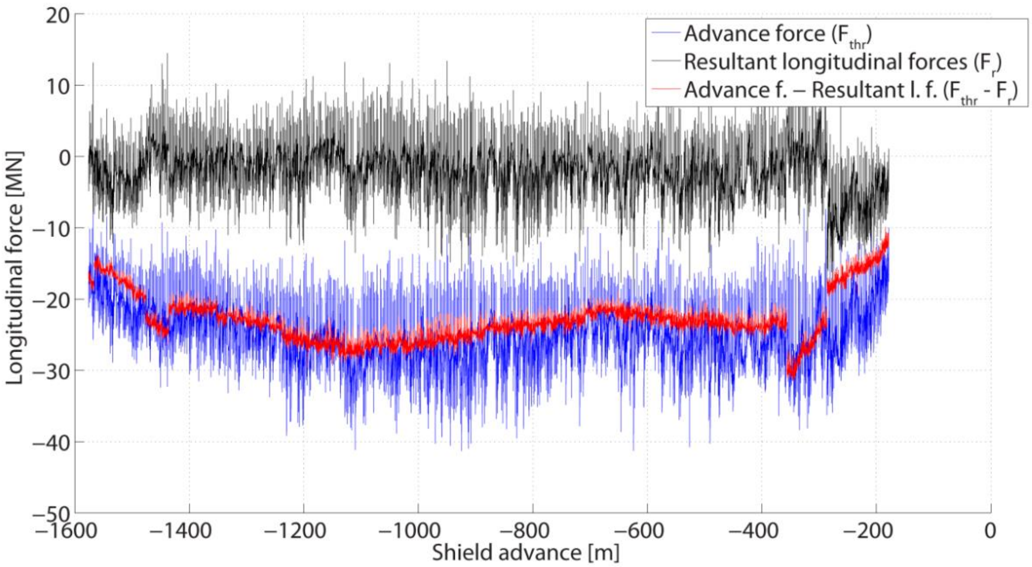

Figure 6.8: Thrust forces, resultant longitudinal forces, and difference between them over the south alignment

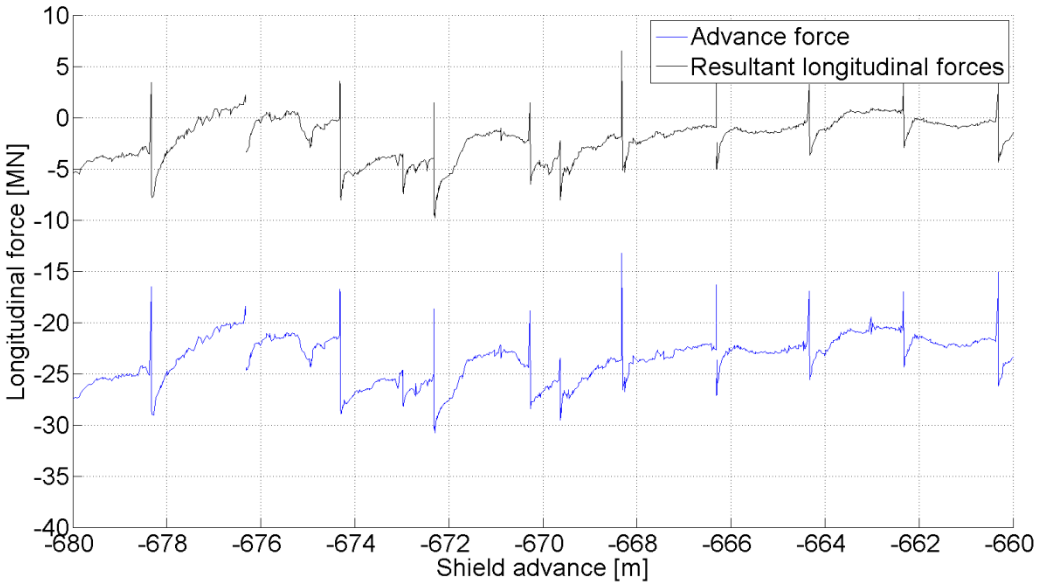

Figure 6.9: Thrust forces and resultant longitudinal forces over a sector of the south alignment

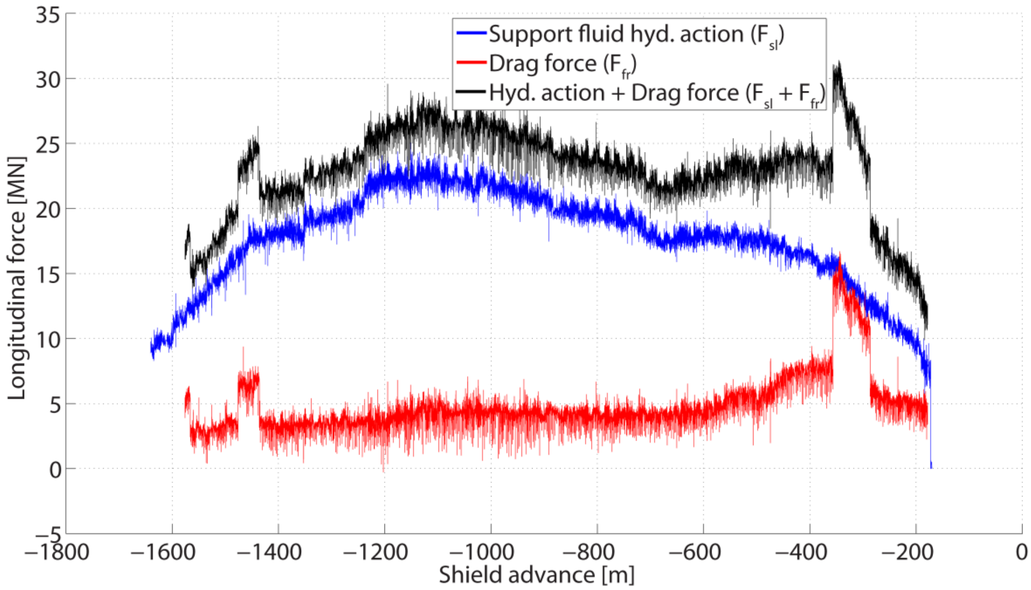

Figure 6.10: Hydrostatic action and drag force over the south alignment

6.3.4 Measured drag force

The relationship between the thrust force and the resultant of the longitudinal forces is best investigated by subtracting the face hydrostatic action from the measured thrust force. The difference between thrust force and hydrostatic force at the shield front is an expression of the *measured* resistance to shield advance (if smaller terms are disregarded), or *measured* drag. The *measured* drag, a direct estimate of the drag effect, differs from the *calculated* drag force. Figures 6.11 and 6.12 plot the resultant of the longitudinal forces versus the *measured* drag. It is recalled that the longitudinal resultants were obtained with a constant average friction coefficient of 0.05.

Figure 6.11 shows that the resultant of the longitudinal forces ranged from -20 to +15 MN. Conventionally, positive resultants are rearward oriented, and that mainly occurred during ring building. Ring building is of limited interest for the estimation of the skin friction. Negative resultants indicate instead that the *calculated* drag force derived with a constant friction coefficient dis not fully balance the advance force.

A variable friction coefficient in place of a constant one would have allowed to achieve longitudinal equilibrium at any advance. Values higher than the reference 5% are needed more often than lower ones. Calculations show that a friction coefficient of 25% would have made longitudinal balance possible even in the most unfavourable conditions, that is when the advance force peaked at -40 MN (Figure 6.8). The resultant of the longitudinal forces fluctuates as much as 5 to 10 MN even during advance for one single ring (Figure 6.9). This confirms that even at a small scale the friction coefficient varies, and the variation appears larger than would be obtained just by differentiating between static and kinematic friction, the latter being usually smaller than the former.

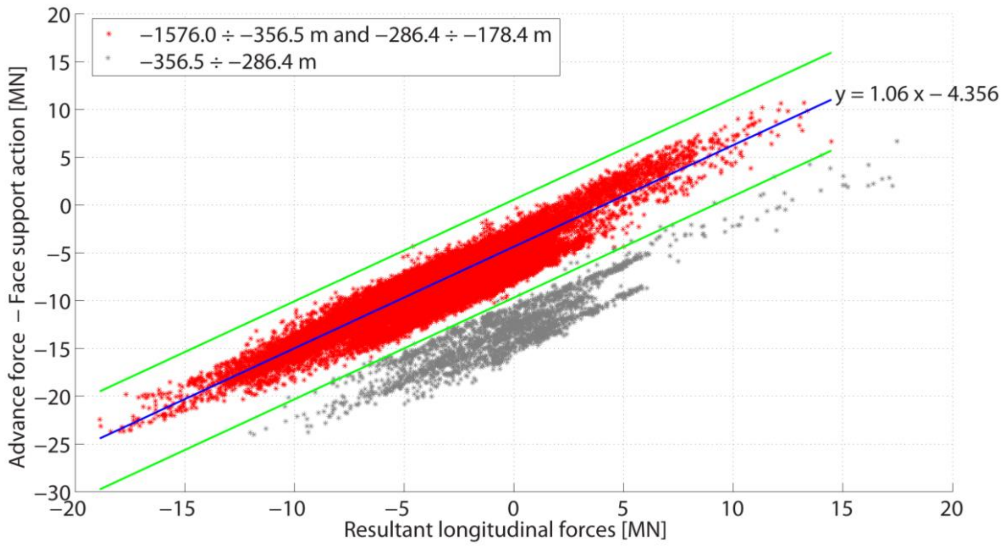

Figure 6.11: Resultant longitudinal forces versus *measured* drag force. South alignment. In red the points along most of the alignment; in grey the points along the stretch -356.5 ÷ -286.4 m affected by logged positioning error

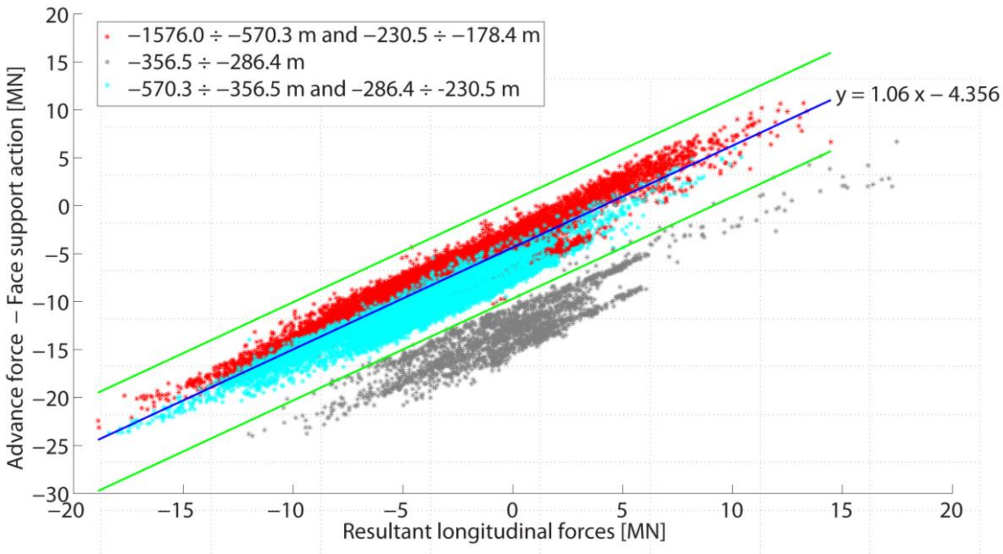

Figure 6.12: Resultant longitudinal forces versus *measured* drag force. South alignment. In red the points along the mostly straight sectors of alignment; in cyan the points along most of the leftward curve with a curvature radius of 542 m; in grey the points along the stretch -356.5 ÷ -286.4 m affected by logged positioning error

The width of the cloud of red points in Figure 6.11 indicates that longitudinal equilibrium was reached for a range of *measured* drag forces. Higher *measured* drag forces indicate larger constraint to the shield motion. The driving of curves is one such constraints. In this respect in Figure 6.12 the same data as in Figure 6.11 is reproduced highlighting the points corresponding to the drive of a leftward curve with a curvature radius of 542.3 m. The position of these points below the best fit of the entire data set indicates that higher drag forces arose in that sector.

The complication of matching the average skin friction coefficient assumed in the model (0.05) with the values derived from experimental results on granular soils (> 0.3) results from the fact that entire sectors of the TBM-shield wall are not in direct contact with the surrounding soil and that an interface layer exists between the excavated soil and the shield wall. Such layer produces a lubricating action around the shield and is thought to be caused by the penetration of the face support fluid (bentonite slurry) and of the tail void grout flowing from the injection openings towards the shield face.

The penetration of fresh fluids into the gap between the walls of the excavated cavity and the shield skin would justify the adoption of an average friction coefficient as low as 0.05. In fact the friction rate between such fluids and smooth steel is lower than 5%, whereas the friction rate in the sectors where direct contact between steel and soil occurs it is higher (30 ÷ 40%). The combination of the two, paired with the information on the extent of the sectors to which those apply, would lead to averaged friction values over the whole shield of 0.05 ÷ 0.25 and that would be enough to provide longitudinal equilibrium of forces over the entire alignment.

The observed decrease of the friction coefficient over a ring advance often turned out too large to be explained through the distinction static/kinematic friction. This strengthens the assumption of a shield not purely surrounded by soil. Moreover, the continuous decrease of the drag as uninterrupted driving increased hints at a direct interaction between the injection of process fluids and the surrounding soil.

6.3.5 On the correlation between tail-void grouting and drag force

Direct observations of the flow of process fluids around the TBM-shield are unfortunately not available at Hubertus, nor were those described in literature in detail. However, cases are orally reported in which the injected grout volumes were so relevant compared to the theoretical injection needs that the most sensible explanation appeared to be the penetration of grout mortar along the shield side until inside the excavation chamber. Given the lack of direct observations an indirect approach based on the TBM monitoring data is attempted here.

It is assumed that higher tail void grout injection pressures decrease the drag force by reducing the friction around the shield. The friction decrease would be due to the penetration of fresh grout between the shield skin and the excavated geometry, with higher grouting pressures producing even more extensive penetration and therefore further reducing the drag force. The grouting pressure contributed also more directly to the longitudinal balance through the hydrostatic action on the thickness of the shield tail, but this effect takes place independently of the penetration around the shield.

The ideal configuration to investigate the correlation between grouting pressures and advance forces would be having all the other TBM parameters constant and only thrust force and grouting pressure changing, possibly showing a direct or inverse correlation. Such ideal configurations are not frequently encountered when dealing with real data.

Both the advance force and the skin friction affect the advance rate of the TBM. Additionally, the advance rate is also affected by the rotational speed of the cutting wheel, and the two values combined are used to define the derived value of penetration. As mentioned, the pressurized grout acting on the combined thickness of the shield tail and tail brushes also produces a frontward oriented longitudinal force. The combined thickness of shield tail and brushes is 145 mm, which over the shield circumference leads to an area of 4.71 m^2. An increase of 100kPa in the grouting pressure would induce an additional advance force of 471 kN. Considering grouting pressures in the order of 500 ÷ 600 kPa, a frontward force of 2 ÷ 3 MN was estimated, which at approximately 10% of the advance force is not disregardable.

Thus if the grout pressure increases and the thrust force stays the same the advance rate is expected to increase, or remain unchanged when the thrust force is lowered proportionally. As said such combination of events is rare, and heavily depends on how the TBM was driven. In particular the TBM driver could aim for different goals. For instance he could aim to reach and maintain a certain advance rate, but also to limit the advance force below a pre-determined threshold in order to prevent ring damage. Similarly the grout operator, physically at a different location than the TBM driver, might at the same time aim for a certain grouting pressure or injection volume. As their motivations were not recorded we assume a hypothetical TBM driver having the goal of keeping a stable advance rate and investigate if such behaviour can be recognized along the tunnel drive.

6.3.6 On standstills and restarts

During standstills of the TBM, for instance during ring building, hydraulic pressure in the advance cylinders and grouting pressures in the grout injection lines usually decayed (Figures 6.13 and 6.14). Sometimes the grouting pressures in the lines remained stable, as Line 6 in Figure 6.14 shows, but that is less common. The grouting pressure measured along the injection lines are only weakly correlated with the grout pressure in the tail void. A rational evaluation of the pressure drop along the injection lines from the location where the pressure gauges were located to the injection openings could have accounted for this. However the lack of specific calibration/validation data available at this project discouraged the author from pursuing that.

The author is aware of experiments conducted at other projects in which pressure sensors were built both along the injection lines and in the shield tail (Amsterdam North-South metro line, private communications [36]). Concerns on the quality of those measurements suggests to not to transfer those results into this project.

At the restart of the drive for a new ring the rotation of the cutting wheel is started first, then the thrust force is progressively increased, and at last the grout injection is resumed. Usually grout injection starts when the advance rate is judged high enough or after advance of few tens of millimetres. During that interval the grouting pressure in the tail void drops further whereas the thrust force increases.

When also the grouting pumps are restarted, the grouting pressure recovers (the “void” created during drive without tail injection is refilled) and the thrust force is reduced. The thrust is reduced because the static condition is usually overcome at that stage, and acceptable advance rate is achieved. As a result on the one hand at each restart the thrust force first increases and then decreases. On the other hand, when also grouting restarts, the grout pressure lost during standstill and during the first steps of the new advance is progressively recovered. In this way the grout pressure at restart first decreases and then increases.

Therefore, grout pressure and thrust force are inversely correlated at most restarts. But that originates from the sequence of the restart operations more than from the interplay between grouting pressure and thrust force against the drag force. Figure 6.15 presents selected relevant TBM parameters recorded during the first 20 minutes of drive for ring 700 (south tube). During the first 4 minutes there is barely any advance of the shield even if the thrust forces increases and the cutting wheel turns. Given the limited advance the grouting process is suspended in that phase, and that leads to diminishing grouting pressure. Further, since the grout pressure is measured in the injection lines, the pressure in the tail void gap might be even lower in reality.

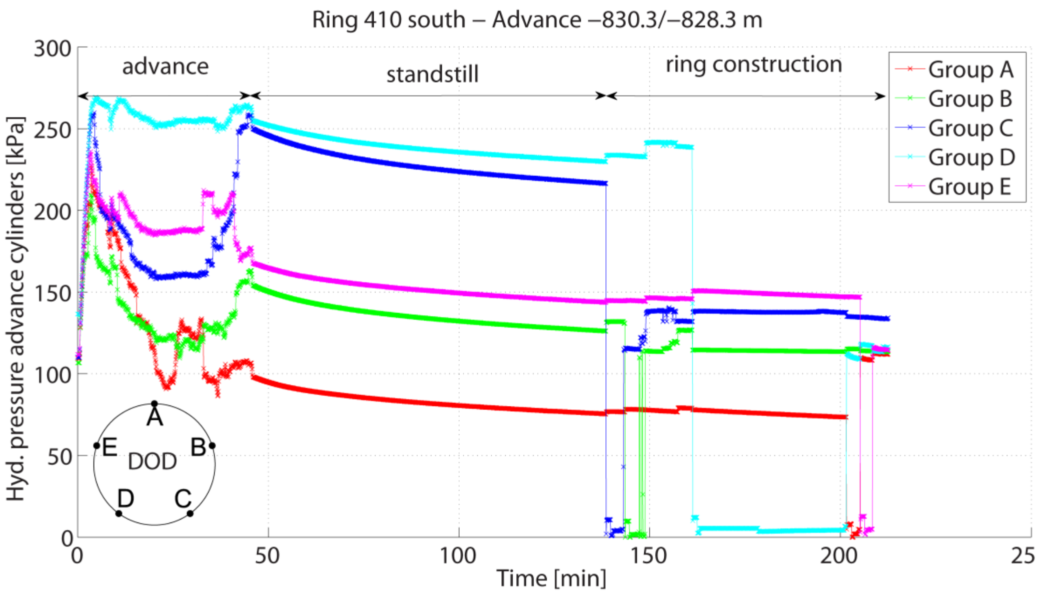

Figure 6.13: Hydraulic pressures in the advance cylinders at ring 410 south

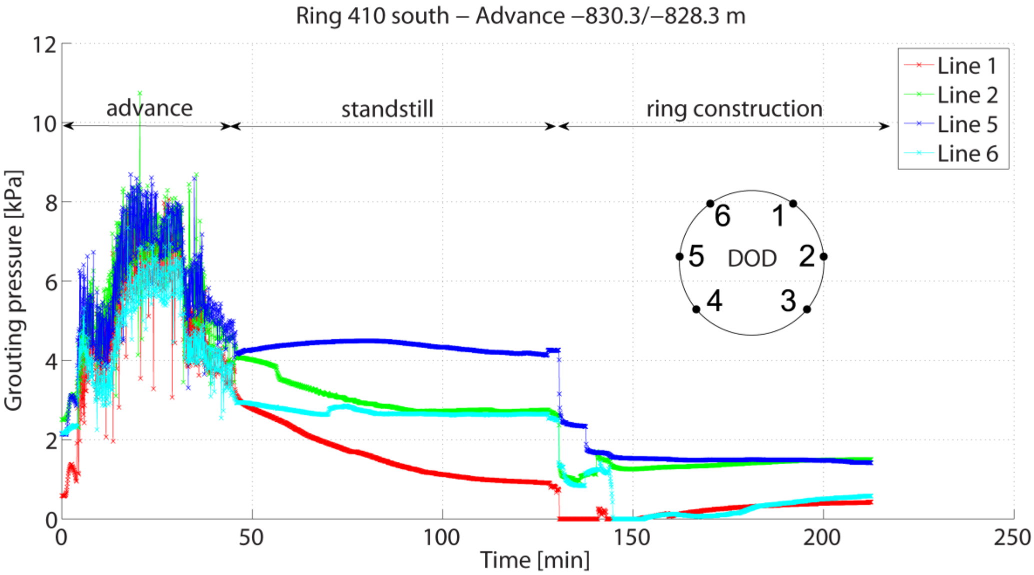

Figure 6.14: Grouting pressures in the injection lines at ring 410 south

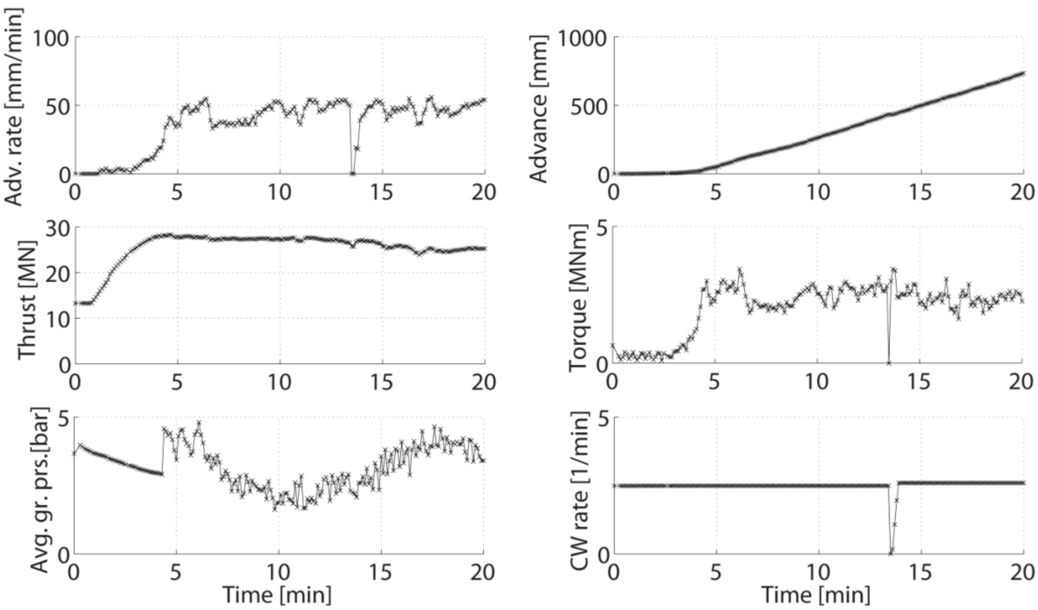

Figure 6.15: Significative parameters at the start of ring 700 south

6.3.7 Tail-void grouting and drag force: examples at specific advances

The inverse correlation between grouting pressure and advance force is observed for example over the intervals -678 ÷ -676 m and -646 ÷ -644 m of the south alignment, corresponding to the drives for rings 486 and 502, respectively. Also the thrust force is relatively regular in one case and the advance rate in the other.

6.3.7.1 Longitudinal equilibrium: advance interval -678 ÷ -676 m

Figure 6.16 shows selected significant TBM driving parameters monitored during drive for ring 486. No intermediate stop was recorded. The grouting pressure underwent quite regular fluctuations in the order of 200 kPa. The advance rate also fluctuated, whereas the advance force did not. The fluctuations are better appreciated at the scales of Figures 6.17, 6.18, and 6.19. The advance force (thrust) shows a peak at the actual start of the TBM movement and then decreases regularly from that moment onwards. Also, the grout injection was resumed when actual movement occurred.

Figure 6.17 shows the absence of any correlation between the grouting pressures and the thrust force. Figure 6.18 instead, in which the average grouting pressure and the advance rate are plotted, demonstrates a certain degree of correlation between the two parameters, as the peaks and the lows of the two curves coincide.

Even if the fluctuations of the grouting pressure and of the advance rate appear well paired, it remains difficult to quantify the actual contribution of the penetration of fresh grout on the reduction of the skin friction. Such difficulty follows what in Section 6.3.5 was shown to be the direct increase of the advance force as a consequence of the hydrostatic pressure on the thickness of the shield tail. Both direct increase of the thrust force due to hydrostatic effect and decreased drag force due to the reduced friction contribute to enhance the shield advance. Their separate effects are difficult to distinguish.

The comparison between the thrust force and the advance rate as in Figure 6.19 confirms the absence of a correlation between them. That underscores that the fluctuation of the advance rate is in this case related to the direct and indirect effects of change in grouting pressure. An interesting aspect also highlighted by Figure 6.19 is the continuously decreasing thrust force required to maintain a constant advance rate. An advance rate of 40 to 50 mm/min was achieved with an initial thrust of about 30 MN. The same speed was still maintained after 2 m of drive and a thrust force of 20 MN only. This hints to a decrease of the drag force during drive beyond the range possibly justified by the distinction between static and kinematic friction coefficient. A reasonable explanation seems to be that of an increasingly larger penetration of fluid grout and bentonite into the shield-soil interface as the advance proceeded.

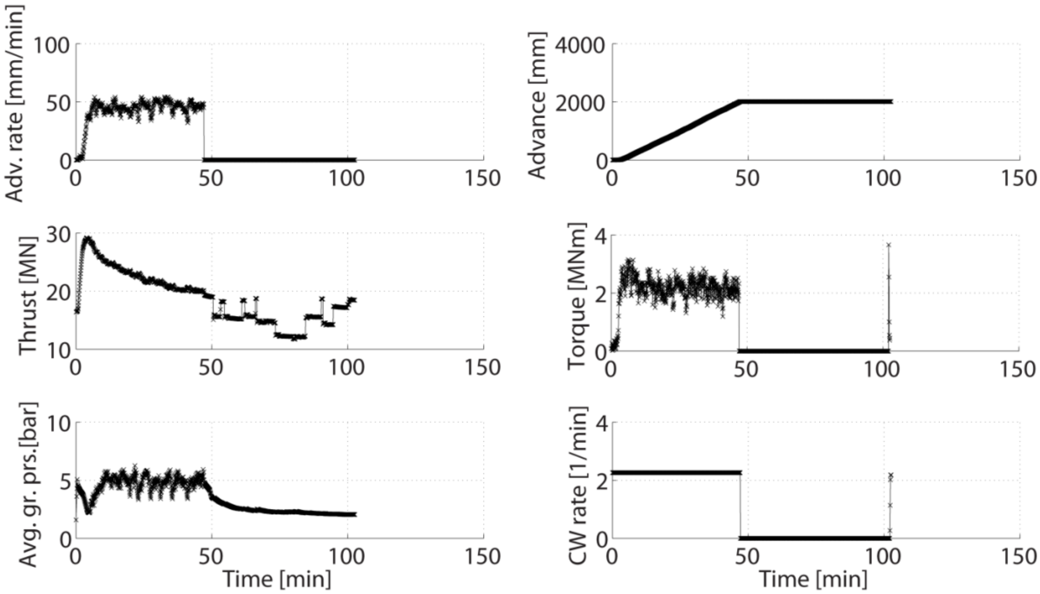

Figure 6.16: Significative parameters over the interval -678 ÷ -676 m (ring 486 south)

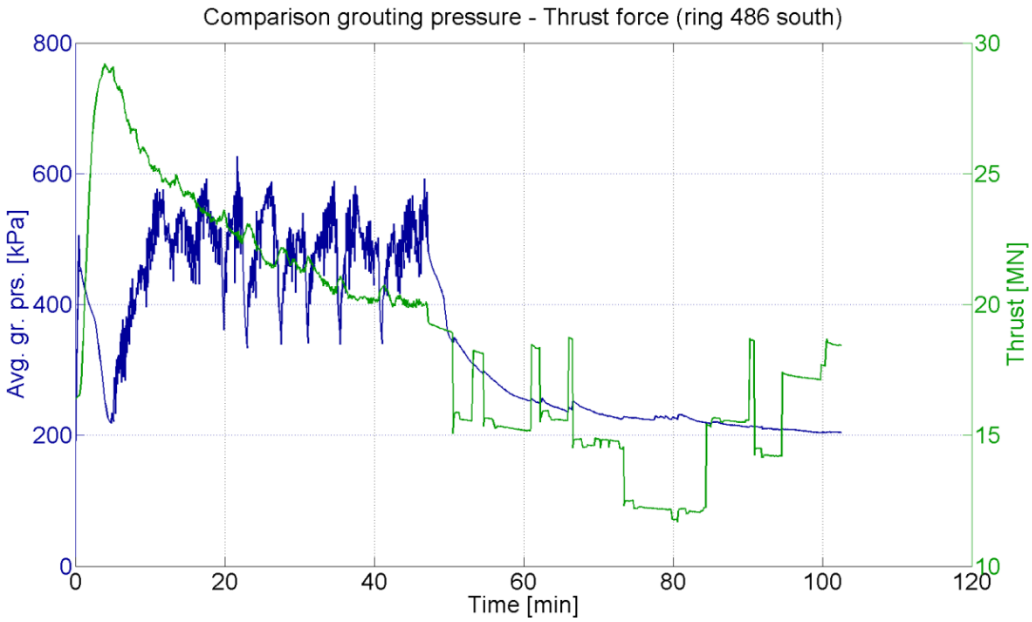

Figure 6.17: Comparison average grouting pressure and advance force (thrust) over the interval -678 ÷ -676 m (ring 486 south)

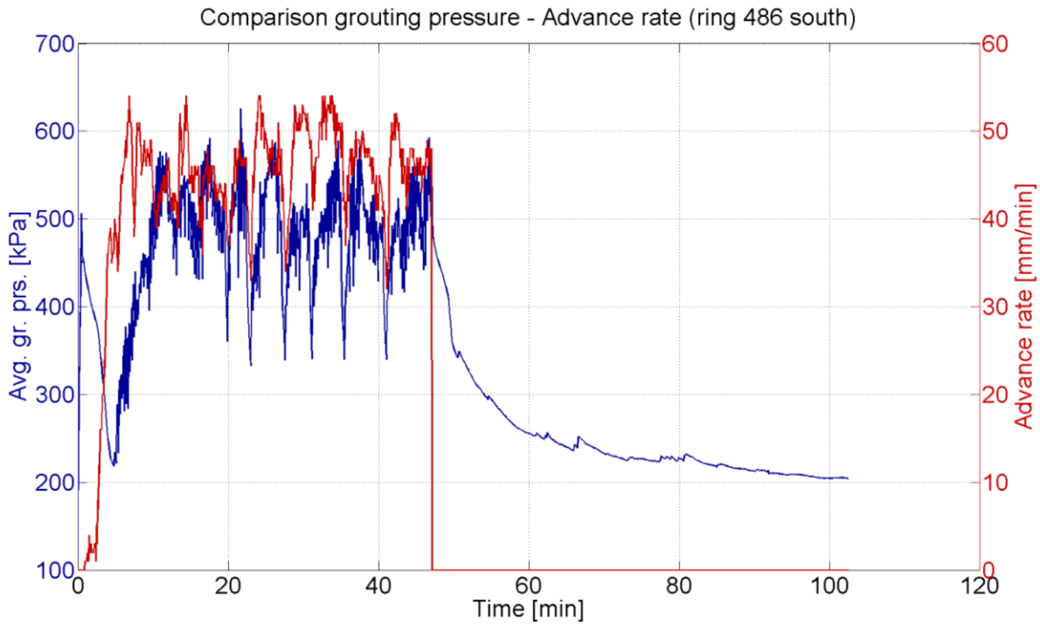

Figure 6.18: Comparison average grouting pressure and advance rate over the interval -678 ÷ -676 m (ring 486 south)

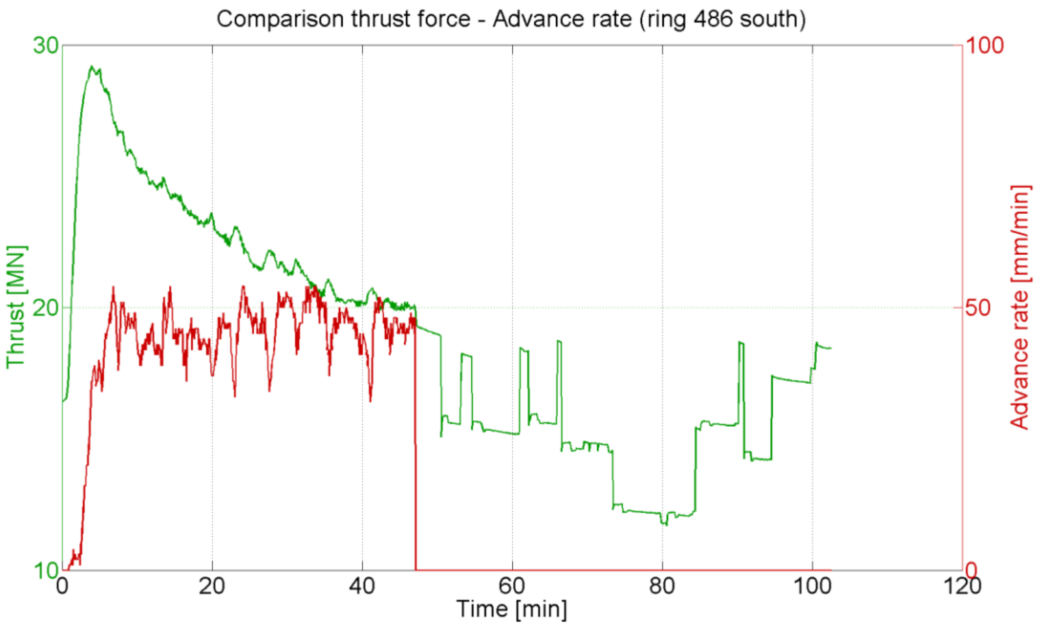

Figure 6.19: Comparison advance force (thrust) and advance rate over the interval -678 ÷ -676 m (ring 486 south)

6.3.7.2 Longitudinal equilibrium: advance interval -646 ÷ -644 m

Figure 6.20 shows selected significant TBM driving parameters monitored during the advance for ring 502. The TBM advance rate proved not completely stable, but only one short stop occurred. The average grouting pressure fluctuated considerably, quite in accordance with the fluctuation of the advance force. The grout pressure decreased nearly 100 kPa after the first few minutes of drive. The actual advance of the TBM started after about 25 min, and at the same moment also the grout injection was resumed.

The grout injection stopped after about 60 minutes, and after that it resumed and stopped again several times at intervals of 5 to 10 minutes (Figures 6.21 and 6.22). Although the reasons for such interruptions are not known, grouting pressure fluctuations result of about 300 kPa. Figure 6.21 shows that the peaks of the grouting pressure match pretty accurately the lows of the thrust force, with fluctuations of the thrust force of about 2 MN. The opposite is also true, with the peaks of the thrust force matching the lows of the grouting pressures. The tunnel driver may have reacted to the drops of the grouting pressure by increasing the thrust force.

Comparing the average thrust adjustment (2 MN) and pressure drop (300 kPa) gives a quantitative indication of their relationship. It was estimated earlier (Section 6.3.5) that a grout pressure increase of 100 kPa provoked an increase of the advance force of 471 kN. Consequently a pressure increase of 300 kPa led to an increase of the longitudinal force of about 1.5 MN, which is already in the order of magnitude of the observed adjustment. But the fact that the hydrostatic effect on the shield tail alone justified a large rate of the variation in advance force leaves little room for the contribution of the mechanism of fresh grout penetration.

It is unlikely that the TBM driver increased the thrust force based on direct observation of the grouting pressure. Most likely the driver reacted to the changes in the shield advance rate trying to compensate it. In Figure 6.22 the grouting pressure is compared to the advance rate. A reasonably good direct correlation is found between the two. Therefore the advance rate, which in the end is the ultimate result of all the processes involved in shield advance, matched the pattern of the grouting pressures. This supports the hypothesis that the driver by reacting to the changes in advance rate (increasing the thrust when the TBM slowed and vice versa) indirectly reacted to the changes in grouting pressure.

The direct comparison between advance rate and thrust force is presented in Figure 6.23. Several *waves* were recorded between minutes 60 and 140, and the two signal mirrored each other. That means that in each *wave* a decrease in the advance rate was paired with an increased thrust force and vice versa. Reference lines (in blue) separate adjacent sectors. Disregarding smaller scale fluctuations on behalf of the advance rate helps to appreciate the correlation.

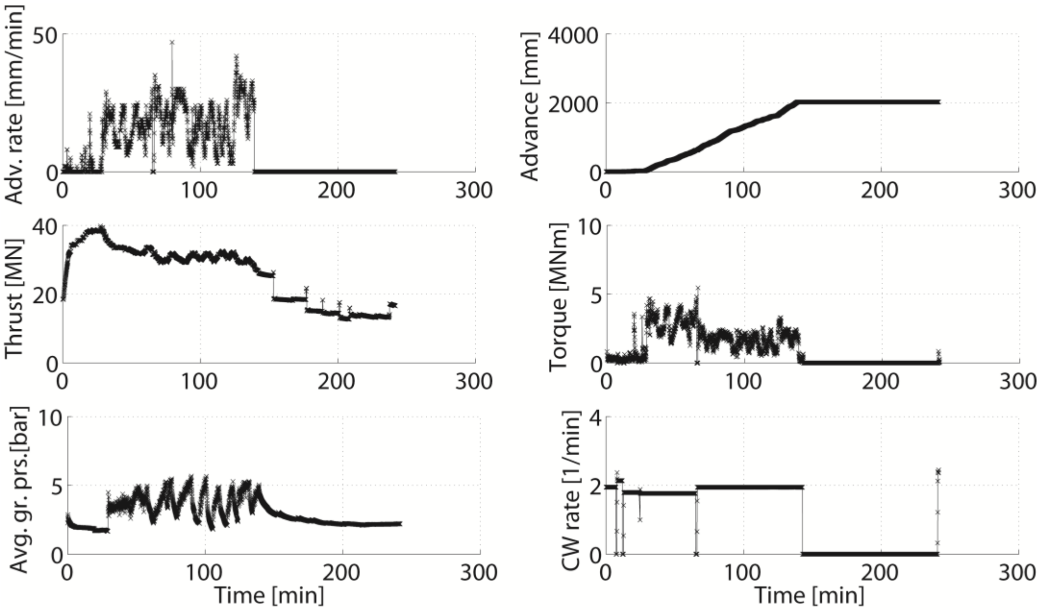

Figure 6.20: Significative parameters over the interval -646 ÷ -644 m (ring 502 south)

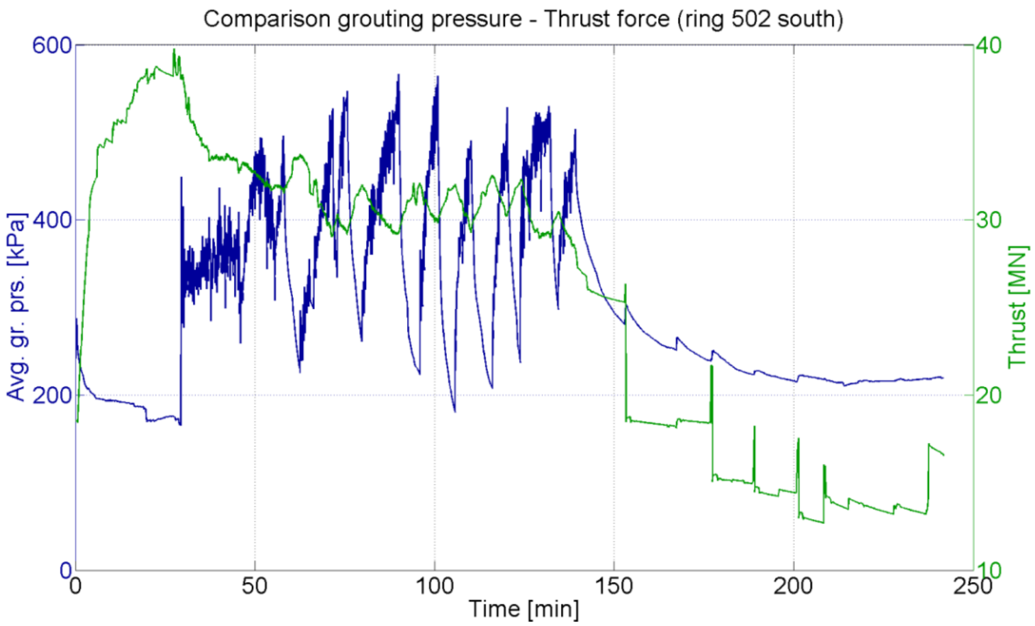

Figure 6.21: Comparison average grouting pressure and advance force (thrust) over the interval -646 ÷ -644 m (ring 502 south)

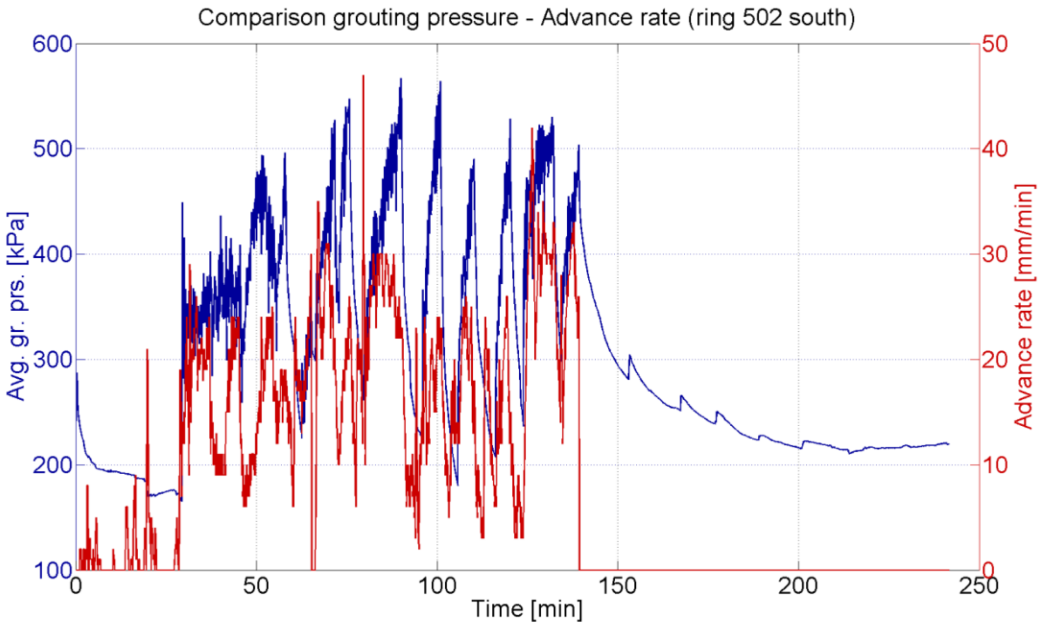

Figure 6.22: Comparison average grouting pressure and advance rate over the interval -646 ÷ -644 m (ring 502 south)

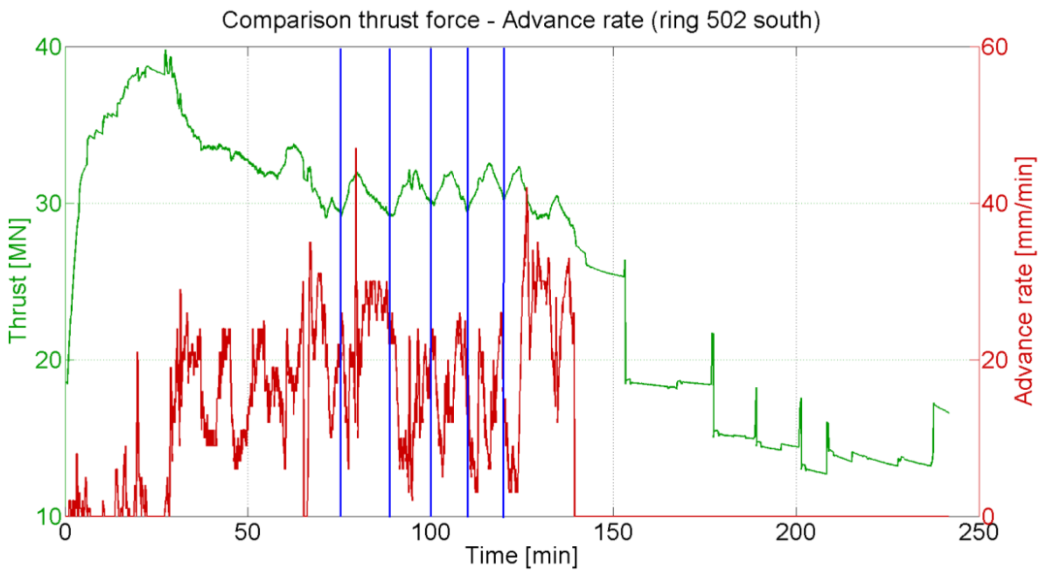

Figure 6.23: Comparison advance force (thrust) and advance rate over the interval -646 ÷ -644 m (ring 502 south)

6.3.8 Longitudinal equilibrium: partial conclusions

The analysis of the longitudinal equilibrium focussed on the correct assessment of the resistance to the shield advance, or drag force. A non-correct assessment of the magnitude of the drag force could be either the consequence of a poor estimation of the normal effective stresses or of the value of the friction coefficient. The first option was rejected based on considerations of transversal and vertical equilibrium that will be detailed in Sections 6.4 and 6.5. The second option, namely the estimate of a proper friction coefficient, was discussed in this section.

The main model limitation resulted in assuming a constant friction coefficient during advance. That choice leads to a relatively good average longitudinal equilibrium, but to a rather poor one at specific advances. Additional analysis shows that an average friction coefficient ranging between 0.05 and 0.25 (or 5% to 25% of the normal effective stress) would have been sufficient for longitudinal equilibrium in most configurations. However such values are still considerably lower than reported in the literature on the shear resistance between steel and sand, usually ranging from 0.30 to 0.40 (or 30% to 40% of the normal effective stress).

The hypothesis of penetration of process fluids around the shield was formulated given the impossibility to match the values of the friction coefficient from literature with those needed. It was assumed that the face support fluid and the tail void grout have the ability to infiltrate into the interspace between the wall of the excavated geometry and the shield-skin acting as a lubricating layer and therefore reducing the actual friction coefficient. Confirmation of that hypothesis was looked for in the relationship between meaningful TBM parameters, namely the grouting pressure, the advance force, and the advance rate.

A correlation between the grouting pressure and the drag force has been only partly established. The alleged inverse correlation between the two is based on the assumption that higher pressures lead to a larger sector penetrated by fresh grout and therefore lower resistance to shield advance. However, the pressurized grout produces also a hydrostatic effect on the shield tail and that contributes to the shield advance mechanism, therefore hiding the more indirect mechanism of varying penetration as consequence of the change in injection pressures.

6.4 Transversal equilibrium

6.4.1 On the investigative approach to transversal equilibrium

In Section 6.1 the direction of the transversal force was defined as horizontal and perpendicular to the TBM-axis. The transversal force is consequently related to the vertical moment which in turn, according to the right-hand rule convention, affects the yaw of the TBM. For that reason the analysis of the transversal shield response and equilibrium will be accompanied by plots of the vertical driving moment.

The shield behaviour will be investigated by focussing on specific advance locations or short stretches of advance over which the combination of driving actions and shield response (horizontal tendency) highlights the existence and the limit of their physical relationship. For instance it will be shown how the shield responded when a certain vertical driving moment was applied. The transversal equilibrium of forces will be analysed as the result of the integral of the normal stresses acting on the shield body. Configurations will be presented in which the transversal equilibrium was achieved and others in which that was not. Particularly when the second was the case, alternative physical explanations will be offered, among which are the adequacy of the assumed soil response curves and the disregarded effect of the penetration of process fluids.

6.4.2 Transversal response: similar driving moments but different reactions

An interesting case to start with is that of two different shield reactions observed in response to comparable vertical driving moments. Figures 6.24 to 6.27 present plots of TBM monitored and calculated data concerning driving moment, shield response, and grouting pressure over the stretch -860 ÷ -820 m of the south alignment. Figure 25 shows that the vertical driving moment tended towards the negative field in the sectors -850 ÷ -846 m and -834 ÷ -828 m with values up to -18 and -21 MNm, respectively. Based on the sign conventions (Section 6.1) negative vertical moments are applied to induce a rightward yaw or, according to another notation, to obtain a positive horizontal tendency.

6.4.2.1 Transversal reactivity

The comparable magnitude of the driving moments and the similar extension of the sectors along which such moments were applied would hint to similar TBM-shield reactions. Figures 6.24 and 6.25 shows that such was not the case. In the first of the two sectors (-850 ÷ -846 m) the shield showed considerably higher reactivity than in the second one, with reactivity the promptness of the horizontal tendency to vary as soon as the vertical moment changes. It is recalled that the sign convention is positive for deviations of the reference points towards the right-hand side of the tunnel alignment.

In sector -850 ÷ -846 m the change in horizontal tendency occurred through a rightward shift of the reference point front (RPF) and a leftward shift of the reference point rear (RPR). In the sector -834 ÷ -828 m, when the negative driving moment was first applied, the horizontal tendency did not change immediately. Both reference points started to move leftwards with similar rate and inversion of tendency was observed at advance -830 m only. Differing tail-grout injection strategies could have been the factor leading to such different shield responses.

The average grouting pressures over the stretch -860 ÷ -820 m are presented in Figure 6.26, whereas Figure 6.27 shows the injection pressures measured in each distinct injection line. The average pressure in sector -850 ÷ -845 m was about 150 kPa higher than in sector -840 ÷ -830 m. The hypothesis is that the higher pressures in the first sector constrained the shield movement more than in the second one.

A mechanism is proposed in which higher confining stresses enhance a more reactive shield response. The higher stress state, supported by higher grouting pressures, is assumed responsible for stiffening the soil around the shield. The stiffer soil does in turn limit the change in terms of horizontal tendency which the shield has to undergo to react to a varying driving moment. This appears compatible with the different shield behaviour observed at the two said sectors in which the change in horizontal tendency was indeed smaller and prompter at the first interval, with higher grouting pressures, than at the second one, with lower pressures.

6.4.2.2 Grouting pressure and transversal response

Over the interval -834 ÷ -828 m the grouting pressure in line 6, located at the left-hand side, 35° from the top, was considerably lower than in the other three injection lines in use (Figure 6.27). The pressure in line 6 fluctuated by 50 to 150 kPa higher compared to line 1 (same height, opposite side). Over the same interval Figure 6.28 shows that the average grouting pressure quite rapidly increased about 200 kPa around advance -830 m. Such observations suggest consistency between the low grouting pressures at the left-hand side and the leftward shift of both RPF and RPR between advance -835 and -830 m. The increase in the grouting pressure at advance -830 m produced instead a quick reaction in horizontal tendency, particularly remarkable in the inversion of trend observed at the RPF.

The resultant transversal forces in the sector -860 ÷ -820 m are shown in Figure 6.28. Because the shield was driven by adjusting magnitude and distribution of the longitudinal forces applied through the thrust cylinders, horizontal transversal forces could only arise as consequence of the shield interaction with the surrounding soil and must by definition be self-balanced. Given the poor transversal balance achieved in the sector we will investigate how the hypotheses in the model may have affected the results.

The first assumption in the model is that the results of the kinematic analysis are correct. This hypothesis might be too optimistic due to the presence of calibration errors affecting the shield positioning system. Such errors were usually recognized when re-calibration was performed at regular intervals. A consequence of a poor calibration could for instance be a signalled tendency of the shield that did not actually occur in practice. However, given the impossibility to fully prove this aspect, the position monitoring data are assumed correct.

The second simplification concerns assuming a lower cut-off on the stress level at the shield-soil interface. The shield advanced interacting with the excavated geometry creating regions of soil compression and soil extension. The interface stresses were in turn determined by processing the calculated displacements by means of appropriate soil reaction curves. The so obtained stress state at the shield-soil interface could be either higher or lower than before tunnelling (undisturbed stress-strain state) depending on the specific deformation pattern at any location. However, through the introduction of a lower cut-off it is assumed that the contact stresses could only be higher than the stresses before tunnelling.

With the lower cut-off hypothesis it was attempted to represent the effect of the penetration of process fluids (tail-grout and bentonite) in the tail void between the shield-skin and the surrounding soil. The hypothesis assumes an infiltrating fluid capable of preserving the initial stress state whenever the calculations lead to lower stress levels. The main risk of such simplification is to misrepresent the stress state in the soil-relaxation sectors. The introduction of the cut-off may in fact have produced two kind of errors. The interface stresses may have been either overestimated, when the grouting pressure is not sufficient to compensate for the kinematic relaxation, or underestimated, when the grouting pressure is particularly high and therefore potentially able to more than compensate the soil relaxation due to the kinematic effect.

With reference to the plot of the transversal equilibrium of forces of Figure 6.28, a particularly unbalanced configuration occurred in the interval -835 ÷ -834 m. That interval might be meaningful to understand how the simplifications above led to the unbalance. The most likely factors were the soil reaction model adopted and the simplistic way in which the grouting process was captured. These factors will be separately investigated in the two following sections.

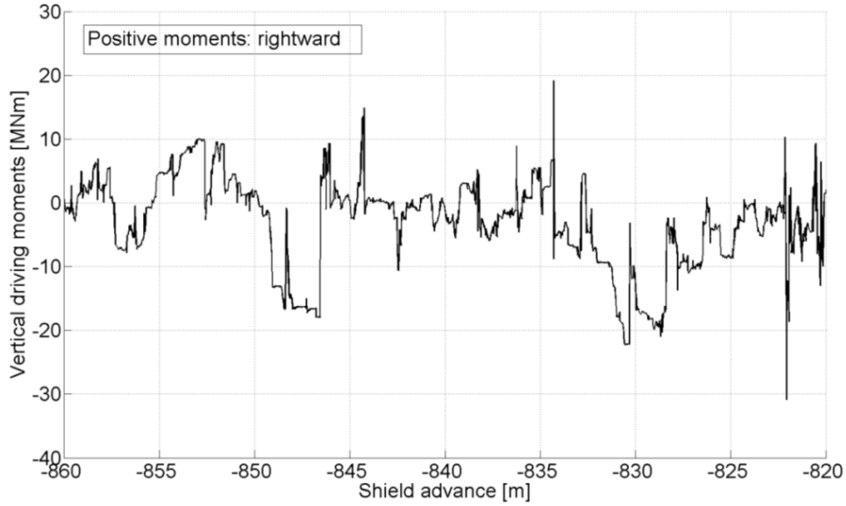

Figure 6.24: Vertical driving moment – sector -860 ÷ -820 m

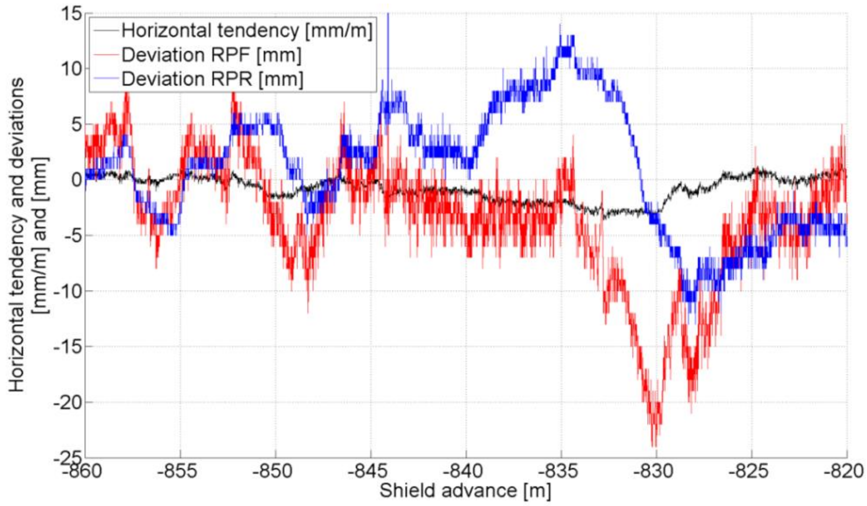

Figure 6.25: Horizontal tendency and deviations of the reference points – sector -860 ÷ -820 m

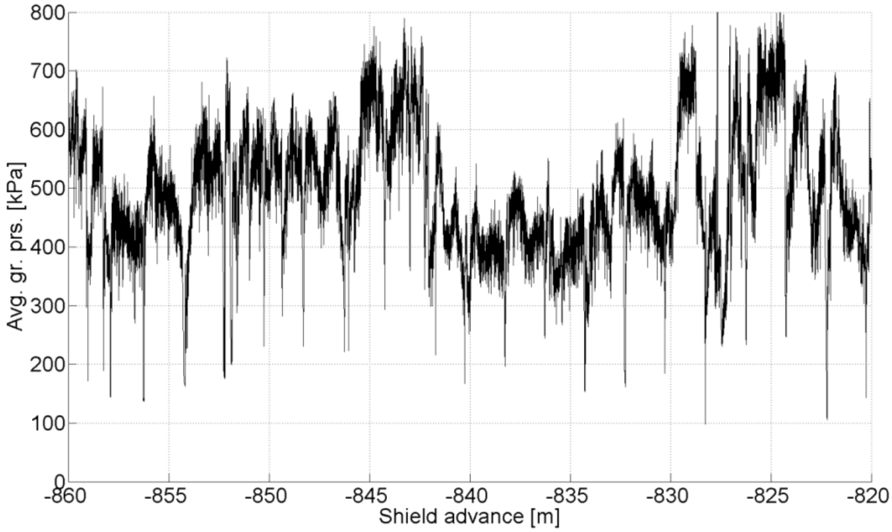

Figure 6.26: Average grouting pressures – sector -860 ÷ -820 m

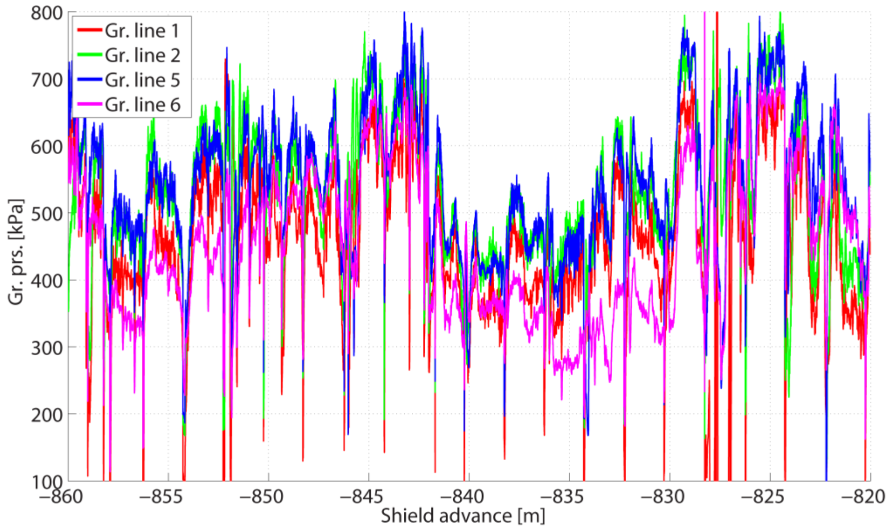

Figure 6.27: Detail grouting pressures – sector -860 ÷ -820 m

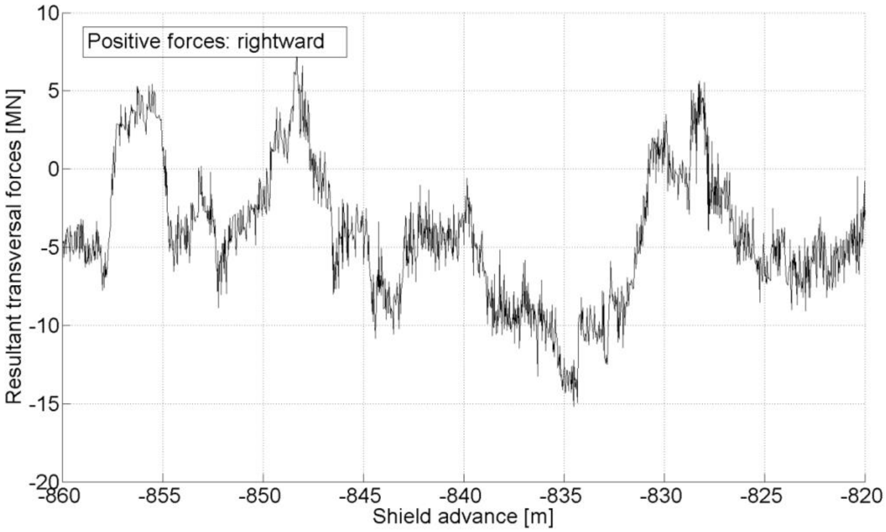

Figure 6.28: Resultant transversal forces – sector -860 ÷ -820 m

6.4.3 On the effect of the soil reaction model

The soil reaction model is based on soil reaction curves obtained from the FE analysis presented in Chapter 5. The commercial software PLAXIS 2D v. 2012.01 is used and the Hardening Soil constitutive model is adopted. Several simulations were performed in order to estimate how the soil reaction curves varies with a number of parameters such as the initial effective stress, the unloading-reloading non-linear soil response, the radial position around the shield, and the deformation history of the soil. The reference soil stiffness $E_{50,ref}$, defined as the triaxial secant elastic modulus at 100 kPa effective confining stress, is the only parameter which was kept constant at 40 MPa throughout the simulations. This choice should be reconsidered in future investigations as it appears to be the largest limitation of the soil reaction model.

A simplified evaluation of the consequences of adopting a different elastic modulus is presented hereafter. Equal displacement patterns are applied to two different soil conditions, one stiffer ($E_{50,ref} = 40$ MPa) and one softer ($E_{50,ref} = 20$ MPa). Two loading patterns are studied, one symmetrical with respect to a vertical line through the tunnel axis, and one anti-symmetrical with respect to the same line. In both cases the tunnel, symbolizing the TBM-shield in this case, was assumed infinitely stiff.

In this subsection, in agreement with the usual soil mechanics sign convention also implemented in PLAXIS, negative sign is assigned to compression stresses. That is in contrast with the convention adopted in the rest of the current section in which positive pressure values indicate compression stresses instead.

6.4.3.1 Dependency of the soil-reaction curves from the soil stiffness in axial-symmetric conditions

The first imposed deformation is a radial contraction followed by equal expansion. Such configuration ideally simulates an axially symmetric “volume loss”, due for instance to overcutting and shield tapering, fully recovered through tail-void grout injection. The implemented contraction rate equals an areal decrease of 2%, equivalent to a decrease of the original radius of 50 mm, from 5.255 m to 5.205 m. The position of the tunnel centre point is fixed, therefore the deformations of the tunnel are purely concentric. Figures 6.29 and 6.31 show the results in terms of horizontal and vertical effective stresses for $E_{50,ref} = 20$ MPa, and Figures 6.30 and 6.32 for $E_{50,ref} = 40$ MPa.

The FE model indicates that the final horizontal effective stress at the tunnel spring level is -420 kPa for the softer soil and -550 kPa for the stiffer one. The final vertical effective stress at the tunnel top is -377 kPa and -463 kPa for soft and stiff soil, respectively. At the tunnel bottom, -355 kPa and -465 kPa.

The horizontal transversal force acting on a half-tunnel is also evaluated. The force (per unit length) is calculated as the integral of the horizontal effective stresses on a vertical line, tangent to the tunnel, and with length equivalent to the tunnel diameter. The value obtained is then extended over the whole shield length therefore providing an estimate of the transversal action on a half-shield undergoing the same displacement pattern.

A scheme of the problem is shown in Figure 6.33. The transversal action is obtained as

$$\Delta\overrightarrow{T_{20}} = \sigma_{xx,20,avg} \times h \times w = 328 \times 10.51 \times 10.235 \cong -35.3 \text{ MN} \quad (6.4)$$

and

$$\Delta\overrightarrow{T_{40}} = \sigma_{xx,40,avg} \times h \times w = 428 \times 10.51 \times 10.235 \cong -46.0 \text{ MN} \quad (6.5)$$

in which $\Delta\vec{T}$ was the resultant transversal force on a half-shield, $\sigma_{xx,20,avg}$ and $\sigma_{xx,40,avg}$ the average horizontal effective stresses correlated with the described loading pattern, h the height of the lateral projection of the TBM-shield, and w the length of the same projection. The difference between the two forces amounts to

$$\Delta\overrightarrow{T_{40}} - \Delta\overrightarrow{T_{20}} = 10.7\ MN \quad (6.6)$$

Such virtual loading pattern, although unlikely to occur in practice, gives an impression of the model’s sensitivity to the elastic modulus of the soil. $\Delta\vec{T}$ indicates the amount of unbalance should such displacements occur at one half of the tunnel only. $\Delta\overrightarrow{T_{40}} - \Delta\overrightarrow{T_{20}}$ quantifies the error on the transversal force that would derive due to a misrepresented soil stiffness of a factor 2. Such uncertainty around the soil stiffness must not be surprising as its accurate experimental determination is complex and considerable errors may occur. The calculated error affecting the transversal force as consequence of an incorrect estimation of the soil stiffness would alone already justify a great deal of the unbalance indicated in Figure 6.28 around advance -835 m.

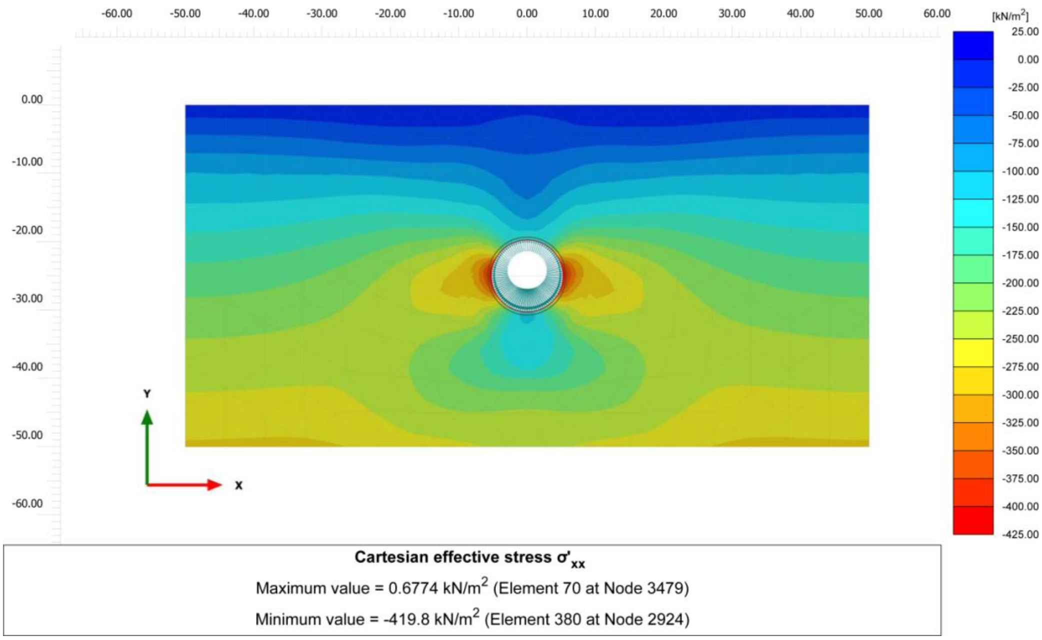

Figure 6.29: Horizontal effective stresses following a fully recovered concentric aeral contraction of 2% ($E_{50,ref}$ = 20 MPa)

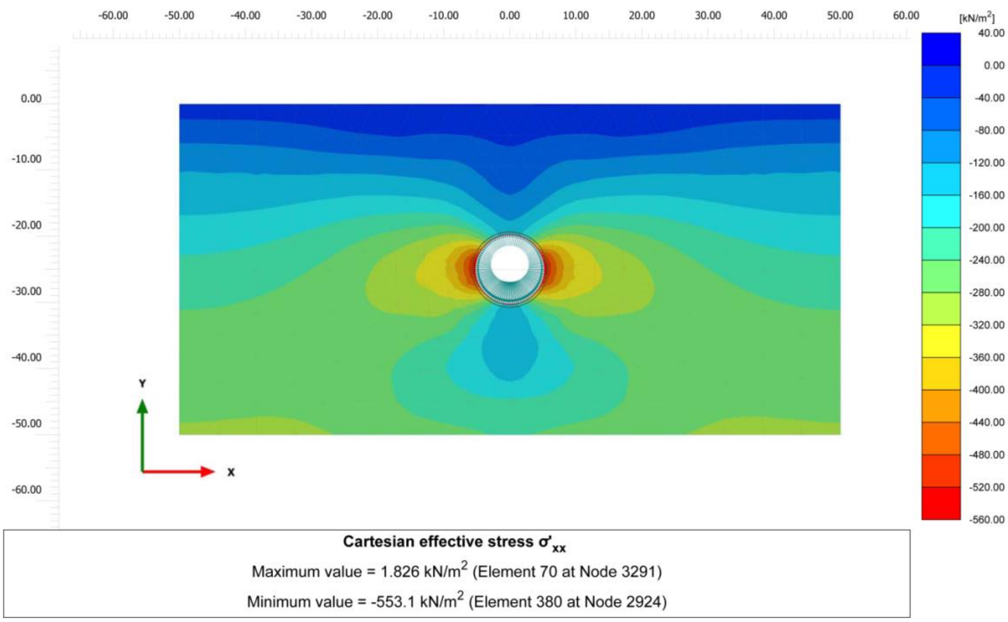

Figure 6.30: Horizontal effective stresses following a fully recovered concentric aeral contraction of 2% ($E_{50,ref}$ = 40 MPa)

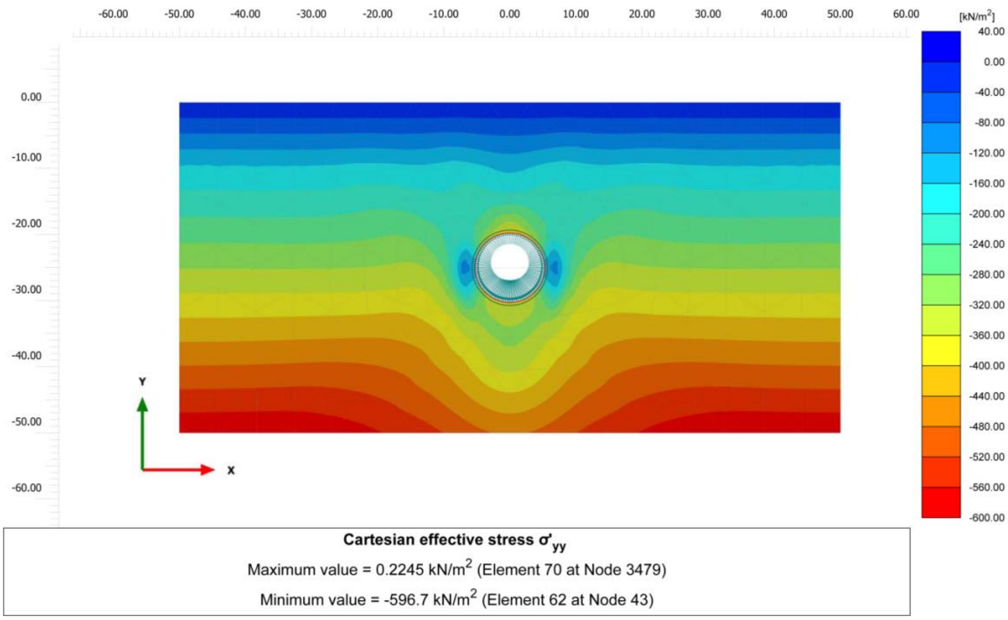

Figure 6.31: Vertical effective stresses following a fully recovered concentric aeral contraction of 2% ($E_{50,ref}$ = 20 MPa)

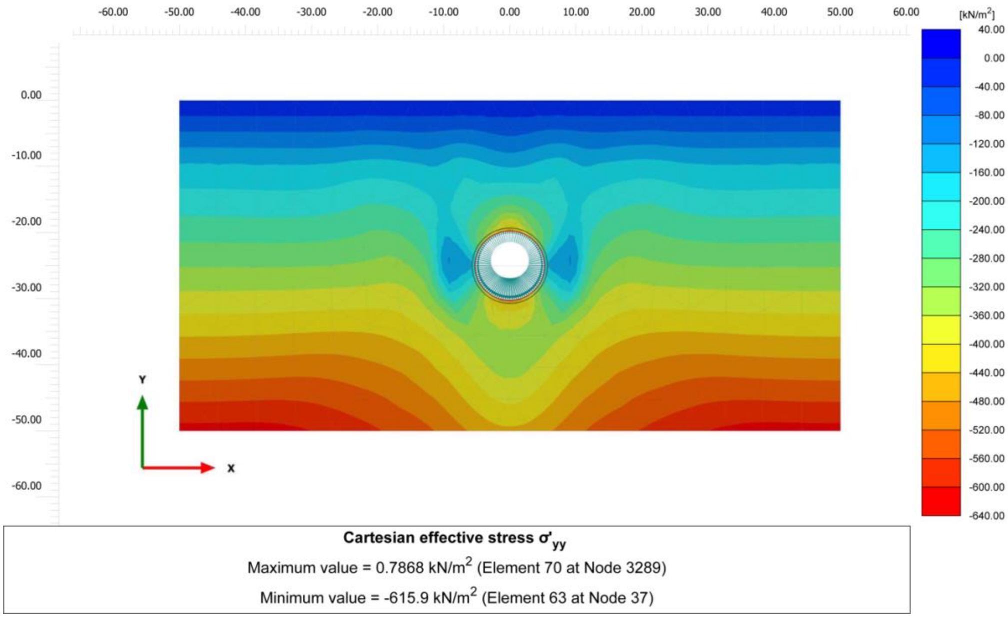

Figure 6.32: Vertical effective stresses following a fully recovered concentric aeral contraction of 2% ($E_{50,ref}$ = 40 MPa)

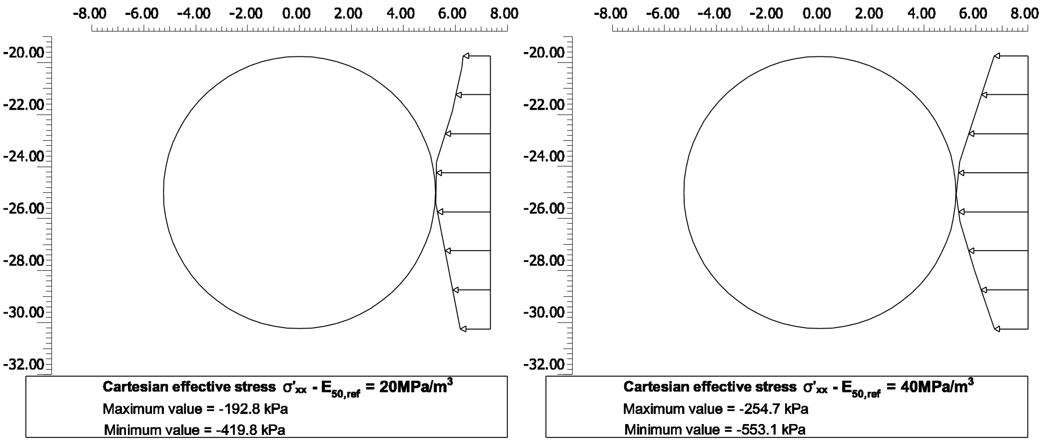

Figure 6.33: Effective stresses on a vertical line tangent to the tunnel with fully recovered concentric aeral contraction of 2%

6.4.3.2 Dependency of the soil-reaction curves from the soil stiffness in anti-symmetric conditions

The second applied deformation is a 50 mm leftward shift then compensated with the repositioning of the tunnel into its initial place (Figures 6.34 and 6.35). The vertical movement of the tunnel is locked. The FE model indicates that the final horizontal effective stress at the tunnel spring level – right-hand side – is -315 kPa for the softer soil and -477 kPa for the stiffer one. At the left-hand side, the soil stress is -131 kPa and -108 kPa with soft and stiff soil, respectively.

The resultant horizontal force is estimated accounting for the normal effective stresses acting at opposite sides of the tunnel. That is done by integrating the horizontal effective soil stresses over two vertical lines tangent to the tunnel at opposite sides and with length equivalent to the tunnel diameter. The effective soil stresses on those lines are shown in Figures 6.36 and 6.37 for soft and stiff soil, respectively.

The resultant horizontal force is calculated as:

$$\Delta\overrightarrow{T_{20}} = \sigma_{xx,20,avg,left} \times h \times w - \sigma_{xx,20,avg,right} \times h \times w = 137 \times 10.51 \times 10.235 - 271 \times 10.51 \times 10.235 \cong -14.4\ MN \quad (6.7)$$

where $\Delta\overrightarrow{T_{20}}$ was the hypothetical resultant transversal force, $\sigma_{xx,20,avg}$ the average horizontal effective stress correlated with the particular loading pattern, h the height of the side projection of the TBM-shield, and w the length of the same projection. For the stiff soil the same expression led to:

$$\Delta\overrightarrow{T_{40}} = \sigma_{xx,40,avg,left} \times h \times w - \sigma_{xx,40,avg,right} \times h \times w = 116 \times 10.51 \times 10.235 - 392 \times 10.51 \times 10.235 \cong -29.7\ MN \quad (6.8)$$

The difference between $\Delta\overrightarrow{T_{40}}$ and $\Delta\overrightarrow{T_{20}}$ amounts to about 15 MN. Should the described applied displacement occur in practice, a wrong estimate of the elastic modulus of a factor 2 would lead to such error in the transversal equilibrium of the shield.

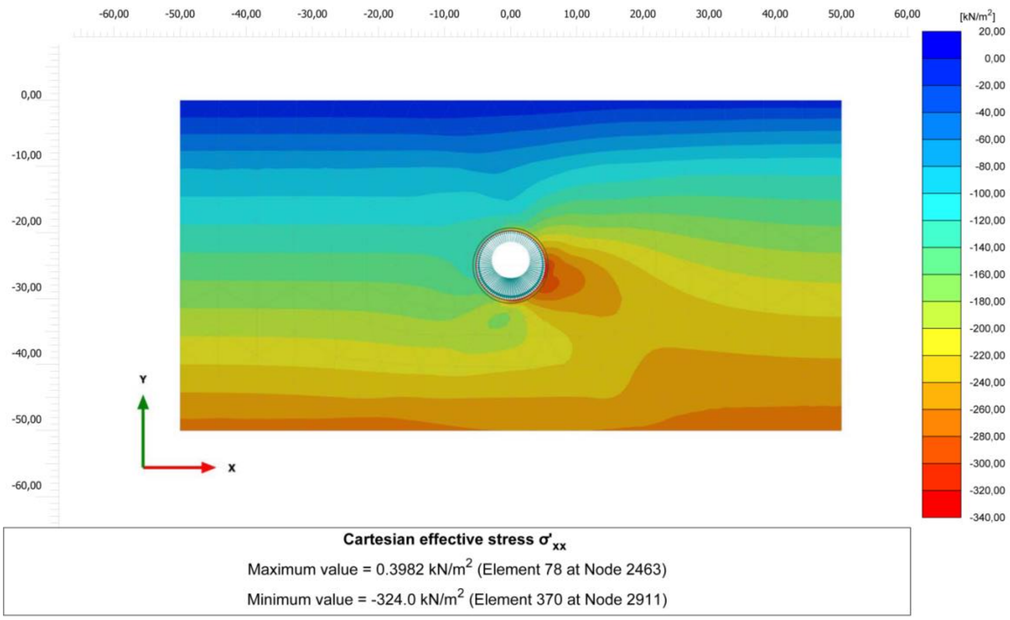

Figure 6.34: Horizontal effective stresses following a fully recovered leftward shift of 50 mm ($E_{50,ref}$ = 20 MPa)

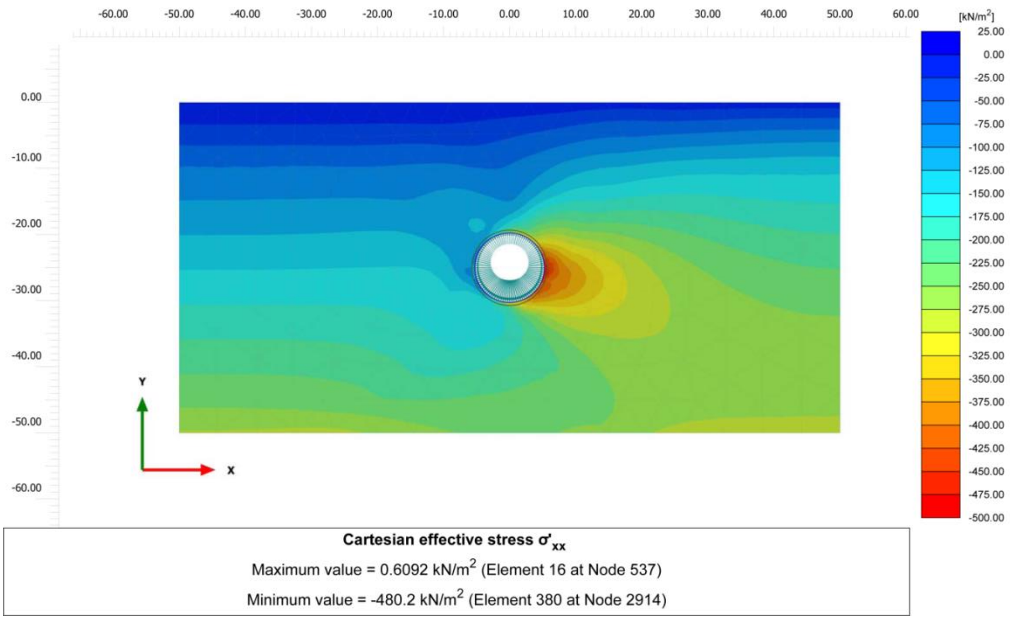

Figure 6.35: Horizontal effective stresses following a fully recovered leftward shift of 50 mm ($E_{50,ref}$ = 40 MPa)

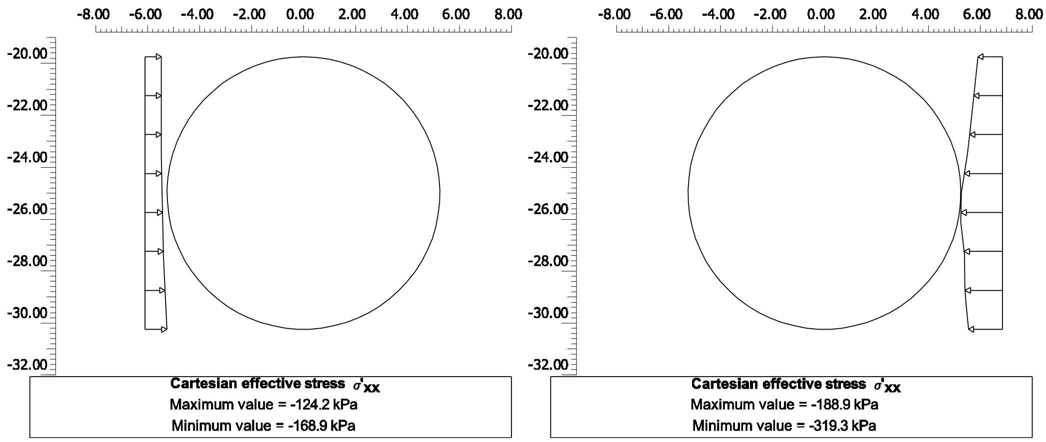

Figure 6.36: Horizontal effective stresses following a fully recovered leftward shift of 50 mm ($E_{50,ref}$ = 20 MPa) on two vertical lines tangent to the spring points of the tunnel

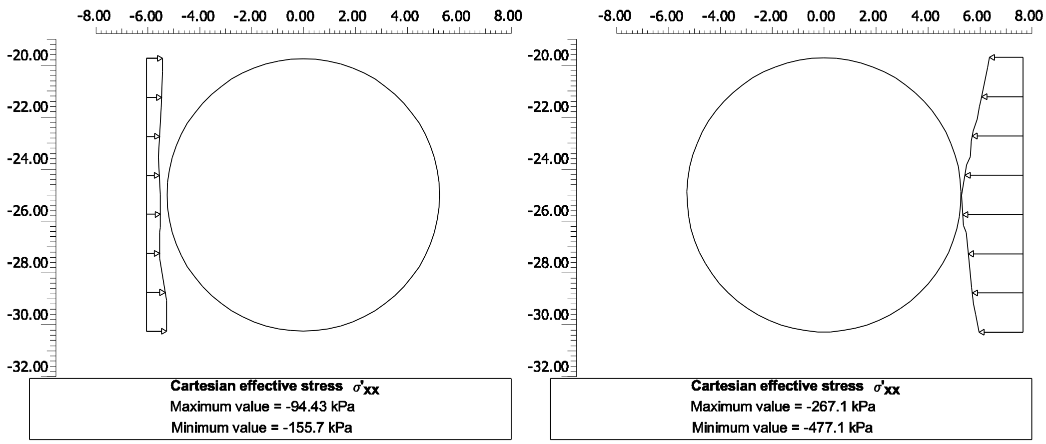

Figure 6.37: Horizontal effective stresses following a fully recovered leftward shift of 50 mm ($E_{50,ref}$ = 40 MPa) on two vertical lines tangent to the spring points of the tunnel

6.4.4 On the simplified approach to the tail-void grouting process

The concept of a lower cut-off was introduced for the normal stresses at the shield-soil interface (Section 6.4.2.2). The cut-off expedient aims to simulate the potential of the pressurized process fluids (face support slurry and tail-void grout) to infiltrate around the shield and preserve the original stress state without allowing soil relaxation to occur. The potential risk of such simplification is to misrepresent the stress state in the soil-relaxation sectors, particularly to overestimate it, when the grouting pressure is not sufficient to compensate for the kinematic relaxation, or underestimate it, when the grouting pressure is particularly high and therefore able to more than compensate the soil relaxation due to kinematic effects.

The effect of the grouting pressure on the stress state around the shield is modelled more explicitly though with a number of simplifying assumptions listed hereafter:

- the tail-grout is assumed able to penetrate the tail void between the shield-skin and the surrounding soil but not able to change its width. The surrounding soil is in other words assumed stiff irrespective of the injection pressure and the width of the kinematic inter-space is also not affected by it;
- the injected grout is modelled like a Bingham fluid, therefore with a non-zero shear strength. An important consequence is the capability of the grout mortar to withstand pressure gradients to some extent even without flowing;
- the grout is able to "flow" along the shield skin in longitudinal direction only. The fluid pressures between adjacent longitudinal flow lines are set to be independent;
- the physical properties of the grout are assumed stable in time, with disregard for consolidation and (possible) hardening;
- the grout pressure is assumed to drop from the shield tail towards the shield front according to the expression

$$\Delta P = \propto \frac{\Delta x}{s} \tau_y \tag{6.9}$$

where ΔP is the pressure change, $\propto$ a parameter equal to 1 if only the shear resistance between grout and soil is considered and 2 if also the shear with the tunnel lining is taken into account, Δx the length increment along the TBM, s the interspace width between the TBM-shield and the soil and τ_y the yield strength of the grout (Bezuijen [1]);

- the grout penetration around a certain radial sector of the shield is only possible when soil extension is present at the shield tail at that specific radial position. This condition is consistent with the hypothesis that the infiltrating grout could not enlarge existing interspaces but only influence the pressure in them.

For calculation purposes the shield is subdivided in 50 times 180 sectors in longitudinal and radial direction, respectively, for a total of 900 sectors. Each sector is approximately a 0.20 by 0.20 m square. The grout pressures in the tail gap are derived from the pressures measured in the injection lines. Two approximation steps are required, the first on the pressure drop occurring in the injection lines between the point of measurement and the opening, and the second concerning the pattern of the grout pressure in the tail-void annulus. The pressure drop in the injection lines was assumed constant and equal to 100 kPa. That is based on preliminary observations at another tunnelling project where the TBM had similar features and the pressure drop was measured (Amsterdam North-South metro line, private communications [36]). Further information on the type of grout employed in the two projects was not available. Determining the pattern of the grout pressure in the tail-void annulus was somewhat more articulated.

6.4.4.1 Grout pressure distribution in the tail-void annular gap

The four grout openings 1, 2, 5 and 6 are located at 35°, 85°, -85° (or 275°), and -35° (or 325°), respectively (Figure 6.38). Angles are measured from top and positive in clockwise direction. The path of the grout pressures in the tail gap could have been obtained through the linear interpolation of the known values at the four locations. However, such assumption would have disregarded both the hydrostatic effect and the non-newtonian behaviour of the grout, in particular its capability to withstand pressure gradients without flowing.

The hydrostatic effect is taken into account by adding or subtracting a hydrostatic component to linearly interpolated values between pairs of openings at the same height (1 and 6, and 2 and 5). For example, in the interpolation between openings 2 and 5, that is over the interval 85° ÷ 275°, the hydrostatic pressures contribution is added by accounting for the height difference. The corrective factor ranges between 0 at 85° and 275° to a maximum of 106.8 kPa at 180° and was obtained as

$$\left[\sin\left(\frac{\vartheta-90}{180}\times\pi\right)+\sin\left(\frac{5}{180}\times\pi\right)\right]\times R\times\gamma_g=\left[\sin\left(\frac{90}{180}\times\pi\right)+\sin\left(\frac{5}{180}\times\pi\right)\right]\times 5.1725\times 19=106.8\ \text{kPa} \tag{6.10}$$

in which ϑ indicates the current radial position, R the radius of the annular gap, and γ_g the specific weight of the grout mortar. A similar approach is adopted over the interval 325° ÷ 35°, in which the hydrostatic correction is subtracted instead. The result of the correction for hydrostatic effect is shown in red in Figure 6.38.

The non-newtonian behaviour of the grout mortar requires considering an additional pressure gradient in the interpolation between injection openings at the same height. Considering for example the interval 85° ÷ 275°, the grout presumably flowed from both openings 2 and 5 towards the tunnel bottom and that took place at the cost of a pressure drop. The gradient of the linear interpolation between the pressures in injection lines 2 and 5 is

$$\frac{p_{275}-p_{85}}{275-85}=\frac{572.2-582.4}{190}=-0.0537\ \text{kPa/°} \tag{6.11}$$

That is corrected for the gradient due to the rheological properties of the grout. With reference to Equation (6.9), the pressure drop in the tail gap is estimated at 12.90 kPa/m (1.1657 kPa/°), in which s = 0.155 m, τ_y = 1 kPa, and α = 2. Figure 6.38 shows the correction for the Bingham behaviour. The combined result of linear interpolation between monitored values, hydrostatic effect, and Bingham behaviour is shown in the same figure.

It is observed how closely the purple line matches the dot-dashed one, which in turn represents the linear interpolation between monitored values over the interval 85° ÷ 275°. This hints to a self-compensation between hydrostatic effect and non-newtonian behaviour, at least within the limits of the model, of the geometry, and of the selected parameters.

The pressure trend over the sectors 35° ÷ 85° and 275° ÷ 325° is assumed linear although that might not represent reality with full accuracy. The pressure distribution obtained through the procedure outlined above is assumed as the boundary condition for the process of grout penetration in the tail void between shield and soil.

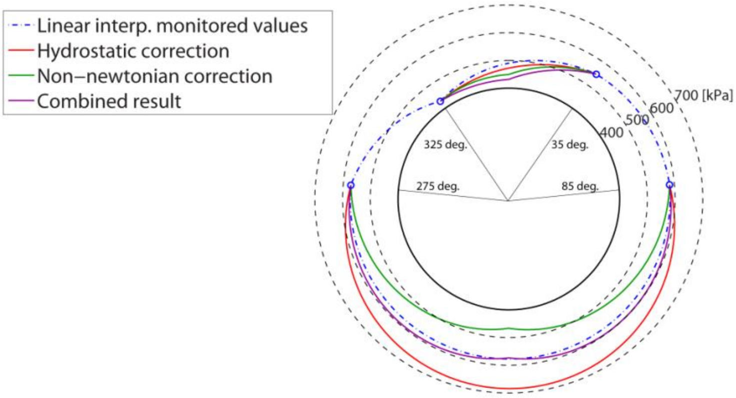

Figure 6.38: Example of grouting pressure distribution over the annular gap

6.4.4.2 Processing of the grouting-pressure fluctuations

During the investigation concerns arose on how well the grout pressure measured in the injection lines represents those present in the tail gap. The grouting pressure in the lines fluctuated considerably (Figure 6.39). Two types of fluctuation are distinguished, each appreciable at a different scale. The first one, due to the use of stroke pumps, shows up through the scattering of the signal and is visible at a small scale. Fluctuations of this kind occurred every few millimetres of advance. The second level of fluctuation is visible at a larger scale such as the drive for one ring.

Both phenomena raise concerns. The narrower fluctuations, consequence of the use of stroke pumps, could be treated like noise and the average value between adjacent peaks and lows represents a good approximation. The pressure trends at larger scale are more complex to tackle.

Let’s consider the example in Figure 6.39. The pressure values 180 and 500 kPa represent the average pressure value at advances -644 and -642.5 m, respectively. However, should one adopt exactly 180 and 500 kPa as boundary conditions for the modelling of the grout penetration at their matching advance, it would implicitly assume that the grouting pressures applied before that point do not play any role. However this hardly reflects reality.

Let’s take the case of a shield advance of several metres characterized by high grouting pressures, then followed by a sudden drop of the pressure itself. Were the new boundary condition only determined by the newly established low grouting pressure, a sudden change in the stress distribution over the entire infiltrated sector would need to follow. But such response must be rejected as it would fit to the case of an incompressible fluid penetrating into a non-deformable volume, and that is clearly not the case here.

To circumvent that a representative value over the last 2 m of advance is chosen instead of assuming the grout pressure at the current advance only. The arithmetic average of the highest 10% injection pressures during the last 2 m of advance is calculated and adopted as boundary condition. At times, the arithmetic average of all observed injection pressures is adopted instead. Only the pressures monitored during actual advance are considered.

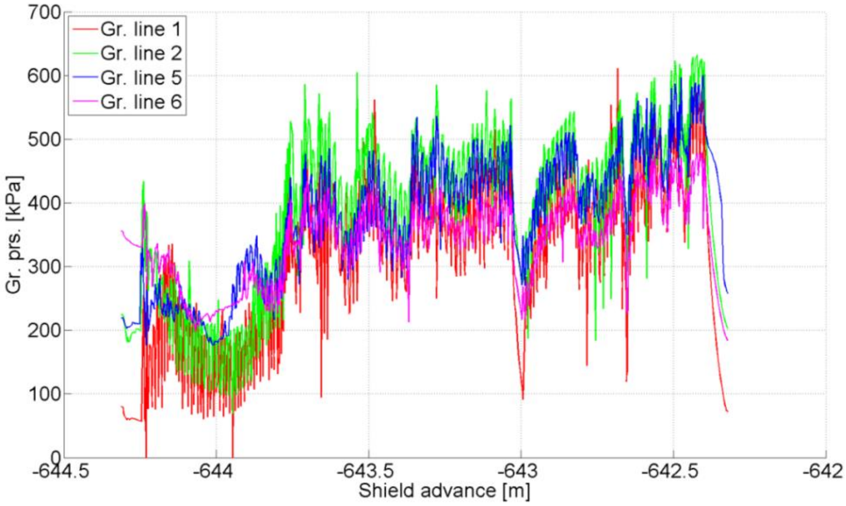

Figure 6.39: Detailed grouting pressures – Ring 503 south alignment

6.4.4.3 An example of the grout injection effect on the interface normal stresses

The model provides a pronounced transversal unbalance for instance at advance -834.815 m at which a pronounced unbalance is observed. The grouting pressures over the last two meters of advance are shown in Figure 6.40, in which the average values of the highest 10% monitored pressures are indicated. The average values are then lowered by 100 kPa due to the losses in the injection lines (Section 6.4.4), and then interpolated over the tail-gap circumference. Corrections for hydrostatic effect and yield strength of the grout are also taken into account (Section 6.4.4.1).

Figures 6.41a and 6.42a show the distribution of the normal total stresses acting on the TBM-shield when the grout penetration is not taken into account, meanwhile the b) parts include the contribution of the grout penetration. The colours are calibrated such that red corresponds to a pressure of 700 kPa and blue to 0 kPa (RGB scale). In the example the maximum pressure is 486 kPa and the minimum one 190 kPa. The difference between normal stress distribution without and with grout penetration can be appreciated for instance at the left-hand side of the shield (seen in Direction Of Drive or DOD). When the grout infiltrates the tail void between the shield and the soil, higher normal stresses originate in the infiltrated sectors. The infiltrating grout produces also larger normal stresses at the shield bottom, particularly in the region of the tail, but that will be discussed when dealing with the vertical equilibrium (Section 6.5).

The redistribution of the normal stresses affects the equilibrium of forces. When the contribution of the infiltrating grout is not considered, the shield is subject to a leftward unbalance of -12.87 MN (see also Figure 6.28 at advance -834.815 m). When grout penetration is considered, the transversal unbalance reduces to -7.72 MN. The order of magnitude of the transversal effect induced by the infiltrating grout is of the same order of magnitude as the transversal unbalance in the simplified model with the grout effect excluded. This proves that the grout around the shield has the potential to influence the transversal equilibrium of the TBM.

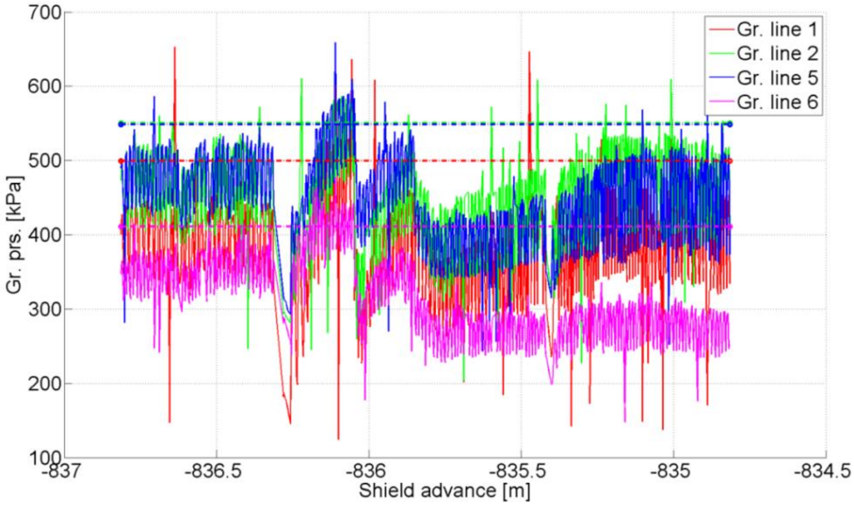

Figure 6.40: Monitored grouting pressures – Advance -836.815 / -834.815 m south alignment.

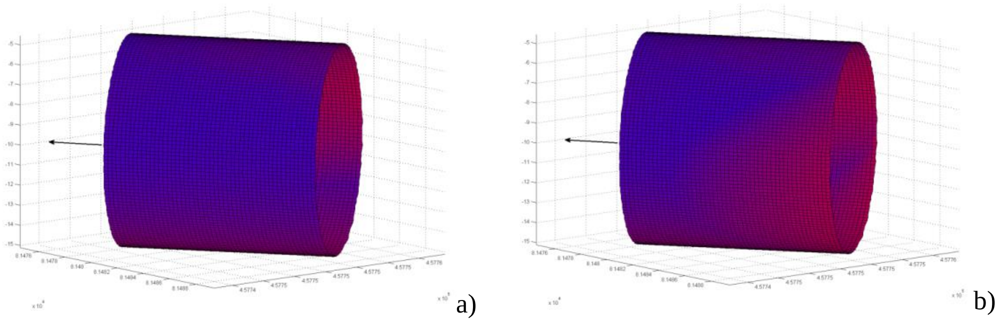

Figure 6.41: Total normal stress distribution without and with grout penetration. Advance -834.815 m south alignment. Left-hand side. Colour calibration: red = 700 kPa; blue: 0 kPa

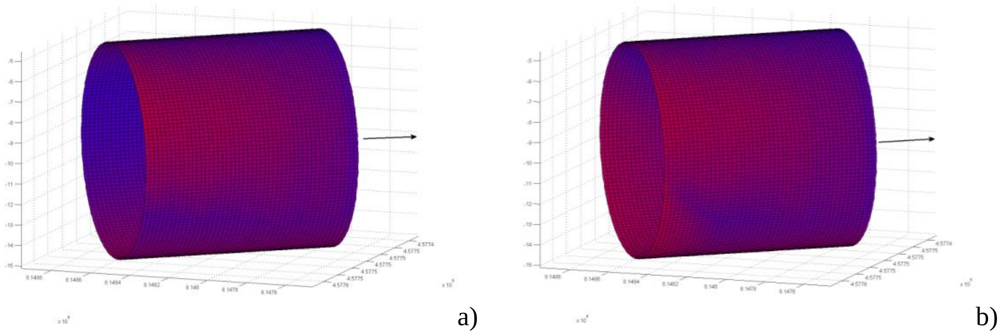

Figure 6.42: Total normal stress distribution without and with grout penetration. Advance -834.815 m south alignment. Right-hand side. Colour calibration: red = 700 kPa; blue: 0 kPa

6.4.5 Review of the transversal equilibrium at selected advance locations

The study of the transversal behaviour continues with the introduction of a number of example locations at which transversal equilibrium was not satisfactorily achieved with the simplified model, that is without considering the effect of grout penetration. At each location several parameters concerned with the transversal balance and response are presented and commented. The aim of such review is to present a more complete although not conclusive overview on a number of configurations encountered in practice and to discuss how the role of the grout injection appears determinant of the transversal equilibrium.

The examples are introduced in order of advance according to the direction of drive. The main characteristics of each configuration are summarized in Table 6.1. The table reports the location of the stretch under investigation, the direction of transversal unbalance, the amount of unbalance without and with grout penetration taken into account, and a very short summary of the peculiarities of each specific case.

Table 6.1: Summary results transversal equilibrium

Interval [m]	Direction of initial unbalance	Transversal unbalance (without grouting) [MN]	Unbalance after corrections [MN]	Description
-1320 ÷ -1260	leftward	-19.33	-4.48	Re-calibration of the positioning system. Adjustment of the boundary grouting pressure due to a local low in the monitored values
-820 ÷ -780	leftward	-10.27	+4.14	Grouting pressures and shield’s transversal reactivity
-710 ÷ -660	leftward	-9.41	+1.21	Grouting pressure and shield’s transversal force

6.4.5.1 Advance interval -1320 ÷ -1260 m

The horizontal tendency and absolute deviation of both reference points varied considerably over the interval -1310 ÷ -1260 m (Figure 6.45). However, such variations are not accompanied by equally large changes in the vertical driving moment (Figure 6.44). The reason is instead sought for in the tail-void grouting process and in the precision of the shield positioning system. The latter is examined first.

At advance -1278.068 m a rightward shift affected both RPF and RPR (Figure 6.45). The cause of such shift is not totally clear, but most likely a realignment of the positioning system occurred there. The sudden horizontal rightward shift is interpreted by the numerical model as a sharp increase of the compression at the right-hand side and of the extension at the left-hand one. This combination leads to a sudden increase of the resultant horizontal force in leftward direction.

The graph in Figure 6.48 shows that the increase is in the order of 5 ÷ 7 MN. Without terms of comparison we tend not to believe that the rightward shift actually occurred and that subsequently the horizontal resultant force jumped. Most probably the calibration of the positioning system deteriorated progressively and the error was finally detected at that specific location. In other words, the idea is that the shift took place progressively, but that it was measured all at a time. As this kind of events occurred quite regularly along both tunnel tubes, at least according to the monitoring data, special attention is recommended when analysing the transversal equilibrium in such proximities.

Graphs such as that in Figure 6.48 were first introduced in Section 6.4.2.2 and show the calculated transversal equilibrium without accounting for the effect of grout penetration. Advance -1276.123 m appears particularly suitable for analysing the consequence of such simplification. In Section 6.4.4.2 it was stated that the arithmetic average of the highest 10% monitored pressures over the last 2 m of advance may represent well the grouting pressure. However, Figures 6.46 and 6.47 show that over the sector -1280 ÷ -1275 m the grouting pressures were significantly lower than before and after that. Therefore, the transversal equilibrium at advance -1276.123 m would end up being very little influenced even if the infiltrating grout were taken into account.

That is confirmed by the comparison between Figures 6.49 and 6.50. The horizontal leftward unbalance amounts to -19.33 MN when no grout penetration is taken into account (Figures 6.49a and 6.50a). When penetration is considered the transversal unbalance is reduced to -16.73 MN (Figures 6.49b and 6.50b) instead, with a correction of only 2.60 MN. This result is obtained by applying the usual rules of pressure averaging over the last 2 m and of 100 kPa pressure loss in the injection lines.

However, as observed the grouting pressures over the sector -1280 ÷ -1275 m were particularly low and incidentally the 2 m averaging sector happened to be entirely included in that sector. To compensate for such coincidence the grout pressures in the tail-void were arbitrarily increased by 100 kPa, which was equivalent to not accounting for the 100 kPa pressure loss in the injection lines. The transversal unbalance is in this way further reduced to -11.48 MN, with a correction of 7.85 MN.

Adding up the error given by the re-calibration of the positioning system (5 ÷ 7 MN) and that due to not accounting for the tail grout penetration (2.60 ÷ 7.85 MN) a considerable rate of the initial transversal unbalance is then justified (7.60 ÷ 14.85 MN). That shows that a decent transversal equilibrium can be found even in such unfavourable conditions, as shown in the pie-chart in Figure 6.43. Improved equilibrium is obtained by applying corrections for the effects of grout penetration around the shield and to counter the effects of the re-calibration of the shield positioning system.

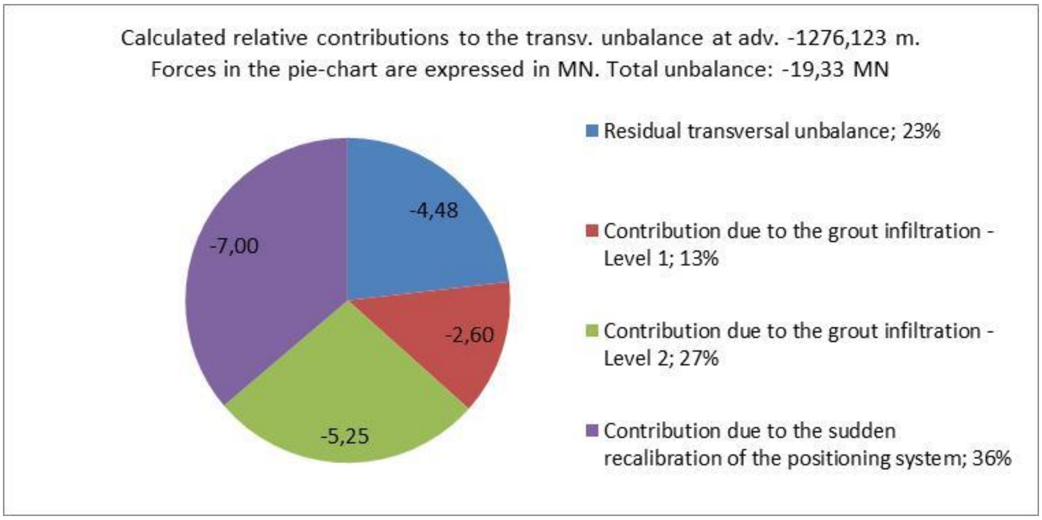

Figure 6.43: The residual transversal unbalance is obtained by accounting for two levels of correction on behalf of the process of grout penetration and for one level of correction on behalf of the recalibration of the shield positioning system

Figure 6.44: Vertical driving moment – sector -1310 ÷ -1260 m

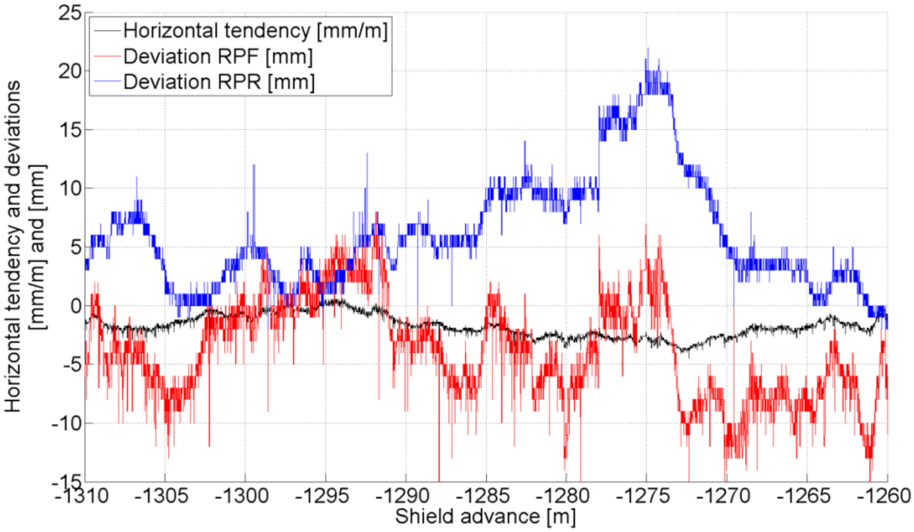

Figure 6.45: Horizontal tendency and deviations of the reference points – sector -1310 ÷ -1260 m

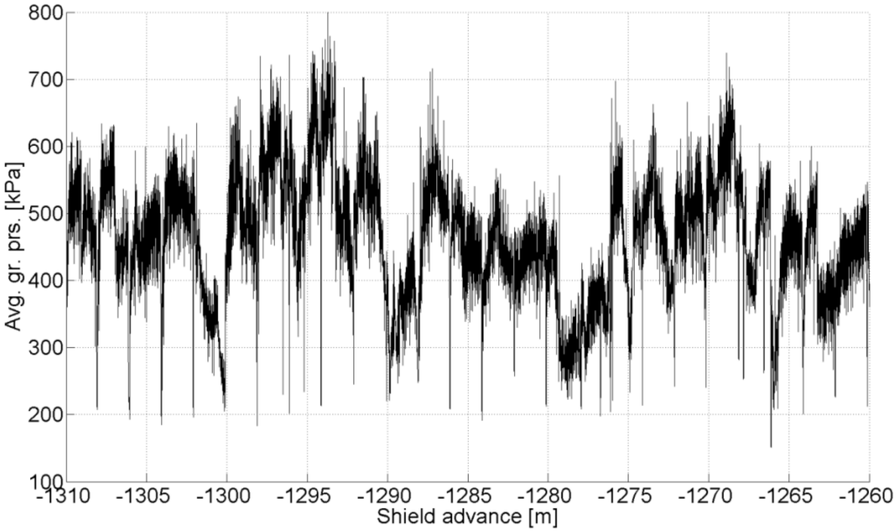

Figure 6.46: Average grouting pressures – sector -1310 ÷ -1260 m

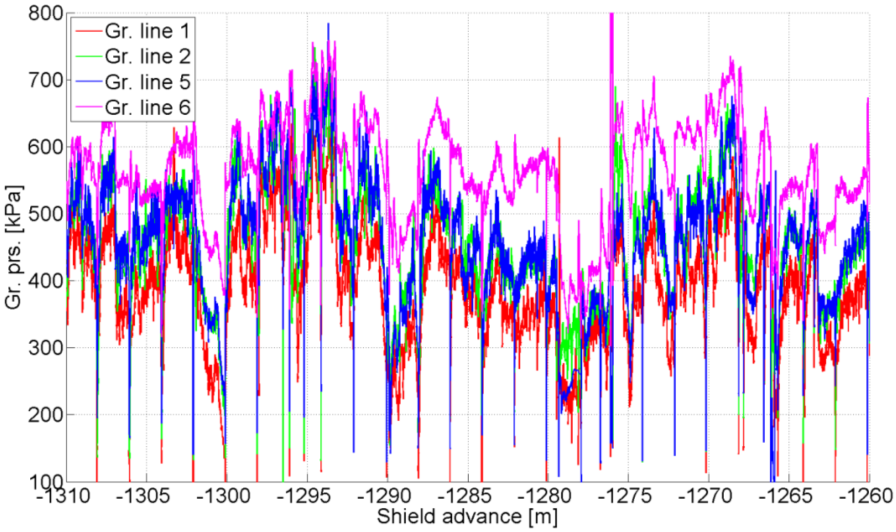

Figure 6.47: Detail grouting pressures – sector -1310 ÷ -1260 m

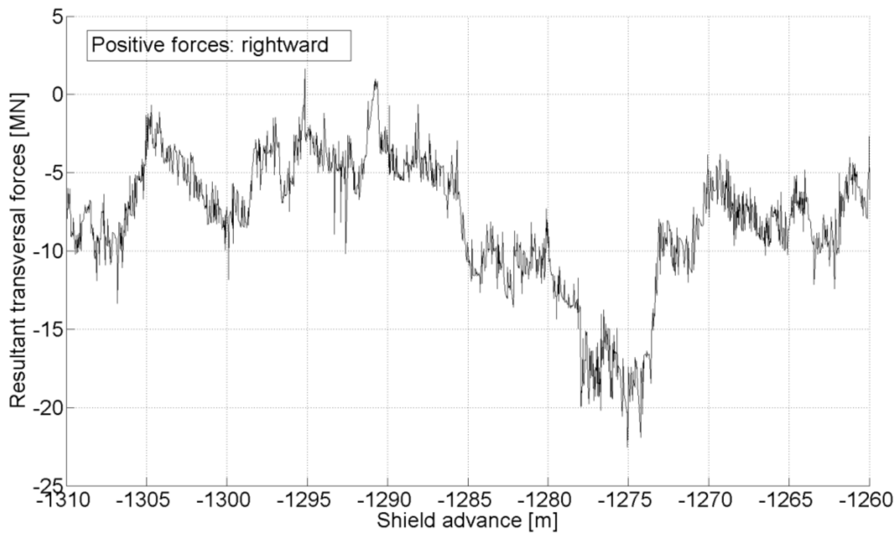

Figure 6.48: Resultant transversal forces – sector -1310 ÷ -1260 m (grout penetration not taken into account)

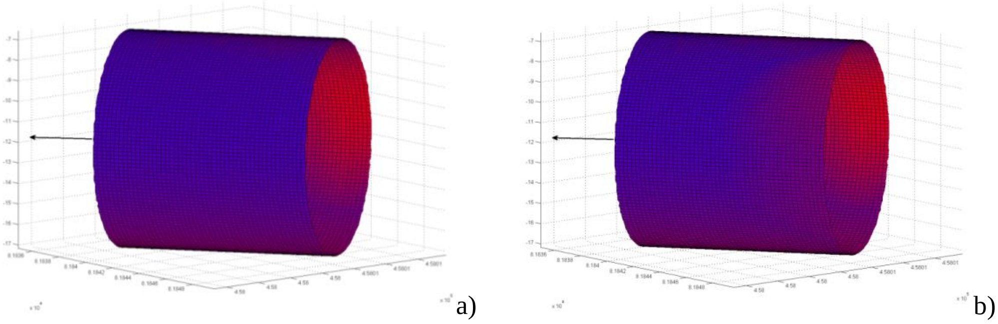

Figure 6.49: Total normal stress distribution without and with grout penetration. Advance -1276.123 m south alignment. Left-hand side. Colour calibration: red = 700 kPa; blue: 0 kPa

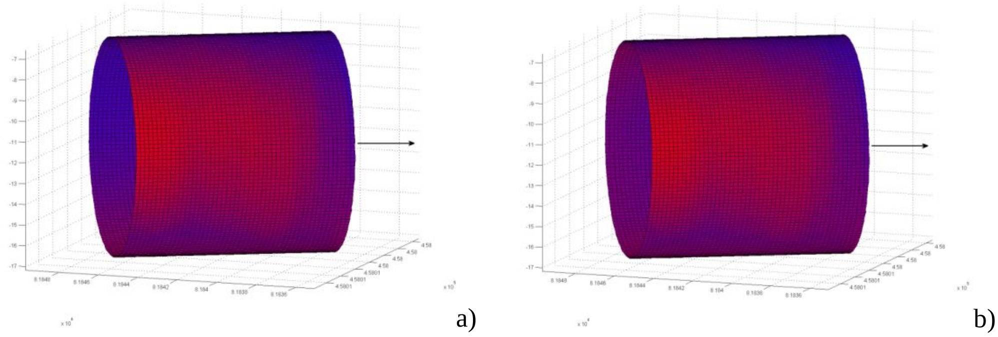

Figure 6.50: Total normal stress distribution without and with grout penetration. Advance -1276.123 m south alignment. Right-hand side. Colour calibration: red = 700 kPa; blue: 0 kPa

6.4.5.2 Advance interval -820 ÷ -780 m

Over the interval -810 ÷ -800 m the vertical driving moment ranges from +20 MNm to -30 MNm (Figure 6.52). The shield horizontal response is, however, not completely consistent (Figure 6.53). For instance, while a considerable negative horizontal tendency was gained when a positive moment was applied (-808 ÷ -806 m), the negative moment applied between -806 and -804 m did not produce the same remarkable and opposite effect. That held at least until advance -804 m, at which a considerable recovery of the horizontal tendency started and continued until -800 m.

The negative tendency at -808 ÷ -806 m was gained through the leftward shift of the RPF and the rightward one of the RPR. Only a modest recovery of the horizontal tendency could be appreciated between -806 and -804 m, but that happened mainly at the cost of a rightward shift of the RPF, with the RPR fixed around +10 mm. Important to recall is that the RPR was located 5.806 m behind the shield face (approximately at the shield’s mid-length). This implies that the rightward shift of the RPF with the RPR fixed in fact describes a rotational movement of the shield hinged on the RPR itself. From advance -804 m onward the RPR started to shift leftward and did so with a rate larger than that of the RPF, thus gaining horizontal tendency.

A possible explanation for such diverse shield response to comparable driving moments (even if with opposite sign) is sought into the tail-void grouting process. Figure 6.54 shows that the average grouting pressure was about 450 kPa over the interval -808 ÷ -806 m (ring 421), increased up to 700 kPa during the following one (-806 ÷ -804 m), and then dropped down to 400 ÷ 500 kPa between -804 and -800 m (rings 423 and 424).

The low injection pressures at ring 421 seem to have facilitated the leftward shift of both reference points. Oppositely, the high injection pressure of ring 422 appears to have constrained the shield movement particularly in the region of the shield-tail. Consequently, the newly applied negative (rightward) driving moment mainly shifted the RPF towards right with little effects on the RPR. However, due to the advanced position of the RPR the shield tail was shifted left approximately the same amount as the RPF moved right producing a sort of rotation around RPR itself.

At ring 423, with lower grouting pressures and persistent negative driving moment, both RPF and RPR moved leftward, the latter more sharply than the former. The increased movement of the RPR is then interpreted as the consequence of the additional manoeuvring room originating in the tail region by the decreased injection pressure. The movement of the RPF is explained instead as the relaxation of the compression accumulated at the shield front – right-hand side – during the drive for ring 422.

Figure 6.55 shows that the grouting pressures were quite well balanced between left and right-hand side. The average value is in this case a good indicator of the overall injection process. The only anomaly are injection pressures about 50 kPa lower in line 6 than in line 1 in the sector -806 ÷ -800 m. However, that did not produce measurable effects.

Figure 6.56 shows an unbalanced transversal configurations in the interval -808 ÷ -804 m. The horizontal resultant of forces, leftward oriented and amounting to -10 ÷ -12 MN, were calculated without taking the grout penetration around the shield into account. The normal total stresses distribution at advance -806.328 m is shown in Figures 6.57a and 6.58a. The same Figures (b) present also the total stresses including the effect of grout penetration. As before (Section 6.4.4.3) the colours are calibrated such that red corresponds to a pressure of 700 kPa and blue to 0 kPa (RGB scale). The difference between normal stress distribution without and with grout penetration can be appreciated for instance at the left-hand side of the shield.

This example demonstrates that the infiltrating grout has the potential to contribute to the transversal equilibrium of the shield, with the resultant of the transversal forces affected by the redistribution of the normal stresses. When the contribution of the infiltrating grout is not taken into account, the shield would be subject to a leftward unbalance of -10.27 MN. When the grout penetration is considered instead, the transversal unbalance is changed into a rightward one of +4.14 MN. The order of magnitude of the transversal effect induced by the grout infiltrating between the shield and the soil is then of the same order of magnitude as the transversal unbalance deriving from the simplified model in which the grout is not taken into account, as shown by means of the column chart of Figure 6.51.

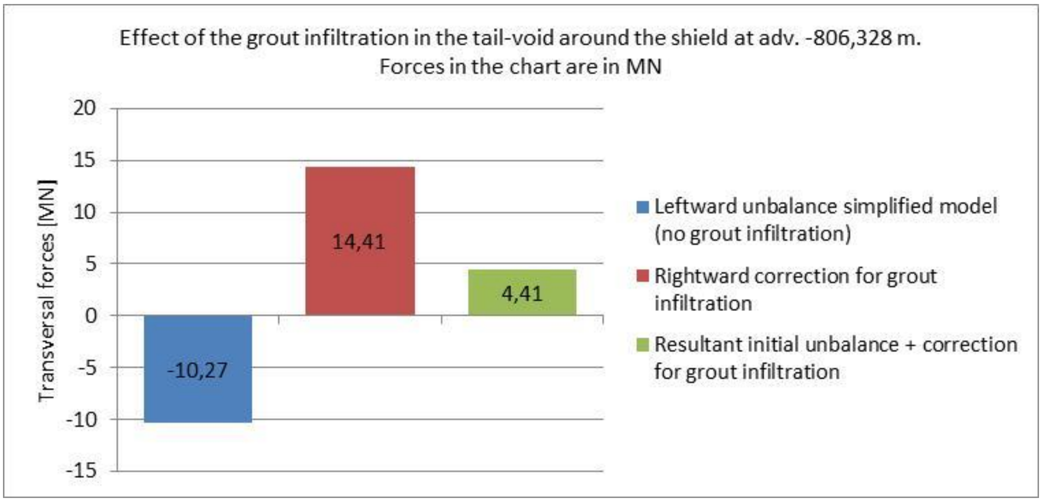

Figure 6.51: The residual transversal unbalance (green) is obtained by combining the unbalance of the simplified model (blue – no grout penetration) with the correction due to the grout penetration in the tail-void around the shield (red)

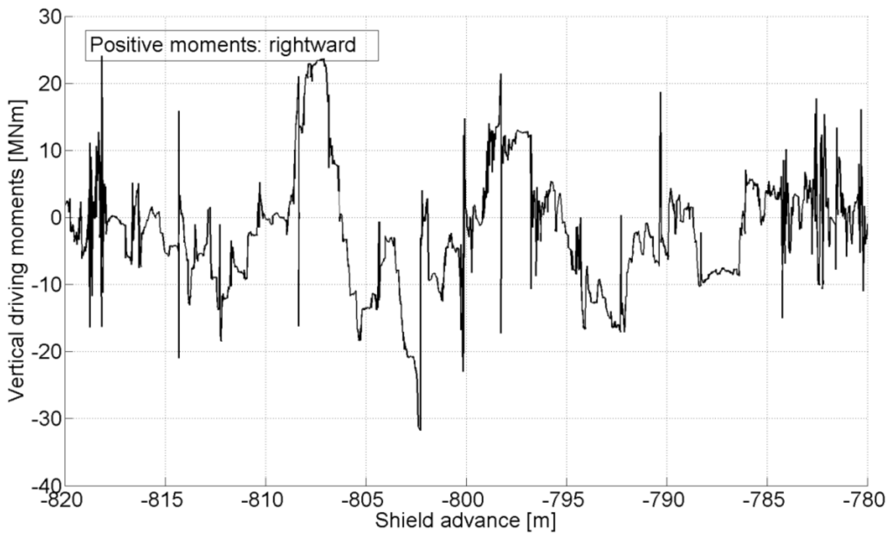

Figure 6.52: Vertical driving moment – sector -820 ÷ -780 m

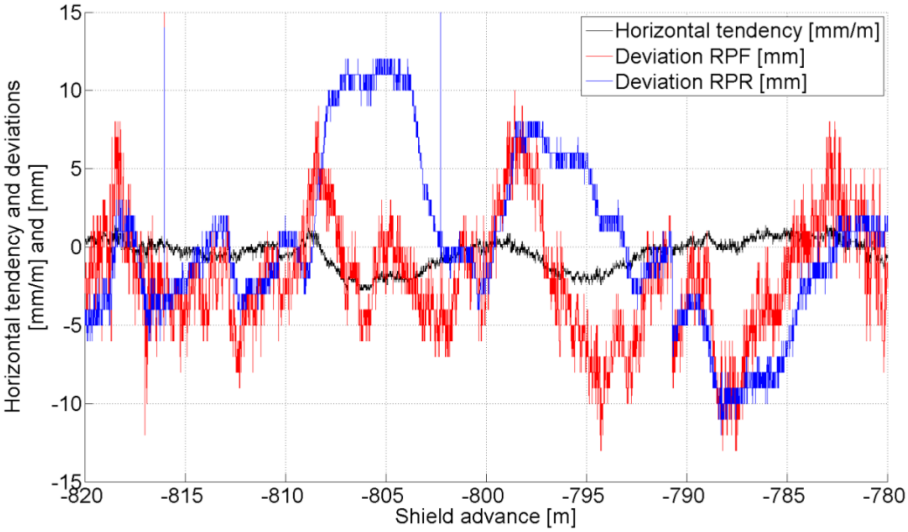

Figure 6.53: Horizontal tendency and deviations of the reference points – sector -820 ÷ -780 m

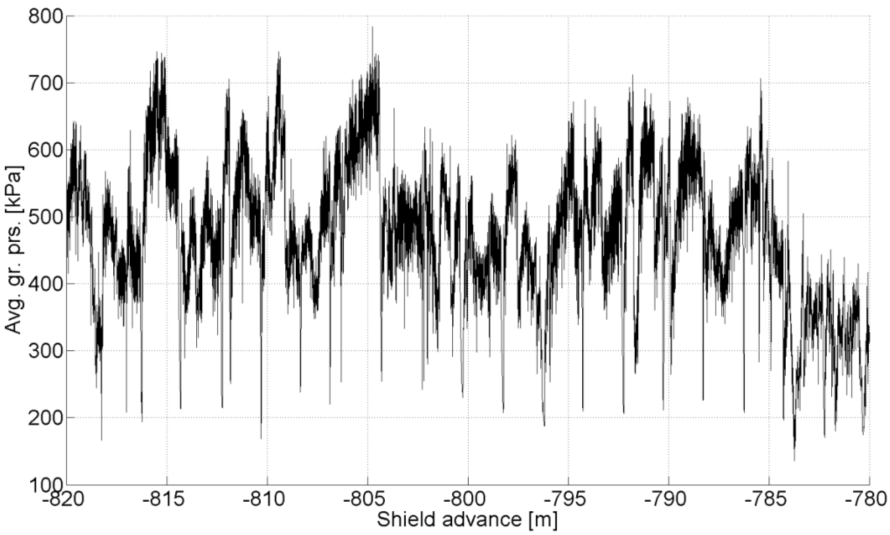

Figure 6.54: Average grouting pressures – sector -820 ÷ -780 m

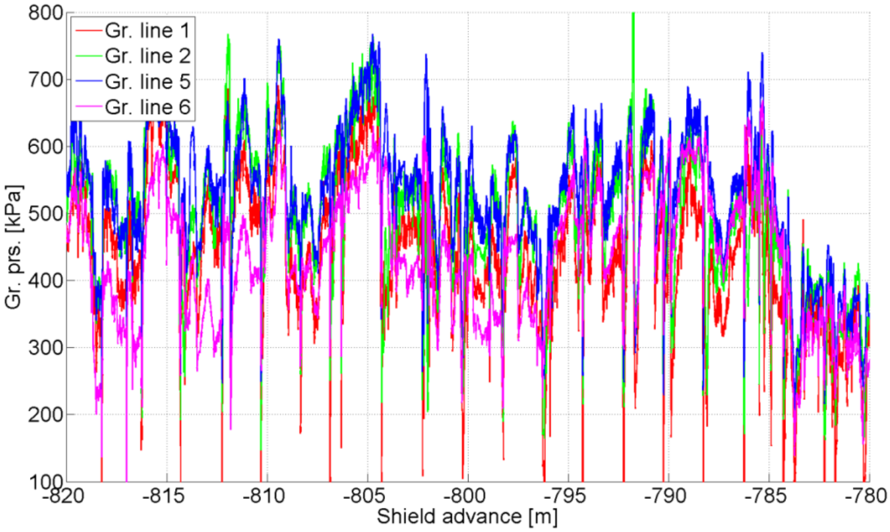

Figure 6.55: Detail grouting pressures – sector -860 ÷ -820 m

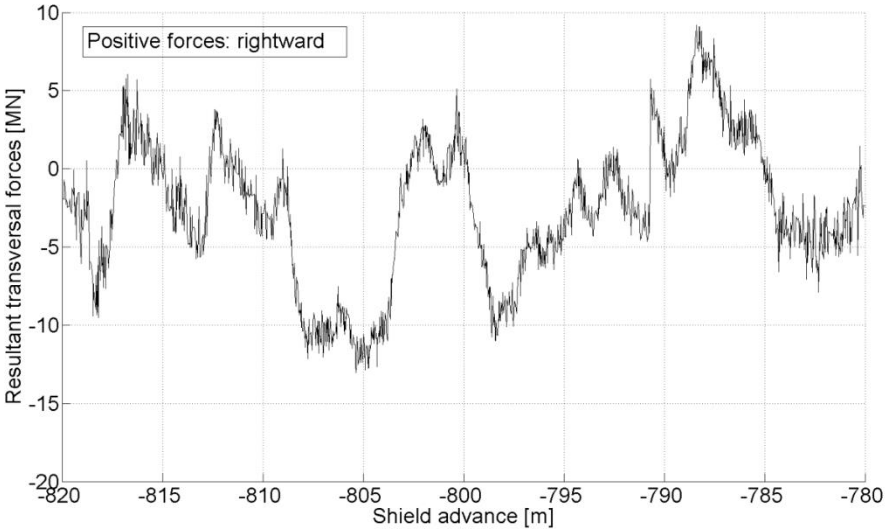

Figure 6.56: Resultant transversal forces – sector -820 ÷ -780 m (grout penetration not taken into account)

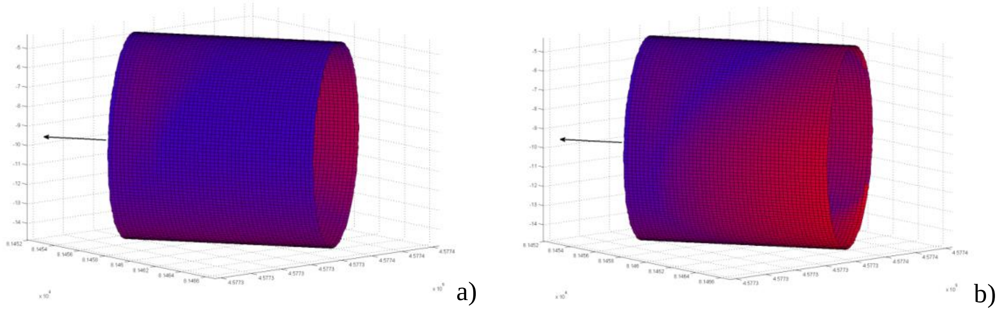

Figure 6.57: Total normal stress distribution without and with grout penetration. Advance -806.328 m south alignment. Left-hand side. Colour calibration: red = 700 kPa; blue: 0 kPa

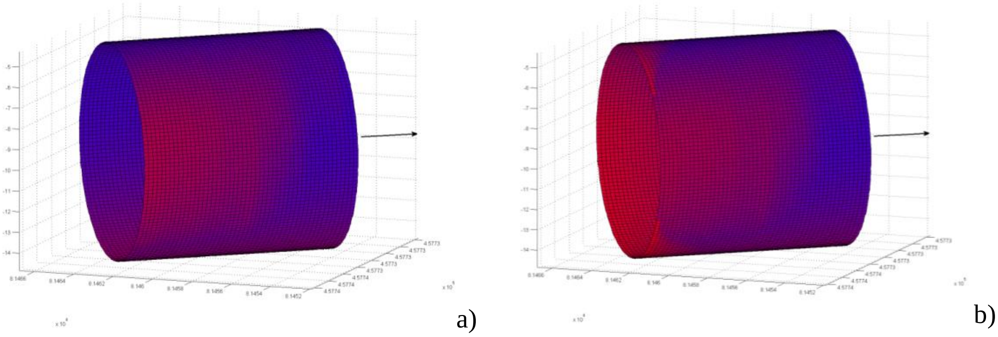

Figure 6.58: Total normal stress distribution without and with grout penetration. Advance -806.328 m south alignment. Right-hand side. Colour calibration: red = 700 kPa; blue: 0 kPa

6.4.5.3 Advance interval -710 ÷ -660 m

The interval -710 ÷ -660 m provided another example that appears to prove that the transversal equilibrium of forces cannot be explained unless the grout penetration around the shield is also modelled. For this aim the shield configuration at advance -680.306 m is selected. The total normal stresses acting on the shield are shown in Figures 6.65 and 6.66.

Figure 6.64 illustrates that at the specified advance the leftward unbalance amounts to -9.41 MN when the infiltrating grout is not taken into account. On the other hand, it can be observed in Figure 6.63 that the grouting pressures are substantially higher at the left-hand side than at the right-hand one over several metres of drive before advance -680.306 m. Implementing also the grouting pressure information into the model the stress distributions of Figures 6.65b and 6.66b are derived, and such new pressure distribution provides a rightward unbalance of +1.21 MN, therefore more than compensating for the previous leftward resultant (see Figure 6.59).

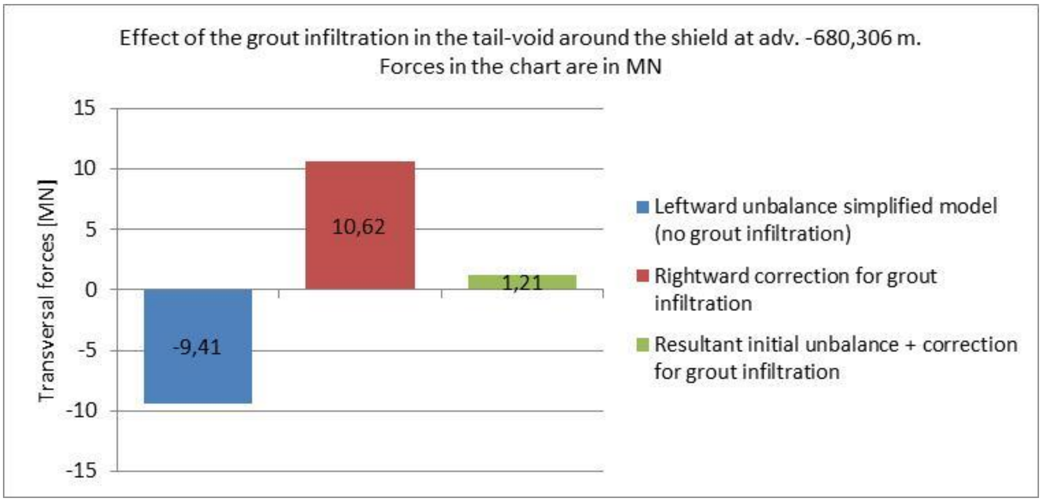

Figure 6.59: The residual transversal unbalance (green) is obtained by combining the unbalance of the simplified model (blue – no grout penetration) with the correction due to the grout penetration in the tail-void around the shield (red)

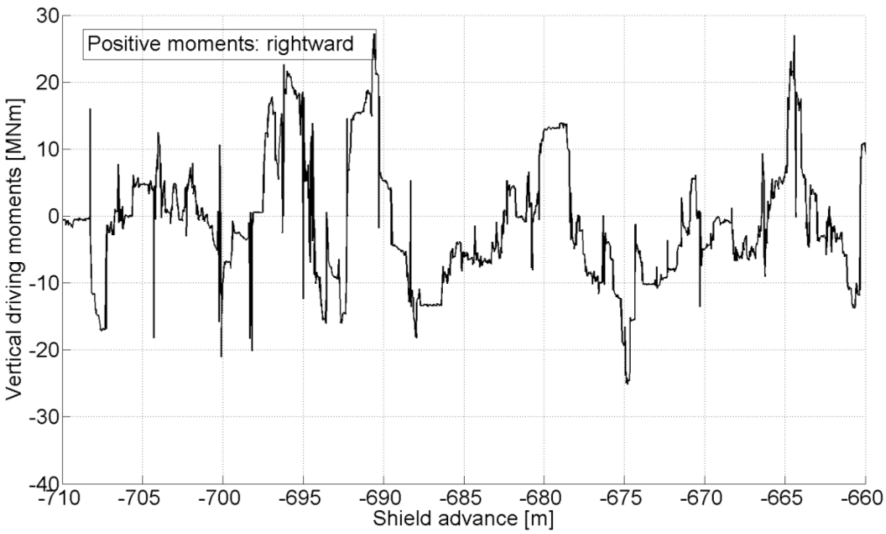

Figure 6.60: Vertical driving moment – sector -710 ÷ -660 m

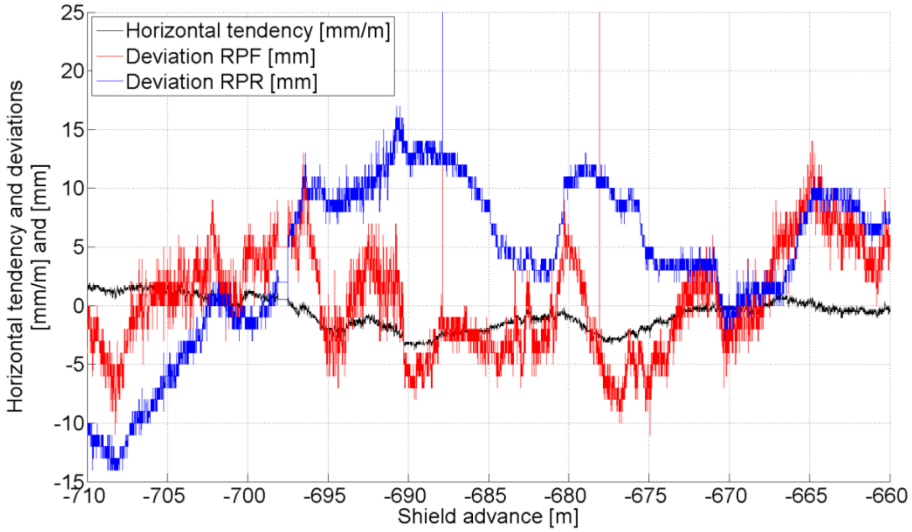

Figure 6.61: Horizontal tendency and deviations of the reference points – sector -710 ÷ -660 m

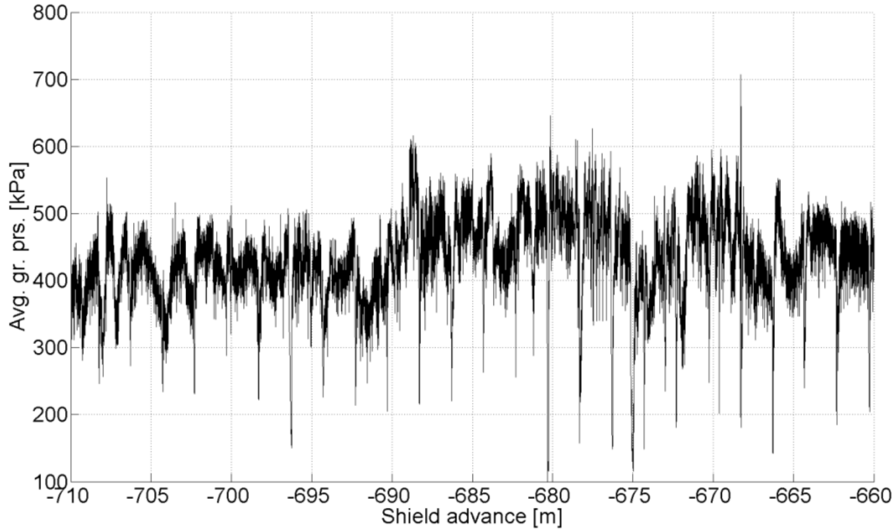

Figure 6.62: Average grouting pressures – sector -710 ÷ -660 m

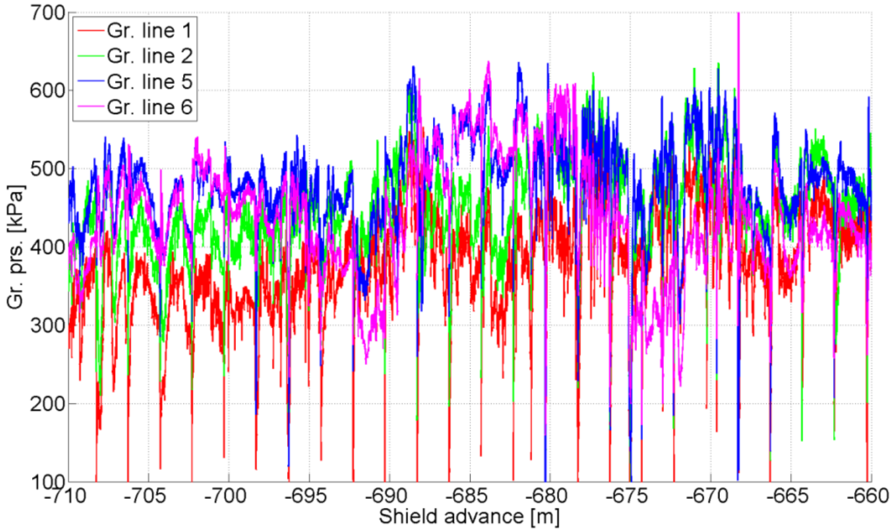

Figure 6.63: Detail grouting pressures – sector -710 ÷ -660 m

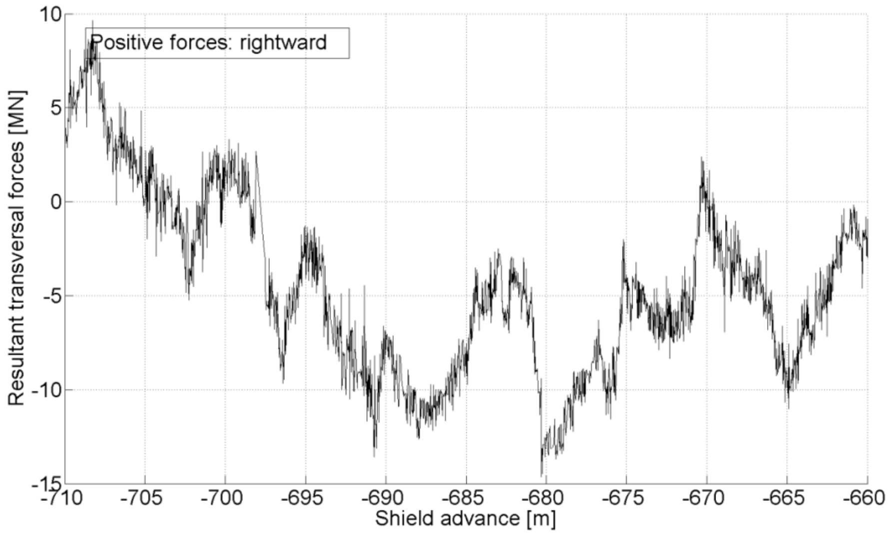

Figure 6.64: Resultant transversal forces – sector -710 ÷ -660 m (grout penetration not taken into account)

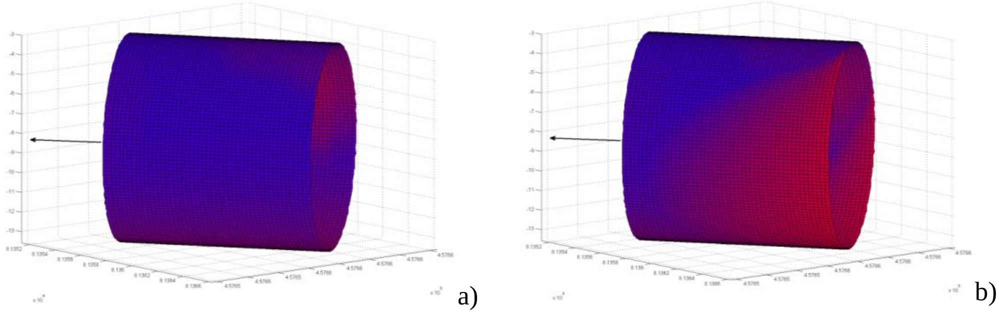

a) b)

Figure 6.65: Total normal stress distribution without and with grout penetration. Advance -680.306 m south alignment. Left-hand side. Colour calibration: red = 700 kPa; blue: 0 kPa

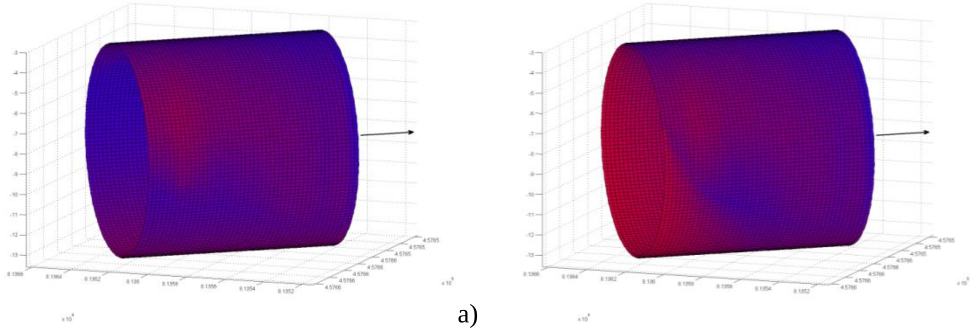

a) b)

Figure 6.66: Total normal stress distribution without and with grout penetration. Advance -680.306 m south alignment. Right-hand side. Colour calibration: red = 700 kPa; blue: 0 kPa

6.4.6 Transversal equilibrium: partial conclusions

The analysis of the transversal equilibrium at a number of specific advances is not meant to cover all the possible configurations encountered during tunnelling. The selection was made with the goal of illustrating how the model approximations may have hindered the achievement of fully satisfactory results. Three aspects seem to have played a determinant role in this sense and those were: 1) the determination of the actual stiffness of the soil; 2) the precision of the shield positioning system and its consistency during drive (re-alignments); 3) the possibility for the tail-void grout to flow around the shield and to influence the normal stress distribution there. It is recalled that an uneven penetration of the process fluids between opposite sides of the TBM-shield may originate unbalanced tangential stresses and, consequently, turning moments (see also Section 6.2). These aspects need to be addressed if better models of shield behaviour are sought for. Specific recommendations will be provided in Chapter 8.

6.5 Vertical equilibrium

6.5.1 Considerations on the balance of the horizontal moments

The horizontal driving moment, intrinsically correlated with the vertical tendency of the shield or pitching, is on average -25 MNm over the whole south alignment. That is now compared with the turning moment due to the misalignment of the resultant of the shield's self-weights and the buoyancy effect acting on the shield volume under groundwater table.

The moment due to the self-weights, as explained in Chapter 3, was obtained by multiplying the overall shield weight by the arm between the point of application of the resultant of the weights and the RPF. The shield weight was frontward shifted due to the specific construction of the shield, which is heavier at the front, the self-weight of the cutting wheel, which is hanging in front of the shield, and the weight of the excavated muck filling the excavation chamber. The moment due to the self-weights amounts to -30 MNm and was subject to disregardable changes during drive.

The moment due to the buoyancy of the shield volume, assuming the entire shield under groundwater table, is obtained as

$$\gamma_w V_s \frac{l}{2} \tag{6.12}$$

in which γ_w is the volumetric specific weight of the groundwater, V_s the volume of the shield body, and $\frac{l}{2}$ half the shield length. Using a water volumetric weight of 10 kN/m^3, the volume 886.25 m^3 and the shield length 10.235 m, a downward tilting moment of +45.35 MNm is derived. Combining the upward tilting moment due to the self-weights with the downward tilting one due to the buoyancy effect give a downward tilting one of about +15 MNm.

From Chapter 3 it is known that two other major moments influence the longitudinal tilting of the shield, namely the hydrostatic action of the face support fluid and the contact stresses between the cutting wheel and the cutting surface. The moment given by the hydrostatic pressure distribution of the face support fluid depends on the volumetric specific weight of the fluid itself, and for a circular surface is

$$\overrightarrow{M_{sl}} = \overrightarrow{F_{slm}} \times (\vec{b} \cdot \frac{R_{front}}{4}) \tag{6.13}$$

$$\overrightarrow{M_{sl}} = \overrightarrow{F_{slm}} \times (\vec{b} \cdot \frac{R_{front}}{4}) \tag{6.14}$$

in which F_{slm} is the longitudinal force given by the triangular part of the hydrostatic distribution, R_{front} the radius of the front part of the shield, and $\vec{b}$ is the unit vector oriented from the bottom to the middle point of the shield face. F_{slm} depends on the fluid specific weight according to the relation

$$F_{slm} = \gamma_{sl} \cdot R_{front} \cdot \left(\pi \cdot {R_{front}}^2\right) \tag{6.15}$$

in which γ_{sl} represents the specific weight of the support fluid. A volumetric weight of 10 kN/m^3 gives a downward tilting hydrostatic moment of +5.98 MNm. As specific weights fall more frequently into the range 12 ÷ 14 kN/m^3, values 20 to 40 % higher are considered (7.17 ÷ 8.37 MNm).

The moment given by the contact stresses between the cutting wheel and the cutting face and derived in Chapter 3 is relatively constant during drive. In Figure 6.67 the two horizontal components of the contact moment are plotted. Given the sign convention and the geometry of the tunnel alignment, the combination of negative and positive sign for the x and for the y-component, respectively, indicates that the contact moment is upward tilting. In other words the contact stresses with the soil were higher in the upper sector of the wheel than in the lower one. Moreover, the combination of x and y components leads to a mean horizontal moment of -0.575 MNm, as seen from Figure 6.68. -0.5 MNm is finally assumed to represent the contact moment between cutting wheel and excavation front.

Combining the moment due to the misalignment of the self-weights and of the buoyancy effect with the two just described (hydrostatic support pressure and face contact forces), a resultant downward tilting moment of +22.27 MNm is derived when a slurry specific weight of 13 kN/m^3 is considered. This value, compared with the average horizontal driving moment of -25 MNm, shows that the latter is still about 10% (2.73 MNm) larger than theoretically "needed" according to calculations.

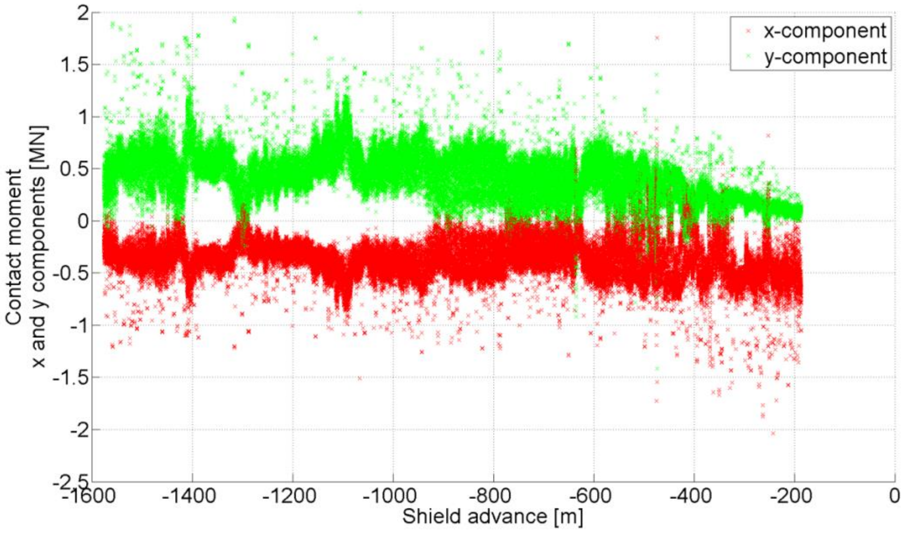

Figure 6.67: x and y components of the contact moment between cutting wheel and excavation front

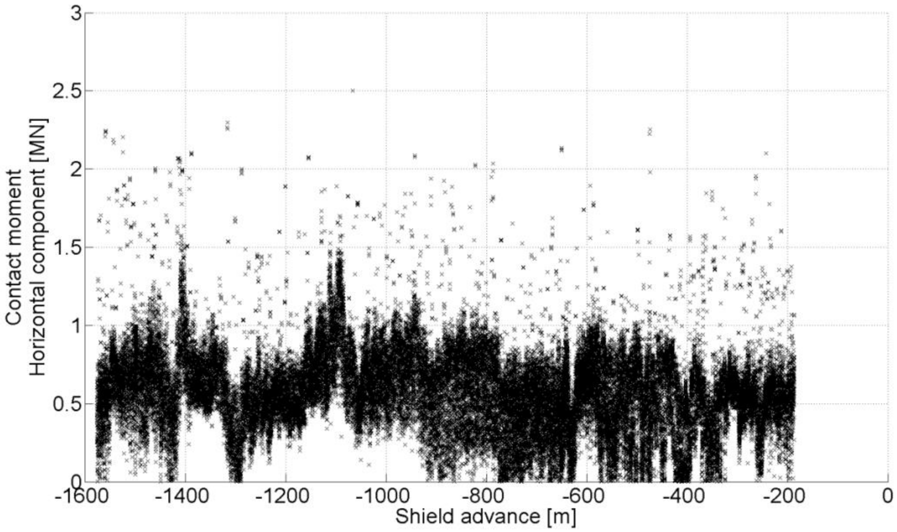

Figure 6.68: Contact moment between cutting wheel and excavation front - Horizontal component

6.5.2 Observed vertical behaviour and shield interaction with the soil

The vertical tendency of the shield over the south alignment (Figure 6.69) is on average -2 mm/m, in which the negative sign represents downward tilting. Extending the average tendency over the shield length (10.235 m) leads to a height difference of 20 mm between the centre points of the shield's front and rear cross sections compared to their ideal positions on the design alignment. In other words, the algebraic difference between the vertical deviations from the theoretical alignment of the centre points of the front and rear cross sections, respectively, added up to -20 mm. Convention holds that deviations of the reference points below the theoretical alignment have a negative sign.

The value of -20 mm is in fact very similar to what was obtained by adding up the built-in radial overcutting of 10 mm and the radial tapering of the shield, also 10 mm. This suggests that during drive the top side of the shield followed closely the upper part of the excavated geometry. Contrarily, at the bottom side a "gap" originated as a consequence of the built-in overcutting and of the shield's tapering. A different shield tapering would have probably led to a different average tendency.

The downward-tilted shield set-up suggests that during advance the initial soil-stress condition was better preserved at the top side, where the shield-skin followed the excavated geometry, than at the bottom one, where a "gap" originated and the surrounding soil could relax. The extent of the relaxation into play at the bottom side was such that the effective soil stress there would become lower than at the top side even considering the depth difference. Based on the evaluations on the soil stiffness and corresponding soil-reaction curves of Chapter 5, a soil relaxation of 20 ÷ 40 mm at the shield bottom is sufficient to lower the effective stress to almost zero in almost every initial stress condition encountered at the Hubertus tunnel.

Soil effective stresses larger at the upper half than at the lower one contributed to the shield equilibrium with an upward tilting moment. However, that conflicts with the conclusive remark of Section 6.5.1 that the average horizontal driving moment was already about 3 MNm larger (-25 MNm) than that strictly needed as from calculations (+22.27 MNm). This condition suggests that the low stresses in the lower half of the shield are in reality compensated, most likely by the penetration of tail-void grout into the shield-soil interface. In the remainder of this section we will go through a number of specific locations trying to demonstrate that that was most likely the case and how the penetration of pressurised grout contributes to achieve vertical equilibrium.

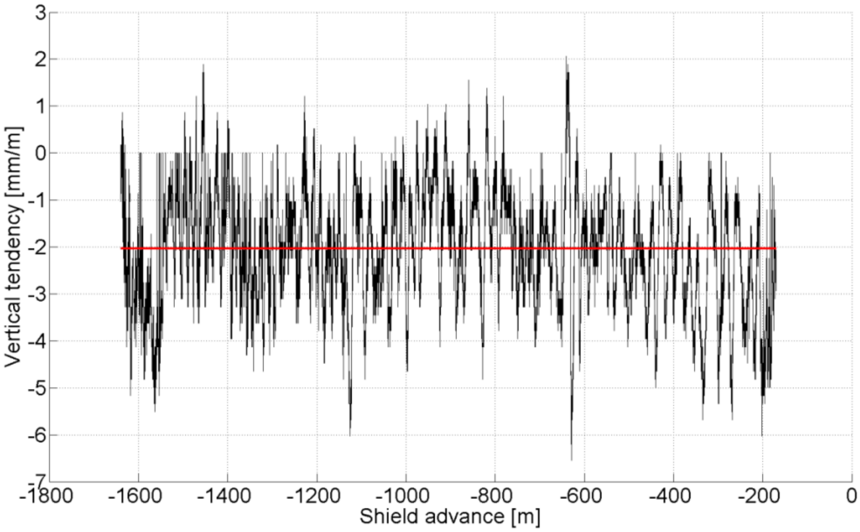

Figure 6.69: Vertical tendencies over the south alignment. In red the average value

6.5.3 Review of the vertical equilibrium at selected advance locations

Several example locations are analysed hereafter. What all such locations have in common is a lack of vertical equilibrium when modelled in the simplified way, that is without considering the effect of grout penetration. At each location several parameters concerned with the vertical balance and response are presented and commented. The aim of this review is to give an overview, although not conclusive, on a number of configurations encountered in practice and to discuss how the role of the grout injection appears determinant of the vertical equilibrium.

The examples are introduced in order of advance according to the direction of drive. The main characteristics of each configuration are summarized in Table 6.2. The table reports the location of the stretch under investigation, the direction of vertical unbalance, the amount of unbalance without and with grout penetration, and a very short summary of the peculiarities of each case.

Table 6.2: Summary of the results of vertical equilibrium

Interval [m]	Direction of initial unbalance	Vertical unbalance (without grouting) [MN]	Unbalance after corrections [MN]	Description
-1005 ÷ -955	downward	-6.40	-2.58	Sharp drop of RPs due to low pressure and peaking negative driving moment. Stresses' overestimation in soil-relaxation sector due to lower cut-off
-925 ÷ -875	downward	-4.58	+2.84	Low driving moment and high grouting pressures contributing to generalized uplift
-815 ÷ -765	downward	-3.56	-1.90	Large downward shift (10 ÷ 20 mm) originating a change in the vertical resultant from -4 MN to +6 MN

6.5.3.1 Advance interval -1005 ÷ -955 m

The sub-sector -985 ÷ -960 m provides several interesting phenomena concerned with the vertical shield behaviour. The first one is the sharp drop of both reference points that occurs over the interval -984 ÷ -982 m (Figure 6.72). The downward shift matches both a drop of the grouting pressures of 150 ÷ 200 kPa (Figures 6.73 and 6.74) and a negative peak of the horizontal driving moment (Figure 6.71).

Negative horizontal driving moments tend to increase the vertical tendency or to reverse it from negative to positive. However, for such inversion to occur sufficient "support" is required at the bottom side. If the grouting pressure becomes too low such support lacks and the shield keeps "drifting" downward until sufficient soil reaction builds up. Actual recovery of the vertical tendency took place from -980 m onwards in parallel with higher grouting pressures.

Another interesting phenomenon is the uplift of the RPR at -973 ÷ -971 m. That coincides with a sharp decrease (in absolute value) of the driving moment and high injection pressures. After that, when the injection pressure decreased and the driving moment increased, RPF and

RPR moved downward, and that continued over the interval -971 ÷ -966 m until enough support was built-up at the bottom through the recompression of the soil and an adequate grouting pressure (-966 ÷ -961 m).

Another kind of numerical experiment, as seen for the transversal balance, concerns the achievement of the vertical equilibrium by implementing the grouting process into the model. Recall that a lower cut-off on the normal effective stresses at the shield-soil interface was among the model simplifications (Section 6.4.2.2). Such cut-off assumes that the interface normal stresses could only be higher than the initial soil stresses at the same location. That hypothesis holds the risk to overestimate the interface stress in the soil-relaxation sectors when the grouting pressure is not sufficient to compensate for the “kinematic gap”.

The interface stresses in a soil-relaxation sector seem for instance overestimated at advance -983 m. Figure 6.75 shows a +6 MN upward oriented vertical resultant. The increasing trend of the vertical resultant matches well the downward movement of RPF and RPR over the couple of meters before the specified advance (Figure 6.72). However, due to the cut-off, the model is not capable of taking into account that over the same interval also the grouting pressure underwent a significant drop (Figures 6.73 and 6.74). Moreover, the pressure drop itself may have primarily caused the downward movement by creating low pressure at the shield bottom. But if low stresses were present there then the cut-off improperly intervened and stresses lower than those before tunnelling were indeed possible. In conclusion, lower stresses at the lower half of the shield would have led to a smaller upward force and therefore a more balanced vertical resultant.

An indication of the stress reduction needed to produce a decrease of the vertical force of 6MN is obtained by dividing the said force by the horizontal projection of the shield, in other words

$$\frac{F}{ld} \tag{6.16}$$

in which F is the force, l is the shield length (10.235 m) and d its diameter (10.50 m). The resulting stress is 56 kPa and that fits well within the extent of the fluctuations of the grouting pressures (Figures 6.73 and 6.74).

Vertical equilibrium is also investigated at advance -970.950 m. With the grouting pressure not taken into account the resultant is a -6.40 MN downward oriented force. The penetration of the tail-void grout into the shield-soil interface is then hypothesised. The boundary grout pressure is assumed equal to the average of all measured values over the last 2 m of advance instead of the average of the top 10% only, diminished by 100 kPa for the pressure losses in the injection lines. When the grouting pressures are considered the downward resultant force is reduced to -2.58 MN. A column chart is shown in Figure 6.70. The comparison between the normal stress distribution without and with grout penetration is schematically shown in Figures 6.76 and 6.77. The usual colour convention held (Section 6.4.4.3).

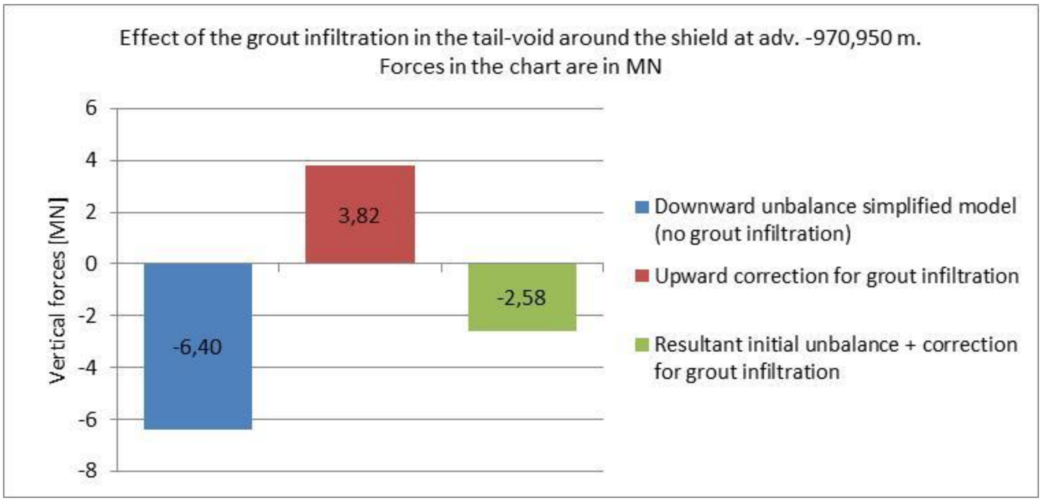

Figure 6.70: The residual downward vertical unbalance (green) is obtained by combining the unbalance of the simplified model (blue – no grout penetration) with the correction due to the grout penetration in the tail-void around the shield (red)

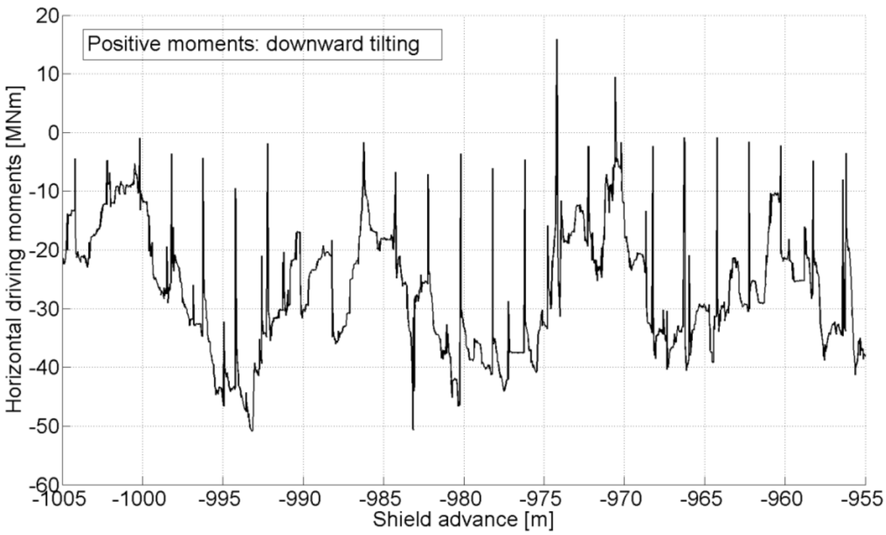

Figure 6.71: Horizontal driving moment – sector -1005 ÷ -955 m

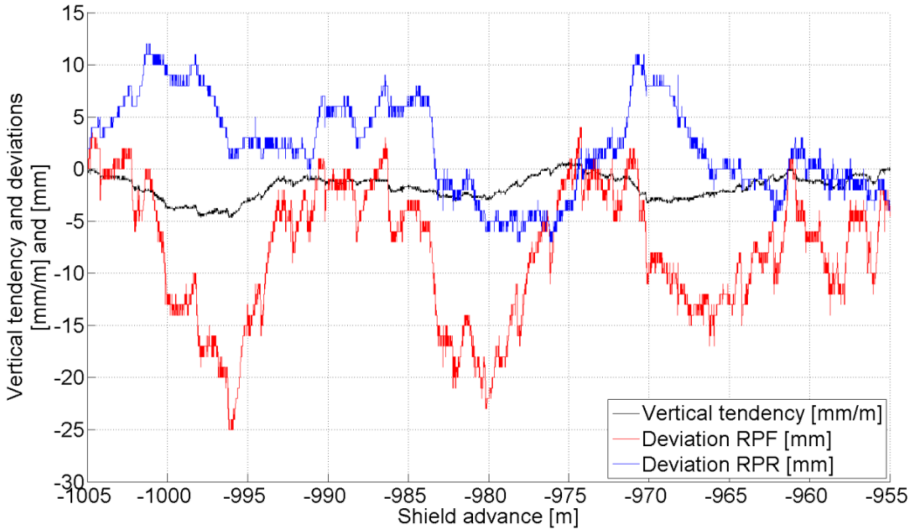

Figure 6.72: Vertical tendency and deviations of the reference points – sector -1005 ÷ -955 m

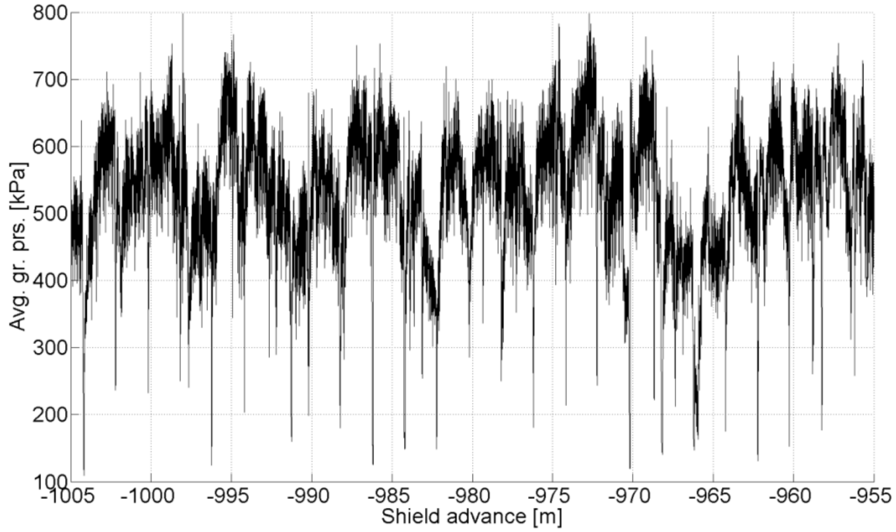

Figure 6.73: Average grouting pressures – sector -1005 ÷ -955 m

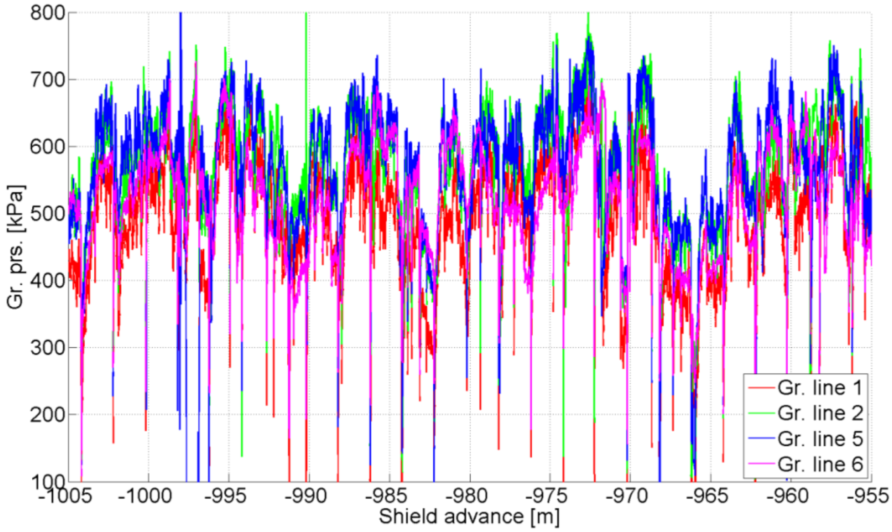

Figure 6.74: Detail grouting pressures – sector -1005 ÷ -955 m

Figure 6.75: Resultant vertical forces – sector -1005 ÷ -955 m (grout penetration not taken into account)

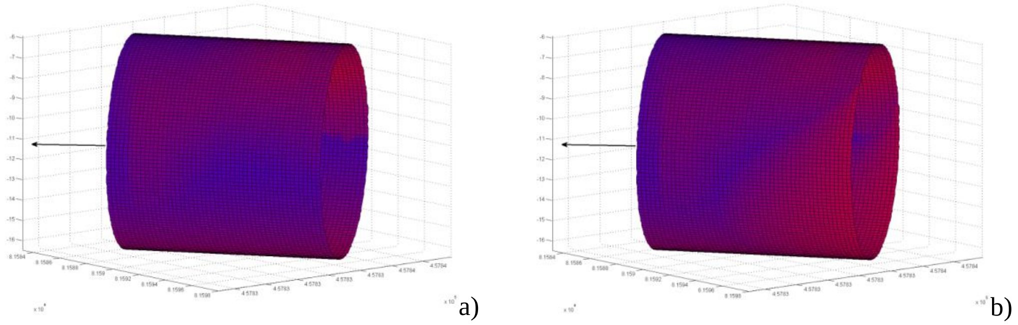

Figure 6.76: Total normal stress distribution without and with grout penetration. Advance -970.950 m south alignment. Left-hand side. Colour calibration: red = 700 kPa; blue: 0 kPa

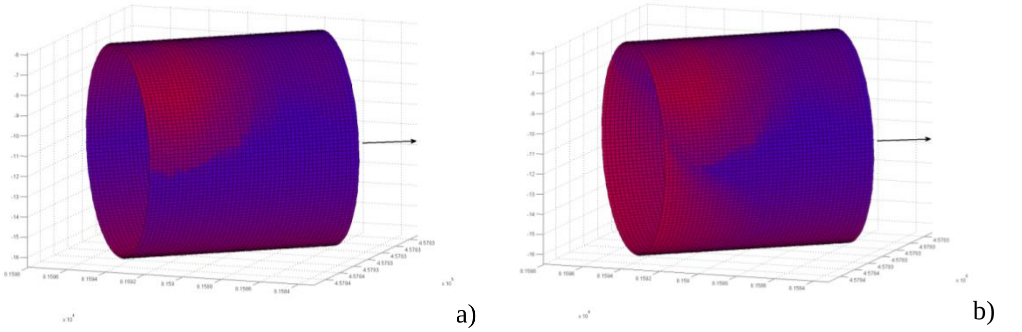

Figure 6.77: Total normal stress distribution without and with grout penetration. Advance -970.950 m south alignment. Right-hand side. Colour calibration: red = 700 kPa; blue: 0 kPa

6.5.3.2 Advance interval -925 ÷ -875 m

Over the interval -900 ÷ -890 m the resultant of the vertical forces shifts from +6 MN to -6 MN (Figure 6.83). That is paired with an uplift of the Reference Point Rear (RPR) of about 15 mm and a less regular response of the \Reference Point Front (RPF) over the same interval (Figure 6.80). The movement of the RPR appears correlated with the decrease (in absolute value) of the horizontal driving moment (Figure 6.79) and the increase of the grouting pressures (Figure 6.81). However, as both mechanisms contribute to produce the same downward tilting effect and both varied over the interval, it becomes challenging to quantitatively correlate each one of them separately with the shield response.

The tail-void grouting and the vertical equilibrium of forces are correlated at advance -891.326 m. With the penetration of the grout mortar around the shield not taken into account a downward oriented force of -4.58 MN resulted at the specified location (see Figure 6.83). When grout penetration is considered, the downward resultant changes into an upward one of +2.84 MN instead. The arithmetic average of all injection pressures observed over the last 2 m of advance is taken as boundary condition. A pressure loss of 100 kPa is considered in order to account for the pressure drop in the injection lines. A column chart of the results is shown in Figure 6.78.

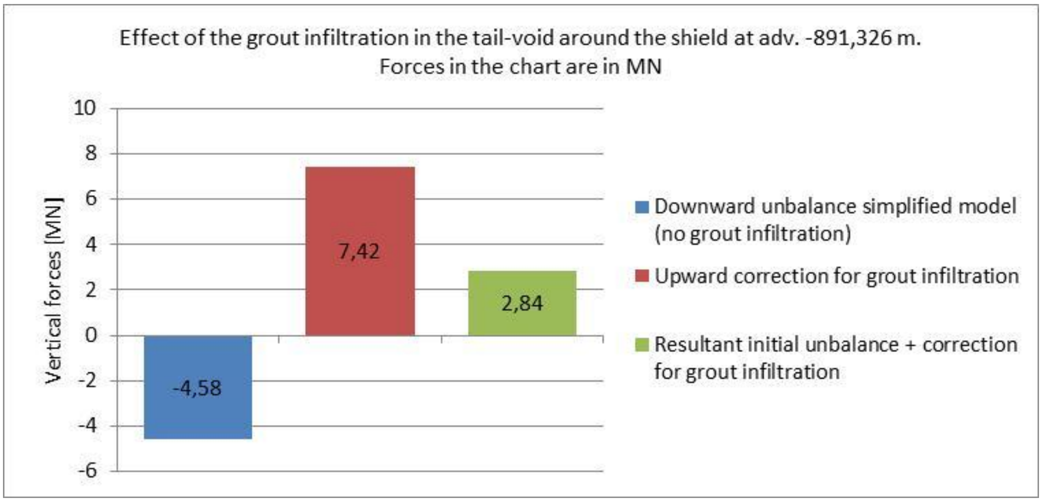

Figure 6.78: The residual downward vertical unbalance (green) is obtained by combining the unbalance of the simplified model (blue – no grout penetration) with the correction due to the grout penetration in the tail-void around the shield (red)

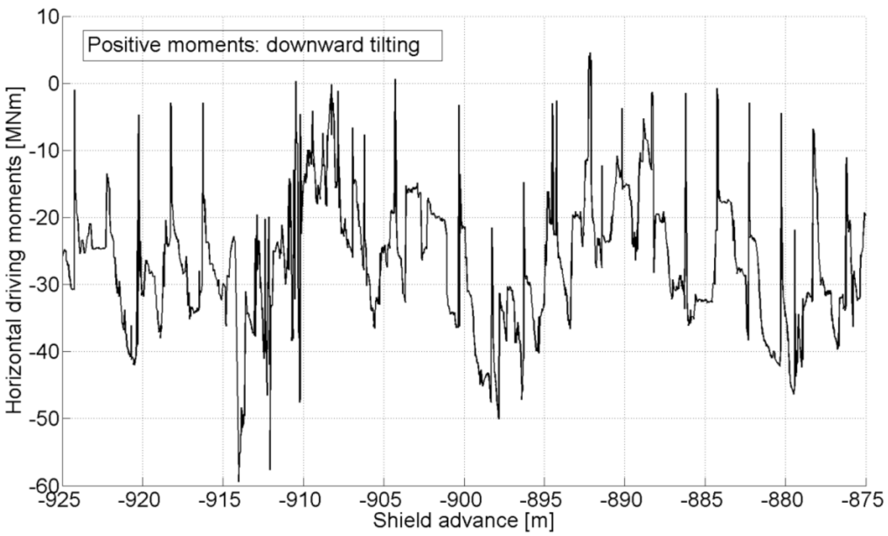

Figure 6.79: Horizontal driving moment – sector -925 ÷ -875 m

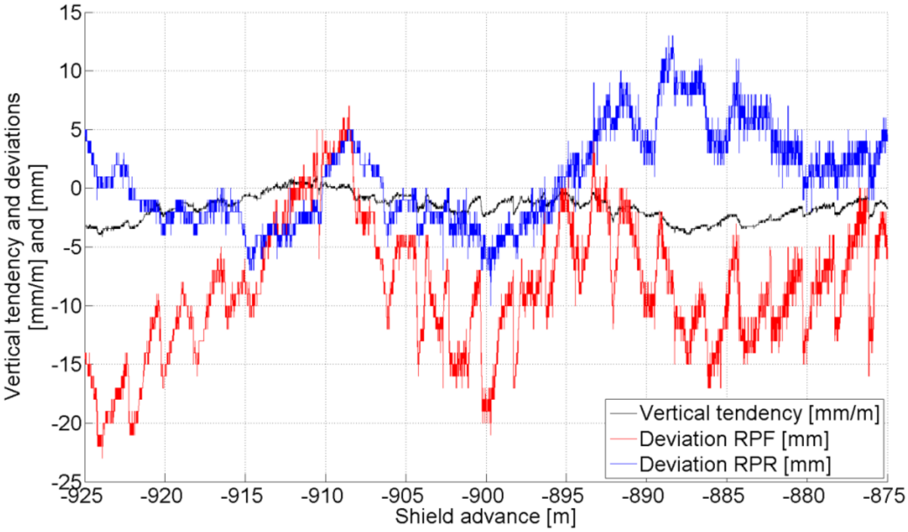

Figure 6.80: Vertical tendency and deviations of the reference points – sector -925 ÷ -875 m

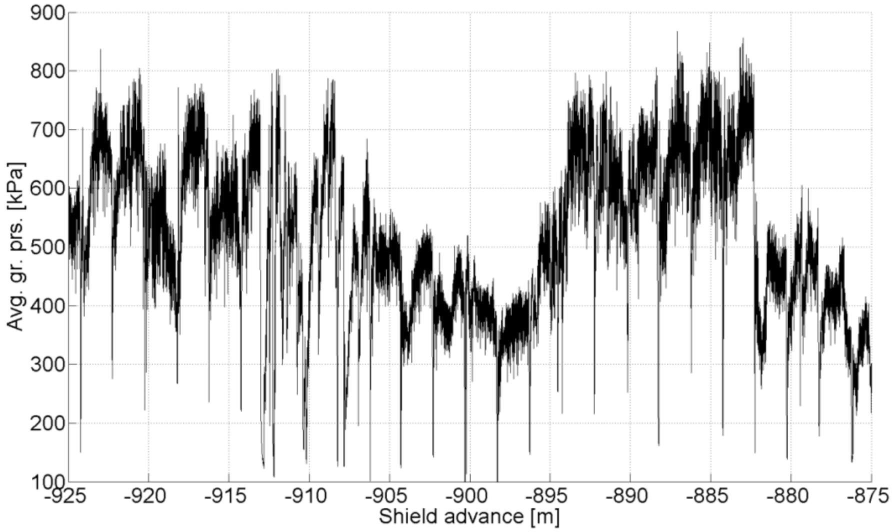

Figure 6.81: Average grouting pressures – sector -925 ÷ -875 m

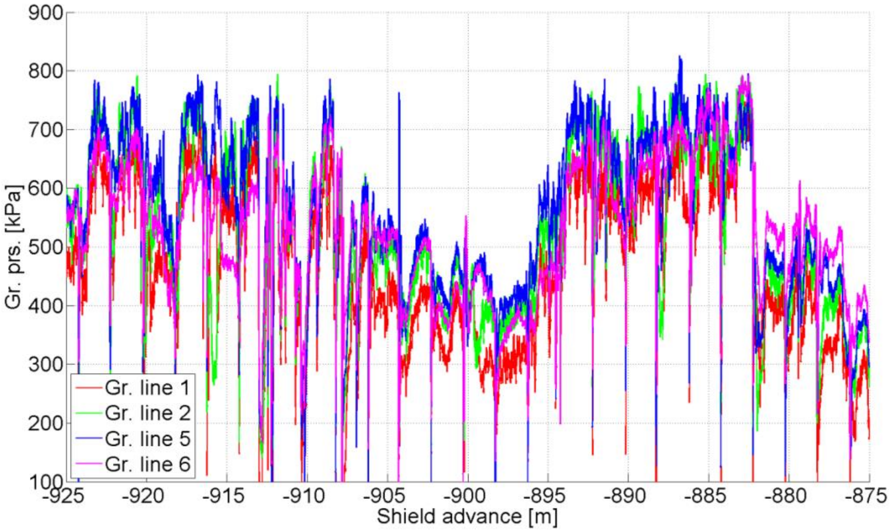

Figure 6.82: Detail grouting pressures – sector -925 ÷ -875 m

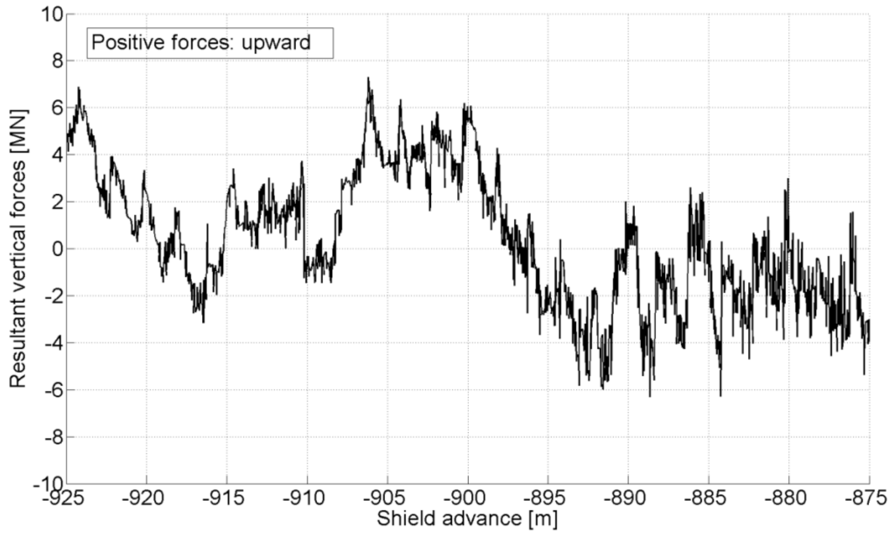

Figure 6.83: Resultant vertical forces – sector -925 ÷ -875 m (grout penetration not taken into account)

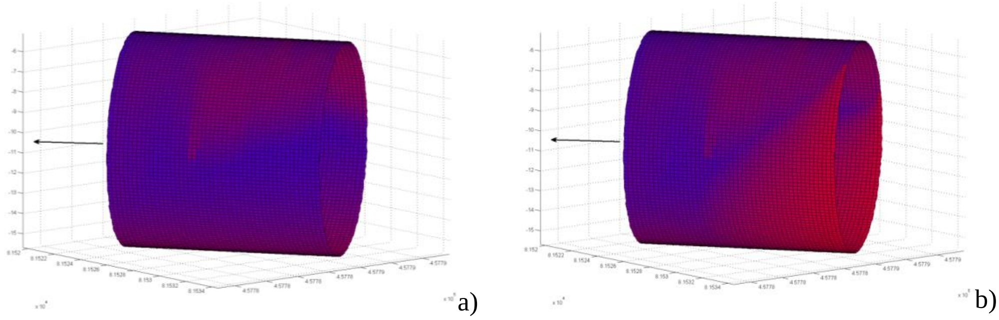

a) b)

Figure 6.84: Total normal stress distribution without and with grout penetration. Advance -891.326 m south alignment. Left-hand side. Colour calibration: red = 700 kPa; blue: 0 kPa

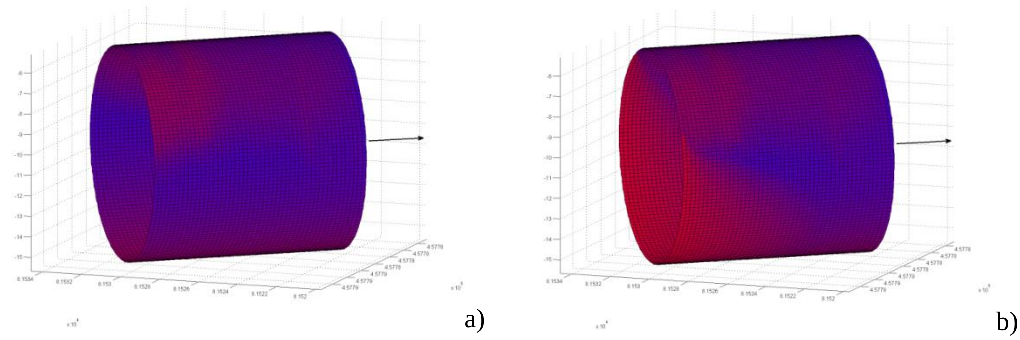

a) b)

Figure 6.85: Total normal stress distribution without and with grout penetration. Advance -891.326 m south alignment. Right-hand side. Colour calibration: red = 700 kPa; blue: 0 kPa

6.5.3.3 Advance interval -815 ÷ -765 m

Over the interval -797 ÷ -792.5 m a sudden drop of the horizontal driving moment provoked downward shifts of about 20 and 10 mm on behalf of the RPF and of the RPR, respectively (Figures 6.87 and 6.88). The vertical resultant force following such displacements is an upward one of +6 MN (Figure 6.91). The unbalance is derived from the standard model in which the grout penetration effect is not taken into account.

Most likely the lower cut-off applied to the effective normal stresses overestimates the stresses at the shield bottom, and this leads to the positive resultant force. It may well have happened instead that the grouting pressure was not sufficient to maintain the stress level before excavation. Figures 6.89 and 6.90 show indeed a pressure drop at advance -797 m. However the drop appears like a local event and the pressure seems promptly recovered after few metres. That undermines the confidence that the vertical equilibrium could have been achieved if only the (low) grouting pressures were modelled correctly and the lower cut-off were switched off.

Differently, as seen at other locations, the simplified model of grout penetration helped to compensate for apparent downward resultant of forces. The vertical balance at advance -803.185

m is -3.56 MN when grout penetration is not considered, then reduced to -1.90 MN when penetration is considered instead. The boundary condition at the shield tail is assumed equal to the average of the top 10 % injection pressures over the last 2 m and the standard pressure loss of 100 kPa is considered as usual. A column chart of the results is shown in Figure 6.86.

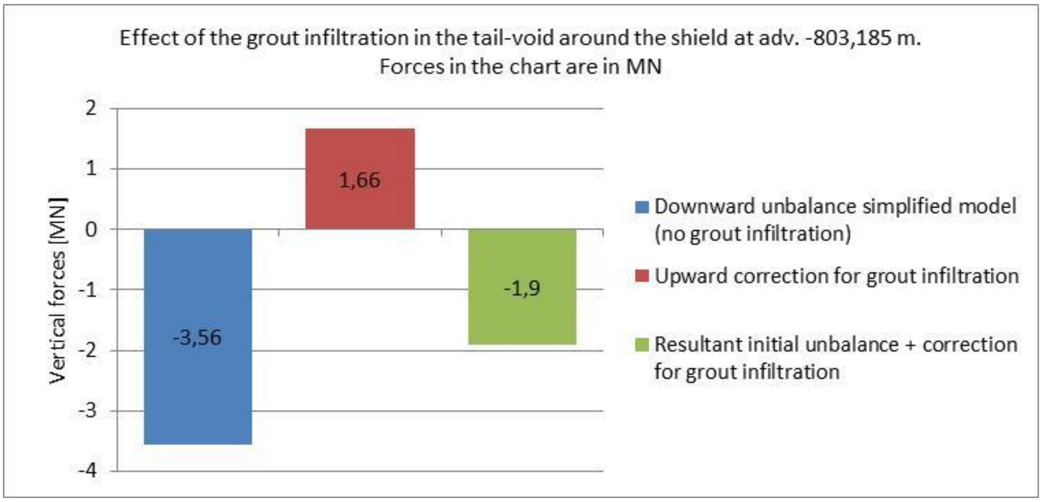

Figure 6.86: The residual downward vertical unbalance (green) is obtained by combining the unbalance of the simplified model (blue – no grout penetration) with the correction due to the grout penetration in the tail-void around the shield (red)

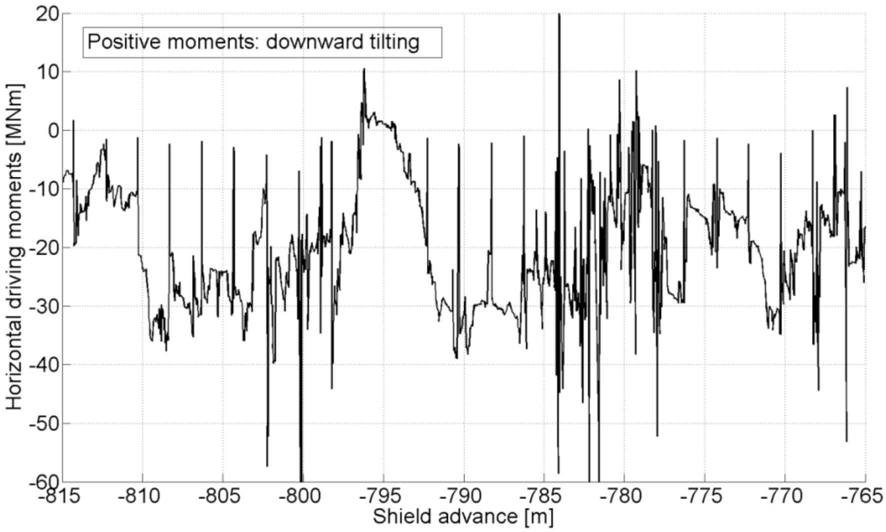

Figure 6.87: Horizontal driving moment – sector -815 ÷ -765 m

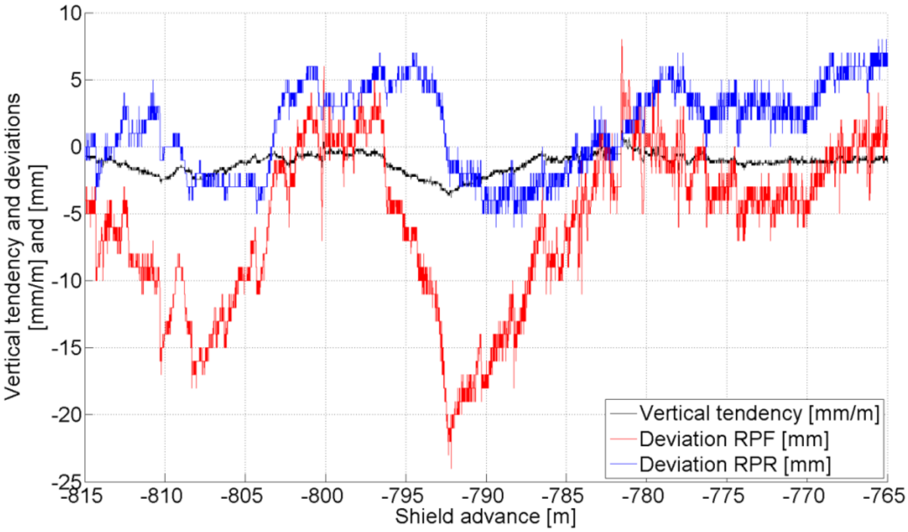

Figure 6.88: Vertical tendency and deviations of the reference points – sector -815 ÷ -765 m

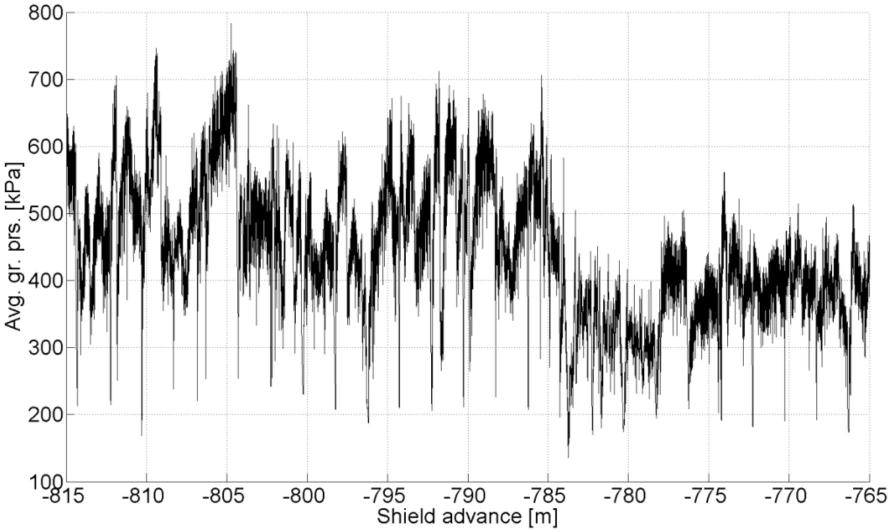

Figure 6.89: Average grouting pressures – sector -815 ÷ -765 m

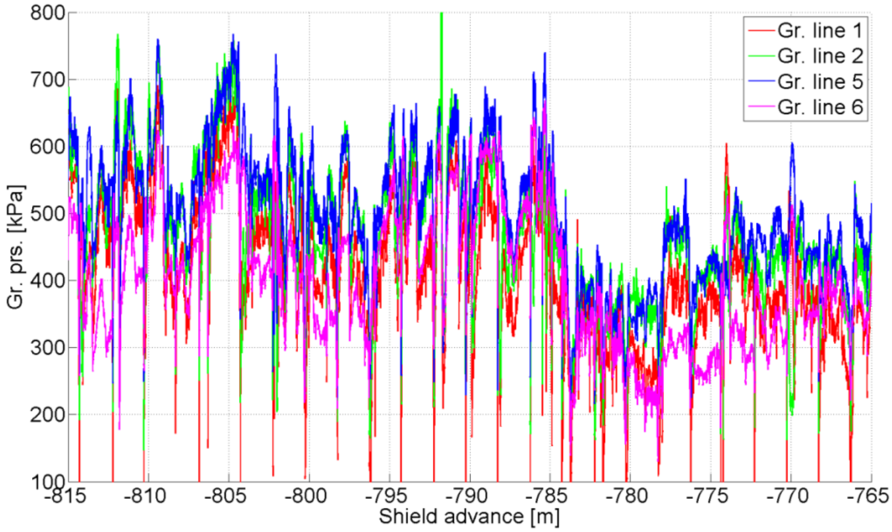

Figure 6.90: Detail grouting pressures – sector -815 ÷ -765 m

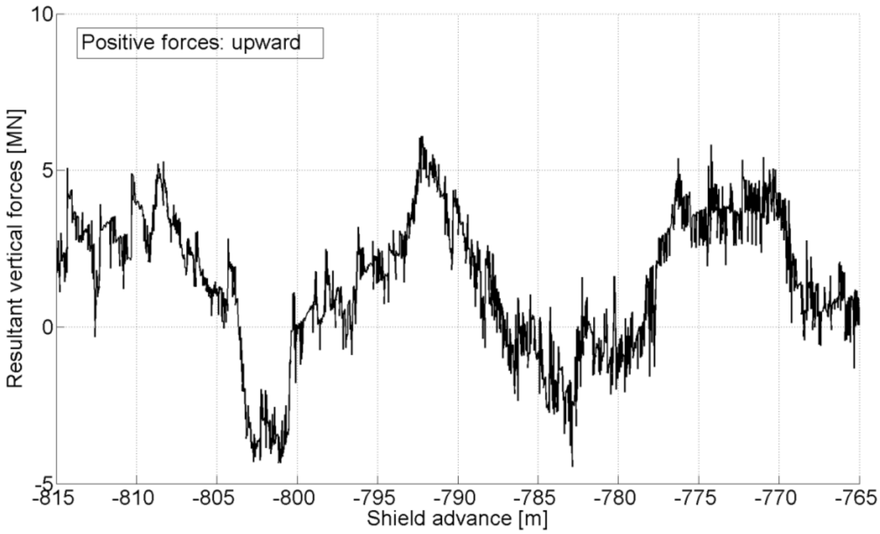

Figure 6.91: Resultant vertical forces – sector -815 ÷ -765 m (grout penetration not considered)

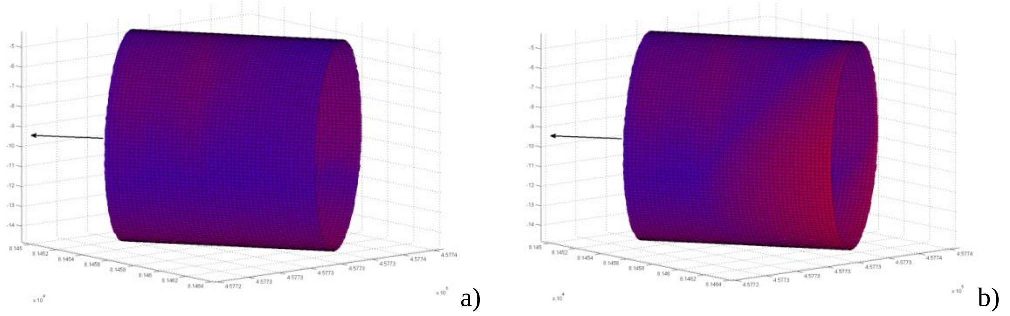

Figure 6.92: Total normal stress distribution without and with grout penetration. Advance -803.185 m south alignment. Left-hand side. Colour calibration: red = 700 kPa; blue: 0 kPa

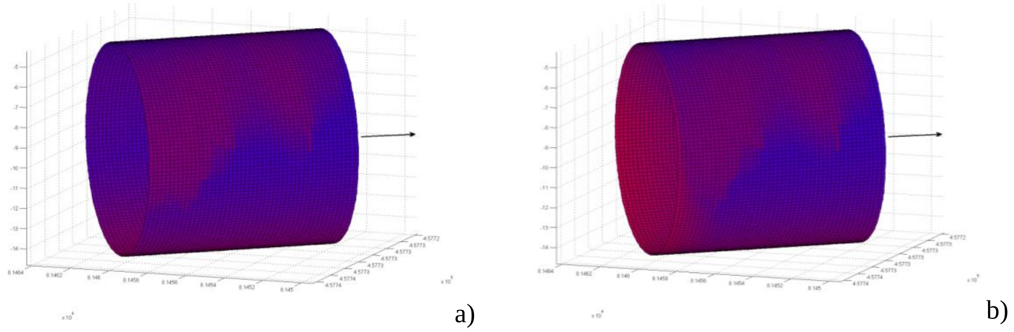

Figure 6.93: Total normal stress distribution without and with grout penetration. Advance -803.185 m south alignment. Right-hand side. Colour calibration: red = 700 kPa; blue: 0 kPa

6.6 Partial conclusions on the mechanical equilibrium of the TBM

The modelling of the tail-void grouting in the calculation of the forces' equilibrium can certainly be improved. That holds for longitudinal, transversal, and vertical directions in which the static problem has been decomposed. Averaging the injection pressures over a certain advance length is a simplistic expedient to overcome the impossibility for the current model to keep track of the injection pressure at earlier advance stages. This last functionality could bring satisfactory achievements if correctly implemented. Similarly, the 100 kPa pressure loss only roughly described the pressure drop in the injection lines. A more accurate representation of that process, supported by experimental data, would allow a more consistent description. Nevertheless, we believe that even such simplified description of the role of the tail grouting on the shield equilibrium manages to show that the grouting pressures into play are capable of originating forces of such extent to balance the other actions.

Chapter 7

TBM kinematics and observed soil displacements

The correlation between the shield geometry, its erratic advance through the soil, and the observed soil displacements is studied in this section. In Chapter 4 it was demonstrated that the snake-like motion of the shield introduced by Sugimoto and Sramoon [42] induces unevenly distributed soil displacements at the shield-soil interface. Those interface displacements, in the absence of other physical processes, are expected to spread through the soil with a similar pattern.

The results of the numerical investigation on the TBM kinematics and the associated observed soil response are compared here in order to quantify their correlation. Results confirm that the geometry and the advance of the TBM-shield through the soil influence the amount and distribution of the induced soil displacements. The analysis also highlights the essential role of the tail-void grouting not only in filling-in the tail-void, but also in compensating the kinematic effects of shield advance.

The current Chapter is based on a paper currently under review (Festa et al. (2014) [17]), on Festa et al. [15], and on Krot [23].

7.1 Subsurface soil displacements

The subsurface displacements were monitored during the construction of both tunnels at 8 cross-sections, of which 4 were equipped with extensometers, and 4 with inclinometers. The locations of the cross-sections are provided in Tables 7.1 and 7.2 and 10 with reference to the tunnel advance. The horizontal distance between two matching monitoring sections (for inclinometers and extensometers) is about 1.2 m. The location of the monitoring sections in terms of tunnel advance differed between the two tubes. That was due to an overall difference in length between the two tubes of about 13 m.

Table 7.1: Locations of the monitoring sections – south alignment

	Section 1	Section 2	Section 3	Section 4
Extensometers	Km -1+588.16	Km -1+556.51	Km -1+149.01	Km -1+095.42
Inclinometers	Km -1+586.59	Km -1+555.22	Km -1+147.87	Km -1+094.20

Table 7.2: Locations of the monitoring sections – north alignment

	Section 1	Section 2	Section 3	Section 4
Extensometers	Km -1+600.57	Km -1+571.24	Km -1+161.58	Km -1+108.04
Inclinometers	Km -1+599.40	Km -1+570.15	Km -1+160.32	Km -1+106.73

Each monitoring section was equipped with 7 boreholes. In the boreholes either extensometers or inclinometers were installed. The boreholes were numbered from 1 to 7 from right towards left, as seen in direction of drive. 5 of the 7 boreholes were actually instrumented during each passage of the shield, namely the closest to the tunnel being bored. For each cross-section the time span investigated ranged from the moment in which the TBM-face was 25 m before the section, until the face was 50 m after the section. These positions are depicted in Figures 7.1 to 7.13 as -25 and +50, respectively.

7.1.1 Extensometers

Extensometers are used to monitor the vertical soil displacements. A reference point is needed for converting the relative movements provided by extensometers into absolute displacements. The reference may be very deep in the ground, where the soil is presumably undisturbed by the construction activity, or at surface level. In this second case, as at the Hubertus tunnel, conventional levelling is used to monitor the vertical movements of the reference point. The movements logged at the four monitoring sections equipped with extensometers are plotted in Figures 7.2 to 7.9. The graphs show the soil displacements during the construction of both tubes.

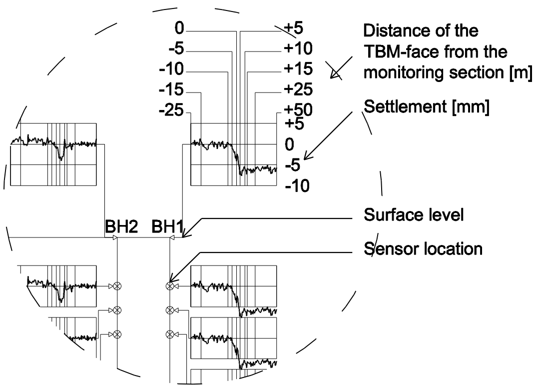

Figure 7.1: Explanation of symbols for extensometers

Each graph refers to one sensor. The initial settlement value (0) was assumed with the shield face 25 m before the monitoring section. Data collection was continuous. At the first passage across section 1 the reference point was taken with the shield face 10 m before the monitoring section. Vertical lines mark relative positions of the TBM-shield face with respect to the monitoring section. The line 0 represents the cutter face crossing the monitoring section; +10.235 stands for the transit of the shield tail across the monitoring section. Settlement troughs at selected advances are shown.

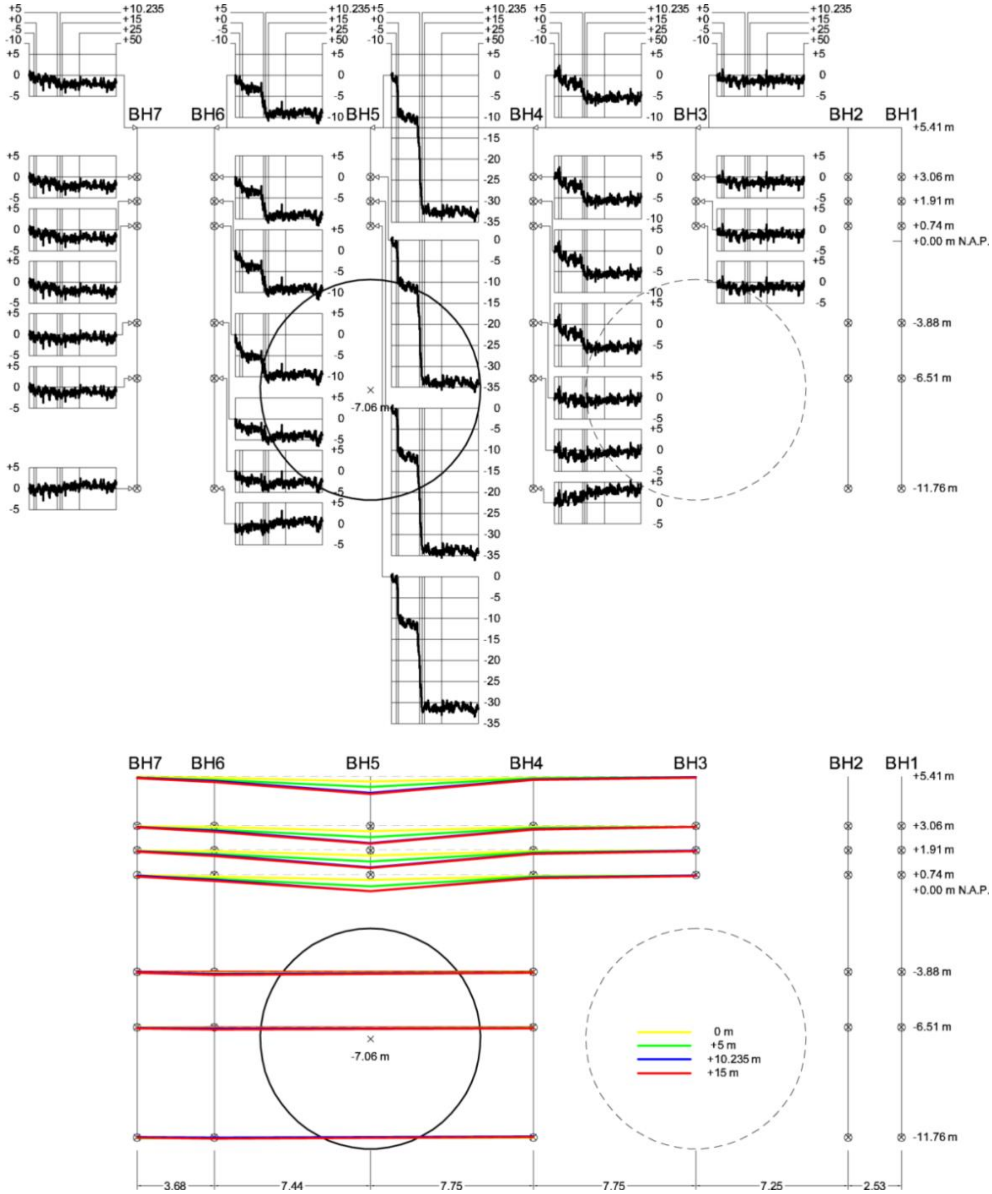

Figure 7.2: Extens. and settlement troughs at monitoring section 1 – first passage (left tube) – south tunnel – 2006. Volume loss at ground level: 0.43 %

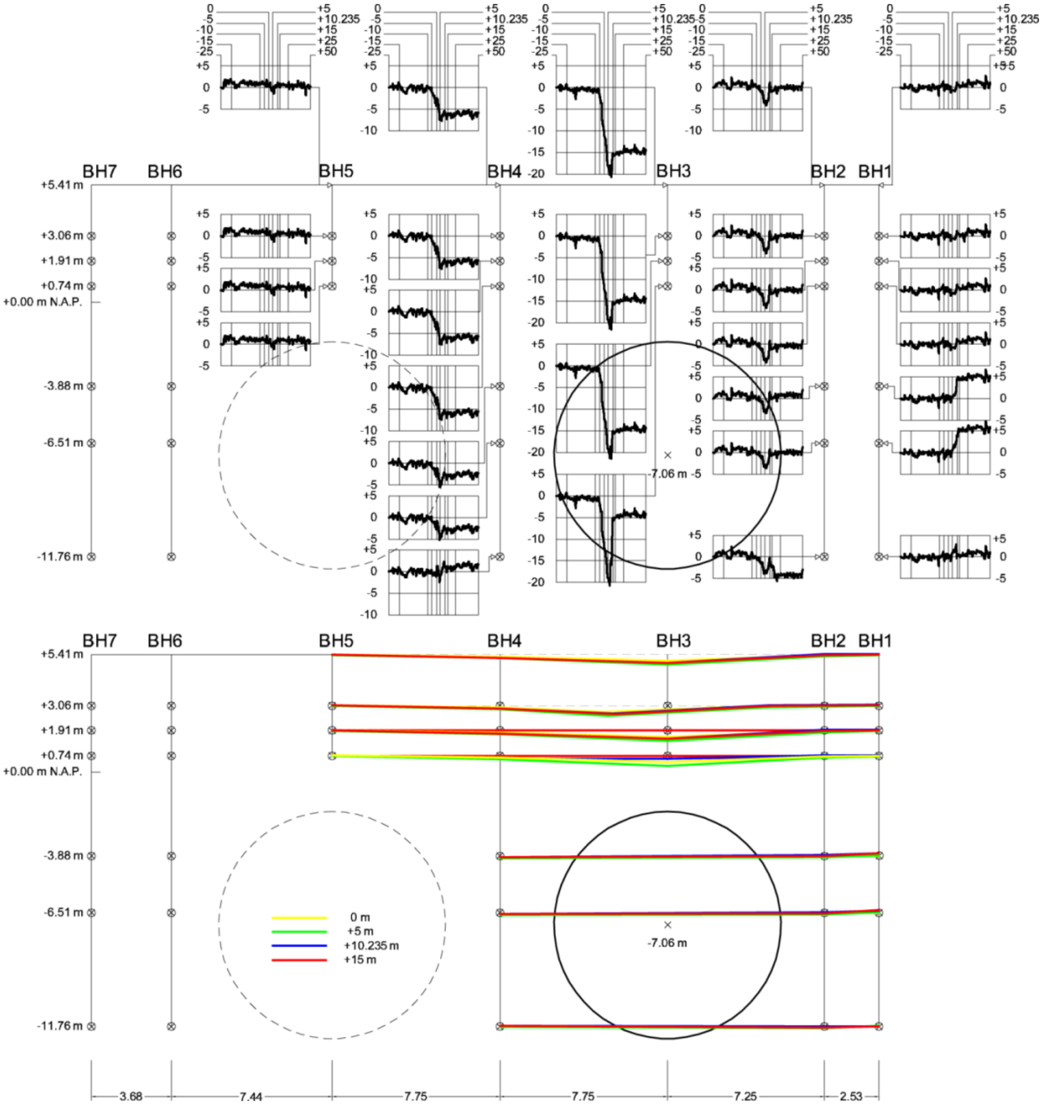

Figure 7.3: Extens. and settlement troughs at monitoring section 1 – second passage (right tube) – north tunnel – 2007. Volume loss at ground level: 0.24 %

The settlement troughs resulting from tunnel construction are at both crossings non-symmetrical with respect to the tunnel axis. Settlements were usually larger at the left-hand side than at the right-hand one. Additionally, a marked and sudden recovery (heave) of the previously occurred settlements was observed, during the second passage, few metres before the shield tail crossed the monitoring section. A similar recovery was not observed during the first passage. The heave during the second passage was more effective close to the tunnel, and especially just above it, than at distance. In borehole 3, located above the second tunnel axis (north), about 75% of the pre-occurred settlements were recovered at the depth of the deepest sensor which was located 2 m above the extrados of the tunnel, while only 25% was recovered at ground level.

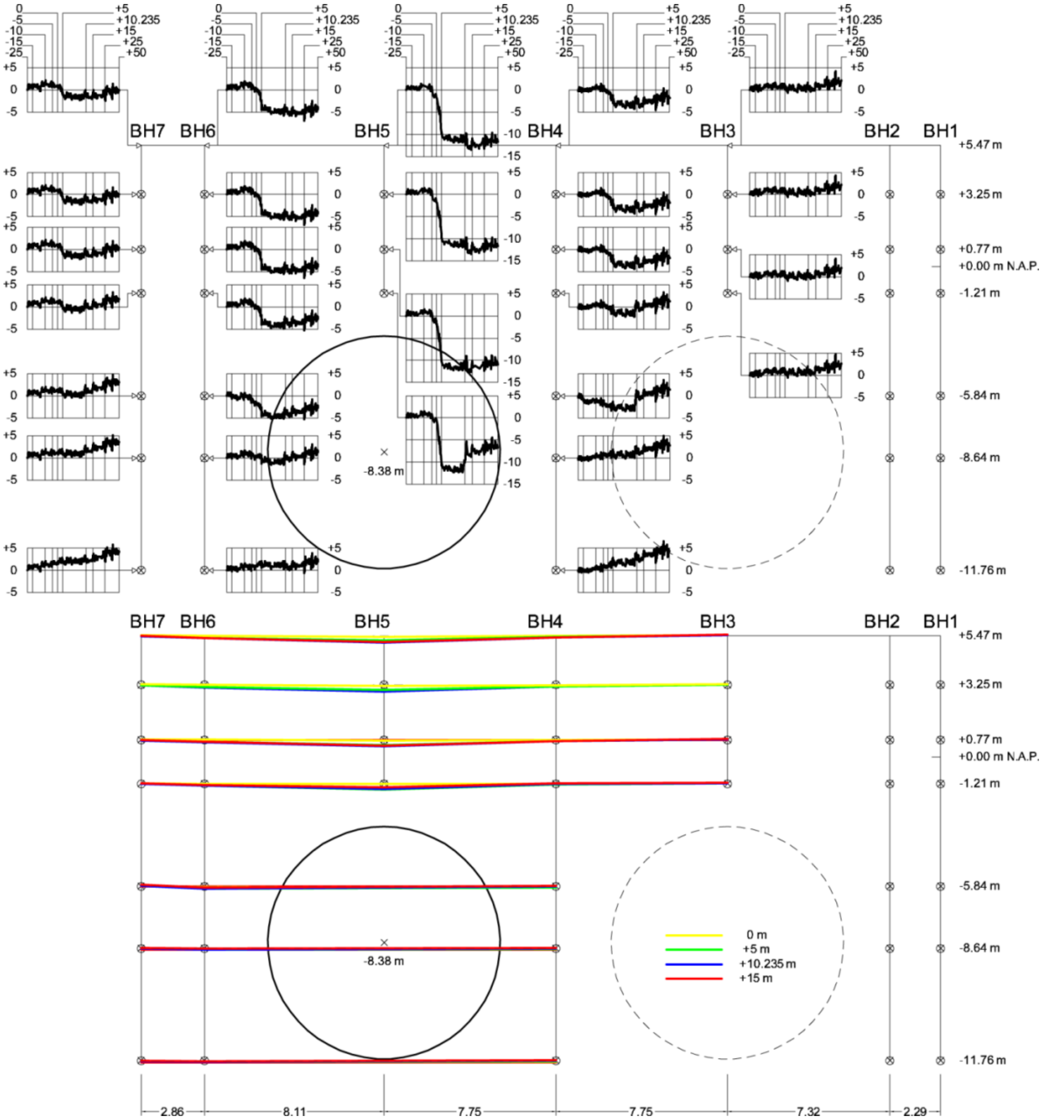

Figure 7.4: Extens. and settlement troughs at monitoring section 2 – first passage (left tube) – south tunnel – 2006. Volume loss at ground level: 0.17 %

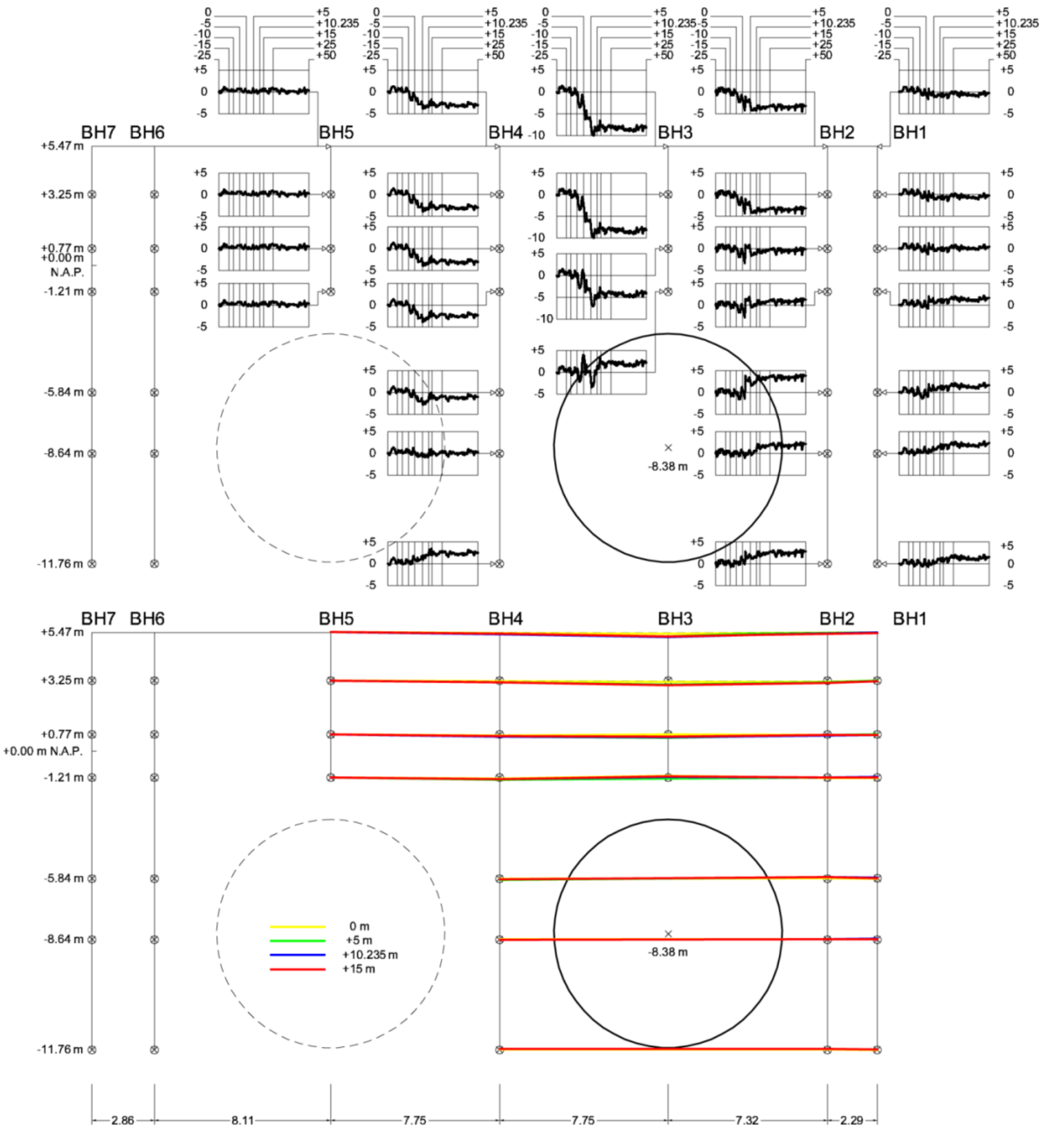

Figure 7.5: Extens. and settlement troughs at monitoring section 2 – second passage (right tube) – north tunnel – 2007. Volume loss at ground level: 0.11 %

The soil response during the crossing of the second monitoring section shows analogies with the crossing of the first one. The non-symmetrical signature of the vertical displacements is still present although less pronounced here. Settlements at the left-hand side of the tunnel under construction were larger than at the right-hand one. And also the pre-occurred soil settlements were more effectively recovered close to the tunnel than at distance. That was particularly well visible in boreholes 5 and 3 at the first and second passage, respectively. At the level of the deepest sensors the downward trend was reversed when the shield face was between +5 to +10.235 m past the monitoring section, therefore before the crossing of the shield tail.

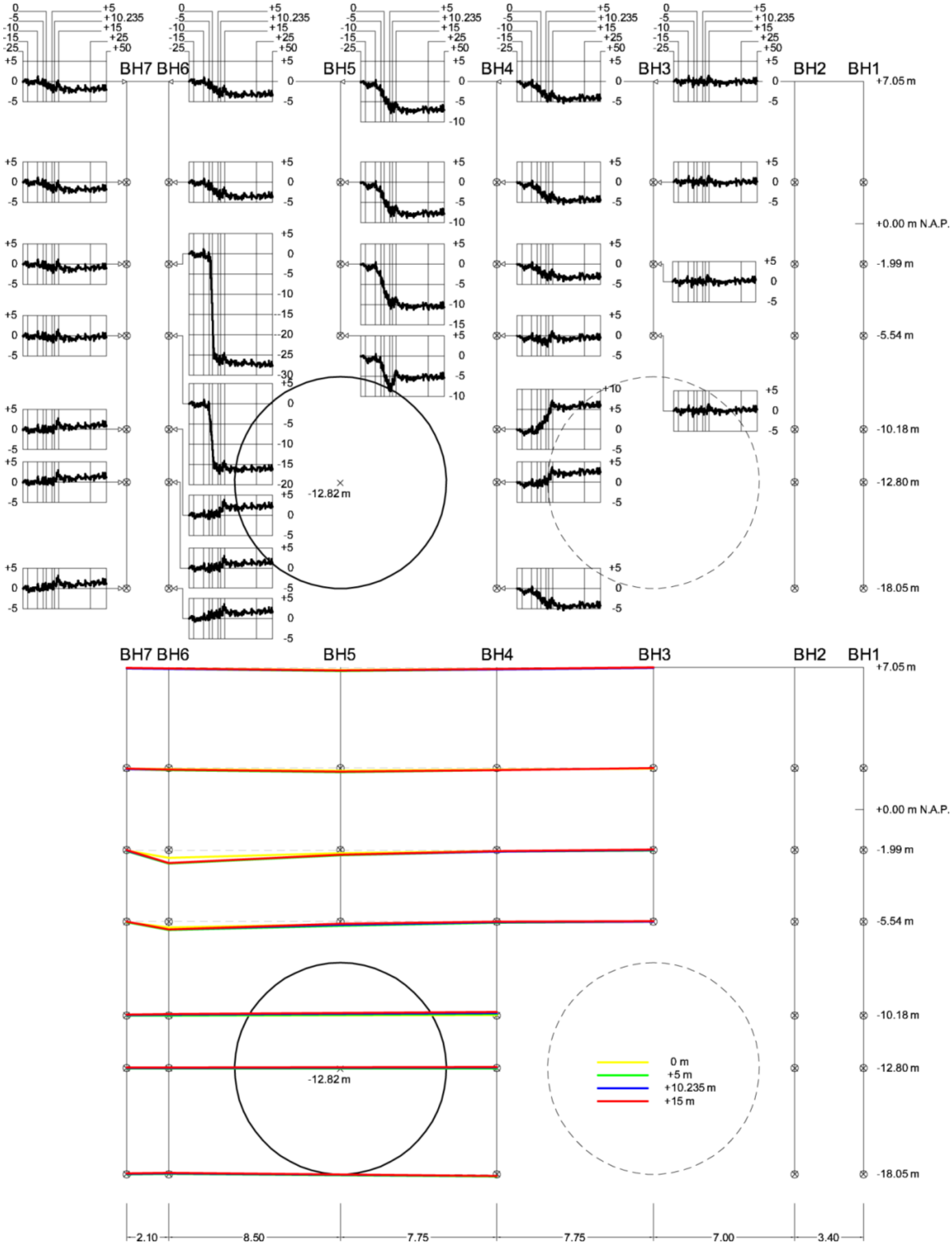

Figure 7.6: Extens. and settlement troughs at monitoring section 3 – first passage (left tube) – south tunnel – 2006. Volume loss at ground level: 0.12 %

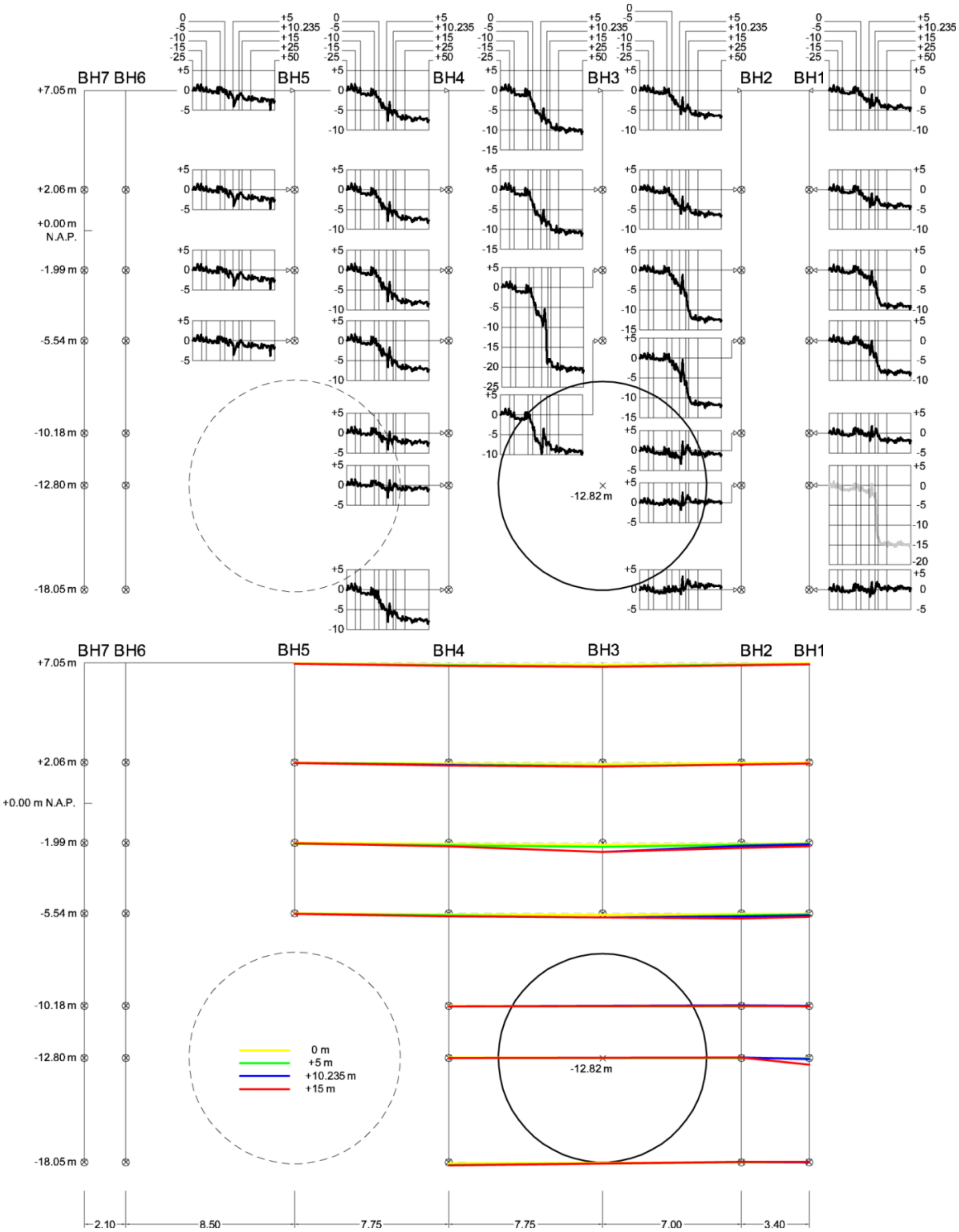

Figure 7.7: Extens. and settlement troughs at monitoring section 3 – second passage (right tube) – north tunnel – 2007. BH1 – sensor 6 out-of-order. Volume loss at ground level: 0.16 %

Observations from the first and second monitoring sections are confirmed in the third one as well. But anomalies also appear. The soil settlement's recovery above the tunnel alignments was captured in boreholes 5 and 3 during the first and second passage, respectively.

The settlements of sensors 2 and 3 in borehole 6 were unusual during the first crossing. In borehole 4 the movements changed (from top to bottom) from downward, to neutral, to upward, to downward again. This behaviour will be discussed later. During the second crossing boreholes 1 and 2 indicate soil settlement between sensors 1 to 3 and at ground level, and neutral or upward at depth. This response will be commented during the discussion of the horizontal displacements. The response of sensor 5 (-12.80 m) in BH1 was archived as reading error.

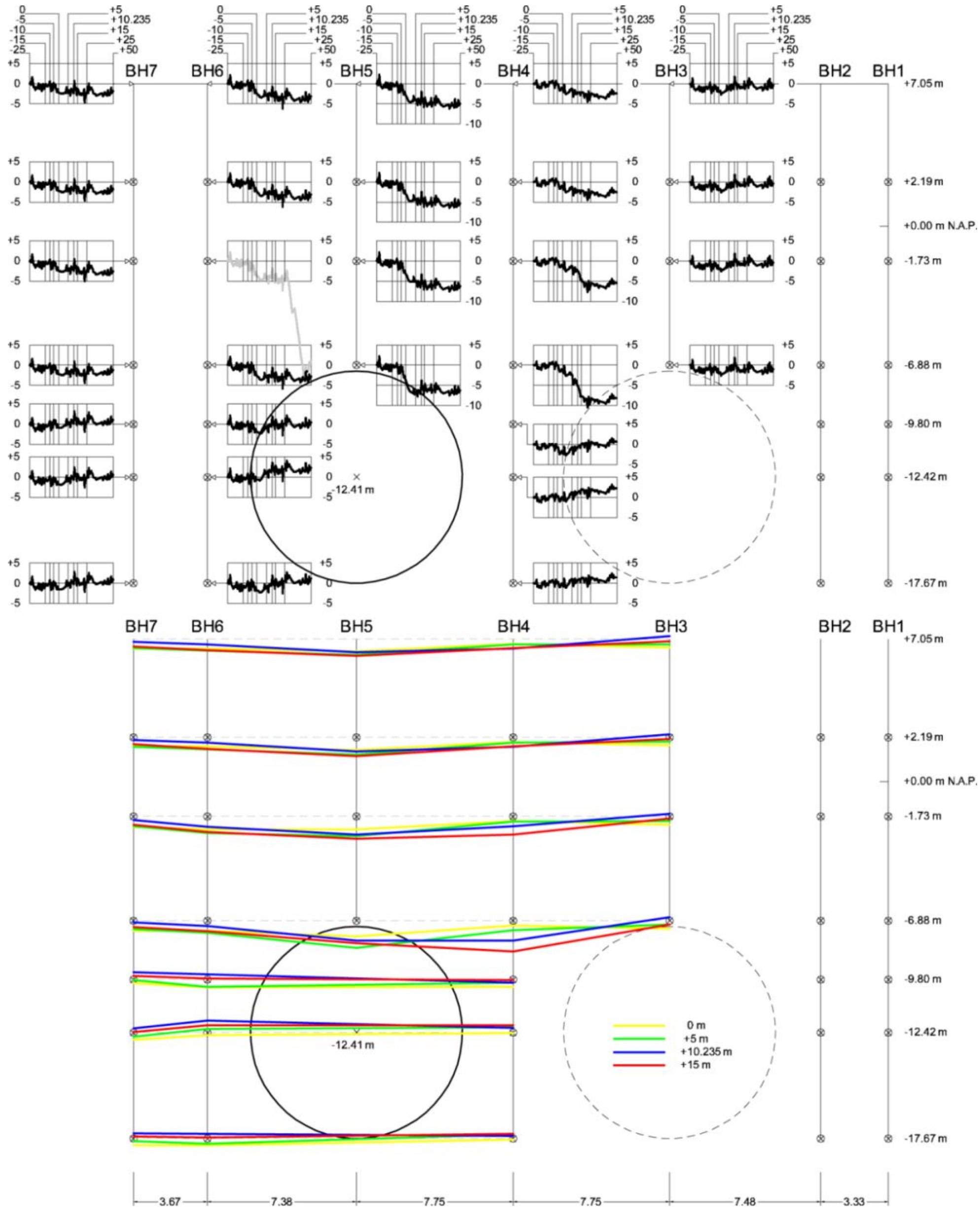

Figure 7.8: Extens. and settlement troughs at monitoring section 4 – first passage (left tube) – south tunnel – 2006. BH6 – sensor 3 out-of-order. Volume loss at ground level: 0.08 %

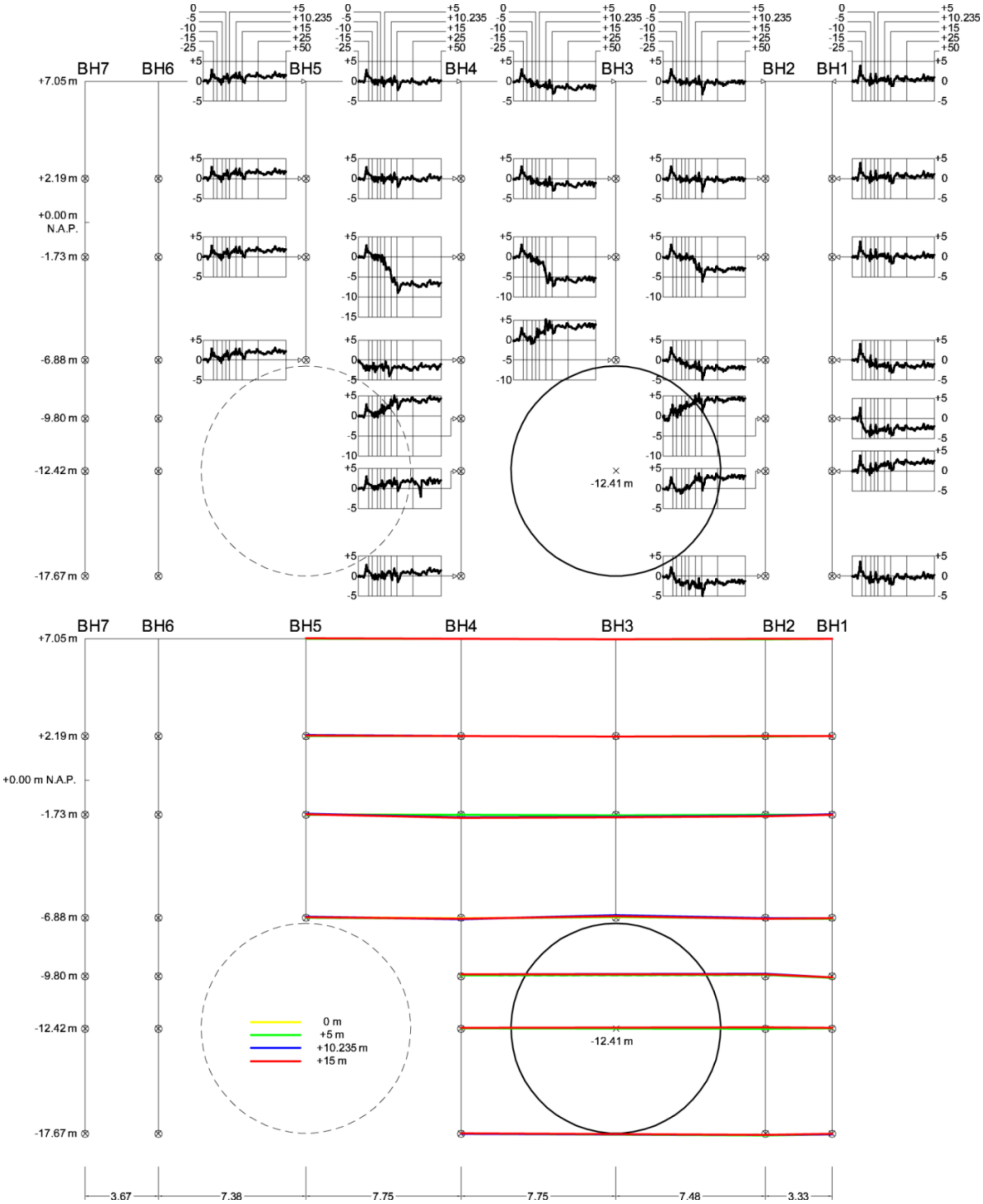

Figure 7.9: Extens. and settlement troughs at monitoring section 4 – second passage (right tube) – north tunnel – 2007. Volume loss at ground level: 0.00 %

The vertical displacements observed at the fourth monitoring section were more modest than at the other locations. During the first crossing no recovery of the modest pre-occurred settlements took place (BH5). The settlement pattern in borehole BH4 may be compared to that observed at boreholes 1 and 2 (BH1 and BH2) during the second crossing of cross-section 3.

During the second crossing of cross-section 4 the region of major interest was the one closest to the tunnel under construction. A fairly symmetrical soil response is observed there, as from the comparison between BH2 and BH4. The settlements along the two specified boreholes range from 0 mm at ground level, to -5 ÷ -10 mm around 4 m above the tunnel crown, to neutral again at the depth of the tunnel crown, to positive (+5 mm) in correspondence of the upper half of the tunnel, and then progressively neutral again at greater depths. In BH3, above the tunnel alignment, opposite behaviour was registered at the deepest and second deepest sensors.

The displacement patterns shown here originated from the analysis of four cross-sections over a 1.5 km long tunnel alignment. The number of cross-section compared to the tunnel length is disproportionately low in order to expect to have identified recurring trends. The observed behaviours do in all probability not represent the average soil response during TBM advance and tunnel construction. However several of the highlighted observations will be used in the following to correlate the TBM operation and its matching soil response.

The vertical displacement fields presented here were in line with observations by Standing and Selemetas [40]. Their work shows that the heave induced by the face support pressure is localized and dissipates quickly at distance. A similar soil response was observed here whenever earlier settlements were recovered due to face support pressures or tail grouting.

7.1.2 Inclinometers

Because inclinometers only provide relative horizontal displacements along the inclinometer's borehole, a reference point is used to convert the relative displacements into absolute ones. The reference point was taken at ground level and its movements monitored with theodolite.

The inclinometers' readings at the first monitoring section are summarized in Figure 7.10. The initial value was taken with the shield face 25 m before cross-section 1. At the first crossing the reference point was taken with the shield face 10 m before section 1.

During the first passage the soil at the left-hand side converged. The maximum convergence of 17 mm is observed at the depth of the first sensor in BH6 which was the closest borehole at the left-hand side. In BH7, about 3 m further left, a horizontal convergence of 8 mm is observed at ground level. Deeper on the same side the observed converging displacements are 10 mm in BH6 and 5 mm in BH7. At the right-hand side, the horizontal displacements ranged from -2 mm (convergence) to +2 mm (divergence) in the sector of BH4 next to the tunnel, and up to -7 mm near surface (convergence). The horizontal displacements observed during the passage of the shield were limited. The movements observed from +10.235 m onwards are likely effects of the tail void grout consolidation and of the tunnel lining deformation. Following the shield transit a convergence of only about 5 mm is observed in BH6 (left-hand side) and a divergence of 2 mm in BH4 (right-hand side).

During the first passage the horizontal displacements of Figure 7.10 are in good agreement with the vertical ones of Figure 7.2. The soil relaxation at the left-hand side (BH6) is appreciable both vertically and horizontally. On the other hand both the soil settlement and the horizontal convergence appear to be well confined at the right-hand side (BH4).

During the second passage at the right-hand side of the tunnel the soil diverged horizontally. The diverging behaviour followed a converging phase with its peak when the TBM was mid-length past the borehole (+5 m line). The maximum rightward displacement amount to 14 mm and was measured at a horizontal distance of 2 m from the tunnel (BH2). 2.44 m further in the same direction (BH1) the displacement decreased to 12 mm.

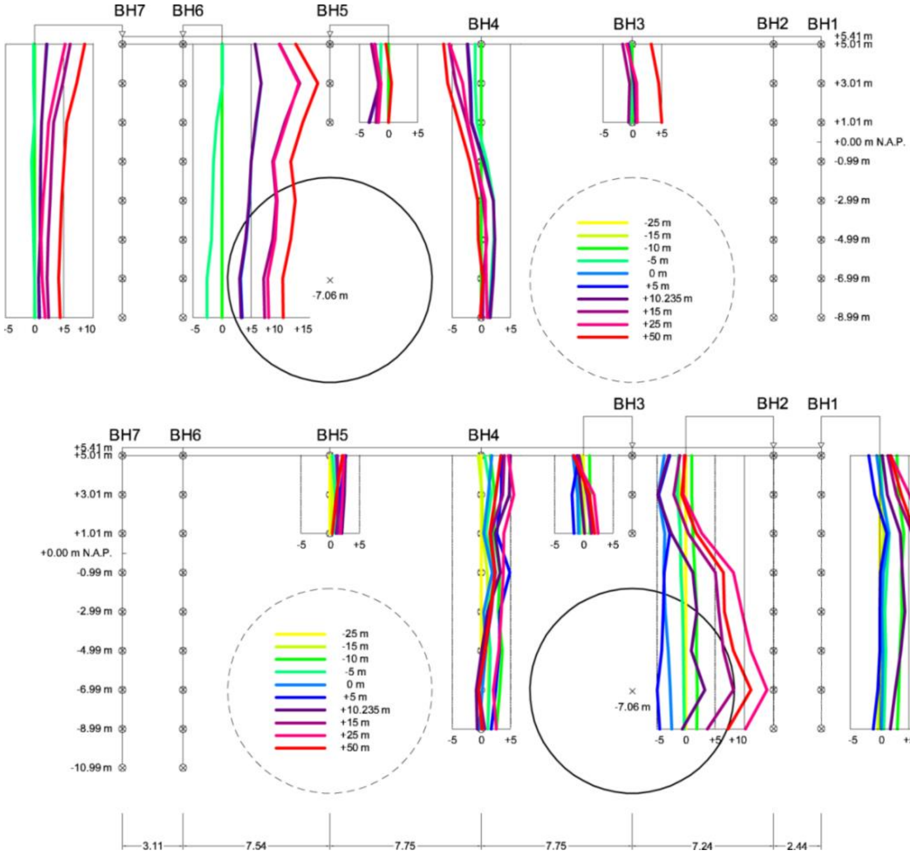

Figure 7.10: Inclinom. at monitoring section 1 – first passage (left) and second passage (right). Displacements in mm

At the second passage in both BH1 and BH2 the diverging displacements increased markedly from the passage of the shield tail onward. The peak was reached when the TBM-face was 25 m past the cross-section. At the left-hand side (BH4) neither a clear convergence nor a divergence are observed at the depth of the tunnel-axis. In the same borehole a converging displacement of 5 mm is observed closer to the ground level.

During the second passage the horizontal displacements fluctuated 5 mm at the left-hand side and 20 mm at the right-hand one. Although tempting to attribute this difference to the presence of the already constructed tunnel at the left-hand side, similar differences were observed also at the first crossing during which no neighbouring tunnel existed. Similarly to what observed at the first crossing soil relaxation occurred at the left-hand side, with vertical displacements but limited horizontal convergence. At the right-hand side, the pre-occurred vertical displacements and horizontal convergence were recovered between +5 and +10.235 m. That was caught in BH2 and BH3 above the tunnel axis (Figures 7.2 and 7.10).

As for the vertical displacements (see Section 7.1.1) also the horizontal displacements during the crossing of cross-section 2 were more limited than at cross-section 1. This was in accordance with the learning process which the tunnel drivers go through when starting the construction of a new tunnel. During the first crossing there was appreciable correlation between the recovery of the vertical movements in BH4 and BH5 in Figure 7.4, and the recovery of the horizontal displacements in BH4 in Figure 7.11. The recovery occurred between +5 and +10.235 m, therefore before the shield tail crossed the monitoring section. The horizontal recovery at the right-hand side was about 5 mm. At the left-hand side that was limited to 2 mm.

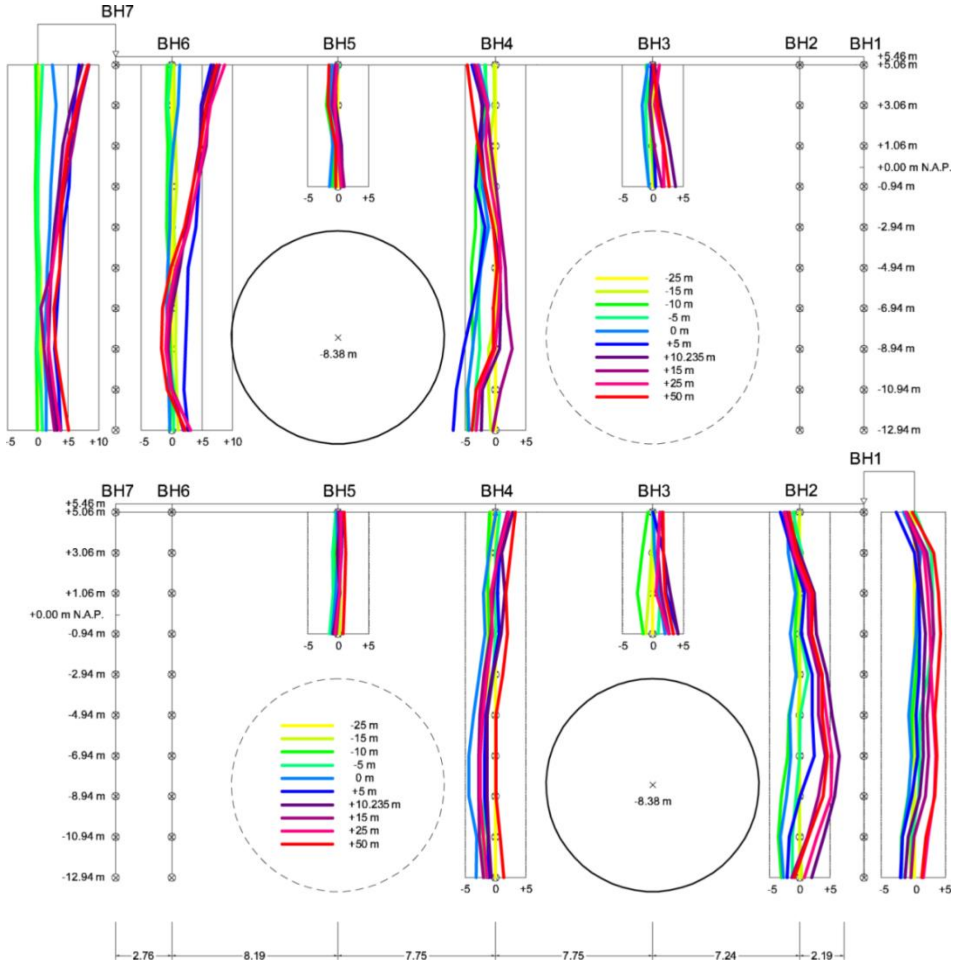

Figure 7.11: Inclinom. at monitoring section 2 – first passage (left) and second passage (right). Displacements in mm

The soil response to the second crossing of section 2 matches qualitatively well that of the first crossing. However, the horizontal divergence is at both sides slightly more pronounced during the second crossing than during the first one.

During the first passage across cross-section 3 horizontal divergence occurred at both sides with the shield face between 0 and +10.235 m. The divergence appears slightly more pronounced at the right-hand side and is in the order of 5 mm. Vertical settlements is partly recovered in boreholes BH4, BH5 and BH6 in Figure 7.6. The said vertical recovery is nicely matched by the modest horizontal diverging trend in BH4 and BH6 (Figure 7.12 – first crossing). The monitored horizontal movements in BH7 are larger than in BH6, which is unusual given that BH7 was farther away from the tunnel side than BH6.

The measured horizontal movements in BH2 during the second crossing appear unusual. The inclinometer indicates pronounced horizontal movements with the shield face still lying 10 to 15 m before the monitoring section. That is hardly correlated with the process of shield advance. However, the horizontal movements in BH1 show the same trend as in BH2 for both vertical and horizontal directions (Figures 7.7 and 7.12). This makes the observed soil behaviour more problematic and not explainable with the TBM data available only.

The horizontal divergence at the left-hand side during the second crossing is slightly smaller than during the first one. That is paired with a better recovery of the vertical settlements during the first crossing than during the second one (Figures 7.6 and 7.7).

During the first crossing of cross-section 4 no recovery of the (modest) pre-occurred vertical displacements took place (Figure 7.8). Horizontally, that could be paired with the observation that during the same crossing no divergence was recorded between 0 and +10.235 m (Figure 7.13). The registered horizontal movements occurred either before the shield face or behind the shield tail, and were therefore not directly correlated with the shield kinematic advance.

On the contrary, during the second crossing there was evidence of horizontal expansion between +5 and +10.235 m, particularly pronounced at the right-hand side. The expansion matches the uplift of the extensometer sensors at depth -9.80 m (BH2 and BH4 in Figure 7.9). The uplift measured at -9.80 m is almost absent at -6.88 m and its sign is even inversed at -1.73 m (settlement). Likewise, the region affected by horizontal divergence is limited and corresponds approximately with the tunnel height. Above that, the disturbance dissipates quickly.

This particular behaviour may explain how sign inversion could occur inside a single extensometer borehole, measurement errors aside. A global effect of tunnel construction and a local effect due to detailed advance operations of the TBM should be distinguished. An example is provided by the vertical displacements during the second crossing of section 4 (Figure 7.9).

Comparing the three settlement troughs at depths +2.19 m, -1.73 m and -6.88 m, the concavity's direction appears to change, with a hogging shape at -6.88 m, and a sagging one at -1.76 and +2.19 m. That means that the effect of the physical process that induced the hogging concavity closer to the tunnel did not propagate farther from it. That also hints that while local inversions of the soil deformation path are achievable, global inversion or complete recovery of all the pre-occurred movements are harder to reach.

The subsurface horizontal soil displacement fields described in this section are in line with those presented in Standing and Selemetas [40] in that the horizontal tunnelling induced soil displacements can be asymmetric between opposite sides and the effect of expansive behaviours (compressive strains) tends to dissipate very quickly through the soil as the distance from the tunnel increases.

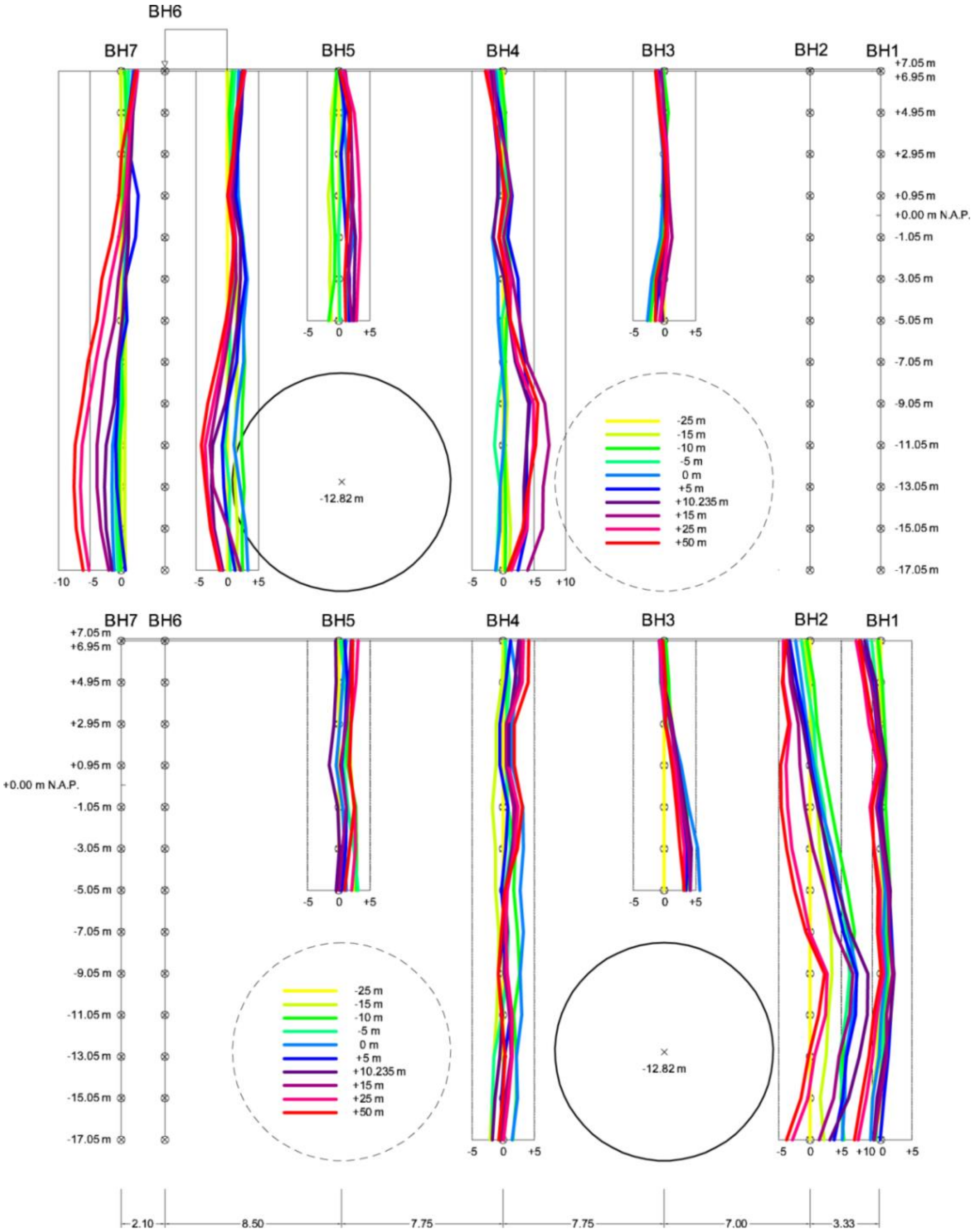

Figure 7.12: Inclinom. at monitoring section 3 – first passage (left) and second passage (right). Displacements in mm

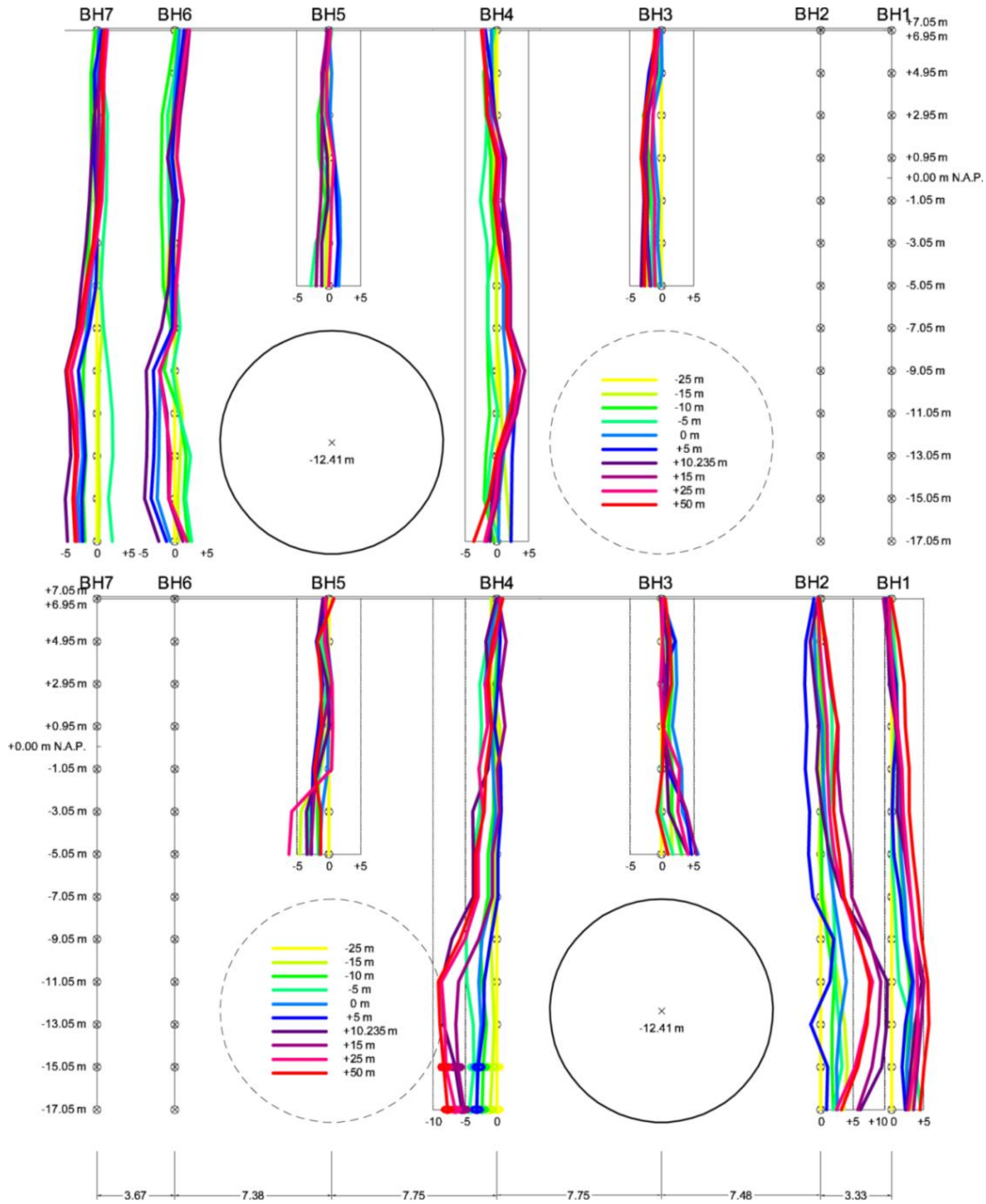

Figure 7.13: Inclinom. at monitoring section 4 – first passage (left) and second passage (right). Displacements in mm

7.2 Propagation of the interface displacements through the soil

The calculated shield-soil interface displacements and the observed soil response are compared. Before entering into such comparative analysis selected results of the kinematic study introduced in Chapter 4 are recalled.

The shield-soil interface displacements were quantified by accounting for the relative distance between the shield-skin and the wall of the excavated geometry. The kinematic interaction was studied both theoretically and based on the logged shield positioning data.

The theoretical analysis, supported by the scheme of Figures 4.1 to 4.4, concluded that the shield advance along a curved alignment can produce both compression and extension, the spatial distribution of which depends on the combination of shield geometry, alignment's features, and arrangement of the shield reference points (RPF and RPR). The analysis produced the progress of the interface displacements along the shield length.

The logged data-based analysis was performed by means of a purpose-built numerical code. The consecutive positions of the shield were compared with the excavated geometry, in turn obtained as the record of the consecutive positions of the cutter head as the TBM advanced, and that allowed to quantify the displacements induced by the advancing shield at the shield-soil interface. The existence of sectors of the shield periphery where the surrounding soil is compressed and others where it is relaxed was demonstrated, as summarized in Figure 7.14. The colour lines represent the interface displacements over the shield length. The black lines connecting the end points of the colour lines represents the soil deformation (compression or extension) at the shield tail.

It is observed that the colour lines start at the front from different interaction values (right-hand end of each line). Were the radius of the cutting wheel smaller than that of the cutting edge, then the excavated geometry would be determined by the cutting edge only. Consequently, at the front the shield-skin and the excavated geometry would be coincident and the interaction distance would be 0. At Hubertus tunnel the radius of the cutting wheel was 0.01 m larger than the cutting edge, also referred to as *standard overcutting*. The excavated geometry was thus defined by the combination of the track of the cutting wheel and that of the cutting edge. Additionally, the articulation of the cutting wheel allowed to increase or decrease the amount of overcutting by adjusting the relative angle between the shield axis and that of the cutting wheel. The combination of standard overcutting and cutting wheel articulation made possible that different interaction distances at the shield front were modelled at different advances.

In Chapter 4 the peculiarity of the unloading-reloading configurations on behalf of the surrounding soil was also underscored. Figure 7.14 (lower half) provides an example of such configuration over the interval -1580 ÷ -1575 of. In that sector the tail interaction line (black line) falls into the domain of the grey lines. That happening in the negative region means that the current soil compression there is lower than that already reached at an earlier stage at the same location. Thus, the pre-loaded surrounding soil is being unloaded.

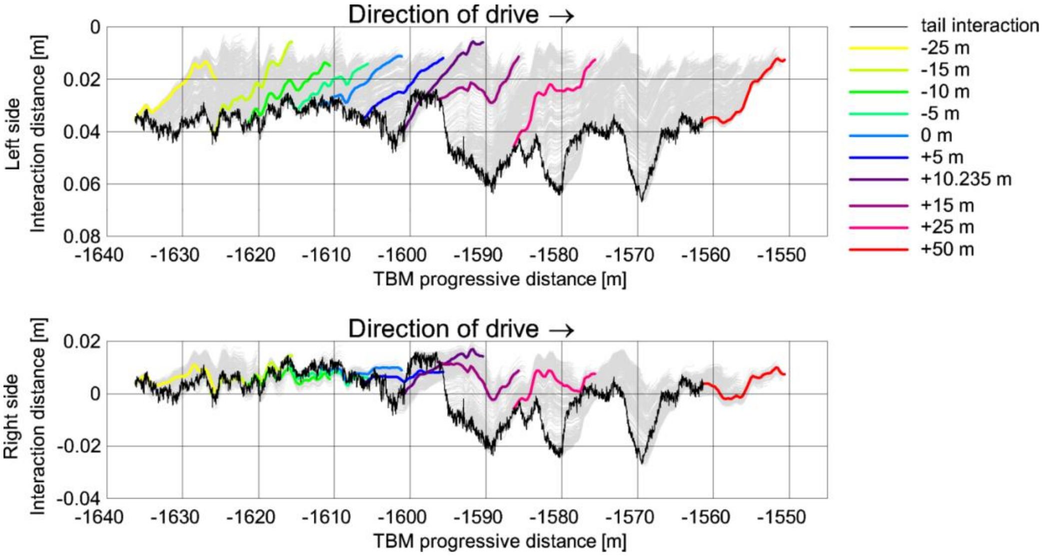

Figure 7.14: Example of shield-soil interface displacements around monitoring section #1 – north tube. The colour lines represent the interaction diagram over the shield length. Each colour represents the interaction at a different advance stage. The intermediate stages are in grey. The black line connecting the end points of the colour lines represents the soil deformation at the shield tail

7.2.1 Calculated interface displacements and observed soil movements

Each of the graphs in Figures 7.17 to 7.20 shows the observed shield-soil interface displacements that occurred at the shield tail along with the corresponding observed soil response. The horizontal soil displacements are presented at the depth of the tunnel axis, the vertical movements are those measured by the first and second extensometers above the tunnel axis. The sign convention differs from that adopted in Figure 7.14 and matches the intuitive meaning of lateral displacement in relation to the position of the tunnel axis. If the shield had no tapering and perfectly followed the excavated geometry, the tail interaction lines would be vertical lines crossing 0. Positive shield-soil interaction represents soil extension on the left-hand side and soil compression on the right-hand one. Vice versa, negative interaction represents soil compression at the left-hand side and soil extension at the right-hand one.

The shield-soil interaction lines (i.e. interaction displacements) represent the amount of displacement induced by the shield tail at the shield-soil interface. In the graphs, when the TBM face is at the monitoring section (0 on the y-axis), the shield tail is 10.235 m behind. Nevertheless, the interaction value is drawn at distance 0, and not at -10.235 m. In this way the consistency is preserved between the shield-soil interaction and the soil response lines and between the values that those represent in time.

At the first cross-section horizontally the soil responded differently between first and second crossing even if the shield-soil interaction was comparable. The sector of major interest is between 0 and 10.235 m, coincident with the crossing of the monitoring section by the shield face and tail, respectively. During the first passage a soil relaxation of 20 ÷ 40 mm occurred at the left-hand side and a relaxation of 0 ÷ 20 mm at the right-hand one, both referred to the shield-soil interface. That is paired with a monitored convergence of less than 10 mm at the left-hand side and a neutral response at the right-hand one.

During the second passage at the left hand side a relaxation of 20 ÷ 60 mm occurred at the shield-soil interface, whereas at the right-hand side the interface displacements ranged between a relaxation of 20 mm and a compression of similar magnitude. The soil responded neutrally at the left-hand side, and first converging than expanding at the right-hand one. At the right-hand side direct correlation can be appreciated between the compression at the shield-soil interface and the measured expansive behaviour farther away from the tunnel.

The diverging displacements measured into the soil at the right-hand side – second passage – were attenuated compared to those calculated at the shield-soil interface. That could be expected for a couple of reasons. First, the closest inclinometer borehole is located at 2.50 m from the shield skin. Second, a plastic zone is likely to have originated in the vicinity of the contact area further limiting the spreading at distance of the induced displacements. This latest aspect is confirmed by the cavity-expansion theory in elastic-plastic soil conditions (Yu [51]).

In case of soil relaxation, even in presence of theoretical extension at the shield-soil interface – left-hand side, both crossings – a feeble convergence shows up during the first crossing and neutral response during the second one. This suggests that a unique deterministic relationship between shield-soil interface displacements and soil response does not exist. Other aspects must have played a role of at least the same order of magnitude as the kinematic interface behaviour.

A possible correlation is sought in the comparison between the grouting pressures during first and second passage of the TBM through the monitoring section. The grouting pressures during first and second passage are shown in Figure 7.15and Figure 7.16, respectively. Quite differently than expected the grouting pressures were not higher during the second passage than during the first one. At least during the transit of the TBM-shield across the monitoring section, that is between 0 and +10 m on the x-axis.

However, data shows that substantially different grouting pressures were applied after +8 m. During the first passage the average injection pressure between +8 and + 16 m fluctuated between 150 and 400 kPa. During the second passage the average pressure remained quite consistently around 400 kPa. This might partly explain the soil expansion at the right-hand side after the second passage and the support of the excavated geometry at the left-hand side during the same passage. This is in agreement with Bezuijen et al. [1] who recognized that the injection strategy can influence the pressure distribution also few metres behind the TBM during drilling.

In the review of the following monitoring cross-sections 2, 3, and 4 similar considerations could be made concerning the compensating effect of the grouting pressures. However, being the found correlation between kinematic behaviour, grouting pressure, and soil response only partially conclusive more comparisons of the same kind are omitted and advice is given for more specific research to be conducted on the topic.

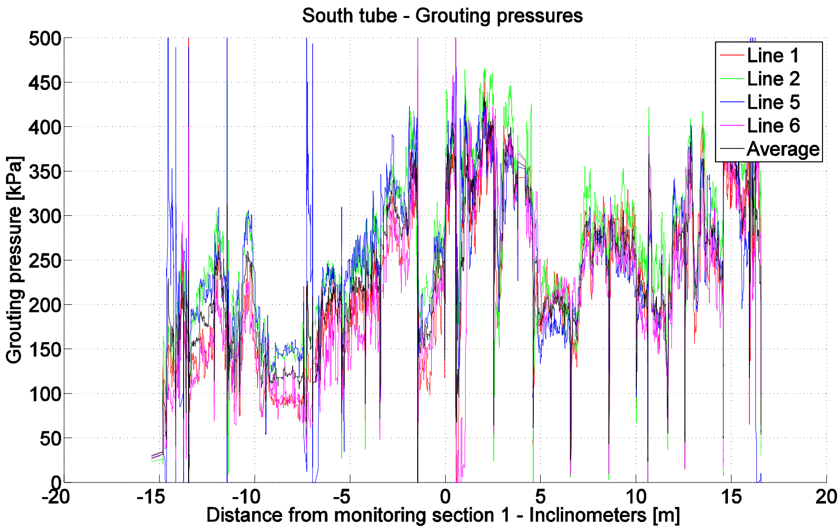

Figure 7.15: Monitored grouting pressures during the transit across the first monitoring section – south tube – first passage (2006). 0 on the y-axes corresponds to the shield face at the monitoring section; 10 corresponds to the face 10 m after the instrumented section

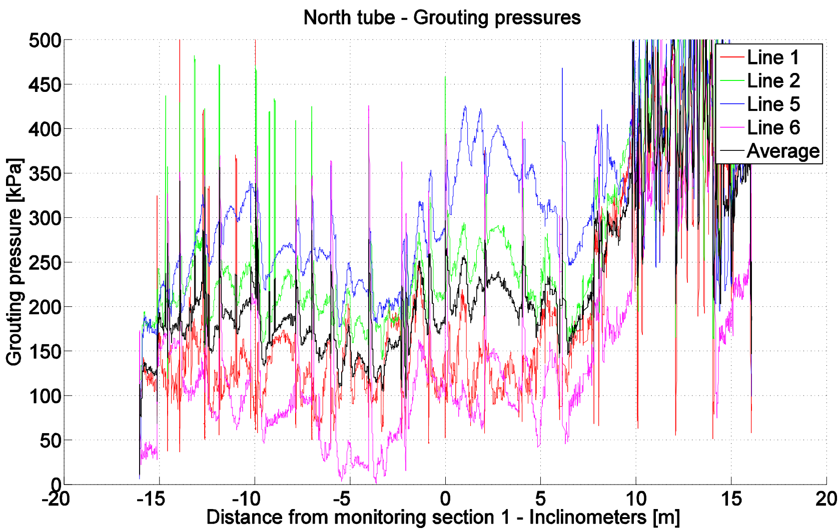

Figure 7.16: Monitored grouting pressures during the transit across the first monitoring section – south tube – second passage (2007). 0 on the y-axes corresponds to the shield face at the monitoring section; 10 corresponds to the face 10 m after the instrumented section

A further clue may be found in the different vertical soil response observed directly above the tunnel between first and second passage. In the sector of interest (shield face between 0 and 10.235 m) no particular "gaps" or compressions were observed at the shield-soil interface in the region of the shield tail. During the first crossing a maximum compression of the shield against the soil of 10 mm was observed, opposed to a maximum relaxation of 20 mm during the second crossing. Nevertheless, while during the first passage the vertical settlements progressed downward without measurable rebound, during the second passage the pre-occurred settlements recovered remarkably. These aspects are clearly visible both in the graphs of Figure 7.17 – top side – and Figures 7.2 and 7.3.

The settlement recovery is particularly effective close to the tunnel top and less and less effective moving further upward. The response of the extensometer sensor closest to the tunnel shows that the upheaval started when the tunnel face was between 5 and 10 m after the control section. This suggests that tail-void grouting can produce a compensating effect even before the shield tail crosses the control section.

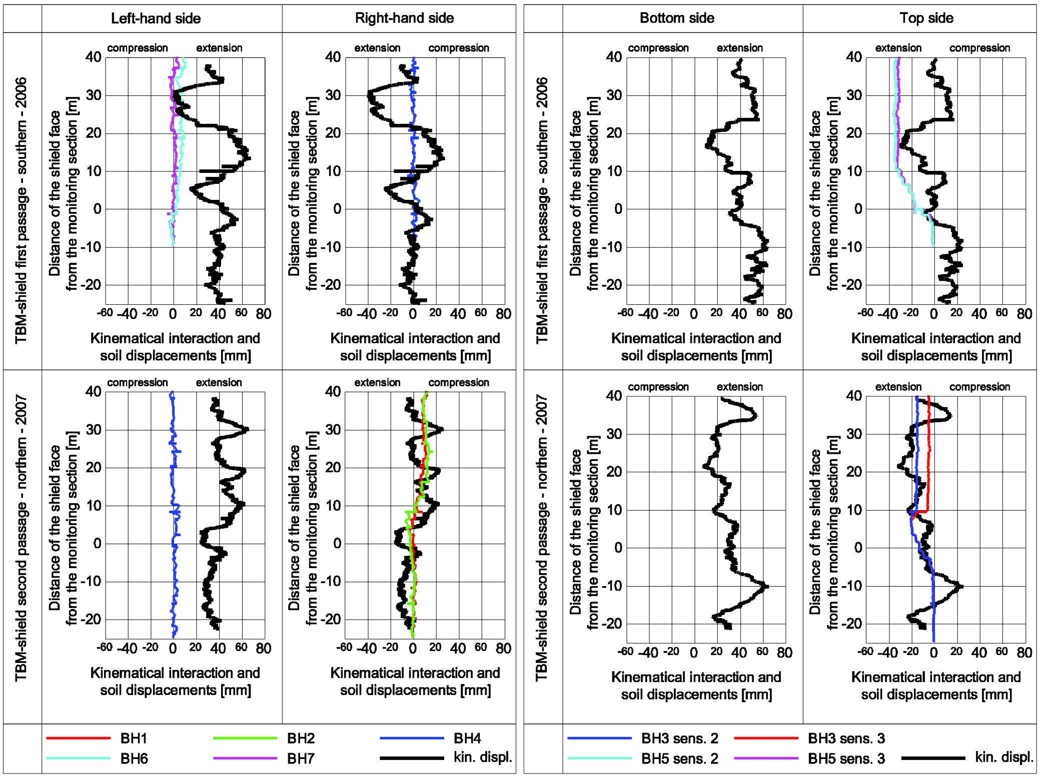

Figure 7.17: Shield-soil interaction and soil response – cross-section 1. On the x-axes: calculated shield-soil interface displacements (black) and observed soil response (colours). On the y-axes: distance of the shield face from the monitoring section. 0 on the y-axes corresponds to the shield face at the monitoring section; 10 corresponds to the face 10 m after the instrumented section

At the second cross-section the horizontal soil response was similar but attenuated compared with that at the first one (Figure 7.18). This held for both crossings. The shield-soil interface displacements were also comparable, with “gaps” of 20 to 60 mm at the left-hand side and compressions up to 20 mm at the right-hand one. During the first crossing the surrounding soil responded with a slight converging trend at the left hand side and a neutral one at the right-hand one. During the second crossing, the convergence at the left-hand side was compensated and a small expansion at the right-hand side was observed. As for the first cross-section, a unique deterministic relationship does not seem to exist between shield-soil kinematic interface displacements and soil response. This confirms that other aspects must have played a role.

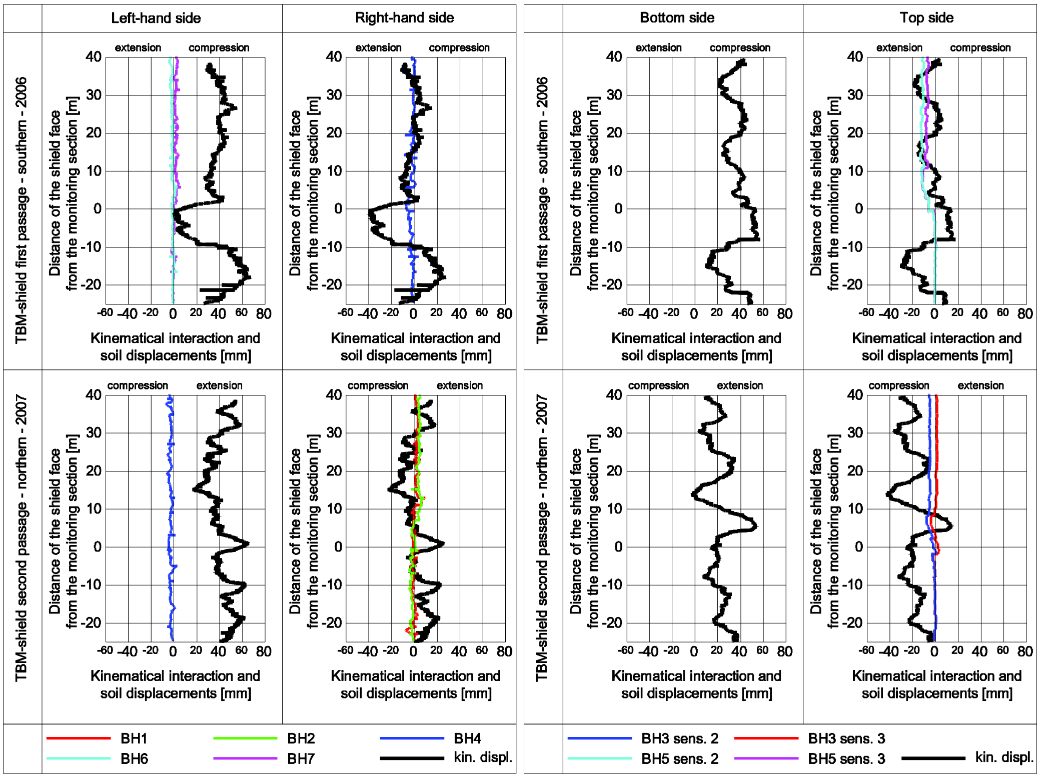

Figure 7.18: Shield-soil interaction and soil response – cross-section 2. On the x-axes: calculated shield-soil interface displacements (black) and observed soil response (colours). On the y-axes: distance of the shield face from the monitoring section. 0 on the y-axes corresponds to the shield face at the monitoring section; 10 corresponds to the face 10 m after the instrumented section

Differences emerged with the first cross-section concerning the vertical response. During both first and second crossing the induced soil settlements were more limited at the second cross-section than at the first one. First of all, at the second cross-section a recovery of the pre-occurred settlements occurred as well as during the first crossing. That was observed close to the tunnel top (sensor number 3 in BH5) and progressively less moving further upward. The pre-occurred settlements were recovered also during the second crossing. In this last case two distinct recoveries occurred, the first upon arrival of the shield face at the cross-section, and the second between +5 and +10.235 m, therefore during the transit of the second half of the shield.

These vertical soil responses were matched with the shield-soil kinematic interaction at the shield tail. During the first crossing the vertical interface interaction at the second cross-section was not much dissimilar to that at the first cross-section. During the second crossing at the first cross-section the shield tail interacted pretty neutrally with the excavated soil but with a relaxation of about 20 mm around +10 m (near the passage of the shield tail through the monitoring section). Differently, during the second crossing at the second cross-section the shield tail interacted with the excavated soil fluctuating between a relaxation of 20 mm and a compression of similar extent. That may have contributed to the reduction of the induced settlements at the second cross section – second passage – compared to the first cross section – second passage.

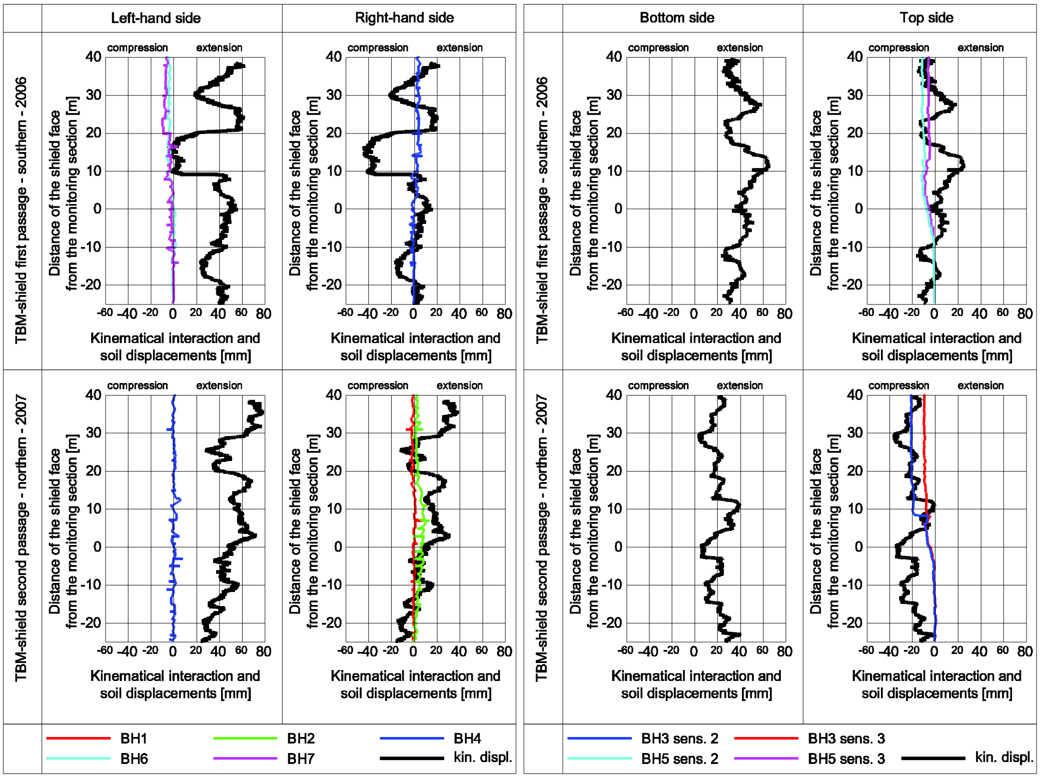

Figure 7.19: Shield-soil interaction and soil response – cross-section 3. On the x-axes: calculated shield-soil interface displacements (black) and observed soil response (colours). On the y-axes: distance of the shield face from the monitoring section. 0 on the y-axes corresponds to the shield face at the monitoring section; 10 corresponds to the face 10 m after the instrumented section

The difference in terms of soil response between second and third cross-sections is not significant. A slightly larger horizontal expansive behaviour (divergence) was observed during the first passage at section 3 when compared with the first passage across sections 1 and 2. Shield-soil interface displacements were similar. Also during the second crossing no relevant differences were observed. When the shield "pushed" against the surrounding soil – as for example at the right-hand side of the second crossing – a somewhat larger divergence occurs. The horizontal displacements measured into the soil were smaller than the ones calculated at the shield-soil interface. The attenuation is attributed to the distance of the borehole from the shield skin (1.80 m in this case) and to the plastic deformation of the soil close to the contact area.

At the left-hand side, where a significant shield-soil interface "gap" was calculated, very limited convergence was measured. This newly demonstrates that, assuming the TBM kinematic model is correct, other relevant processes occur that have not been quantified yet. A likely candidate is the penetration of tail grout in the tail-void between the shield skin and the excavated geometry. Partial or complete "compensation" of the converging effect in the sectors where the soil is relaxed is observed at all three cross-sections so far investigated.

The observed vertical soil response and the calculated vertical kinematic interaction at cross-section 3 are in line with those at cross-sections 1 and 2. A modest recovery of the pre-occurred settlements appears during the first passage and more markedly during the second one. The graph of the vertical displacements at the top side during the second passage confirms that the recovery of the pre-occurred settlement is usually achievable close to the tunnel top but much less at distance. This behaviour is recurrent in all three cross-sections so far investigated.

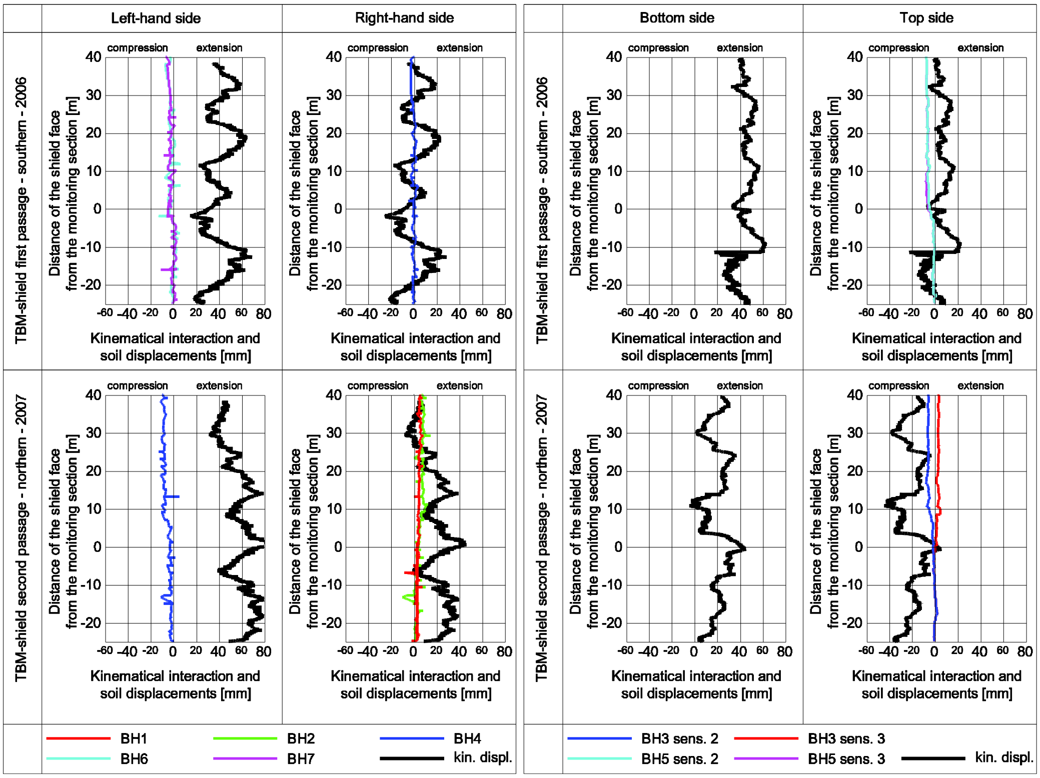

Figure 7.20: Shield-soil interaction and soil response – cross-section 4. On the x-axes: calculated shield-soil interface displacements (black) and observed soil response (colours). On the y-axes: distance of the shield face from the monitoring section. 0 on the y-axes corresponds to the shield face at the monitoring section; 10 corresponds to the face 10 m after the instrumented section

At the fourth cross-section the horizontal soil response during the first crossing was similar to those already observed at the other sections. The overall horizontal displacements were almost neutral on both sides. Also the shield-soil horizontal interface displacements during the first crossing were in the range observed at other locations. Differently, during the second crossing, the horizontal diverging trend was quite symmetrical and larger than at all other sections. The soil relaxation at the shield-soil interface at the left-hand side, with a peak value of 80 mm, was the largest among all the monitored cross-sections.

The fourth cross-section shows peculiarities also concerning the vertical soil response and the associated interface displacements. During the first crossing the shield-tail stayed constantly in contact with the excavated soil, the interface compression ranging from 0 to 20 mm. That leads to one of the smallest settlements so far observed. Moreover, the soil above the tunnel was well supported all along the transit of the shield, and that prevented larger settlements to occur. Those settlements, as seen before, once occurred are hardly recoverable except for the near vicinity of the tunnel being built.

During the second crossing of cross-section 4 the pronounced recovery of the pre-occurring settlements led to an inversion in the direction of the total vertical displacements in the soil sector above the tunnel axis. The vertical displacements turned upward closer to the tunnel and remained downward oriented farther from it.

The displacements applied at the boundary between the tunnel and the surrounding soil dissipate into the soil farther from the tunnel cavity. Figures 7.21 and 7.22 show the numerical results of how the applied displacements dissipate when a purely horizontal or an axial-symmetric expansion are applied, respectively. Both models assume planar conditions, which overestimates the soil deformations at distance. Nevertheless, at a distance comparable to the tunnel radius (about 5 m here) the soil displacements are about half than applied at the tunnel-soil interface. The dissipation at the extension side (left-hand side in Figure 7.21) is even more rapid with the distance from the tunnel. This must be considered as the boreholes with inclinometers and extensometers are installed approximately at 2.50 and 7.50 m from the tunnel periphery. A strong dissipation of the applied displacements may then be expected.

Combining the observed horizontal and vertical soil response it seems that even if the shield-soil kinematic interaction plays a role on the tunnelling-induced soil displacements, an even or more important role was played by the grouting process. This is suggested by three observations: 1) the surrounding soil often did not converge towards the tunnel even in presence of a theoretical relaxation at the shield-soil interface; 2) in several circumstances the soil response was more expansive than in others even if the kinematic interaction at the shield-soil interface was comparable; 3) most rebounds from the pre-occurred vertical displacements could not be explained from kinematics-related reasons.

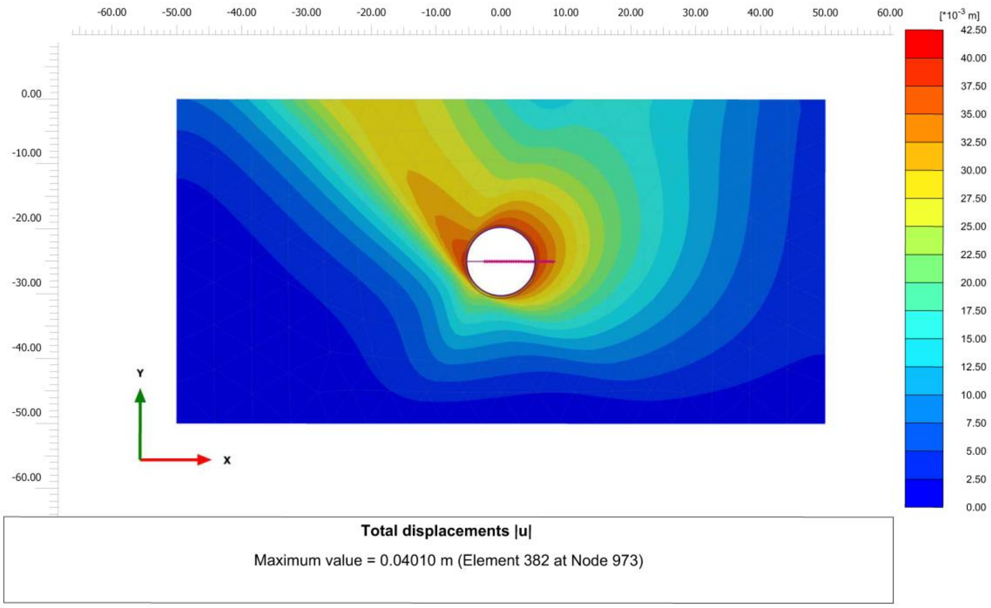

Figure 7.21: Soil displacements induced by a purely rightward horizontal translation of the tunnel cavity of 40 mm

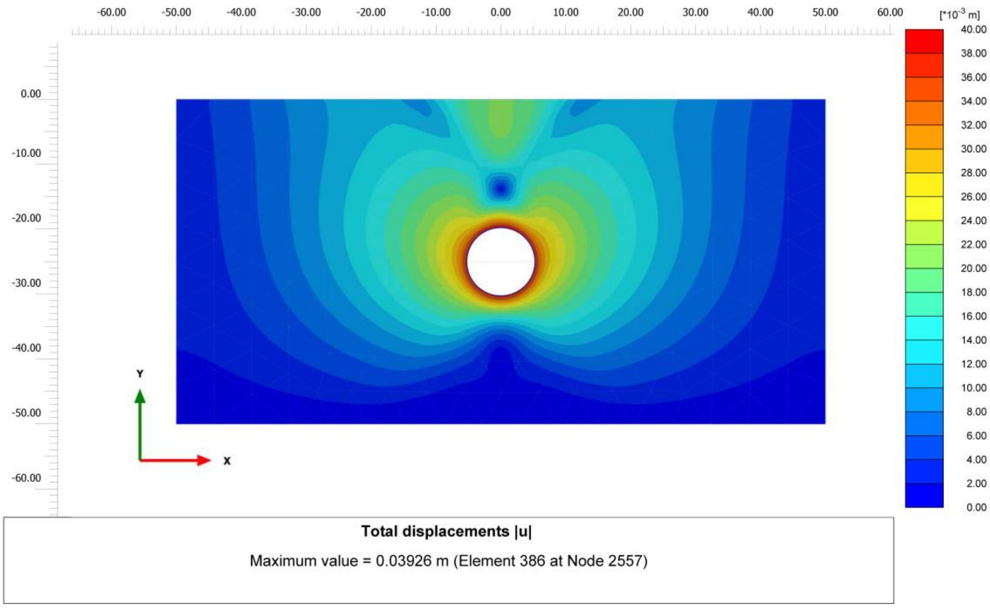

Figure 7.22: Soil displacements induced by a radial axial-symmetric expansion of the tunnel cavity (with fixed tunnel axis) of 40 mm

Chapter 8

Conclusions and recommendations

This thesis investigated the interaction between a TBM-shield and the surrounding soil focussing on the static equilibrium of the TBM and on the soil response. Results shed new light on stresses and soil deformations at the shield-soil interface.

The analysis, based on data derived from the Hubertus tunnel bored in Pleistocene sands, was limited to soft-soil conditions. Drained soil behaviour has been assumed. The construction of the Hubertus tunnel, thanks to extensive TBM and soil-displacement monitoring data, gave the opportunity to derive physical relationships between those two data-sets.

8.1 Conclusions

The kinematic model, based on theoretical assumptions and on TBM monitoring data, demonstrates that the advancing shield produces a more complex soil deformation pattern than simplistically assumed by the 'volume loss' scheme. The processed TBM positioning data show that the shield advance induces an irregular pattern of compression and relaxation zones at the shield-soil interface up to 50÷100 mm. Relaxation is usually larger than compression due to the tapering of the shield. Such interface deformations are calculated comparing the position of the actual excavated geometry, including the overcut effect due to the orientation of the cutting wheel, with the exact shield position and orientation within the longitudinal cavity. The proposed kinematic model is capable to distinguish between virgin loading and unloading-reloading configurations by keeping memory of the displacements occurring at each location of the excavated geometry. It is therefore capable to model the history of the soil deformation around the shield. A realistic picture of the soil deformation path proves essential given the strongly non-linear soil behaviour. The extent and spatial distribution of compressions and extensions is the input to model the soil stress distribution on the shield periphery.

Internal and external forces acting on the TBM are studied in the model of static equilibrium. The internal – active – forces are retrieved from the TBM-monitoring data with limited processing, whereas the stress distribution on the shield periphery – passive force – derives from the output of the kinematic model combined with a suitable stress-strain relation. The stress-strain relation is obtained from the actual deformation path by means of novel soil reaction curves which are analytical approximations of the results of FEM calculations. The approach proves fast and effective within the scope of the present analysis.

In a simplified framework in which the penetration of process fluids around the shield-periphery is excluded it is demonstrated that over several advance sectors the static equilibrium of the TBM can be achieved satisfactorily via its exact interaction with the soil. However, numerous locations with only poorly achieved equilibrium point to excessive model simplifications. Two aspects emerge: first, a component of the transversal force appears to lack in order to achieve global equilibrium in the sectors of soil relaxation; second, the hypothesis of a constant friction coefficient between the shield and the soil is found little realistic and not capable to guarantee consistent longitudinal equilibrium. The overall reliability of the shield positioning system is also questioned. In this respect the logged shield positioning data, although generally reliable, show several scatters which are most probably the consequence of recalibrations of the measuring system. Lack of log books means this cannot be settled conclusively.

The presence of process fluids in the interspace between the shield skin and the excavated geometry is added to the static model and found to provide for better equilibrium. The enhanced model assumes that pressurized grout mortar injected at the shield-tail may infiltrate the interspace around the TBM-shield when the fluid pressure is larger than the total radial soil stress at the same location. In this framework the infiltrating pressurized mortar can support a higher stress level and provide a complementary transversal force. The infiltrating mortar also affects the extent of the friction between the shield and the soil in this way determining improved TBM longitudinal equilibrium.

The complexity of the relation between shield advance and soil response, hardly considered in literature relating surface and subsurface displacements to machine parameters (Mair et al. [26]), is also investigated in this thesis with promising results. Good relation is found between the shield-behaviour and the observed soil response when the shield ‘pushes’ against the excavated geometry creating compression zones. The surrounding soil appears to diverge consistently. The match is less clear when soil relaxation is induced. Even when relaxation of the excavated geometry of several centimetres is expected the convergence of the surrounding soil is in fact hardly observed. This indicates that the process fluids are capable of compensating for the kinematic effect of shield advance by infiltrating around the shield, and thereby of limiting the amount of soil deformation actually induced.

With the limit of the investigated soil type (drained granular material – sand) it is concluded that tail-void grouting, although necessary is in fact little effective at recovering pre-occurred settlements. Observed subsurface displacements show that recovery is limited to few meters beyond the shield periphery. Analytical cylindrical cavity expansion theory confirms that also in elastic-perfectly plastic conditions the mass of soil undergoing expansion is limited compared to purely elastic conditions. Yielding occurs in a region nearby the tunnel, and that region absorbs most of the strains inducing even more rapid strains’ decay farther away. This leads to the important conclusion that avoiding settlements is essential since recovering them afterwards is challenging.

Predictions of tunnelling-induced soil displacements are still often based on the experience gained from previous projects in similar conditions and based on the ‘volume loss’ indicator. ‘Volume loss’, although a good marker of the overall quality of tunnel construction, performs poorly when used to explain the mechanisms that cause such displacements. Aspects like the TBM features and its real kinematic behaviour are not usually incorporated in prediction models, and cannot be addressed via the volume loss scheme.

Some of the concepts proposed in this thesis may lead to more innovative TBM driving strategies and to more consistent surface and subsurface soil settlement predictions. The current trial-and-error TBM driving procedure could for instance be enhanced by means of an algorithm which, based on the proposed framework of TBM static balance, aims to minimise the driving forces. Similarly, predictions of soil displacement could be based on the anticipated TBM-shield kinematic interaction, in turn obtained combining TBM properties (geometry and weights), soil characteristics, and driving strategy (fluid pressures and advance rate).

Examples of complete models of shield advance have been proposed by others in recent years (Nagel [32]). Even if such models are enviably close to becoming of practical use, they at times lack in incorporating fundamental principles governing the shield-soil interaction, either at the excavation front, or at the shield tail, or between them. This thesis investigated more in depth the phase of temporary support of the soil. It would be valuable extending the analysis to other parts of the construction sequence as well.

8.2 Recommendations

TBM and soil displacement logs are a valuable source of information usually available as part of the normal tunnel construction process. However, had the scope of this research been defined before the design and operation of the monitoring facilities even better quality control on the monitoring data could have been possible. Such coordination is recommended in the future to guarantee the adequacy of the measurements’ precision both for production and research standards. Planning and performing additional measurements is also far more sustainable if coordinated in advance.

Recent successes in the use of the tunnel boring technique in urban environment should not distract from the need for a continuous strive for improvement. TBM tunnel construction, even if more technologically advanced than other construction methods, is still heavily based on the experience from previous projects. When that is the case, learning curves are long, overall risk profile remains high, precautions are extensive, and overall construction costs remain higher than necessary. Preservation, evaluation, and transfer of the acquired experience should be encouraged in pair with renovated urge for research.

Additional research is recommended on the correlation between the TBM kinematics and the induced soil displacements in light of the compensating effect which the grout mortar proved to have on the kinematic effects of shield advance. Such research should include accurate measurement of the grouting volumes and pressures in the tail void and around the shield. A detailed numerical model of the grout injection and penetration would also help to evaluate its influence. The role of the face support fluid typically used in slurry TBMs should also be investigated because that too could contribute to reducing the effect of soil relaxation by infiltrating around the shield.

The number of simplifications introduced in the model of mechanical equilibrium proposed in this thesis can be reduced. Possible aspects of further refinement include the transfer of a transversal force between the TBM and the tunnel lining, a more sophisticated model to describe the flow of grout around the TBM-shield, and the effect of the face support fluid (bentonite slurry) on the friction rate between the TBM-skin and the surrounding soil.

As stated in Section 8.1 innovative TBM driving strategies and more consistent soil settlement predictions seem to be in sight. A possible approach addressing both aspects would entail modelling the displacements induced by the TBM on the body of soil surrounding it. Such model would have to account for, at least, the real kinematic behaviour of the TBM-shield and for the penetration of the tail grout and of the face support fluid in the interspace between the shield-skin and the excavated geometry. Aspects such as soil excavation at the TBM-front, face support strategy, tail-grout consolidation and hardening, and loading of the tunnel lining were not part of this research but should be included as well. Also important to observe is that should future TBM-driving algorithms be based on the TBM-soil interface displacements, reliability, consistency, and precision of the shield positioning system would need to undergo stricter surveillance being the positioning data the foundation of the kinematic analysis.

Bibliography

[1] A. Bezuijen et al.. Field Measurements of Grout Pressures during Tunnelling of the Sophia Rail Tunnel. *Soils and Foundations*, Vol. 44, No. 1, 39-48, Feb. 2004

[2] A. Bezuijen. Bentonite and grout flow around a TBM. In *Proceedings of the ITA-AITES World Tunnel Congress. Underground Space – the 4th Dimension of Metropolises*. Prague, 2007

[3] A. Bezuijen and A.M. Talmon. Processes around a TBM. In *Proceedings of the International Symposium on Geotechnical Aspects of Underground Construction in Soft Ground (Shanghai, 2008)*. CRC Press, 2009

[4] P.J. Bogaards and K.J. Bakker. Longitudinal bending moments in the tube of a bored tunnel. In *Numerical Models in Geomechanics, Numog VII*, Graz, Austria, Sept. 1999

[5] W. Broere. Tunnel Face Stability & New CPT Applications. *Ph. D. dissertation*, Delft University of Technology, 2001

[6] W.F. Brumund, G.A. Leonards. Experimental Study of Static and Dynamic Friction Between Sand and Typical Construction Materials. *Journal of Testing and Evaluation*, 1(2):162-165, 1973

[7] R. Butterfield and K. Z. Andrawes. On the angles of friction between sand and plane surfaces. *Journal of Terramechanics*, 8(4):15-23, 1972

[8] DAUB - Deutscher Ausschuss für unterirdisches Bauen. Recommendations for Static Analysis of Shield Tunnelling Machines. *Tunnel*, 7/2005

[9] R. Debrauwer. Groutbelasting op een tunnellining. *Eindrapport van Afstudeeronderzoek*, Delft University of Technology, 2002

[10] J. Düllmann et al.. Analysis of Soil-Machine-Interactions (Part 1): Processing of TBM-Machine-Data and Extraction of excavation-specific data. *EURO:TUN 2013. 3rd International Conference on Computational Methods in Tunnelling and Subsurface Engineering*. Bochum, 2013

[11] J. Düllmann et al.. Practical TBM Excavation Data Processing. *Tunnels and Tunnelling – International Edition*. May 2014

[12] D. Festa et al.. Tunnel-boring process in urban environment. Modelling for reliability. In *Proceedings of the 7th International Symposium on Geotechnical Aspects of Underground Construction in Soft Ground (Rome, 2011).* CRC Press, 2012

[13] D. Festa et al.. Tunnel-boring process in soft soils: improved modelling for reliability enhancement. Kinematic behaviour and tail grouting monitoring. In *Proceedings of the*

ITA-AITES World Tunnel Congress. Underground Spaces in the Service of a Sustainable Society. Helsinki, 2011

[14] D. Festa et al.. An investigation into the forces acting on a TBM during driving – Mining the TBM logged data. *Tunnelling and Underground Space Technology*, 32:143-157, 2012

[15] D. Festa et al.. Tunnelling in soft soil: Tunnel Boring Machine operation and soil response. In *International Symposium on Tunnelling and Underground Space Construction for Sustainable Development*. Seoul, 2013

[16] D. Festa et al.. Kinematic behaviour of a Tunnel Boring Machine in soft soil: theory and observations. *Tunnelling and Underground Space Technology.* 2014(1) (under review)

[17] D. Festa et al.. Correlation between the kinematics of a Tunnel Boring Machine and the observed soil displacements. *Tunnelling and Underground Space Technology*. 2014(2) (under review)

[18] T. Hashimoto et al. Study on earth pressure acting upon shield tunnel lining in clayey and sandy grounds based on field monitoring. In *Proceedings of the International Symposium on Geotechnical Aspects of Underground Construction in Soft Ground (Shanghai, 2008).* CRC Press, 2009

[19] F.J. Kaalberg and V. Hentschel. Tunnelling in Soft Soil with a High Water Level and Piled Foundations. In *Proceedings of the ITA-AITES World Tunnel Congress. Challenge for the 21st Century.* Oslo, 1999

[20] T. Kasper and G. Meschke. A 3D finite element simulation model for TBM tunnelling in soft ground. *International Journal for Numerical and Analytical Methods in Geomechanics*, 28:1441-1460, 2004

[21] T. Kasper and G. Meschke. On the influence of face pressure, grouting pressure and TBM design in soft ground tunnelling. *Tunnelling and Underground Space Technology*, 21:160-171, 2006

[22] K. Komiya et al.. Finite element modeling of excavation and advancement processes of a shield tunneling machine. *Soils and Foundations*, 39:37-52, 1999

[23] R. Krot. On the effects of the passage of a TBM-shield on the surrounding soil. *Master thesis.* Delft University of Technology, June 2012

[24] G.A. Lancea and J.M. Anderson. The risk to third parties from bored tunnelling in soft ground. *HSE – Health and Safety Executive, Research Report 453*. Norwich, 2006

[25] B. Maidl et al.. Mechanised Shield Tunnelling. Ernst & Sohn LTD., 2012

[26] R.J. Mair et al.. Subsurface settlement profiles above tunnels in clay. *Géotechnique*, 43(2):315-320, 1993

[27] R. J. Mair and R.N. Taylor. Prediction of clay behaviour around tunnels using plasticity solutions. In *Predictive Soil Mechanics. Proceedings of the Worth Memorial Symposium*. St. Catherine’s College, Oxford, pages 449-463, 1992

[28] R. J. Mair et al.. Prediction of ground movements and assessment of risk of building damage due to bored tunnelling. In *Proceedings of the International Symposium on Geotechnical Aspects of Underground Construction in Soft Ground (London, 1996).* Balkema, 1996

[29] R.J. Mair and R.N. Taylor. Bored tunnelling in the urban environment. State-of-the-art Report and Theme Lecture. In *Proceedings of 14th International Conference on Soil Mechanics and Foundation Engineering*, Vol. 4, pages 2353-2385. Hamburg, 1997

[30] R.J. Mair. Muir Wood Lecture: Tunnelling in urban areas and effects on infrastructure – Advances in research and practice. In *Proceedings of the ITA-AITES World Tunnel Congress. Underground Spaces in the Service of a Sustainable Society*. Helsinki, 2011

[31] D. Muir Wood. Soil behaviour and critical state soil mechanics. Cambridge University Press, 1990

[32] F.J. Nagel. Numerical modelling of partially saturated soil and simulation of shield-supported tunnel advance. *Ph.D. dissertation*, Ruhr-University Bochum, 2009

[33] F.J. Nagel et al.. Process-oriented numerical simulation of shield tunneling in soft soils. *Geomechanics and Tunnelling*, 3(3):268-282, 2010

[34] H. Netzel. Building Response Due to Ground Movements. *Ph.D. dissertation*, Delft University of Technology, 2009

[35] J. Ninič and G. Meschke. Model update and real-time steering of tunnel boring machines using simulation-based meta models. *Tunnelling and Underground Space Technology*, 45:138-152, 2015

[36] North-South Metro Line, Amsterdam, 2010-2013 (private communications)

[37] R.B. Peck. Deep excavations and tunnelling in soft ground. In *Proceedings of the 7th International Conference Soil Mechanics and Foundation Engineering*, State of the Art Volume, pages 225-290. Mexico City, 1969

[38] J.G. Potyondy. Skin Friction between Various Soils and Construction Materials. *Géotechnique*, 11(4):339-353, 1961

[39] A. Sramoon and M. Sugimoto. Development of ground reaction curve for shield tunnelling. *In Proceeding of the 3rd International Symposium on Geotechnical Aspects of Underground Construction in Soft Ground (Tokyo, 1999)*. Balkema, 2000

[40] J.R. Standing and D. Selemetas. Greenfield ground response to EPBM tunnelling in London Clay. *Géotechnique*, 63(12):989-1007, 2013

[41] M. Sugimoto and N.T.H. Luong. Soil properties based on in-situ data of the shield driven method. In *Proceedings of the International Symposium on Geotechnical Aspects of Underground Construction in Soft Ground (London, 1996)*. Balkema, 1996

[42] M. Sugimoto and A. Sramoon. Theoretical model of shield behavior during excavation. I: Theory. *Journal of Geotechnical and Geoenvironmental Engineering*, 128(2):138-155, 2002

[43] M. Sugimoto et al.. Simulation of Shield Tunnelling Behavior along Curved Alignment in a Multilayered Ground. *Journal of Geotechnical and Geoenvironmental Engineering*, 133(6):684-694, 2007

[44] A.M. Talmon et al.. Grout pressures around a tunnel lining. *Tunneling. A decade of progress*. Taylor & Francis/Balkema, 2001

[45] A.M. Talmon and A. Bezuijen. Analytical model for the beam action of a tunnel lining during construction. *International Journal for Numerical and Analytical Methods in Geomechanics*, 37:181-200, 2013

[46] TEC – Tunnel Engineering Consultants. Hubertustunnel – Geotechnisch Basis Rapport, HT-GBR. 2005

[47] TEC – Tunnel Engineering Consultants. Hubertustunnel – Geotechnisch Interpretatie Rapport, HT-GIR. 2005

[48] A. Verruijt. A complex variable solution for a deforming circular tunnel in an elastic halfplane. *International Journal for Numerical and Analytical Methods in Geomechanics*, 21:77-89, 1997

[49] A. Verruijt. Deformations Westerschelde Tail Skin. *Delft University of Technology*, 2003

[50] C. Vliet, van der et al. Shield Tail Deformations: Experience, Mechanics and Lessons. In *Proceedings of the ITA-AITES World Tunnel Congress. Safe Tunnelling For The City and For The Environment*. Budapest, 2009

[51] Hai-Sui Yu. Cavity Expansion Methods in Geomechanics. Springer Science + Business Media, Dordrecht, 2000

Appendix A

TBM Monitoring data

#	Parameter	Unit		#	Parameter	Unit
1	Date	jjjjmmdd		132	Bentonite level point 1	0/1
2	Time	s		133	Bentonite level point 2	0/1
3	Ring number	-		134	Bentonite level point 3	0/1
4	Status	-		135	Bentonite level point 4	0/1
5	Seconds since 1/1/1970	s		136	Bentonite level point 5	
6	CW rotations (cumulative)	-		137	Bentonite level point 6	0/1
7	Tangential distance covered by CW	m		138	Bentonite level point 7	0/1
8	Total number grout injection strokes	-		139	Bentonite level point 8	0/1
9	Shield tail sealant (front) – Total strokes	-		140	Bentonite level point 9	0/1
10	Shield tail sealant (rear) – Total strokes	-		141	Bentonite level point 10	0/1
11	Back-train pulling force	kN		142	Weekend transport circuit	0/1
12	Discharged soil volume	m^3		143	Valve V030 open	0/1
13	Theoretical TBM discharged volume	m^3		144	Valve V030 closed	0/1
14	Theoretical discharged volume	m^3		145	Valve V031 (bypass) open	0/1
15	Path actually covered	mm		146	Valve V031 (bypass) closed	0/1
16	Factor of soil structure	%		147	Valve V032 open	0/1
17	Mean value (last 10) of excavated soil	m^3		148	Valve V032 closed	0/1
18	Discharged weight	t		149	Valve V050 open	0/1

#	Parameter	Unit		#	Parameter	Unit
19	Theoretical discharged weight	t		150	Valve V050 closed	0/1
20	Mean value (last 10) of discharged weight	t		151	Valve V051 open	0/1
21	Roll	mm/m		152	Valve V051 closed	0/1
22	Reservoir temperature	°C		153	Position thrust cylinders A	mm
23	Level water reservoir	m		154	Position thrust cylinders B	mm
24	Pressure bentonite tank	kPa		155	Position thrust cylinders C	mm
25	Pressure transmission oil 1	bar		156	Position thrust cylinders D	mm
26	Pressure transmission oil 2	bar		157	Position thrust cylinders E	mm
27	Transmission oil temper-ature	°C		158	CW position adjustment A	mm
28	Density in the return line	t/m^3		159	CW position adjustment B	mm
29	CW shift pressure A (bottom side)	bar		160	CW position adjustment C	mm
30	CW shift pressure A (rod side)	bar		161	Current CW	A
31	CW shift pressure B (bottom side)	bar		162	Frequency FU 01	Hz
32	CW shift pressure B (rod side)	bar		163	Rotational speed engine FU 01	1/min
33	CW shift pressure C (bottom side)	bar		164	Current FU 01	A
34	CW shift pressure C (rod side)	bar		165	Torque FU 01	kNm
35	Thrust cylinders avg. pressure	bar		166	Desired internal moment FU 01	%
36	Thrust cylinders group A	bar		167	Frequency FU 02	Hz
37	Flow rate return water	m^3/h		168	Rotational speed engine FU 02	1/min
38	Thrust cylinders group B	bar		169	Current FU 02	A
39	Density in the supply line	t/m^3		170	Torque FU 02	kNm
40	Thrust cylinders group C	bar		171	Desired internal moment FU 02	%

#	Parameter	Unit	#	Parameter	Unit
41	Temperature supplied cooling water	°C	172	Frequency FU 03	Hz
42	Thrust cylinders group D	bar	173	Rotational speed engine FU 03	1/min
43	Pressure supplied cooling water	bar	174	Current FU 03	A
44	Thrust cylinders group E	bar	175	Torque FU 03	kNm
45	Pressure tail sealant front (1.01)	bar	176	Desired internal moment FU 03	%
46	Pressure tail sealant front (1.02)	bar	177	Frequency FU 04	Hz
47	Pressure tail sealant front (1.03)	bar	178	Rotational speed engine FU 04	1/min
48	Pressure tail sealant front (1.04)	bar	179	Current FU 04	A
49	Pressure tail sealant front (1.05)	bar	180	Torque FU 04	kNm
50	Pressure tail sealant front (1.06)	bar	181	Desired internal moment FU 04	%
51	Pressure tail sealant front (1.07)	bar	182	Frequency FU 05	Hz
52	Pressure tail sealant front (1.08)	bar	183	Rotational speed engine FU 05	1/min
53	Pressure tail sealant rear (3.01)	bar	184	Current FU 05	A
54	Pressure tail sealant rear (3.02)	bar	185	Torque FU 05	kNm
55	Pressure tail sealant rear (3.03)	bar	186	Desired internal moment FU 05	%
56	Pressure tail sealant rear (3.04)	bar	187	Frequency FU 06	Hz
57	Pressure tail sealant rear (3.05)	bar	188	Rotational speed engine FU 06	1/min
58	Pressure tail sealant rear (3.06)	bar	189	Current FU 06	A
59	Pressure tail sealant rear (3.07)	bar	190	Torque FU 06	kNm

#	Parameter	Unit		#	Parameter	Unit
60	Pressure back-train	kPa		191	Desired internal moment FU 06	%
61	Pressure tail sealant rear (3.08)	bar		192	Frequency FU 07	Hz
62	Bentonite level ultrason-ic probe	m		193	Rotational speed engine FU 07	1/mi n
63	Flow rate supply pump P0.1	m^3/h		194	Current FU 07	A
64	Flow rate return line	m^3/h		195	Torque FU 07	kNm
65	Pressure supply line at the back train	kPa		196	Desired internal moment FU 07	%
66	Flow rate shield skin lubrication fluid	m^3/h		197	Frequency FU 08	Hz
67	Pressure bentonite shield skin	kPa		198	Rotational speed engine FU 08	1/mi n
68	Pressure injected grout 1	kPa		199	Current FU 08	A
69	Pressure injected grout 2	kPa		200	Torque FU 08	kNm
70	Pressure injected grout 3	kPa		201	Desired internal moment FU 08	%
71	Pressure injected grout 4	kPa		202	Frequency FU 09	Hz
72	Pressure injected grout 5	kPa		203	Rotational speed engine FU 09	1/mi n
73	Pressure injected grout 6	kPa		204	Current FU 09	A
74	Pressure excavation chamber centre-right	kPa		205	Torque FU 09	kNm
75	Pressure excavation chamber top-right	kPa		206	Desired internal moment FU 09	%
76	Air pressure working chamber	kPa		207	Frequency FU 10	Hz
77	Flow rate feed pump	m^3/h		208	Rotational speed engine FU 10	1/mi n
78	Flow rate at the sub-merged wall	m^3/h		209	Current FU 10	A
79	Flow rate right stator	m^3/h		210	Torque FU 10	kNm
80	Flow rate left stator	m^3/h		211	Desired internal moment FU 10	%
81	Pressure excavation chamber centre-left	kPa		212	Grout injection strokes A1	-

#	Parameter	Unit	#	Parameter	Unit
82	Pressure excavation chamber top-left	kPa	213	Grout injection strokes A2	-
83	Air flow 1	m^3/min	214	Grout injection strokes A3	-
84	Flow rate grout line A1	m^3/h	215	Grout injection strokes A4	-
85	Flow rate grout line A2	m^3/h	216	Grout injection strokes A5	-
86	Flow rate grout line A3	m^3/h	217	Grout injection strokes A6	-
87	Flow rate grout line A4	m^3/h	218	Active grease valve	-
88	Flow rate grout line A5	m^3/h	219	Strokes tail sealant front L01	-
89	Flow rate grout line A6	m^3/h	220	Strokes tail sealant front L02	-
90	Air flow 2	m^3/min	221	Strokes tail sealant front L03	-
91	Current agitator 2 (left)	A	222	Strokes tail sealant front L04	-
92	Current agitator 1 (right)	A	223	Strokes tail sealant front L05	-
93	Current pump P0.1	A	224	Strokes tail sealant front L06	-
94	Pressure extension return pipes	kPa	225	Strokes tail sealant front L07	-
95	Rotational speed suction pump P2.1	1/min	226	Strokes tail sealant front L08	-
96	Current suction pump P2.1	A	227	Strokes tail sealant rear L01	-
97	Inlet pressure suction pump P2.1	kPa	228	Strokes tail sealant rear L02	-
98	Outlet pressure suction pump P2.1	kPa	229	Strokes tail sealant rear L03	-
99	Total driving tilting moment	kNm	230	Strokes tail sealant rear L04	-
100	Application point in X direction	m	231	Strokes tail sealant rear L05	-
101	Application point in Y direction	m	232	Strokes tail sealant rear L06	-
102	Titling moment My	kNm	233	Cascade bridging time	s
103	Tilting moment Mx	kNm	234	Transmission oil bridging time	s

#	Parameter	Unit		#	Parameter	Unit
104	Thrust on the CW	kN		235	Grease injection bridging time	s
105	Advance rate	mm/min		236	Cutting wheel cooling time	s
106	Penetration	Mm		237	Bentonite level bridging time	min
107	Torque on the CW	kNm		238	Tail sealant bridging time	s
108	Thrust applied by thrust cylinders	kN		239	Removal blocked grease bridging time	s
109	Rotational speed CW	1/min		240	Rolling bridging time	s
110	CW position adjustment left	mm		241	Strokes tail sealant rear L07	-
111	CW position adjustment right	mm		242	Strokes tail sealant rear L08	-
112	VMT: reference station rear	m		243	VMT: longitudinal slope	m
113	VMT: reference station front	m		244	VMT: roll	m
114	VMT: global X-coordinate reference point front	m		245	VMT: RP CW horizontal	m
115	VMT: global Y-coordinate reference point front	m		246	VMT: RP CW vertical	m
116	VMT: global Z-coordinate reference point front	m		247	VMT: RP TBM horizontal	m
117	VMT: global X-coordinate reference point rear	m		248	VMT: RP TBM vertical	m
118	VMT: global Y-coordinate reference point rear	m		249	VMT: CW horizontal position	m
119	VMT: global Z-coordinate reference point rear	m		250	VMT: CW vertical position	m
120	Rotational speed suction pump P1.1	1/min		251	VMT: tunnel meter (station)	m

#	Parameter	Unit	#	Parameter	Unit
121	Current suction pump P1.1	A	252	VMT: horizontal trend TBM	m
122	Inlet pressure suction pump P1.1	kPa	253	VMT: vertical trend TBM	m
123	Outlet pressure suction pump P1.1	kPa	254	VMT: horizontal trend CW	rad
124	Rotational speed suction pump P2.2	1/min	255	VMT: vertical trend CW	rad
125	Current suction pump P2.2	A	256	Total volume grout mortar	m^3
126	Inlet pressure suction pump P2.2	kPa	257	Volume grout mortar line Gr. 1	m^3
127	Outlet pressure suction pump P2.2	kPa	258	Volume grout mortar line Gr. 2	m^3
128	CW rotation clockwise	0/1	259	Volume grout mortar line Gr. 3	m^3
129	CW rotation counter clockwise	0/1	260	Volume grout mortar line Gr. 4	m^3
130	Drilling status	0/1	261	Volume grout mortar line Gr. 5	m^3
131	Ring building status	0/1	262	Volume grout mortar line Gr. 6	m^3

Acknowledgements

First and foremost I wish to thank my supervisors, Prof. Johan Bosch and Dr. Wout Broere. Johan, Wout, from the very beginning of my doctoral period you have always been tremendously supportive. I found your coordination in supervising me simply amazing. You guys magnificently combined and complemented your very own qualities and experience with the exclusive aim of creating the best possible working environment. The trust that you put in me will not be forgotten.

A considerable part of the research was performed in parallel with the construction of the North-South metro line in Amsterdam. Although that does not emerge from the thesis, in which data from another project is analysed, the North-South metro line provided the opportunity to observe from very close an example of tunnel construction. It would be lengthy to mention all the people from *Projectbureau Noordzuidlijn* that made that possible. I will limit myself to recall Joost Joustra and Hans Gaumann, and I hope that all other people involved will feel recalled through them as well. Joost, Hans, your support was very much appreciated.

A special thanks goes to my friends and roommates at the TU Delft Jan van Dalen and Rodriaan Spruit. Mates, the easiness in the relationship with the two of you made my stay in Delft kind of natural. My decision to continue my professional life in the Netherlands is largely due to having met the two of you.

I am grateful to André Heim (Herrenknecht AG), Andreas Beyer (VMT GmbH), and Vincent Schuurmans (Fugro N.V.) for their useful and patient technical support. I am also grateful to Professor Arnold Verruijt for his brilliant advices particularly in the initial stage of my PhD.

I like to mention all the colleague PhD-students and staff members of the Geo-Engineering Section of the TU Delft. Many useful conversations influenced this work and also sustained me particularly in some (unavoidable) difficult days. A special mention is for Jon Nuttall and for his heroic patience at helping to solve my informatics problems.

A personal thanks to my family of origin. Mamma, papà, Nicola, you started to support me in this doctoral project much earlier than it actually started. And continued to do so all through it. You only know how tiring your supporting me must have been. Grazie di cuore.

My last and most personal thanks goes to Annalisa, my wife. Decisions in life are sometimes easy, just a matter of yes or no. Well, on that winter day by the sea in Ravenna you said yes to many things altogether. And you were tremendously consistent with that afterwards. I will never manage to reward you enough for that.

Biographical note

Daniele Festa was born in Faenza (Italy) in 1980. After attending the *Liceo Scientifico* E. Torricelli in Faenza he studied Civil Engineering at the *Alma Mater Studiorum A.D. 1088* University of Bologna where he graduated in 2006. After a professional experience as civil engineering consultant Daniele joined the Delft University of Technology (Netherlands) in 2009.

In Delft Daniele performed a doctoral research on the reliability and predictability of mechanised shield tunnelling in soft soil. The research was performed within the Chair of Underground Space Technology under the guidance of Prof. J.W. Bosch and Dr. W. Broere.

During his doctoral years Daniele gained considerable insight in soft soil tunnelling particularly by taking part, as observer, to the construction of the North-South metro line in Amsterdam. He presented his research work at several international conferences and had papers accepted by international journals. In 2014, after the completion of his doctoral programme, he went back to the professional sector as consultant.

In 2000 Daniele obtained the Cello Performing Diploma from the Cesena Conservatory of Music (Italy).